VOLUME 34 JANUARY 1956 NUMBER 1

Canadian Journal of Physics

Editor: G. M. VOLKOFF

Associate Editors:

L. G. ELLIOTT, *Atomic Energy of Canada, Ltd., Chalk River*
J. S. FOSTER, *McGill University*
G. HERZBERG, *National Research Council of Canada*
L. LEPRINCE-RINGUET, *Ecole Polytechnique, Paris*
R. W. PRINGLE, *University of Manitoba*
B. W. SARGENT, *Queen's University*
Sir FRANCIS SIMON, *Clarendon Laboratory, University of Oxford*
W. H. WATSON, *University of Toronto*

Published by THE NATIONAL RESEARCH COUNCIL

OTTAWA CANADA

CANADIAN JOURNAL OF CHEMISTRY

(*Formerly Section B, Canadian Journal of Research*)

Under the authority of the Chairman of the Committee of the Privy Council on Scientific and Industrial Research, the National Research Council issues THE CANADIAN JOURNAL OF CHEMISTRY and six other journals devoted to the publication, in English or French, of the results of original scientific research. Matters of general policy concerning these journals are the responsibility of a joint Editorial Board consisting of: members representing the National Research Council of Canada; the Editors of the Journals; and members representing the Royal Society of Canada and four other scientific societies.

The Chemical Institute of Canada has chosen the Canadian Journal of Chemistry and the Canadian Journal of Technology as its medium of publication for scientific papers.

EDITORIAL BOARD

Representatives of the National Research Council

A. N. Campbell, *University of Manitoba*
G. E. Hall, *University of Western Ontario*
E. G. D. Murray, *McGill University*
D. L. Thomson, *McGill University*
W. H. Watson (Chairman), *University of Toronto*

Editors of the Journals

D. L. Bailey, *University of Toronto*
T. W. M. Cameron, *Macdonald College*
J. B. Collip, *University of Western Ontario*
G. A. Ledingham, *National Research Council*
Léo Marion, *National Research Council*
R. G. E. Murray, *University of Western Ontario*
G. M. Volkoff, *University of British Columbia*

Representatives of Societies

D. L. Bailey, *University of Toronto*
Royal Society of Canada
T. W. M. Cameron, *Macdonald College*
Royal Society of Canada
J. B. Collip, *University of Western Ontario*
Canadian Physiological Society
R. G. E. Murray, *University of Western Ontario*
Canadian Society of Microbiologists
H. G. Thode, *McMaster University*
Chemical Institute of Canada
T. Thorvaldson, *University of Saskatchewan*
Royal Society of Canada
G. M. Volkoff, *University of British Columbia*
Royal Society of Canada; Canadian Association of Physicists

Ex officio

Léo Marion (Editor-in-Chief), *National Research Council*
F. T. Rosser, Director, Division of Administration, *National Research Council*

Manuscripts for publication should be submitted to Dr. Léo Marion, Editor-in-Chief, Canadian Journal of Chemistry, National Research Council, Ottawa 2, Canada.
(For instructions on preparation of copy, see **Notes to Contributors** (inside back cover).)

Proof, correspondence concerning proof, and orders for reprints should be sent to the Manager, Editorial Office (Research Journals), Division of Administration, National Research Council, Ottawa 2, Canada.

Subscriptions, renewals, requests for single or back numbers, and all remittances should be sent to Division of Administration, National Research Council, Ottawa 2, Canada. Remittances should be made payable to the Receiver General of Canada, credit National Research Council.

The journals published, frequency of publication, and prices are:

Canadian Journal of Biochemistry and Physiology	Bimonthly	$3.00 a year
Canadian Journal of Botany	Bimonthly	$4.00 a year
Canadian Journal of Chemistry	Monthly	$5.00 a year
Canadian Journal of Microbiology	Bimonthly	$3.00 a year
Canadian Journal of Physics	Monthly	$4.00 a year
Canadian Journal of Technology	Bimonthly	$3.00 a year
Canadian Journal of Zoology	Bimonthly	$3.00 a year

The price of single numbers of all journals is 75 cents.

Reprinted in entirety by photo-offset from the original issue.

VOLUME 34 1956

Canadian Journal of Physics

Editor: G. M. VOLKOFF

Associate Editors:

L. G. ELLIOTT, *Atomic Energy of Canada, Ltd., Chalk River*
J. S. FOSTER, *McGill University*
G. HERZBERG, *National Research Council of Canada*
L. LEPRINCE-RINGUET, *Ecole Polytechnique, Paris*
R. W. PRINGLE, *University of Manitoba*
B. W. SARGENT, *Queen's University*
Sir FRANCIS SIMON, *Clarendon Laboratory, University of Oxford*
W. H. WATSON, *University of Toronto*

Published by THE NATIONAL RESEARCH COUNCIL

OTTAWA CANADA

Canadian Journal of Physics

Issued by THE NATIONAL RESEARCH COUNCIL OF CANADA

VOLUME 34 JANUARY 1956 NUMBER 1

THE GEOMAGNETIC LATITUDE EFFECT ON THE NUCLEON AND MESON COMPONENT OF COSMIC RAYS AT SEA LEVEL[1]

BY D. C. ROSE AND J. KATZMAN

ABSTRACT

Measurements have been taken on the changes in intensity of the nucleon and meson components of cosmic rays during a cruise of the Canadian Naval Icebreaker *Labrador* into the Arctic, through the North West Passage, and circumnavigating the North American Continent. The geomagnetic latitudes covered extend from 18°N. to 89°N. The latitude knee is clearly shown at a geomagnetic latitude of about 52° in the case of the nucleon component and less definitely between 40° and 50° in the case of the meson component. The rigidity of particles arriving in a vertical direction at 52° is 2.1 Bv. and at 45° is 3.7 Bv. Meyer and Simpson have shown that changes in the primary spectrum between 1948 and 1954 probably extend up to these rigidities and such changes should, therefore, be observable at sea level. The longitude effect at low latitudes is clearly shown by differences in intensity between the measurements on the east and west sides of North America. In the case of the meson component, the magnitude of the longitude effect at these longitudes was found to be greater than that shown by Millikan and Neher in 1936. The interpretation of the meson component results above the knee is complicated by difficulties in temperature correction. In the case of the nucleon component, an apparent longitude effect exists above the knee in that there was a small difference in the intensity at high latitudes in the eastern and western parts of the North American Arctic. No satisfactory explanation is offered for this. The diurnal variation of the nucleon component at high latitudes is shown but no unusual features were found. Appreciation is expressed to the Royal Canadian Navy for making these measurements possible.

I. INTRODUCTION

The interaction between primary cosmic rays and the earth's magnetic field is explained by the Lemaitre–Vallarta theory of allowed and forbidden orbits. Detailed agreement between theory and measurements is complicated by the fact that the earth's field is not quite equivalent to a centered dipole and because the effects of the atmosphere make extensive direct measurements of primary cosmic rays virtually impossible. Extensive measurements covering an appreciable part of the earth's surface involve the organization of large expeditions and therefore have not very often been undertaken.

The new measurements to be described here were taken at sea level on board the Canadian Navy Icebreaker *Labrador* during its 1954 cruise through the North West Passage and circumnavigating the North American Continent. Both the nucleon and the meson component were measured. The range of latitudes covered (from 18° to 89° N. geomagnetic latitude) includes the so-

[1]Manuscript received August 5, 1955.
Contribution from the Division of Pure Physics, National Research Council, Ottawa, Canada. Issued as N.R.C. No. 3805.

called knee in the intensity vs. geomagnetic latitude curves, that is the point above which the intensity does not increase or increases very slowly.

The position of the knee both at sea level and at high altitude in the atmosphere is very important in analyzing cosmic ray data. Neher, Peterson, and Stern (1953) using measurements taken near the top of the atmosphere in 1951 show that the knee is close to a geomagnetic latitude of 58°N. with reference to the centered dipole magnetic field. Van Allen (1953) and Ellis, Gottlieb, and Van Allen (1954) taking measurements outside the atmosphere at the same epoch confirm a cutoff in the primary spectrum. More recent measurements of Neher and Stern (1955) show that the position of the knee near the top of the atmosphere is not fixed, being much further north in 1954 than in 1951. That this shift in the knee extends well down into the atmosphere was shown by Simpson (1951), Simpson, Fonger, and Treiman (1953), and Meyer and Simpson (1955), taking measurements at airplane altitudes. The change in the position of the knee between 1948 and 1954 was quite appreciable and represents an estimated change in total intensity of as much as 13%.

The position of the knee at low altitudes gives some information about the minimum energy of primary particles that can contribute through the atmosphere to the observed effects. Since it is much easier to take extensive measurements at ground or sea level than higher up in the atmosphere, an accurate knowledge of the latitude effect and its variations is still sufficiently important to justify extensive expeditions. Further, there is the fact that, though it is assumed that the interaction of the earth's magnetic field on primary cosmic rays is effective so far from the earth's surface that the field may be treated as a dipole, the effective position of the dipole or the extent to which this assumption is true is not at all certain. In taking early measurements on the latitude effect, Compton (1933) pointed out that the north and south knees of constant intensity correlate better with geomagnetic latitude than with geographic and it has been the custom since then to relate variations in intensity of cosmic rays with the geomagnetic axis or the axis of the nearest equivalent uniformly magnetized sphere. The longitude effect due to the eccentricity of the nearest equivalent dipole is well known but the analysis by Millikan and Neher (1936) shows that the cosmic ray data such as were then available are not in agreement with the position of the dipole indicated by magnetic analyses (Chapman and Bartels 1940), the minimum intensity at the equator being at approximately 90° E. longitude rather than at 161.8° E. as estimated by Chapman and Bartels (1940).

Probably the most comprehensive previous study of the latitude effect at sea level is that of Compton and Turner (1937) who measured the hard component during several trips between Vancouver and Sydney. The latitude range covered is between 40° S. and 52° N. geomagnetic and indicates a knee at between 35° and 40° though some earlier work placed it at a little higher latitude (Clay 1933). The effect of the atmosphere makes interpretation of measurements of the hard or meson component at high latitude difficult since this component is subject to the well-known temperature effect, the corrections depending on the temperature throughout the atmosphere and for which there is no simple practical method of correcting a large body of data.

The nucleon component measured by neutron production in a "neutron monitor" is believed not to be subject to changes due to temperature variation in the atmosphere. The geomagnetic effect for this component has been observed at airplane altitudes by Simpson (1951), and Simpson, Fonger, and Treiman (1953) have also shown that the temperature effect on this component is zero or very small. In the present experiment both the nucleon component and the meson component were recorded and the advantages of working with the nucleon component because of its lack of a temperature effect are very apparent.

During the period the measurements to be described here were taken (July 23 to November 21, 1954), a neutron monitor and a large counter telescope were also kept in continuous operation at Ottawa. The neutron monitor in particular showed no evidence of appreciable changes in intensity of the type usually associated with solar activity, that is variations in intensity with a 27-day recurrence interval. The sun during that period apparently was unusually quiet. The results, therefore, should represent background without disturbances of the type studied by Simpson (1954).

II. APPARATUS AND EXPERIMENTAL TECHNIQUE

(1) *The Nucleon Component*

The nucleon component was measured using the technique described by Simpson, Fonger, and Treiman (1953) wherein the nucleon component, believed to be protons and neutrons, is detected by the production of neutrons in lead. The neutrons are slowed down in paraffin and detected by boron trifluoride proportional counters. Fig. 1 shows a schematic diagram of the

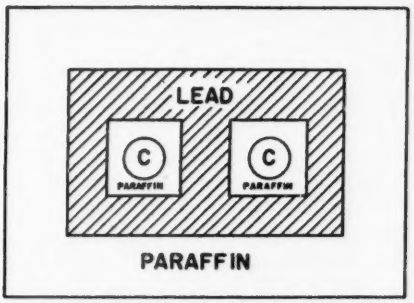

FIG. 1. Schematic arrangement of the neutron monitor.

"neutron monitor" used in this experiment. Two BF_3 (enriched with B^{10}) counters were used, their diameters being 2½ in. and the effective length being 27 in. The counters were mounted in a tubular opening in the center of aluminum tanks 45 in. long and 6 in. square. These two tanks were surrounded by lead for a length of 2 ft. at the center along the axis of the pile, the lead being

in sheets ½ in. thick. There were 4 in. of lead between the central paraffin tanks carrying the counters, 4 in. on top, 3 in. underneath, and 3 in. on the sides. Surrounding this was an outer layer of paraffin 5 in. thick. The outer paraffin was also carried in aluminum tanks 45 in. long so built that there were two tanks on top, two underneath, and one on each side. Since the lead occupied only 24 in. of the 45-in. length of the pile, the spaces at the end of the lead were filled in with paraffin again in suitably shaped aluminum tanks. The aluminum tanks containing the paraffin were welded from 1/8-in. 1S aluminum sheet (the smaller tanks from 1/16-in. sheet). The whole pile when fitted together had over-all dimensions of 45 in. long, 32 in. wide, and 23 in. high. This was housed in a steel frame, the sides of which could be drawn together to clamp the whole pile solidly. The steel frame was then bolted to suitable supports welded to the ship's deck.

The use of aluminum tanks to hold the paraffin was adopted to make the structure reasonably free from danger due to fire and to keep the paraffin from flowing when operating at summer temperatures. The tank structure was readily demountable, the largest tank being $45\times16\times5$ in., and could be handled easily by two men. 1S aluminum was chosen as it was the purest commercial grade and hence would represent the best construction for a minimum absorption of slow neutrons.

The amplifier and recording equipment was as follows. Each neutron counter had a preamplifier located just outside the pile at the head of the counter. The preamplifier was a conventional three-tube ring with feedback and needs no further description here. The preamplifiers had a voltage amplification factor of about 65. These were followed by the main amplifier which consisted of a second ring of three tubes with the same voltage amplification. Operating the counters at 2500 volts gave output pulses due to the boron 10 plus neutron alpha particles of about fifteen volts. The amplifiers were designed to accept a pulse with a time rise of about 0.5 μsec. and had a clipping time of about 10 μsec. The output of the amplifier was fed into a biased diode discriminator and a pulse shaping circuit. From this the pulses were fed into binary scaling circuits of six stages making a scaling factor of 64. The output from the scalers was fed to a 20-pen Esterline Angus operations recorder. The two outer pens, Nos. 1 and 20, were fed minute pulses from a precision chronometer. The Esterline Angus tape was operated at one foot per hour. Message registers were connected in parallel with the 20-pen recorder.

The counting rate at sea level in northern latitudes averaged about 82 pips on the tape per hour, that is 82×64 counts per hour from each neutron counter. The hourly values were usually read by counting the pips for each hour on the tape. The interval between pips on the hour was estimated to the nearest 10th of the distance between pips making a measurement error of not more than $\pm0.2\%$ for hourly values. Since the hourly counting rate gave a standard deviation of 1.4% for each counter or 1% when the two were added, the measurement error was, therefore, trivial. For 12-hr. or daily averages, this error would be even more negligible. The message registers were read every 12 hr. or could have been read oftener if anything had gone wrong with the recorder.

This method of recording has been found very useful in the cosmic ray observatory at Ottawa. Counting the pips on the Esterline Angus tape is somewhat tedious but operating the recorder continuously at 0.2 in. per min. and adjusting scaling factors to give between 50 and 100 pips per hour gives a very good record of what is happening. If power troubles cause the equipment to be off for a few minutes, or even seconds, or intense line transients produce extra counts (a thing that is almost impossible to eliminate completely on shipboard though they were never more than a few a day), it is always apparent on the Esterline Angus record. The bad minutes can be dropped and the statistical error for that hour is not increased appreciably. Further, if intensity fluctuations such as solar flare phenomena occur, the recorder tape gives a great deal of detail. Averaging times down to a minute can be used, of course, with corresponding loss of accuracy.

At the Ottawa observatory where a similar neutron monitor is kept in continuous operation, an additional scaler is added to each channel, recording an additional set of pips four times fewer in number but matching every fourth pip. This eases the counting of the hourly values and we have found this method simpler than photographic recording of message registers. The neutron counters had been thoroughly tested and were tested and calibrated periodically throughout the voyage. A cadmium sheath could be slipped in the tube carrying the counters to surround the counters. The sheath consisted of two layers of 25 mils cadmium sheet which would reduce the count of neutrons to negligible numbers if the neutrons were all in the energy band below the absorption edge for cadmium. Actually tests of cosmic-ray-produced neutrons of different fluxes moderated by paraffin in this type of experiment show that the reduction factor is more like 30 or 40. The fact that boron 10 has an appreciable cross-section for neutrons of energies above the cadmium absorption energy makes this quite understandable. The actual cadmium background at high latitudes was 140 ± 13 counts per hour but the majority of these were those transmitted by the cadmium and absorbed by the boron. The true background is believed to be not more than 12 counts per hour and to be consistent. This represents only 0.25% of the counting rate. Neglecting it would not affect any of the results to be discussed here and, therefore, no correction was made for background.

Tests were also made periodically for the flatness of the plateau of counting rate with varying the high voltage on the neutron counters. The plateau was not as flat as had been hoped, a variation of 1% on the high voltage causing an average variation of 0.9% in the counting rate. The regulation of the high voltage was accomplished by using a Sorensen electronic regulator on the a-c. side of the high voltage power pack. This method had been found very satisfactory at Ottawa and it involved no complicated high voltage electronic regulators. An accurate Weston voltmeter was kept in the high voltage circuit continuously and the variation observed many times per day. The variations noted were practically always less than $\pm 0.25\%$.

Tests were also made for variation with biasing of the pulse height discriminator. The mean pulse height was about fifteen volts. The noise level was

less than one volt. Varying the discriminator by 0.1 volt made 0.16% change in the counting rate and regular checking of the bias voltage indicated that it did not change by more than ±0.1 volt.

The flatness of these plateaus for neutron counters of this sort can be shown to be a function of the amplifier design. A relatively slow amplifier with a long clipping time gives a much better plateau than a fast amplifier. A rise time as long as one microsecond and a clipping time of twenty or more microseconds would have given better plateaus. Some experiments carried out with faster amplifiers having a rise time of 0.1 μsec. or better and short clipping times (0.5 to 2 μsec.) demonstrate this effect very clearly. For such fast amplifiers and short clipping times the pulse shape depends considerably on where the α particle occurs in the counter, and a wide range in shapes can be seen on a fast oscilloscope. The present amplifiers were too fast to give the best plateaus but were quite satisfactory for the purpose and of very simple design.

For plateau tests and calibration a neutron source was available. This introduced some difficulties on the shipboard monitor since a strong source would have been troublesome in cramped quarters and a very weak source would not give a high counting rate. The spontaneous fission of uranium metals has been found to be useful as a steady source of neutrons and for shipboard calibration a box of uranium strips* bound in an aluminum case was occasionally put in a hole in the monitor pile cut in the lead and paraffin for that purpose. The calibration rate was a little too slow for good results, it being necessary to leave the source in for six hours to get 0.3% statistics. The actual calibrations were not as successful as expected since the method was planned only just before the equipment was installed, and was not properly tested. The calibration was very sensitive to the position of the uranium source which could not be sufficiently accurately maintained during different calibrations. Calibrations every two or three weeks showed a standard deviation of ±0.9% rather than the 0.3% statistics and it is believed the stability of the counters and circuitry was much better than this. No attempt was made to correct for individual calibrations.

(2) *The Meson Component*

The meson component was observed by a triple coincidence telescope. Each of the three trays of Geiger counters contained eight counters 1 in. in diameter and 16 in. effective length. The telescope was made very compact, the top two trays were separated by only ½ in. with no shielding between them except the aluminum case carrying the counters. The second and third trays were separated by 5½ in., there being 5 in. of lead shielding between them. It was considered at first that a cubical design of telescope should be adopted such as has been recommended for cosmic ray observations for the international geophysical year. Such a telescope has been in operation at Ottawa for some time but at sea and at remote stations it has been decided to keep the equipment as simple as possible so that it will operate reliably with a minimum of testing. Using

*The uranium strips were loaned to us by Atomic Energy of Canada Limited and we wish to thank Dr. W. B. Lewis for arranging this loan.

the eight counters per tray in a compact telescope, the triple coincidence counting rate was close to 14,000 per hour in northern latitudes.

Each counter tray contained a preamplifier and a cathode follower stage in the end of the tray. The high voltage circuit was split so that either four of the eight counters could have their voltage taken off without affecting the capacity of the coupling circuit to the preamplifier. This gave a simple method of testing because when a scaler is operated directly from a counter tray, the difference between three counters (if one had failed) and four could be detected in a minute or so, whereas the difference between seven and eight would have required a much more careful test. The operation of the whole telescope could be checked in this way in a few minutes.

The pulses from the trays were fed to a pulse shaping circuit and a coincidence circuit which has been used successfully for several years in the Ottawa observatory. It is slightly unconventional in that coincidences are formed by adding at the biased grid of the mixing tube rather than the more usual Rossi circuit. The resolving time was about 2 μsec. To give a thorough check on the operation of the circuits, the coincidence channels and scalers were duplicated. We have found this duplication to be very useful in detecting trouble. Almost any trouble in the pulse shaping or coincidence part of the circuit will put the two recording channels out of synchronism and a glance at the recorder chart shows this up. This is of value because normally this equipment in the observatory at Ottawa runs continuously for months with a minimum of routine checking and when a large quantity of such equipment is kept in continuous operation, it is necessary to keep the time required for testing at a minimum.

Triple coincidences were recorded using a scaling factor of 256, the output being put on the Esterline Angus 20-pen operations recorder. Double coincidences were recorded between trays 1 and 2 using a scaling factor of 1024. The counting rate for doubles was about 40,000 per hour. This included the total component except for the shielding of the roof of the hut housing the equipment. The double telescope is also almost omnidirectional since the two trays were very close together. Correction for the total component is very uncertain, and though a great deal of data on it have been collected, little use has been made of them and they will not be reported here.

(3) *Location of the Equipment*

The neutron monitor and the counter telescope were housed in a hut about 8 ft. square built into the base of the mast of H.M.C.S. *Labrador*. This was the best position available, it being the highest position on the ship and free from changes in surrounding material that might produce secondary neutrons, such as moving cargo or boats. The hut was heated and insulated and though there was no automatic temperature control the temperature was kept at $80\pm10°$F. The temperature of the neutron monitor would change only very slowly since it weighed in all over 3000 lb. There was no evidence of any effect due to temperature changes.

The Geiger counter telescope was housed in a special box which was insulated

and temperature controlled. The temperature was kept at 90°F. Coincidence counting of this sort has been found to be quite insensitive to the telescope temperature provided it does not go low enough for the alcohol in the counters to start to condense. Our experience is that these counters do not change their rate sufficiently to affect coincidences until the temperature is below about 55°F. The failure of a thermostat at one time brought the temperature of the box up to 110°F. with no apparent effect on the coincidence rate.

The shielding in the roof of the hut was 4 in. of cork and $\frac{1}{4}$ in. of steel. The mast was an open tower structure and carried several radar antennae. This made the exact shielding rather uncertain but since all the equipment was either omnidirectional or accepted a very large solid angle, the effect of the mast structure and the radar antennae overhead was probably very small.

For comparison with the results during the voyage around the North American continent an identical neutron monitor was kept in operation at Ottawa, the shielding over it being of the same order and the amplifiers and recording equipment identical.

A large cubical counter telescope was also operated at the cosmic ray observatory at Ottawa during the time of the voyage.

At Resolute (lat. 74° 41′ N., long. 94° 54′ W., geomag. lat. 83° N.) a small triple coincidence telescope had been in operation since 1949. This was replaced in August by a larger telescope identical with that aboard the *Labrador* described above. The results of the Resolute observations during the Arctic part of the voyage will be discussed later in this paper.

(4) *Meteorological Data*

The *Labrador* carried a full surface meteorological station but did not have sonde equipment for upper atmosphere measurements. Pressure and temperature data were supplied by the meteorological office.

An accurate measure of pressure aboard a ship is difficult. There were several barographs and a mercury barometer. A barograph was located in the cosmic ray hut and checked regularly with the mercury barometer in the meteorological office. The meteorological office was below the main deck of the ship but sufficiently near open hatches that ventilation pressures should not affect the readings. When the cosmic ray hut was closed up in cold weather whistling winds in the ventilators often caused barometer movements of a fraction of a millibar. Rolling of the ship makes an instrument relying partially on a gravity balance inaccurate even if it is well damped. Carefully comparing hourly readings on the mercury barometer with the barograph in the cosmic ray hut indicated that pressure effects due to wind could not be eliminated and variable differences between the two positions of a fraction of a millibar and occasionally as high as a millibar which must be due to eddy pressures of the wind were apparent. For hourly values the mercury barometer was taken as standard except when there appeared to be obvious occasional errors or when hourly readings on it were missed. The daily means were taken from the average of the hourly readings. Although the barometric data were kept to the nearest 10th of a millibar, because of the above difficulties it is felt that an accuracy greater than ± 0.3 millibars cannot be claimed. This is a problem

that will always occur in shipboard experiments of this type. This makes a small contribution to the statistical error.

Since upper atmosphere temperatures were not available and it is generally accepted that surface temperature is not a satisfactory variable in correcting for meteorological effects on the meson component, a detailed record of the temperature was not kept with the cosmic ray records. It was, of course, kept in the meteorological office and hourly values and thermograph records are available. The temperature effect on the meson component will be discussed after the results are presented. No temperature effect was expected in the case of the nucleon component.

(5) *Latitude and Longitude*

The position of the ship was reported every three hours to the meteorological office and this record was used for the cosmic ray results. Navigation problems in the Arctic are difficult because charts are imperfect, and often the sun was not visible for days. Navigation in close waters was visual or by radar on shore prominences which may or may not be correctly charted. Further, while icebreaking the dead-reckoning method of navigation is useless. The position of the ship was kept as well as possible and for the most part it was known to within two or three miles but sometimes this uncertainty would be as high

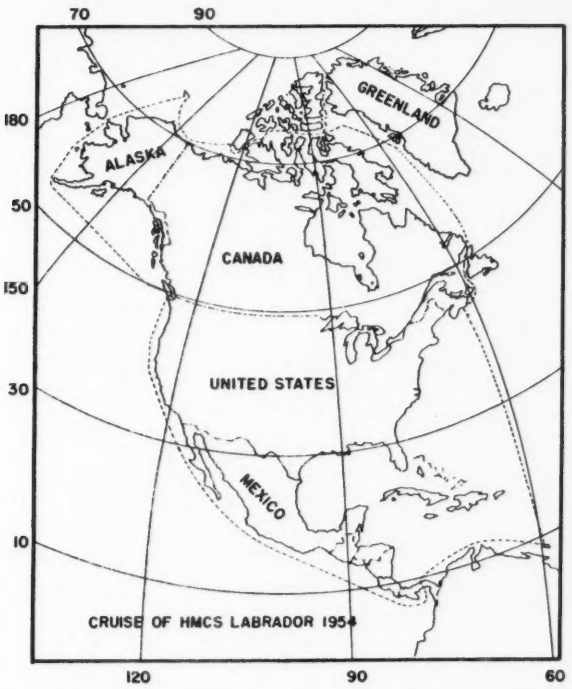

FIG. 2. Map of North America showing the course where cosmic ray measurements were taken.

as ten to twenty miles. This represents about 20 minutes in latitude but may be a degree or more in longitude at high latitudes.

When travelling north or south at open water cruising speeds, the ship covered about 6° of latitude per day. In analyzing the results for the latitude effect, therefore, 12-hr. averages were used. The position latitudes and longitudes of the three-hourly records were averaged to give a mean latitude and longitude for the 12-hr. period. Fig. 2 shows a map of North America and the course of the ship. The voyage started from Halifax on July 23, 1954. The highest latitude was reached on August 9 and the ship stayed in that area for four days. Considerable time was spent in the North West Passage at a latitude of about 75° and between longitudes 85° W. and 100° W. Some time was also spent in the Chukchee Sea area north of Alaska. The cruise reached Victoria on September 28, Panama on November 3, Grenada on November 10, and returned to Halifax on November 21, 1954.

III. RESULTS

(1) *The Nucleon Component*

Fig. 3 shows the results of the measurements of the nucleon component plotted day by day throughout the voyage. Corrections have been made for pressure using a barometer coefficient of -9.9% per cm. of mercury or -0.74% per millibar. This corresponds to absorption lengths of 136 gm./cm.^{2} This was

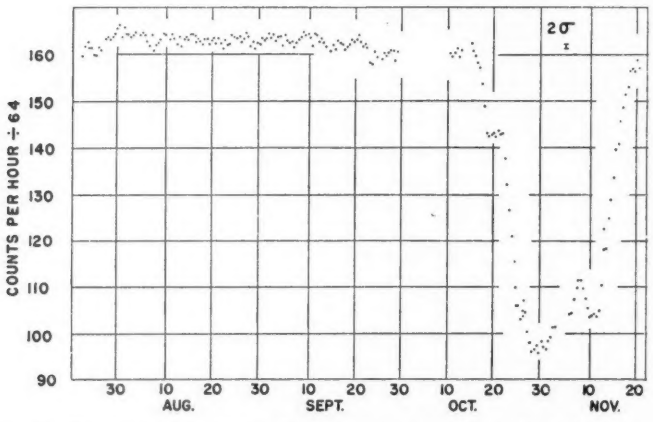

FIG. 3. The nucleon component. Twelve-hour averages throughout the voyage.

the actual coefficient found during the northern part of the expedition, that is from July 28 at lat. 67° N., long. 55° W. to September 23, lat. 57° N., long. 167° W. A linear regression was calculated between pressure and intensity giving the value $-0.744\pm0.007\%$ per mb. For the Ottawa neutron data the barometer coefficient is evaluated for each month. The mean during the months of August, September, and October, 1954, was -0.76% per mb. A previous set of measurements of a six-month period in 1952–53 at a time of low solar

activity gave a value of -0.72% per mb. Simpson, Fonger, and Treiman (1953) also give a value of -0.72% per mb. but point out the difficulty of getting a good barometer effect when other intensity variations are present. The monthly values at Ottawa show a much greater variation than the statistical variance derived from each month's analyses.

The method used in making the barometer corrections merits some discussion. Using a linear expression the correction should be

$$\delta I = -I_m \beta \delta p, \tag{1}$$

I_m being the mean intensity over the whole period of observations. The actual absorption is, however, closely exponential in which case for small variations the correction

$$\delta I = -I\beta\delta p \tag{2}$$

can be used, I being the intensity observed during the immediate period for which the correction is made. For larger variation in pressure, the integral value should be used and

$$\delta I = I(1-e^{-\beta(p-p_m)}), \tag{3}$$

where the m subscript again refers to means over the whole period of the experiment. Equation (2) is a first approximation to equation (3) and this method of correction was used, β being the coefficient found by linear regression during the part of the cruise north of the latitude knee. Using equation (1) would lead to difficulties below the knee where the intensity change due to latitude was rapid. The difference between (2) and the more accurate expression (3) was considered too small to justify the computation necessary to use (3).

An attempt was made to derive a barometer coefficient in the tropics during the present voyage but was complicated by the rapid changes due to latitude. Picking a few days of nearly equal mean intensity near Panama and using three-hour averages produced a barometer coefficient of $-0.81\pm0.38\%$ per mb. This is not significantly different from that in the north but is of very low accuracy partly because the extremes of barometer variation at that time were only a few millibars.

It should be noted in Fig. 3 that the intensities at Halifax on July 23 and on November 20 are significantly different. This may be a seasonal or annual change in intensity and is consistent with changes in the Ottawa value at the same time. The changes in the Ottawa value were taken to represent a world-wide annual variation and the shipboard results were corrected proportionately. This brought the Halifax values at the beginning and end of the voyage together and the corrected results are shown in Fig. 4, the intensity being plotted against geomagnetic latitude.

The geomagnetic latitude for each 12-hr. average was estimated by using McNish (1936) curves, but correcting for a change in the position of the geomagnetic axis given by the more recent calculations of Vestine *et al.* (1947). McNish's curves were based on a pole at lat. 78.5° N., long. 69.0° W., while the later analysis gives lat. 78.6° N., long. 70.1° W. The latitude correction

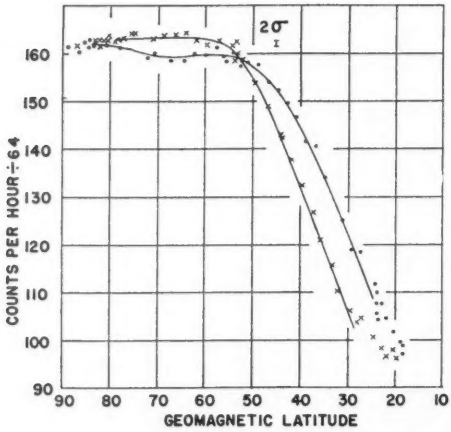

FIG. 4. The nucleon component. Intensity plotted as a function of geomagnetic latitude. The solid circles represent measurements on the eastern side of the North American Continent and crosses, the western side.

was not used since it was small and would involve considerable computation, but the longitude correction was readily made to McNish's curves. A few actual calculations showed that his method was well within the accuracy of known positions of the ship. In Fig. 4 the solid circles represent the east side of the continent and the crosses the west. The east side gives a truer picture of the geomagnetic latitude effect since the curve from Grenada right to within a degree of the geomagnetic pole was almost on one longitude circle, deviating only by a few degrees.

Each point on the curve represents a minimum of 12 hr., that is a standard deviation due to counting variations of 0.3%. Allowing for errors of 0.2% due to voltage variation, and 0.1% due to difficulties in getting good pressure readings (averaged over 12 hr., this is probably a fair estimate of the error) an over-all standard deviation of 0.4% is quite generous. The value of 2σ shown in Fig. 4 is the counting rate error only. For points where the ship was at anchor for some days or when the geomagnetic latitude was changing only very slowly, longer averages were used, otherwise some parts of the curve would be too cluttered with points to be intelligible. The counting rate error for such points is, of course, smaller than that shown. At low latitudes where the longitude was changing rapidly, the curve is not completed.

The important features of this result are: (1) the position of the latitude "knee" at sea level, (2) the demonstration of the longitude effect, and (3) the difference in the curves at high latitude representing the voyage north and the return south. These points will be discussed separately. The position of the latitude knee appears to be further north than in the case of the meson component. Its position outside the earth's atmosphere during 1951 was shown by Neher, Peterson, and Stern (1953) to be about 58°. At 30,000 ft., Meyer and

Simpson (1955) show the knee at about 55° N. in 1954 though it was as low as 50° in 1948. The present result places the knee at sea level at around 52° but it is very difficult to define it sharply. The rigidity of particles for these latitudes according to the Stormer theory is such that the minimum energies for protons arriving vertically are 0.6 Bev. for 58°, 1.0 Bev. for 55°, and 1.5 Bev. for 52° or a little less than half that value per nucleon for particles of mass $2Z$. If one can assume that the yield of neutrons at sea level is closely related to the number of vertical primaries, these figures indicate that an appreciable portion of primary particles with energies as low as 1.5 Bev. can contribute to neutron production at sea level. At points where the geomagnetic cutoff and the cutoff in the primary spectrum are near each other, the effect low down in the atmosphere may depend to some extent on the angular distribution of secondaries produced by primary particles. The Stormer and shadow cone is still opening for particles in the east and north at large zenith angles with energies well above the supposed spectral cutoff.

That primaries of energies as low as 1.5 Bev. may contribute to neutron production at sea level is not surprising. The energy loss of a singly charged ionizing particle in penetrating the atmosphere to sea level is about 2 Bev. The absorption length is about 140 gm./cm.^{2} but the geometric cross-section for energetic nucleon interactions in air is about 68 gm./cm.^{2} The sea level nucleon is probably 15 to 20 generations from the primary particle and since the interactions involved are probably charge independent, half the ancestors are likely to be neutral. The limiting energy loss by ionization, therefore, will be much smaller than for the mesonic component of cosmic rays. On the other hand, in each collision the secondary nucleon will usually have only a fraction of the energy of the colliding particle.

Meyer and Simpson (1955) show that the change in primary spectrum between 1948 and 1954 extends up to quite high rigidities, probably as high as 4 or 5 Bv. For such rigidities the energy of vertically incident nucleons would be quite sufficient to contribute appreciably to neutron production at sea level. Measurements of the latitude effect at latitudes around the knee should be repeated as often as possible at sea level since they will give information on changes in the primary spectrum.

The exact position of the knee also depends on longitude as the curves in Fig. 4 show. The calculations for minimum vertical energy given above are based on a centered dipole without correction for longitude. The present measurements on the east side of the continent and those of Neher, Peterson, and Stern (1953) and Neher and Stern (1955) were taken on approximately the same course and therefore, are comparable. If, however, the position of the magnetic axis which controls the motion of cosmic rays differs appreciably from that derived from surface magnetic measurements, these energies are wrong. A more quantitative analysis of the behavior around the knee is best left until more complete knowledge becomes available. The same equipment used for these measurements has recently been taken to the Antarctic aboard the U.S.N. Icebreaker *Atka* and much information will be available from that expedition.

The longitude effect is shown in Fig. 4, referring particularly to the differences between the two curves at low latitude. For comparison with other measurements the value of $\left(\frac{\delta I}{\delta \phi} \Big/ \frac{\delta I}{\delta \lambda}\right)_{\lambda}$ at $\lambda = 40°$ has been calculated, where ϕ and λ are geomagnetic longitude and latitude. At airplane altitudes Simpson (1951) found a value of 0.33 for geographic longitudes between 95° and 110° W. The present data gave a value considerably lower, 0.1 (geographic longitude was used for ϕ rather than geomagnetic since the difference would not affect the present discussion). Close agreement with Simpson's value should not be expected at sea level where the total latitude effect is much smaller than at airplane altitudes.

The third prominent feature of these results, namely the difference in intensity above the knee on the east and west sides of the Canadian Arctic, is very interesting. The effect is shown in Fig. 4 by the difference in the east and west curves between geomagnetic latitudes of 55° to 80° and is large enough to be significant. A careful analysis of all possible errors indicates that this difference is real, but it should be pointed out that the lower curve from geomagnetic latitudes 56° to 80° N. represents only the first five days the equipment was operating, and on two of these days there were some minor circuit troubles. These, however, resulted in the loss of data for only a few hours. Making all possible corrections, the mean difference between the eastern and western curves, including all data between geomagnetic latitudes 55° and 80°, is 1.8%. Omitting the correction for world-wide changes based on the monitor at Ottawa, this difference is 0.7% which is still a significant amount in consideration of the data used.

This difference may be due to (1) the seasonal or annual variation being different in northern regions from that at Ottawa (the eastern and western measurements in this area were separated in time by over a month), (2) some residual meteorological or instrumental temperature effect, or (3) a distortion in the earth's magnetic field. Unfortunately none of these can be eliminated completely though the second, that is a meteorological or instrumental temperature effect, seems very unlikely. In regard to (3), the true geomagnetic axis is, of course, not at the center of the earth and the field is not quite equivalent to a simple dipole.

(2) *The Meson Component*

Fig. 5 shows the meson component measurements corrected only for barometric pressure. The correction used was that actually found in the Arctic part of the voyage. The same period was used as in the case of the nucleon component. The value is $2.5 \pm 0.1\%$ per cm. of mercury or $0.19 \pm .01\%$ per mb. The difference in the two curves above the latitude knee is assumed to be largely due to differences in temperature. The need for temperature correction is, therefore, very obvious. The surface temperatures between latitudes 60° and 70° were uniformly 11°C. higher on the eastern part of the voyage than on the western. Since the intensity was also fairly uniform over these latitudes, a correction coefficient could be worked out from the data in this interval.

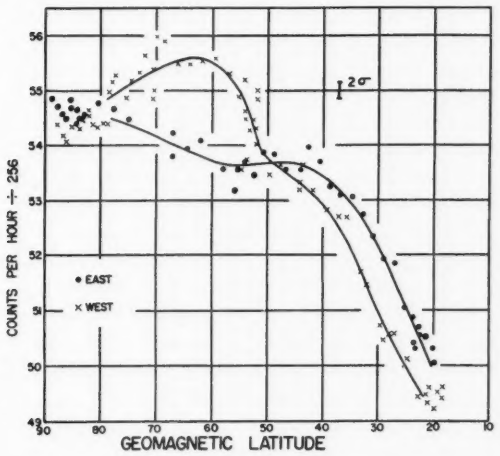

FIG. 5. The meson component. Intensity plotted as a function of geomagnetic latitude. The solid circles represent measurements on the eastern side of the North American Continent and crosses, the western side.

Such a correction applied to the results throughout the voyage based on surface temperatures gave an impossible result and is not reproduced. Another method was tried, namely using the Resolute data. Assuming that during the period the ship was in Arctic waters, that is above geographic latitudes of about 55° N., the mean vertical distribution of meterological conditions would be roughly the same over the whole area or the same over the ship and over Resolute, the meson intensity at Resolute could then be taken as an index of temperature and annual variations. A smooth curve was therefore drawn through the Resolute data (corrected, of course, for pressure variations) and the ship results were corrected (after pressure correction) proportionately to the variation of the Resolute data from its mean.

The difficulty with this correction was that a purely arbitrary tapering off of the correction had to be adopted as the ship moved out of the Arctic area into the Pacific, as here the air mass was bound to be different. The results shown in Fig. 6 have the Arctic parts of the curve corrected in the above manner but no corresponding correction for the parts of the curve below geomagnetic latitudes of about 50°. The only justification for this is that it gives a result that looks reasonable. It makes the measurements on the eastern and western parts of the voyage comparable, but the magnitude of the intensity change from north to south will be unreal. This magnitude is also unreal without any temperature correction as in Fig. 5. In Fig. 5 and Fig. 6, as in the case of the nucleon data, 12-hr. averages were used but where the latitude was changing so slowly that too many points had to be placed on the curve, consecutive groups were averaged. The smooth line in Fig. 6 was drawn through the points above the knee without reference to the easterly and westerly differences since the spread in the points was considerable.

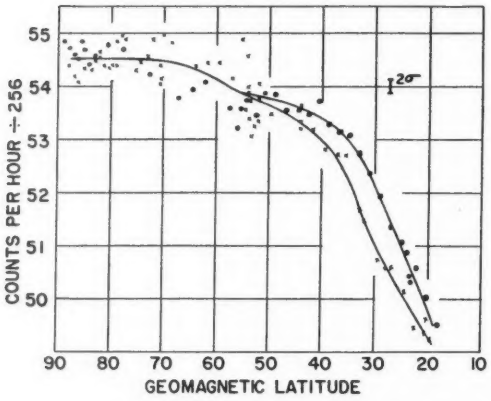

FIG. 6. The meson component. As in Fig. 5 but corrected for intensity variations at Resolute.

Two features to be noted in these results are: (1) They show the advantages of working with the nucleon component where the complication of temperature correction throughout the atmosphere is very small if it exists at all. (2) The position of the latitude knee (best shown in Fig. 5) is not very definite although it is considerably farther north than in the most comprehensive work published previously on this type of measurement. Compton and Turner (1937) place the knee at between 35° and 40° but show a considerable increase in intensity above it, the most northerly measurements shown being about 52° N. geomagnetic latitude. The present data would place it between 40° and 50°. The rigidity of particles arriving vertically at 45° is 3.7 Bv. or the minimum energy for protons is 3.1 Bev. It is still possible that the variations in the primary spectrum could affect measurements at these latitudes.

The longitude effect is shown clearly at lower latitudes and is in agreement in direction with that found by Millikan and Neher (1936). The value of

$$\left(\frac{\delta I}{\delta \phi} \Big/ \frac{\delta I}{\delta \lambda}\right)_{\lambda=30^\circ} = 0.14.$$

To compare these with Millikan and Neher's curves, it is more satisfactory to examine the quantity $\delta I \Phi / I_k \, \delta \Lambda$, where Λ and Φ refer to geographic latitude and longitude and I_k is the intensity above the knee. The present results give a value of 0.078% per degree of longitude for this quantity at $\Lambda = 20°$, while Millikan and Neher's curves give a value of 0.040%. The present results, therefore, indicate a greater slope in the variation of intensity with longitude than is shown by Millikan and Neher. This would suggest that the maximum in intensity at the geomagnetic equator is farther east than is shown by Millikan and Neher or is more in agreement with the position that would be expected from the eccentricity of the dipole as calculated from geomagnetic measurements.

IV. THE DIURNAL VARIATION OF THE NUCLEON COMPONENT

Since changes in the diurnal variation show some relation to solar activity (Firor, Fonger, and Simpson 1954), differences in the diurnal variation at different latitudes might be expected due to the sun as a possible source of at least part of the cosmic ray flux (Firor 1954). The results of the Arctic part of the cruise were examined for diurnal variation. The hourly values were used for this analysis and only the data from July 28 to September 22, that is during the part of the cruise well above the latitude knee. The diurnal values at lower latitudes where the intensity was changing rapidly due to latitude would be impossible to sort out. The barometer variation for the northern part was eliminated by taking the differences from the hourly values and the value indicated by the regression line for the pressure during that hour.

The diurnal variation is shown in Fig. 7, the interval being divided into two parts, the period of July 28 to August 31 and September 1 to September 22. The first part covers the period the ship was at higher geomagnetic latitude

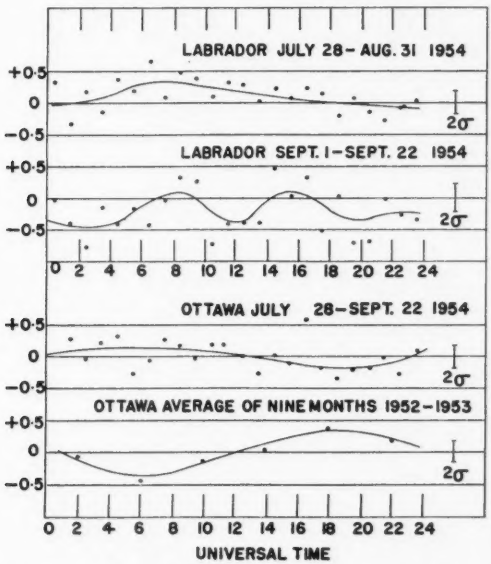

FIG. 7. The diurnal variation of the nucleon component. The first curve (at the top) represents the measurements above geomagnetic latitude 78°N. from July 28 to August 31, 1954. The second curve represents measurements in the western Arctic area from September 1 to September 22, 1954. The third curve shows the diurnal variation at Ottawa from July 28 to September 22, 1954, and the fourth curve shows the diurnal variation at Ottawa for nine months during 1952–53.

than 78° N. During this period the cruise covered a large range of geomagnetic longitudes and for a few days was within one degree of the geomagnetic pole. Since the effective position of the pole is not certain, to try to convert to geomagnetic time seemed useless and, therefore, the results are plotted on uni-

versal time. The usual curve for local time variation (see, for instance, Firor, Fonger, and Simpson 1954, or Fonger 1953) shows a variation of the order of 1% amplitude with a maximum just after local noon though the amplitude and shape of the diurnal curve varies with solar activity. The data for the top curve in Fig. 7 were also converted to local solar time but the smooth curve looks practically the same except for a phase shift of about six hours and that would be roughly the difference between universal time and the local time for the mean position of the ship. This curve does show a diurnal variation but with almost the opposite phase of that usually found during the past few years and with a low amplitude of a little over $\frac{1}{2}$% and not very high statistical significance. The second curve shows the results from September 1 to 22. Here the local geomagnetic time variation due to changing position of the ship would be spread over only about three hours and, therefore, the universal time plot would not be appreciably different from that for local time except for an appropriate phase shift. Actually this curve shows too wide a scatter to interpret any diurnal variation.

The third curve represents the data for Ottawa during the whole period July 28 to September 22. The variation is small and irregular. Since solar activity was low during that period, this is consistent with other results. The fourth curve shows some previous data taken at Ottawa with an older neutron monitor of much lower counting rate. The statistics were so low that four-hour averages were used and the period covered is nine months during 1952–53. The diurnal variation with a peak a little after local noon is shown. Noon at Ottawa is 17 hr. U.T.

V. DISCUSSION AND SUMMARY

The data presented here show the variation in intensity of cosmic rays from geomagnetic latitudes of about 18° N. to 89° N., of both the nucleon component (measured by local neutron production) and the meson component (triple coincidence counter telescope) at sea level. The measurements were taken on both sides of the North American Continent and show the longitude effect very clearly. The series on the eastern side represent a narrow range of longitudes and give the true latitude effect at a longitude of approximately 60° W. The knee in the latitude effect is at about 52° in the case of the nucleon component and between 40° and 50° in the case of the meson component. The minimum energy of protons in allowed orbits reaching the earth vertically at these latitudes is 1.5 Bev. and about 3 Bev. Since Meyer and Simpson (1955) have shown that the low energy primary spectrum in this range has changed considerably since 1948, the exact position of the knee and the shape of the curve probably changes from time to time, and such sea level measurements should be repeated several times during a solar cycle. The knee in the meson component variation is not sharp and the interpretation of the results is complicated by difficulties in temperature correction. The knee is, however, considerably farther north than it was placed by a previous comprehensive set of measurements by Compton and Turner (1937).

The nucleon component shows a significant difference in intensity between measurements going north roughly along the geographic meridian containing the geomagnetic pole and going westward from there through the North West Passage and the Beaufort Sea. This difference is interesting and the present data indicate a high probability that it is real though no definite explanation for it is presented. Residual meteorological effects, an annual variation differing at different latitudes, or distortions in the earth's magnetic field are suggested as possible causes.

The diurnal variation of the nucleon component in Arctic regions is small and irregular as would be expected during low solar activity. The diurnal variation in the meson component was not analyzed since it would be complicated by temperature effects.

These data represent the northern part of a set of data taken with the same equipment going from the Arctic to the Antarctic. The southern part was carried out in collaboration with J. A. Simpson and with the assistance of the U. S. Navy and will be published separately. The complete measurements will give a more accurate presentation of the effect of the earth's field on cosmic rays than has been available previously.

ACKNOWLEDGMENT

The authors wish to express appreciation to the Royal Canadian Navy for carrying the equipment during the 1954 cruise of H.M.C.S. *Labrador*. A special hut was built in the ship to house the equipment. Our particular thanks are due to Captain O. C. S. Robertson, R.C.N., and the Officers of the ship who contributed greatly to the success of the investigation.

REFERENCES

CHAPMAN, S. and BARTELS, J. 1940. Geomagnetism. The Clarendon Press, Oxford.
CLAY, J. 1933. Naturwissenschaften, **21**: 43.
COMPTON, A. H. 1933. Phys. Rev. **43**: 387.
COMPTON, A. H. and TURNER, R. N. 1937. Phys. Rev. **52**: 799.
ELLIS, R. A., GOTTLIEB, M. B., and VAN ALLEN, J. A. 1954. Phys. Rev. **95**: 147.
FIROR, J. W. 1954. Phys. Rev. **94**: 1017.
FIROR, J. W., FONGER, W. H., and SIMPSON, J. A. 1954. Phys. Rev. **94**: 1031.
FONGER, W. H. 1953. Phys. Rev. **91**: 351.
MCNISH, A. G. 1936. Terrestrial Magnetism and Atm. Elec. **41**: 37.
MEYER, P. and SIMPSON, J. A. 1955. Phys. Rev. **99**: 1517.
MILLIKAN, R. A. and NEHER, H. V. 1936. Phys. Rev. **50**: 15.
NEHER, H. V., PETERSON, V. Z., and STERN, E. A. 1953. Phys. Rev. **90**: 655.
NEHER, H. V. and STERN, E. A. 1955. Phys. Rev. **98**: 845.
SIMPSON, J. A. 1951. Phys. Rev. **83**: 1175.
——— 1954. Phys. Rev. **94**: 426.
SIMPSON, J. A., FONGER, W., and TREIMAN, S. B. 1953. Phys. Rev. **90**: 934.
VAN ALLEN, J. A. 1953. Nuovo cimento, **10**: 630.
VESTINE, E. H., LAPORTE, L., LANGE, I., and SCOTT, W. E. 1947. The geomagnetic field, its description and analysis. Dept. of Terrestrial Magnetism, Carnegie Inst. Wash. Publ. 580.

SOME NOTES ON THE THEORY OF THERMAL-NEUTRON REACTORS[1]

By J. D. Stewart

ABSTRACT

Equations for the asymptotic steady-state distribution of neutrons in homogeneous and lattice-type reactors are derived without making any assumptions about the mechanism of diffusion, except the obviously necessary one that the probability for a neutron which is born at one given point to be captured at a second given point is a function only of the distance between these two points. The equations are seen to be of a form that admits of exponential solutions, these are written down, and equations for the Laplacians are derived. A clear-cut definition of the migration area of a lattice reactor is given, and it is pointed out that in a reactor of this type there is no unique value of the Laplacian but rather a range of values.

INTRODUCTION

We assume that the reader has some knowledge of reactor theory (Glasstone and Edlund 1952; Goodman 1947; Soodak and Campbell 1950; Weinberg 1952). The reactor theory discussed in this paper is restricted to steady states of thermal-neutron reactors of either the homogeneous (part I) or the lattice (part II) type, but it should be noted that some of the ideas may be applicable to other types of reactor. The necessity of applying boundary conditions is avoided by assuming that the reactors extend to infinity; the solutions of the equations for neutron density etc. are then said to be asymptotic, and they can be negative in some parts of space outside the actual reactor. In any real reactor the finite boundary introduces a perturbation that is appreciable over a fraction of the reactor, and this fraction increases as the excess of the multiplication factor k over 1 increases. Very roughly speaking if $k > 1.3$ the asymptotic solution will not approximate the true density in any appreciable fraction of the reactor.

The reader will recall that one can make any one of several different assumptions about the diffusion process in a reactor (elementary one-group diffusion theory, two-group theory, elementary diffusion theory of thermal neutrons plus age theory of slowing-down, etc.) and still arrive at the same equation for the asymptotic thermal-neutron density ρ:

$$\Delta\rho(\mathbf{r})+K^2\rho(\mathbf{r}) = 0, \tag{1}$$

where Δ is the three-dimensional Laplacian operator, $\mathbf{r}$ is the position vector, and K^2 is called the Laplacian of the reactor. The reason all these assumptions lead to the same equation is that they have an important component in common: the probability that a neutron which is born at one point will be captured at a second point is a function only of the distance between the two points. In this paper we take this necessary common component as our *only* assumption about the diffusion process and derive an equation equivalent to

[1]Manuscript received in original form April 14, 1955 and, as revised, July 25, 1955.
Contribution from Atomic Energy of Canada Limited, Chalk River, Ontario. Issued as A.E.C.L. No. 257.

(1); by substituting an exponential solution in our derived equation we obtain an expression for the Laplacian in terms of the moments of the above probability. Reference is made at the appropriate places to the work of Placzek and Volkoff (1947) and Plass (1952).

I. EQUATIONS FOR NEUTRON DISTRIBUTION AND LAPLACIAN OF A HOMOGENEOUS REACTOR

Let $\rho(\mathbf{r})$ = number of thermal neutrons being captured per cc. per sec. at $\mathbf{r}$ (the neutron density is proportional to ρ),

k = multiplication factor of the reactor

= number of thermal neutrons produced per thermal neutron captured,

$P(|\mathbf{r}-\mathbf{r}'|)d\mathbf{r}'$ = probability that a neutron which is produced in fission caused by the capture of a thermal neutron at $\mathbf{r}$ and which escapes resonance capture suffers thermal capture in the element of volume $d\mathbf{r}'$ at $\mathbf{r}'$.

The desired equation for $\rho(\mathbf{r})$ is obtained by equating $\rho(\mathbf{r})$ to the sum of all the neutrons being created per second throughout the reactor and being captured per cc. as thermal neutrons at $\mathbf{r}$:

$$\rho(\mathbf{r}) = k \int_{\substack{\text{all}\\ \text{space}}} \rho(\mathbf{r}')P(|\mathbf{r}'-\mathbf{r}|)d\mathbf{r}'. \tag{2}$$

We can at once write down an exponential solution of (2):

$$\rho(\mathbf{r}) = \exp i\mathbf{K}\cdot\mathbf{r} = \exp i(K_x x+K_y y+K_z z), \tag{3}$$

where $\mathbf{K}$ must satisfy

$$k\int P(|\mathbf{r}'-\mathbf{r}|) \exp [i\mathbf{K}\cdot(\mathbf{r}'-\mathbf{r})]\, d(\mathbf{r}'-\mathbf{r}) = 1. \tag{4}$$

(Note that (3) satisfies (1).)

In order to get an explicit expression for K^2 we proceed as follows. Choose the x-axis parallel to $\mathbf{K}$. Then $\mathbf{K}\cdot\mathbf{r} = Kx$. Expand the exponential in powers of Kx and change the order of integration and summation; the result is

$$k\sum_{j=0}^{\infty} (-1)^j K^{2j} M_{2j} = 1, \tag{5}$$

where

$$M_{2j} = \frac{1}{(2j)!}\int\int\int P(\sqrt{x^2+y^2+z^2})\, x^{2j} dx\, dy\, dz$$

is $1/(2j)!$ times the $(2j)$th moment of $P(r)$ in the x-direction. M_2 is called the migration area of the neutrons and is usually denoted by M^2. Using the expansion of the reciprocal of the series in (5) we get

$$k = 1+M_2K^2+(M_2^2-M_4)K^4+(M_2^3-2M_2M_4+M_6)K^6+\ldots, \tag{6}$$

or

$$k-1 = M_2K^2+\ldots. \tag{6a}$$

Finally we invert this series, i.e. get K^2 as a series in powers of $k-1$ instead of $k-1$ in powers of K^2:

$$(7)\quad K^2 = \frac{k-1}{M_2}\left[1-\left(1-\frac{M_4}{M_2^2}\right)(k-1)+\left(1-\frac{2M_4}{M_2^2}-\frac{M_6}{M_2^3}+\frac{2M_4^2}{M_2^4}\right)(k-1)^2+\ldots\right].$$

The above treatment would seem to be the most direct way of obtaining equation (7) and of showing that one gets solutions of the form (3) independently of the diffusion mechanism that is assumed. One could, however, obtain the same results by a simple extension of the work of Placzek and Volkoff (1947); they showed by the Fourier-transform method that in an infinite uniform multiplying medium with $k < 1$ the rate of creation of fission neutrons falls off as $\exp -\mu|z|$ at great distances $|z|$ from a plane source of neutrons *independently of the diffusion mechanism*, and they also obtained the equivalent of the first two terms of (7).

II. EQUATIONS FOR NEUTRON DISTRIBUTION AND LAPLACIAN OF A LATTICE-TYPE REACTOR

An exact theory of the distribution of neutron density is more complicated for this type than for a homogeneous reactor. The method that is usually used to get an approximate equation for this distribution is that of the equivalent homogeneous reactor. Plass (1952) has treated the problem of a lattice-type reactor by using the elementary equation for microscopic diffusion and solving it approximately by the cellular method. In this paper we treat the problem by essentially the same method we have used for the homogeneous reactor. In addition to a spatial periodicity we make some other assumptions in order to get simple derivations of the equations for neutron distribution and Laplacian; one could, however, drop these assumptions without changing the essential form of the derived equations, but the theory would then be considerably more complicated. We accordingly assume that

(i) the reactor consists of a lattice of parallel and exactly similar rods of fissile material;

(ii) the medium between the rods contains no fissile material and has the same periodicity as the lattice of rods;

(iii) the cross-section of the reactor, the neutron density, etc., are independent of distance parallel to the rods (this makes the problem two-dimensional);

(iv) the thermal-neutron absorption in a rod can be considered as taking place on its axis.

The notation is essentially the same as for the homogeneous reactor but it is adapted as follows to our lattice reactor:

k is the number of thermal neutrons of one generation captured in fissile material per thermal neutron of the preceding generation captured in fissile material,

$\mathbf{r}$ is the position vector in a plane normal to the rod axes,

$\rho_a(\mathbf{r})$ is the number of thermal neutrons captured per second per unit length of the rod whose axis is at position $\mathbf{r}$,

$P(\mathbf{s})=P(-\mathbf{s})$ is the probability that a neutron which has escaped resonance capture and also thermal capture in the medium between rods suffers thermal capture in the rod whose position is $\mathbf{s}$ with respect to the rod in which the parent thermal neutron was captured (note that $\sum_{\mathbf{s}} P(\mathbf{s}) = 1$),

$$M_{2j} = \frac{1}{(2j)!}\sum_{\mathbf{s}} x^{2j}P(\mathbf{s}). \tag{8}$$

To get the counterpart of equation (2) we simply equate to $\rho_a(\mathbf{r})$ the total number of thermal neutrons that originate per second throughout the reactor and are captured at $\mathbf{r}$:

$$\rho_a(\mathbf{r}) = k\sum_{\mathbf{s}} \rho_a(\mathbf{r}+\mathbf{s})P(\mathbf{s}), \tag{9}$$

which admits of solutions of the form (3), provided that

$$k\sum_{\mathbf{s}} \exp(i\mathbf{K}\cdot\mathbf{s})P(\mathbf{s}) = 1. \tag{10}$$

(10) is the counterpart of (4), and (7) follows from it as from (4) when the moments are defined by (8). It should be noted that the values of the M_{2j} will depend on the direction chosen for the x-axis. This means that the lattice-type reactor has no unique Laplacian but rather a range of Laplacians. Usually, however, this range is so small that for practical purposes it can be considered to be zero.

To get an expression for the rate of capture of thermal neutrons at any point $\mathbf{r}$, $\rho(\mathbf{r})$, let $f(\mathbf{r}'-\mathbf{r})$ be the value of $\rho(\mathbf{r})$ due to unit value of $\rho_a(\mathbf{r}')$. Then

$$\begin{aligned}\rho(\mathbf{r}) &= \sum_{\mathbf{r}'} \rho_a(\mathbf{r}')f(\mathbf{r}'-\mathbf{r}) \\ &= \sum_{\mathbf{r}'} \exp(i\mathbf{K}\cdot\mathbf{r}')f(\mathbf{r}'-\mathbf{r}) \\ &= \exp(i\mathbf{K}\cdot\mathbf{r})\sum_{\mathbf{r}'} \exp[i\mathbf{K}\cdot(\mathbf{r}'-\mathbf{r})]f(\mathbf{r}'-\mathbf{r}),\end{aligned}$$

i.e.

$$\rho(\mathbf{r}) = \exp(i\mathbf{K}\cdot\mathbf{r})\,Q(\mathbf{r}), \tag{11}$$

where $Q(\mathbf{r})$ has the periodicity of the lattice. Plass (1952) quotes a formula (his number (10)) which is equivalent to (11). His justification would appear to be based on the assumption of the validity of elementary diffusion theory in both moderator and fissile material, whereas our derivation is independent of this assumption.

REFERENCES

GLASSTONE, S. and EDLUND, M. C. 1952. The elements of nuclear reactor theory. D. Van Nostrand Company, Inc., New York.

GOODMAN, C. 1947. *Editor*. The science and engineering of nuclear power. Vol. II. Addison-Wesley Publishing Company, Inc., Cambridge, Mass.

PLACZEK, G. and VOLKOFF, G. 1947. Can. J. Research, A, **25**: 276.

PLASS, G. 1952. J. Appl. Phys. **23**: 621.

SOODAK, H. and CAMPBELL, E. C. 1950. Elementary pile theory. John Wiley & Sons, Inc., New York.

WEINBERG, A. M. 1952. Am. J. Phys. **20**: 40.

RADIATION RESISTANCE OF DIPOLES IN AN INTERFACE BETWEEN TWO DIELECTRICS[1]

By James R. Wait[2]

ABSTRACT

Exact expressions are derived for the radiation resistance of electric and magnetic dipoles located in the plane interface between two semi-infinite lossless dielectrics.

The radiation resistances of both electric and magnetic dipoles situated in lossless media of infinite extent are well-known quantities (Schelkunoff 1943). For example, if the length of the current element or electric dipole is dl the resistance R_0 is given by

$$R_0 = 80\pi^2(dl/\lambda_1)^2 \text{ ohms} \tag{1}$$

where λ_1 is the wavelength of the radiation. The corresponding value $\bar{R}_0$ for a small loop of area ds or magnetic dipole is given by

$$\bar{R}_0 = 320\ \pi^4(ds/\lambda_1^2)^2 \text{ ohms.} \tag{2}$$

When the dipoles are situated in an inhomogeneous medium the values of R_0 and $\bar{R}_0$ can be somewhat different. Sommerfeld and Renner (1942) have studied the case where electric dipoles are situated in a medium of dielectric constant ϵ_1 at a height h over a flat interface, below which there is a medium of dielectric constant ϵ_2. Their solution for the radiation resistance R for an electric dipole oriented parallel to the interface is given by

$$\frac{R}{R_0} = 1 - \frac{3\sin\alpha}{2\alpha} + \frac{3(\sin\alpha - \alpha\cos\alpha)}{2\alpha^3} + \frac{3L}{2} \tag{3}$$

where

$$\alpha = 2k_1 h, \qquad k_1 = 2\pi/\lambda_1,$$

and

$$L = \text{real part of } \frac{i}{k_1}\int_0^{\infty} \frac{(\lambda^2 - 2u_1u_2)\lambda e^{-2u_1 h}d\lambda}{k_1^2u_2 + k_2^2u_1} \tag{4}$$

with

$$u_1 = (\lambda^2 - k_1^2)^{\frac{1}{2}}, \qquad u_2 = (\lambda^2 - k_2^2)^{\frac{1}{2}},$$

and

$$k_2 = (\epsilon_2/\epsilon_1)^{1/2}\, k_1.$$

Sommerfeld and Renner were mainly interested in the case where ϵ_2 was complex with a large imaginary part corresponding to a highly dissipative medium. They have evaluated the integral L in an approximate manner with the restriction that $|k_2|$ was much greater than the real quantity k_1 and the height h is not too small.

It is possible to derive an exact expression for the ratio for the interesting

[1]Manuscript received September 21, 1955.
Contribution from the Department of Electrical Engineering, University of Toronto, Toronto, Ontario.
[2]Present address: National Bureau of Standards, Boulder, Colorado, U.S.A.

case when the dipole is situated within the interface, (i.e., $h = 0$) with the restriction that k_2 and k_1 are real. That is, both media are perfect dielectrics. The ratio R/R_0 is now given by:

(5) R/R_0 = imaginary part of

$$-\frac{3}{4k_1}\lim_{h\to 0}\int_0^\infty\left[\frac{\rho-2(\rho-k_1^2)^{\frac{1}{2}}(\rho-k_2^2)^{\frac{1}{2}}}{k_1^2(\rho-k_2^2)^{\frac{1}{2}}+k_2^2(\rho-k_1^2)^{\frac{1}{2}}}\right]\exp[-2h(\rho-k_1^2)^{\frac{1}{2}}]\,d\rho.$$

The integral can be broken into two symmetrical parts so that

$$\frac{R}{R_0} = -\frac{3}{4k_1(k_2^2-k_1^2)}(\Delta_{12}-\Delta_{21}) \tag{6}$$

with

$$\Delta_{12} = \int_0^{k_1^2}\frac{(2k_1^2+k_2^2)\rho-2k_1^2k_2^2}{(k_1^2+k_2^2)\rho-k_1^2k_2^2}(k_1^2-\rho)^{\frac{1}{2}}d\rho, \tag{7}$$

where Δ_{21} is identical in form to Δ_{12} but with k_1 interchanged with k_2. These integrals can be evaluated by standard means, to give

$$\Delta_{12} = \frac{2k_1^2+k_2^2}{k_1^2+k_2^2}\frac{k_1^3}{3}+\frac{k_1^3k_2^4}{(k_1^2+k_2^2)^2}+\frac{k_1^4k_2^4}{2(k_1^2+k_2^2)^{5/2}}\log\left|\frac{(k_1^2+k_2^2)^{\frac{1}{2}}-k_1}{(k_1^2+k_2^2)^{\frac{1}{2}}+k_1}\right|. \tag{8}$$

The ratio R/R_0 is plotted in Fig. 1 as a function of the relative refractive index N defined by

$$N = k_2/k_1 = (\epsilon_2/\epsilon_1)^{1/2}.$$

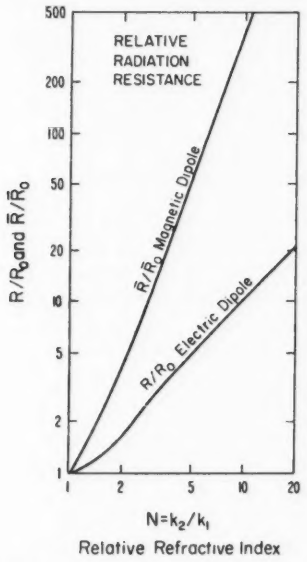

FIG. 1. The ratio of the radiation resistance of electric and magnetic dipoles in an interface to the corresponding value in free space.

At values of N greater than about 5 the following expression is valid to within one per cent:

$$R/R_0 \approx N.$$

The corresponding result for a magnetic dipole or small wire loop can also be derived in a similar manner. For a magnetic dipole oriented normally to the interface it was shown previously (Wait 1952) that the radiation resistance $\bar{R}$ is given by

$$\frac{\bar{R}}{\bar{R}_0} = 1 - \frac{3(\sin\alpha - \alpha\cos\alpha)}{\alpha^3} + \frac{3\bar{L}}{2} \tag{9}$$

where

$$\bar{L} = \text{real part of } \frac{2i}{k_1^3}\int_0^\infty e^{-2u_1 h}\frac{\lambda}{u_1+u_2}\,d\lambda. \tag{10}$$

When the height h of the dipole is allowed to approach zero it easily follows that

$$\frac{\bar{R}}{\bar{R}_0} = -\frac{3}{k_1^3(k_2^2-k_1^2)}\left[\int_0^{k_1\rho}(k_1^2-\rho)^{\frac{1}{2}}\rho\,d\rho - \int_0^{k_2\rho}(k_2^2-\rho)^{\frac{1}{2}}\rho\,d\rho\right] \tag{11}$$

which is evaluated to give

$$\frac{\bar{R}}{\bar{R}_0} = \frac{2}{5}\frac{k_2^5-k_1^5}{k_1^3(k_2^2-k_1^2)}.$$

This ratio for the vertically oriented magnetic dipole or small loop situated in the interface is also plotted in Fig. 1 as a function of the relative refractive index N. For large values greater than about 5, the corresponding approximate relation is

$$\frac{R}{R_0} \approx \frac{2}{5}N^2.$$

It is probable that these results can be generalized to radiating systems of finite size, lying on a dielectric medium (i.e., frozen ground or ice), as long as their dimensions are small compared to the wavelength.

REFERENCES

SCHELKUNOFF, S. A. 1943. Electromagnetic waves. D. Van Nostrand Company, Inc., New York. pp. 136, 148.

SOMMERFELD, A. N. and RENNER, F. 1942. Ann. Physik, **41**: 1.

WAIT, J. R. 1952. J. Appl. Phys. **24**: 646.

TRANSIENT FIELDS OF A VERTICAL DIPOLE OVER A HOMOGENEOUS CURVED GROUND[1]

By James R. Wait

ABSTRACT

Expressions are derived for the transient fields of a short vertical antenna, situated on a smooth spherical conducting earth, and energized by a current which is discontinuous in time. When the antenna current is a linear function of time, the radiation field on a flat perfectly conducting earth is of step-function form. The departure from the step shape of the field is shown to be due to the finite conductivity and dielectric constant of the ground, the induction and static fields of the antenna, and the curvature of the earth.

INTRODUCTION

Some interest has been shown recently in the fields of an electric dipole excited by a transient current. Van der Pol (1955) has recently presented a solution for the dipole, whose moment is proportional to a step function of time, located at the plane interface of two different dielectrics. A similar problem was presented concurrently by Poritsky (1955) who employed the artifice of representing the radiation from the dipole as a superposition of plane waves. The case where the transient dipole is located over an imperfect dielectric or dissipative medium is of even greater interest. An approach to this problem was published recently by Wait and Froese (1955) who considered the source to be a plane wave incident obliquely on the plane interface of a semi-infinite homogeneous dissipative medium. The electric vector which was taken in the plane of incidence was proportional to a step function of time. Sometime earlier the author (1953) derived an exact solution for a magnetic dipole or small loop situated in an infinite conducting medium and excited by a step-function current. The case (Wait 1951) of the transient magnetic dipole over a stratified ground has also been treated using an approximate method which is valid when the observer is near the source. The latter problem has recently been extended by Belluigi (1954).

It is the purpose of this paper to present a derivation for a dipole or short vertical antenna located just above a spherical dissipative smooth earth. The solution is facilitated by employing a new type of series expansion due to Bremmer (1949) for the fields of a dipole whose current $I(i\omega)$ varies harmonically as $e^{i\omega t}$. The first term of this expansion corresponds to the field of a dipole over a flat earth as given by Sommerfeld (1926) and Norton (1937). The succeeding terms are proportional to ascending powers of $(1/a)$ where a is the radius of the earth. By employing techniques equivalent to a Laplace or Fourier analysis, the transient fields of the dipole are found by using a suitable frequency spectrum for the antenna current $I(i\omega)$.

FLAT EARTH CASE

As a starting point the earth is considered to be flat and homogeneous with a conductivity σ and relative dielectric constant K. For a short vertical antenna

[1]Manuscript received September 21, 1955.
Contribution from the Central Radio Propagation Laboratory of the National Bureau of Standards, Boulder, Colorado, U.S.A.

of height dl excited by a current $I(i\omega)e^{i\omega t}$, the vertical electric field $E(i\omega)e^{i\omega t}$ a distance D, on the ground, is given by (Bremmer 1949; Norton 1937; Sommerfeld 1926)

$$(1) \qquad E(i\omega)\,e^{i\omega t} = \frac{i\mu\omega I(i\omega)\,e^{i\omega t}dl}{2\pi D}\left[1+\frac{c}{i\omega D}+\left(\frac{c}{i\omega D}\right)^2\right]e^{-i\omega D/c}F(i\omega)$$

where

$$(2) \qquad F(i\omega) = 1-i2\rho^{\frac{1}{2}}e^{-\rho}\int_{i\rho^{\frac{1}{2}}}^{\infty}e^{-y^2}dy$$

with

$$(3) \qquad \rho(i\omega) = -\frac{(i\omega)^2 D}{2c(Ki\omega+\sigma\mu c^2)}\left[\frac{(K-1)i\omega+\sigma\mu c^2}{Ki\omega+\sigma\mu c^2}\right]$$

and $c = 3\times10^8$, $\mu = 4\pi\times10^{-7}$. It should be pointed out that equation (1) is not exact (Norton 1937), being an approximation valid for

$$\left|\frac{i\omega}{Ki\omega+\sigma\mu c^2}\right|^2 \ll 1.$$

The antenna current is now expressed as a function of time as $I_0 f(t)\,u(t)$ where $u(t) = 1$ for $t > 0$, $= 0$ for $t < 0$. It then follows that the frequency spectrum $I(i\omega)$ is given by

$$(4) \qquad I(i\omega) = I_0\int_{-\infty}^{\infty}f(t)\,u(t)\,e^{-i\omega t}dt = I_0\int_0^{\infty}f(t)\,e^{-i\omega t}dt.$$

In other words $I(s)$ is the Laplace transform of $f(t)$ where s replaces $i\omega$. Written symbolically $I(s) = L_t f(t)$. Furthermore, s can be considered to have a small real part to insure convergence for various forms of $f(t)$. The corresponding transient electric field $e(t)$ is then related to $E(i\omega)$ by

$$(5) \qquad E(i\omega) = E(s) = \int_0^{\infty}e(t)\,e^{-st}dt$$

or $E(s) = L_t\,e(t)$. Since $f(t)$ and $I(s)$ are specified, $E(s)$ can be obtained from equation (1). The problem is then to find $e(t)$ from $E(s)$, being equivalent to the evaluation of the Bromich contour integral

$$(6) \qquad e(t) = \frac{1}{2\pi i}\int_{c-i\infty}^{c+i\infty}E(s)\,e^{st}ds$$

which is written symbolically as

$$(7) \qquad e(t) = L_t^{-1}E(s).$$

For convenience, the function $f(t)$ is replaced by t/t_0 so that current in the antenna is a linearly increasing function of time being equal to I amp. at $t = t_0$. Then

$$(8) \qquad I(s) = L_t\,I_0\,t/t_0 = I_0/s^2\,t_0.$$

It then follows without difficulty that

$$(9) \qquad e(t) = \frac{I_0 dl\mu}{2\pi D t_0}\,B(t')\,u(t')$$

where $t' = t - D/c$ and

$$B(t') = L_{t'}^{-1} \frac{F(s)}{s}\left[1+\frac{c}{Ds}+\left(\frac{c}{Ds}\right)^2\right]. \tag{10}$$

For a perfectly conducting ground the factor F is unity and consequently $L^{-1} F(s)/s$ in the above equation is unity. It, therefore, is concluded that for large distances or small times, such that $t' \ll D/c$, the field is characterized by a step-function form. If the antenna current was a step function ($I_0 u(t)$) instead of a linearly rising function, the response would be

$$e(t) = \frac{I_0 dl\mu}{2\pi D} B_1(t')\, u(t') \tag{11}$$

where

$$B_1(t') = B(0)\, \delta(t') + dB(t')/dt' \tag{12}$$

with $\delta(t')$ being the unit impulse function at $t' = t - D/c = 0$. With similar reasoning it follows that if the current is impulsive ($I_0 t_1 \delta(t)$) the response is

$$e(t) = \frac{I_0 dl\mu t_1}{2\pi D}[B_2(t')]\, u(t) \tag{13}$$

with

$$B_2(t') = B(0)\, \delta'(t') + \left[\frac{dB(t)}{dt}\right]_{t=0} \delta(t') + \frac{d^2 B(t')}{dt'}, \tag{14}$$

where $\delta'(t')$ is the doublet impulse function at $t' = 0$.

The core of the problem is then to evaluate the inverse transform of $F(s)/s$ to obtain the response function $B(t)$. An approach is to expand $F(s)/s$ in an asymptotic expansion in $\rho(s)$ as follows:

$$\frac{F(s)}{s} = -\frac{1}{s}\sum_{m=1}^{\infty} \frac{(2m-1)!}{(m-1)!2^{m-1}} \frac{1}{[2\rho(s)]^m}. \tag{15}$$

Furthermore, if displacement currents in the ground are neglected such that $Ks \ll \sigma\mu c^2$,

$$\rho(s) = -\alpha^2 s^2$$

where $\alpha^2 = D/2\sigma\mu c^3$. It then follows that

$$\frac{F(s)}{s} = \sum_{m=1}^{\infty} \frac{(2m-1)!}{(m-1)!2^{2m-1}\alpha^{2m} s^{2m+1}}. \tag{16}$$

The inversion of this transform is readily carried out to give

$$L_{t'}^{-1} \frac{F(s)}{s} = \sum_{m=1}^{\infty} \frac{(-1)^{m-1}}{m!}(t'/2\alpha)^{2m} \tag{17}$$

which of course is identical to

$$L_{t'}^{-1} \frac{F(s)}{s} = 1 - \exp\left[-(t'/2\alpha)^2\right]. \tag{18}$$

This equation can be checked directly by taking the Laplace transform of the right-hand side leading to

$$\left[1-2\alpha s\, e^{\alpha^2 s^2}\int_{\alpha s}^{\infty} e^{-z^2}dz\right]\frac{1}{s}, \tag{19}$$

which is identical to the function $F(s)/s$ given by equation (2) with the substitution $\rho = -\alpha^2 s^2$. It now readily follows that

$$L_{t'}^{-1}\frac{F(s)}{s^2} = \frac{1}{(D/c)}\int_0^{t'}[1-e^{-\tau^2/4\alpha^2}]\,d\tau \tag{20}$$

and

$$L_{t'}^{-1}\frac{F(s)}{s^3} = \frac{1}{(D/c)}\int_0^{t'}\int_0^{\tau}[1-e^{-\tau^2/4\alpha^2}]\,d\tau\,d\tau. \tag{21}$$

These integrations can be carried out to yield

$$L_{t'}^{-1}\frac{F(s)}{s^2} = \frac{t}{(D/c)}\left[1-\frac{2}{z}\int_0^{z/2}e^{-z^2}dx\right] \tag{22}$$

and

$$L_{t'}^{-1}\frac{F(s)}{s^3} = \frac{t^2}{2(D/c)^2}\left[1-\frac{4}{z}\int_0^{z/2}e^{-z^2}dx+4\,\frac{(1-e^{-z^2/4})}{z^2}\right] \tag{23}$$

with $z = t'/\alpha$.

It is now proposed to obtain a correction for the displacement currents in the ground. This is effected by expanding $1/\rho(s)$ in a series of ascending powers of β $(=1/\sigma\mu c^2)$ so that

$$\begin{aligned}\left[\frac{1}{2\rho(s)}\right]^m = (-1)^m(2\alpha s)^{-2m}\{&1+m\beta(K+1)s\\ &+[m(2m-1)K^2-2m^2K(K-1)+m(m+1)(K-1)^2/2]\beta^2s^2\\ &+\text{terms in } s^3,\ s^4,\text{ etc.}\}.\end{aligned} \tag{24}$$

It is doubtful if the coefficients of powers of s higher than one are meaningful since the stated error in the defining equation, (3), for $\rho(s)$ is of the order of the term in $\beta^2 s^2$. Inserting this expression into the series formula for $F(s)/s$ and retaining only the first correction term leads to

$$L_{t'}^{-1}\,F(s)/s = 1-\exp[-(t'/2\alpha)^2]+2\beta(K+1)J(t'/2\alpha)/t' \tag{25}$$

where

$$J(x) = \sum_{m=1}^{\infty}\frac{(-1)^{m-1}x^{2m}m^2}{m!}. \tag{26}$$

It can be verified that

$$J(x) = x^2(1-x^2)\,e^{-x^2}. \tag{27}$$

The correction term proportional to β can be neglected when

$$t' \gg \beta K,$$

where for a typical soil with $\sigma = 10^{-2}$, $K = 10$ and therefore $\beta K \simeq 10$ mμsec. It is, therefore, reasonably justified to neglect displacement currents in the ground if $t' > 0.1$ μsec.

CORRECTION FOR CURVATURE

The expansion formula due to Bremmer (1949) for the field of a vertical electric dipole on a spherical earth is given by equation (1) if $F(i\omega)$ is replaced by $\bar{F}(i\omega)$ where*

$$\bar{F}(i\omega) = F(i\omega) - \tfrac{1}{2}\Delta[1 - i(\pi\rho)^{\frac{1}{2}} - (1+2\rho)F(i\omega)] + \Delta^2[1 - (\pi\rho)^{\frac{1}{2}}(1-\rho) - 2\rho + \tfrac{5}{6}\rho^2 + (\tfrac{1}{2}\rho^2 - 1)F(i\omega)] + \text{terms in } \Delta^3, \Delta^4, \text{ etc.}, \tag{28}$$

where

$$\Delta(i\omega) \simeq \frac{(i\sigma\mu\omega)^{3/2}}{(i\omega/c)^4 a} \quad \text{and} \quad \rho(i\omega) \simeq -\frac{D(i\omega)^2}{2\sigma\mu c^2}, \tag{29}$$

where a is the radius of the earth. Replacing $i\omega$ by s and expanding $\bar{F}(i\omega)$ in inverse powers of s it follows that

$$\frac{\bar{F}(s)}{s} = \frac{F(s)}{s} + T\left[\frac{\pi^{\frac{1}{2}}a}{2s^{5/2}} - \frac{1}{s^{7/2}} + \frac{1}{\alpha^2 s^{11/2}} - \frac{9}{2\alpha^4 s^{15/2}} + \cdots\right] + T^2\left[\frac{5\alpha^4}{6s^2} - \frac{\pi^{\frac{1}{2}}\alpha^3}{s^3} + \frac{9\alpha^2}{4s^4} - \frac{\pi^{\frac{1}{2}}\alpha}{s^5} + \frac{5}{8s^6}\cdots\right] + \text{terms in } T^3, T^4, \text{ etc.} \tag{30}$$

where $T = -(\sigma\mu)^{3/2}c^4/a$. The inversion of the inverse powers of s can be readily carried out. Using this result, the final expression for the response function $B(t')$ is given by

$$B(t') \simeq 1 - e^{-z^3/4} + y\left[1 - \frac{2}{z}\int_0^{z/2} e^{-x^3}dx\right] + \frac{y^2}{2}\left[1 - \frac{4}{z}\int_0^{z/2} e^{-x^3}dx + 4\,\frac{1-e^{-z^3/4}}{z^2}\right] - X\left(\frac{x}{\pi}\right)^{\frac{1}{2}}\left(\frac{2\pi^{\frac{1}{2}}z}{3} - \frac{8z^2}{15} + \frac{32z^4}{945} - \frac{64z^6}{15015} + \cdots\right) + X^2\left(\frac{5z}{6} - \frac{\pi^{\frac{1}{2}}z^2}{2} + \frac{3z^3}{8} - \frac{\pi^{\frac{1}{2}}z^4}{24} + \frac{z^5}{192} - \cdots\right) \pm \text{terms in } X^3, X^4, \text{ etc.} \tag{31}$$

where

$$y = ct'/D, \qquad X = \left(\frac{D}{a}\right)\left(\frac{15\pi\sigma D}{4}\right)^{1/4},$$

and

$$z = ct\left(\frac{240\pi\sigma}{D}\right)^{\frac{1}{2}}.$$

The above formula neglects displacement currents throughout. A first order correction for these was given by equation (25). That is, the quantity $2\beta(K+1)J(z/2)/t'$ is to be added to the right-hand side of equation (31).

Formally the response functions $B_1(t')$ and $B_2(t')$ for step function and im-

*Equation (28) in its present form was communicated to the author privately by Dr. H. Bremmer. It is believed to be more accurate than equation (IV–30) in Bremmer (1949).

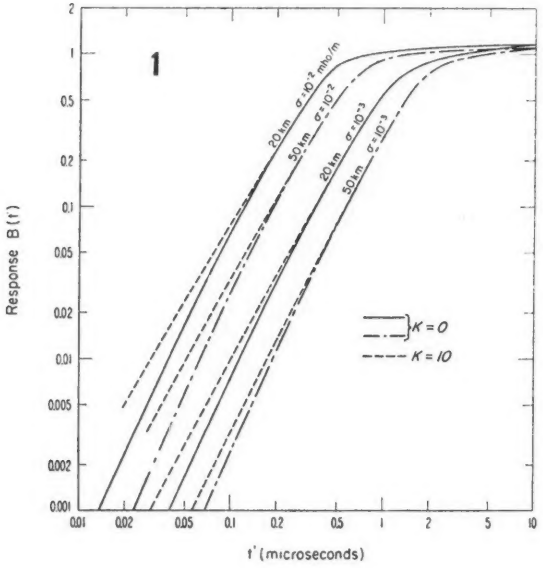

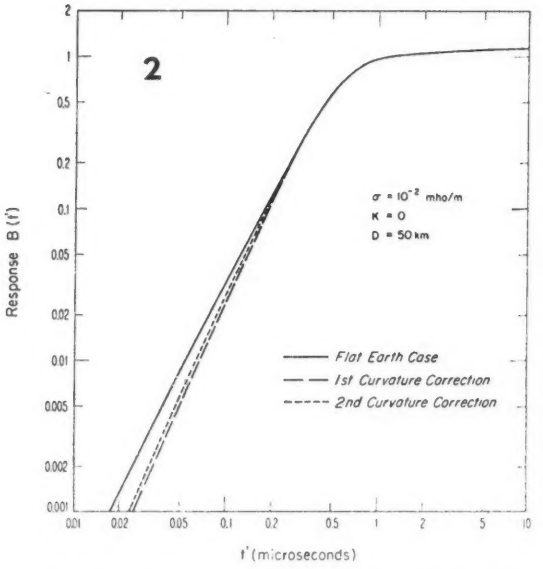

FIG. 1. The transient response at distances of 20 and 50 km. for an electric dipole energized by a linearly rising current and located on a smooth spherical earth.

FIG. 2. The transient response at a distance of 50 km. showing the effect of curvature of the earth, for an electric dipole energized by a linearly rising current.

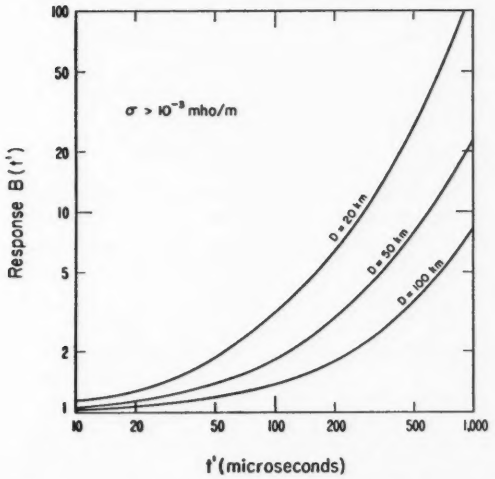

FIG. 3. The transient response at distances of 20, 50, and 100 km. for longer times where the static and induction fields are significant, for an electric dipole energized by a linearly rising current.

pulse function sources, respectively, can be obtained from $B(t')$ by carrying out the operations indicated by equations (12) and (14).

Some numerical calculations were carried out for the function $B(t')$ and they are illustrated in Figs. 1 to 3. In Fig. 1 the response calculated from equation (31) is plotted as a function of t' $(=t-D/c)$ in microseconds for $D = 20$ and 50 km. and $\sigma = 10^{-2}$ and 10^{-3} mhos per meter. The solid curves correspond to $B(t')$ when displacement currents are considered to be negligible. The dotted curves show the first order correction for displacement currents assuming $K = 10$. The effects of the curvature corrections to the flat earth formula are illustrated in Fig. 2. The first curvature correction refers to equation (31) with the term proportional to X^2 being omitted. The second curvature correction includes terms proportional to both X and X^2.

It is interesting to note that the flat earth formula differs only appreciably from the curvature corrected formula at small times such that $t' < 0.1$ μsec. At distances greater than 50 km., however, the curvature correction becomes significant at larger times. Unfortunately the series type of solution here becomes very poorly convergent and terms proportional to X^3, X^4, etc. would be needed for greater distances or smaller times.

At times greater than 1 μsec. the induction field becomes significant. This is indicated in Figs. 1 and 2 by the slight rise of $B(t')$ above unity for t' in the range 1 to 10 μsec. For greater times, both the induction and static field become quite significant as illustrated in Fig. 3 for $D = 20$, 50, and 100 km. In this region of the time domain, the field is almost independent of ground conductivity and the curvature corrections are negligible at these distances.

EXPONENTIAL EXCITATION

It is rather striking that the transient responses for a dipole over a flat highly conducting ground can be expressed in a quite simple form. Another case that yields an answer in closed form is when the dipole is energized by an exponential current ($I_0\, e^{-\Gamma t}$). Note that

$$L_t\, I_0\, e^{-\Gamma t} = I_0/(s+\Gamma). \tag{32}$$

The response a distance D along the surface of a flat earth, neglecting displacement currents, is then given by

$$e(\Gamma, t) = L_t^{-1}\, E(s) \tag{33}$$

where

$$E(s) = \frac{I_0 dl\mu}{2\pi D}\left[1+\frac{c}{sD}+\frac{c^2}{s^2D^2}\right]\frac{F(s)s}{s+\Gamma}\, e^{-sD/c} \tag{34}$$

and where $F(s)$ is given by equation (2).

This can be conveniently rewritten as

$$E(s) = \frac{I_0 dl\mu}{2\pi D}\left[\frac{sF(s)}{s+\Gamma}+\left(\frac{c}{D}-\frac{c^2}{\Gamma D^2}\right)\frac{F(s)}{s+\Gamma}+\frac{c^2F(s)}{\Gamma D^2 s}\right] e^{-sD/c}. \tag{35}$$

Therefore

$$e(\Gamma, t') = \frac{I_0 dl\mu}{2\pi D}\left[\frac{\partial G(t')}{\partial t'}+\left(\frac{c}{D}-\frac{c^2}{\Gamma D^2}\right) G(t')+\frac{1-e^{-(t'/2\alpha)^2}}{\Gamma(D/c)^2}\right] u(t') \tag{36}$$

where

$$G(t') = L_{t'}^{-1}\frac{F(s)}{s+\Gamma}. \tag{37}$$

Using the convolution theorem it follows that

$$G(t') = e^{-\Gamma t'}\left[2\alpha\Gamma\, e^{\Gamma^2\alpha^2}\int_{-\alpha\Gamma}^{t'/2\alpha-\alpha\Gamma} e^{-x^2}dx+1\right]-e^{-(t'/2\alpha)^2} \tag{38}$$

and therefore

$$\frac{\partial G(t')}{\partial t'} = +\left(\frac{2t'}{4\alpha^2}+\Gamma\right) e^{-t'^2/4\alpha^2}-\Gamma\, e^{-\Gamma t}\left[1+2\alpha\Gamma\, e^{\Gamma^2\alpha^2}\int_{-\alpha\Gamma}^{t'/2\alpha-\alpha\Gamma} e^{-x^2}dx\right]. \tag{39}$$

When these values for $G(t')$ and $\partial G(t')/\partial t'$ are inserted into equation (36), the response $e(\Gamma, t')$ to a current $I_0\, e^{-\Gamma t}\, u(t)$ is completely specified. The above exponential source can be easily extended to a suddenly applied sinusoidal source. For example, if the current is $I_0 \sin \Omega t\, (t)$ where Ω is real, then the response is the imaginary part of $e(-i\Omega, t)$. Similarly if the current were $I_0 \cos \Omega t\, u(t)$ the response would be the real part of $e(-i\Omega, t)$. It is interesting to note that when $t' \gg 2\alpha$ the response to the current, $I_0\, e^{i\Omega t}$, is simply the steady state value $E(i\Omega)$ characteristic of a vertical dipole on a flat earth. Since

$$\frac{t'}{2\alpha} = \frac{15 t_\mu'[24\pi\sigma]^{\frac{1}{2}}}{(D_{\text{km}})^{\frac{1}{2}}}, \tag{40}$$

where t_μ' is t' expressed in microseconds, and D_{km} is D in kilometers, it is seen that if $t_\mu' > 2$ or 3 for $D_{\text{km}} = 50$, $\sigma = 10^{-2}$, the response has essentially

reached the steady state condition. It is quite possible, using tables of the probability integral with complex argument, to evaluate the way in which the response $e(\Gamma, t)$ or $e(-i\Omega, t)$ builds up to its steady state value. For smaller times, however, the form of the curves would be affected by curvature and the displacement currents, both of which have not been considered in this section.

CONCLUDING REMARKS

The behavior of a transient dipole over a smooth spherical conductor has been shown to be mainly determined by the finite conductivity of the ground. For distances greater than 50 km. and times less than 0.1 μsec. following the first arrival of the signal the curvature of the earth begins to have a marked effect. At distances between 20 and 100 km. the induction field of the source dipole becomes appreciable for times greater than 10 μsec.

The extension of the results in this paper to distances out to 2000 km. would require the use of a different approach. In this case it would probably be desirable to start with the complete residue series (Bremmer 1949) for the field and then to apply a suitable Fourier transformation.

ACKNOWLEDGMENT

The author has had the benefit of several valuable discussions with Messrs. Glenn Jean and William Lupton of this Laboratory. The computations for Figs. 1 to 3 were carefully carried out by Mrs. Annabeth Murphy.

REFERENCES

BELLUIGI, A. 1954. Bollettino del Servizio Geologico d'Italia, **25**: 913.
BREMMER, H. 1949. Terrestial radio waves. Elsevier Publishing Co., New York.
NORTON, K. A. 1937. Proc. Inst. Radio Engrs. **25**: 1203.
PORITSKY, H. 1955. Symposium on Electromagnetic Theory, Ann Arbor, Michigan, June 20–25, Paper 6C: 3.
SOMMERFELD, A. N. 1926. Ann. Physik, **81**: 1135.
VAN DER POL, B. 1955. Symposium on Electromagnetic Theory, Ann Arbor, Michigan, June 20–25, Paper 4: 6.
WAIT, J. R. 1951. Can. J. Phys. **29**: 577.
——— 1953. J. Appl. Phys. **24**: 341.
WAIT, J. R. and FROESE, C. 1955. J. Geophys. Research, **60**: 97.

SMALL-ANGLE SCATTERING OF FAST POLARIZED NEUTRONS BY HEAVY NUCLEI[1]

By J. T. Sample

ABSTRACT

Detailed calculations have been carried out which indicate that the small-angle scattering of fast neutrons by lead depends on the polarization, or spin orientation, of the neutrons. When the scattering of neutrons whose spin vectors point upward is observed in the horizontal plane, more neutrons should be found scattered to the right than to the left. For completely polarized 3.1 Mev. neutrons, the theory predicts a maximum "right to left" intensity ratio of 14.5 : 1 at a scattering angle of 0.5°, the ratio decreasing to 1.6 : 1 at 5°, and approaching unity rapidly as the scattering angle increases.

INTRODUCTION

To date, most successful methods of measuring the percentage polarization of fast neutrons (Adair, Darden, and Fields 1954; Huber and Baumgartner 1953; Ricamo 1953 *a*, *b*) have involved resonant elastic scattering, with the attendant uncertainties due to the variation with energy of the polarization dependence of the scattering cross-section. Adair *et al.* (1954) have discovered a non-resonant polarization dependence in the 90° scattering of neutrons by nuclei in the region $A \approx 110$. This effect, at most a 20% difference in intensity between left- and right-scattered neutrons for 50% polarized 0.4 Mev. neutrons, is rather weak for use in a neutron polarimeter. Schwinger (1948) showed, by the Born approximation method, that small-angle scattering by heavy nuclei should be strongly polarization dependent because of the interaction of the Coulomb field of the nucleus with the magnetic moment of the moving neutron. Calculation of the perturbation of a "hard sphere" wave function by this magnetic interaction yields an expression for the differential cross-section differing from Schwinger's only in that the polarization dependent term is about 25% greater.

CALCULATION OF THE SCATTERING CROSS-SECTION

The Schrödinger equation describing the motion of the neutron may be written

$$(\nabla^2+k^2)\psi = \epsilon(\mathbf{L}\cdot\mathbf{S}/r^3)\psi, \tag{1}$$

where $k^2 = 2mE/\hbar^2$,

$\epsilon = 2|\mu_n|Ze^2/mc^2$,

$\mathbf{L}$ = orbital, $\mathbf{S}$ = spin } angular momentum of the neutron in units of $\hbar$,

m = neutron mass,

E = total neutron energy,

$\mu_n = -1.9135$ nuclear magnetons, the neutron magnetic moment,

Ze = charge of target nucleus.

[1]Manuscript received September 22, 1955.
Contribution from the Physics Department, University of British Columbia, Vancouver, British Columbia.

The expression $\epsilon\,\mathbf{L}\cdot\mathbf{S}/r^3$, representing the magnetic interaction, may be derived by considering the force exerted on a magnetic dipole by the apparent magnetic field arising from its motion in the electrostatic field of a nucleus. (The magnetostatic fields of nuclei and electrons may be safely neglected.)

Experiment (Whitehead and Snowdon 1953) shows that the differential elastic scattering cross-section of lead for neutrons of energy about 3 Mev. resembles closely that of a perfectly elastic sphere at scattering angles less than 60°. The "hard sphere" wave function should then be a good approximation from which to begin perturbation calculations.

If $\psi = \psi_0+\psi_1$, where ψ_0 is the solution of equation (1) with $\epsilon = 0$, obeying the boundary conditions

$$\begin{aligned} &\psi_0(\mathbf{r}) = 0 \quad \text{for } r < R, \quad \text{the nuclear radius,} \\ &\psi_0(\mathbf{r}) \underset{r\to\infty}{\to} \left[e^{ikz}+\frac{e^{ikr}}{r}f(\theta)\right][\alpha(\tfrac{1}{2})\ \chi_{\frac{1}{2},\frac{1}{2}}+\alpha(-\tfrac{1}{2})\ \chi_{\frac{1}{2},-\frac{1}{2}}], \end{aligned} \tag{2}$$

where the expression $\alpha(\frac{1}{2})\chi_{\frac{1}{2},\frac{1}{2}}+\alpha(-\frac{1}{2})\chi_{\frac{1}{2},-\frac{1}{2}}$ describes the spin orientation of the neutron, $\chi_{\frac{1}{2},\frac{1}{2}}$ and $\chi_{\frac{1}{2},-\frac{1}{2}}$ being the usual spin eigenfunctions, and $\alpha(\frac{1}{2})$ and $\alpha(-\frac{1}{2})$ obey $|\alpha(\frac{1}{2})|^2+|\alpha(-\frac{1}{2})|^2 = 1$, then ψ_0 may be written

$$\psi_0(\mathbf{r}) = \frac{2\pi^{\frac{1}{2}}}{\rho}\sum_{l=0}^{\infty}\sum_{m'=-\frac{1}{2}}^{\frac{1}{2}}\{i^l(2l+1)^{\frac{1}{2}}[G_l v_{\mathrm{R}}{}^l(\rho)+iH_l v_{\mathrm{I}}{}^l(\rho)]\ Y_{l,0}(\theta)\,\alpha(m')\ \chi_{\frac{1}{2},m'}\}, \tag{3}$$

where $\rho = kr$,

$v_{\mathrm{R}}{}^l(\rho)$ = "regular solution" $= (\frac{1}{2}\pi\rho)^{\frac{1}{2}}J_{l+\frac{1}{2}}(\rho) \underset{\rho\to\infty}{\to} \sin(\rho-\frac{1}{2}l\pi)$,

$v_{\mathrm{I}}{}^l(\rho)$ = "irregular solution" $= -(\frac{1}{2}\pi\rho)^{\frac{1}{2}}N_{l+\frac{1}{2}}(\rho) \underset{\rho\to\infty}{\to} \cos(\rho-\frac{1}{2}l\pi)$,

$$G_l = G_l(b) = \frac{[v_{\mathrm{I}}{}^l(b)]^2-iv_{\mathrm{I}}{}^l(b)\,v_{\mathrm{R}}{}^l(b)}{[v_{\mathrm{R}}{}^l(b)]^2+[v_{\mathrm{I}}{}^l(b)]^2},$$

$$H_l = H_l(b) = \frac{[v_{\mathrm{R}}{}^l(b)]^2+iv_{\mathrm{R}}{}^l(b)\,v_{\mathrm{I}}{}^l(b)}{[v_{\mathrm{R}}{}^l(b)]^2+[v_{\mathrm{I}}{}^l(b)]^2},$$

$b = kR$,

$Y_{l,m}(\theta, \phi)$ are the spherical harmonics defined as in Condon and Shortley (1951).

Equation (1) becomes

$$(\nabla^2+k^2)\psi_1 = \epsilon(\mathbf{L}\cdot\mathbf{S}/r^3)\,\psi_0, \tag{4}$$

where ψ_1 has been neglected with respect to ψ_0 on the right.

To obtain the radial equation corresponding to (4), it is convenient to expand ψ_0 and ψ_1 in terms of eigenfunctions $\mathcal{Y}^M_{J,l,s}$ of J^2 and M, where $\mathbf{J} = \mathbf{L}+\mathbf{S}$ and M is the z component of $\mathbf{J}$. Then

$$\mathbf{L}\cdot\mathbf{S}\ \psi_0(\mathbf{r}) = \sum_{l=1}^{\infty}\sum_{J=|l-\frac{1}{2}|}^{l+\frac{1}{2}}\sum_{M=-J}^{J}\sum_{m'=-\frac{1}{2}}^{\frac{1}{2}} D^{M,m'}_{J,l}\left[\frac{G_l v_{\mathrm{R}}{}^l(\rho)+iH_l v_{\mathrm{I}}{}^l(\rho)}{\rho}\right]\mathcal{Y}^M_{J,l,\frac{1}{2}}, \tag{5}$$

where

$$\begin{aligned} D^{M,m'}_{J,l} &= \pi^{\frac{1}{2}}i^l(2l+1)^{\frac{1}{2}}\alpha(m')(l, \tfrac{1}{2}, 0, m'|l, \tfrac{1}{2}, J, M)[J(J+1)-l(l+1)-\tfrac{3}{4}] \\ &= 0 \qquad \text{for } l = 0, \end{aligned}$$

and $(l, \frac{1}{2}, 0, m'|l, \frac{1}{2}, J, M)$ are the Clebsch-Gordan coefficients defined as in Condon and Shortley (1951);

$$\psi_1(\mathbf{r}) = \sum_{l=1}^{\infty} \sum_{J=|l-\frac{1}{2}|}^{l+\frac{1}{2}} \sum_{M=-J}^{J} \sum_{m'=-\frac{1}{2}}^{\frac{1}{2}} D^{M,m'}_{J,l} \frac{u_l(\rho)}{\rho} \mathcal{Y}^{M}_{J,l,\frac{1}{2}}, \tag{6}$$

where $u_l(\rho)$ is to be determined. Because of the orthogonality of the $\mathcal{Y}$'s, substitution of equations (5) and (6) in (4) gives

$$\frac{d^2u_l(\rho)}{d\rho^2} + \left[1 - \frac{l(l+1)}{\rho^2}\right] u_l(\rho) = \frac{k\epsilon}{\rho}[G_l v_R{}^l(\rho) + iH_l v_I{}^l(\rho)] \tag{7}$$

with the boundary conditions

$$u_l(\rho) = 0 \quad \text{for } \rho \leqslant b,$$

$$u_l(\rho) \propto e^{i\rho} \qquad \text{for large } \rho.$$

The particular integral of equation (7) may be found in terms of $v_R{}^l(\rho)$ and $v_I{}^l(\rho)$ by constructing a Green's function satisfying the boundary conditions. The asymptotic expression for $u_l(\rho)$ is

$$u_l(\rho) \to -k\epsilon e^{i(\rho - \frac{1}{2}l\pi)} S_l(b), \tag{8}$$

where

$$S_l(b) = G_l{}^2 K_l - H_l{}^2 T_l + 2iH_l G_l Q_l,$$

$$K_l(b) = \int_b^{\infty} \frac{[v_R{}^l(\rho)]^2}{\rho^3} d\rho,$$

$$T_l(b) = \int_b^{\infty} \frac{[v_I{}^l(\rho)]^2}{\rho^3} d\rho,$$

$$Q_l(b) = \int_b^{\infty} \frac{v_R{}^l(\rho)\, v_I{}^l(\rho)}{\rho^3} d\rho.$$

Evaluation of the necessary integrals in terms of tabulated functions is carried out in Appendix I.

When (8) is substituted in equation (6), the $\mathcal{Y}$'s being expressed in terms of spherical harmonics, and the result is added to the difference between equation (3) and the incident wave, $e^{ikz}[\alpha(\frac{1}{2})\chi_{\frac{1}{2},\frac{1}{2}} + \alpha(-\frac{1}{2})\chi_{\frac{1}{2},-\frac{1}{2}}]$, the resulting asymptotic expression for the scattered wave is

$$\psi_{sc}(\mathbf{r}) = \frac{ie^{ikr}}{kr}\left\{\chi_{\frac{1}{2},\frac{1}{2}}\left[\alpha(\tfrac{1}{2})\, A(\theta) + i\alpha(-\tfrac{1}{2})\, \frac{k\epsilon}{2} e^{i\phi} B(\theta)\right] + \chi_{\frac{1}{2},-\frac{1}{2}}\left[\alpha(-\tfrac{1}{2})\, A(\theta) - i\alpha(\tfrac{1}{2})\, \frac{k\epsilon}{2} e^{i\phi} B(\theta)\right]\right\}, \tag{9}$$

where

$$A(\theta) = \sum_{l=0}^{\infty} (2l+1) H_l P_l(\cos\theta),$$

$$B(\theta) = \sum_{l=1}^{\infty} (2l+1) S_l P_l{}^1(\cos\theta).$$

For convenience in numerical calculation, the spherical harmonics have been expressed in terms of associated Legendre polynomials, P_l and $P_l{}^1$, as tabulated by Jahnke and Emde (1945).

The polarization vector, $\mathbf{P}$, of the incident beam is defined by

$$\mathbf{P} = [\alpha^*(\tfrac{1}{2})\,\chi^{\dagger}_{\frac{1}{2},\frac{1}{2}}+\alpha^*(-\tfrac{1}{2})\,\chi^{\dagger}_{\frac{1}{2},-\frac{1}{2}}]\,\boldsymbol{\sigma}[\alpha(\tfrac{1}{2})\chi_{\frac{1}{2},\frac{1}{2}}+\alpha(-\tfrac{1}{2})\chi_{\frac{1}{2},-\frac{1}{2}}]$$

where $\boldsymbol{\sigma}$ is the Pauli spin vector, and *,† indicate respectively complex conjugate and Hermitean adjoint. Introducing the unit vector $\mathbf{n}$, normal to the plane of the reaction, defined by

$$\mathbf{n} = \mathbf{k} \times \mathbf{k}_0/|\mathbf{k} \times \mathbf{k}_0|, \qquad |\mathbf{k}| = |\mathbf{k}_0|,$$

the differential cross-section obtained from equation (9) may be written

$$(10) \qquad \sigma(\theta, \mathbf{n}) = \frac{1}{k^2}|A(\theta)|^2+\frac{\epsilon^2}{4}|B(\theta)|^2 + \frac{\epsilon}{k}(\mathbf{P}\cdot\mathbf{n})[\mathrm{Re}A(\theta)\mathrm{Re}B(\theta)+\mathrm{Im}A(\theta)\mathrm{Im}B(\theta)],$$

where "Re" and "Im" indicate respectively the real and imaginary parts of the quantity. Evaluation of the terms in $A(\theta)$ and $B(\theta)$ is outlined in Appendix II.

DISCUSSION

It can be seen from equation (10) that polarization has maximum effect on the cross-section when the direction of observation is chosen so that $\mathbf{P}$ is normal to the plane of the reaction. In this case the interference term, the third term in (10), has its maximum absolute value. This term changes sign

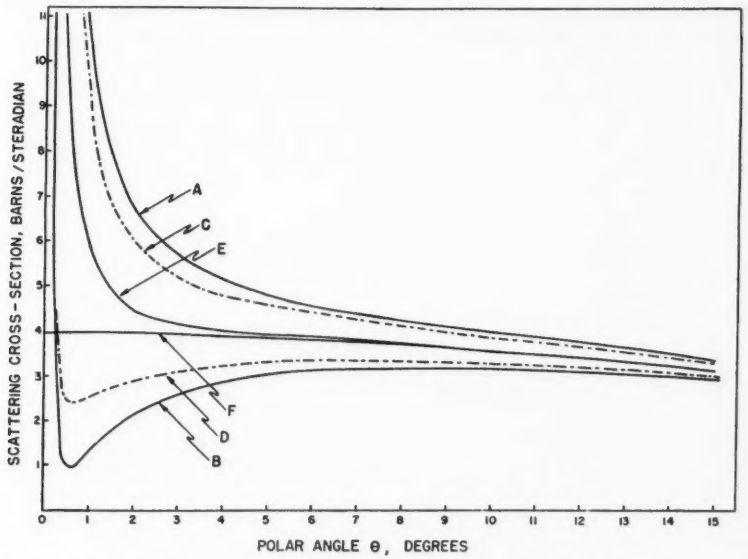

FIG. 1. Differential scattering cross-section of lead for polarized 3.1 Mev. neutrons.

A—Equation (10), $\mathbf{P}.\mathbf{n} = 1$
B—Equation (10), $\mathbf{P}.\mathbf{n} = -1$
C—Schwinger, $\mathbf{P}.\mathbf{n} = 1$
D—Schwinger, $\mathbf{P}.\mathbf{n} = -1$
E—Equation (10), $\mathbf{P}.\mathbf{n} = 0$
F—Hard-sphere scattering

accordingly as the scattering is in the right or left sense, that is, as ϕ is changed by π. The differential scattering cross-section for 100% polarized ($|\mathbf{P}| = 1$) 3.1 Mev. neutrons scattered by lead is plotted as a function of scattering angle θ in Fig. 1. The reaction is appreciably polarization sensitive only for θ less than 10°. For comparison, Schwinger's expression for the cross-section is plotted in Fig. 1 with $A(\theta)$ inserted for $f_0(\theta)$, the nuclear scattering amplitude (Schwinger 1948, equation 10). The only difference between the two expressions is that the polarization dependent term in equation (10) is 25% larger.

An attempt by Longley *et al.* (1952) to measure the polarization of neutrons from $D(d, n)He^3$ by scattering in Pb led to inconclusive results. An attempt by a somewhat different method at this laboratory (Sample, Neilson, and Warren 1955) failed because of the difficulty in collimating fast neutrons sufficiently well to investigate scattering at very small angles.

ACKNOWLEDGMENTS

The author is indebted to his wife for much of the numerical work, and to Dr. W. Opechowski for checking some of the calculations. He also would like to thank Dr. A. J. Ferguson and Dr. S. A. Kushneriuk for helpful suggestions.

APPENDIX I

Evaluation of $S_l(b)$

It can be shown (Watson 1945) that

$$(11)\quad (g+\mu+\nu)\int^{\rho}\rho^{g-1}C_{\mu}(\rho)\bar{C}_{\nu}(\rho)d\rho+(g-\mu-\nu-2)\int^{\rho}\rho^{g-1}C_{\mu+1}(\rho)\bar{C}_{\nu+1}(\rho)d\rho = \rho^{g}\{C_{\mu}(\rho)\bar{C}_{\nu}(\rho)+C_{\mu+1}(\rho)\bar{C}_{\nu+1}(\rho)\},$$

where C and $\bar{C}$ are any cylinder functions. Expressing the integrands in K_l, T_l, and Q_l in terms of Bessel and Neumann functions (equation 8), and putting $g = -1$, $\mu = \nu = l-\frac{1}{2}$, equation (11) gives

$$K_l = \frac{l-1}{l+1}T_{l-1}+\frac{\pi}{4b(l+1)}\{[J_{(l-\frac{1}{2})}(b)]^2+[J_{(l+\frac{1}{2})}(b)]^2\},$$

$$(12)\quad T_l = \frac{l-1}{l+1}T_{l-1}+\frac{\pi}{4b(l+1)}\{[J_{-(l-\frac{1}{2})}(b)]^2+[J_{-(l+\frac{1}{2})}(b)]^2\},$$

$$Q_l = \frac{l-1}{l+1}Q_{l-1}+\frac{(-1)^{l+1}\pi}{4b(l+1)}\{J_{(l-\frac{1}{2})}(b)J_{-(l-\frac{1}{2})}(b)+J_{(l+\frac{1}{2})}(b)J_{-(l+\frac{1}{2})}(b)\}.$$

H_l is readily expressed in terms of Bessel and Neumann functions, and $G_l = 1-H_l$, so S_l may be calculated for all l. As l increases, $H_l \to 0$, $G_l \to 1$, and $S_l \to K_l \to [(l-1)/(l+1)]\,K_{l-1}$. Thus

$$(13)\qquad S_l \simeq a/[l(l+1)] \qquad \text{for large } l,$$

where $a = l_0(l_0+1)K_{l_0}$, l_0 being the lowest value of l for which these approximations have the desired degree of accuracy.

APPENDIX II

Calculation of the Terms in Equation (10)

Since $A(\theta)$ converges rapidly, calculation of numerical values is straightforward. $B(\theta)$, on the other hand, converges slowly, so that it is necessary to obtain an approximate closed form for the sum of high order terms. From equation (13)

$$(14) \qquad B(\theta) = \sum_{l=1}^{l_0} (2l+1)\, S_l P_l^1(\cos\theta) + a \sum_{l=l_0+1}^{\infty} \frac{2l+1}{l(l+1)} P_l^1(\cos\theta).$$

$P_l^1(\cos\theta)$ may be written in one of the forms of the Laplace integral:

$$P_l^1(\cos\theta) = \frac{i(l+1)}{\pi} \int_0^{\pi} (\cos\theta - i\sin\theta\cos\phi)^l \cos\phi\, d\phi.$$

The second sum in equation (14) becomes

$$(15) \qquad \frac{i}{\pi} \sum_{l=l_0+1}^{\infty} \frac{2l+1}{l} \int_0^{\pi} (\cos\theta - i\sin\theta\cos\phi)^l \cos\phi\, d\phi$$

$$= \frac{i}{\pi} \int_0^{\pi} \cos\phi \left\{ 2 \sum_{l=l_0+1}^{\infty} z^l + \sum_{l=l_0+1}^{\infty} \frac{z^l}{l} \right\} d\phi,$$

where $z = \cos\theta - i\sin\theta\cos\phi$. The sums are

$$\sum_{l=l_0+1}^{\infty} z^l = \frac{1}{1-z} - \sum_{l=0}^{l_0} z^l,$$

$$\sum_{l=l_0+1}^{\infty} \frac{z^l}{l} = -\ln(1-z) - \sum_{l=1}^{l_0} \frac{z^l}{l}.$$

Substituting these values in equation (15), and rewriting the finite sums in terms of associated Legendre polynomials, gives

$$(16) \qquad \sum_{l=l_0+1}^{\infty} \frac{2l+1}{l(l+1)} P_l(\cos\theta) = \frac{i}{\pi} \int_0^{\pi} \left\{ \frac{2}{1-z} - \ln(1-z) \right\} \cos\phi\, d\phi$$

$$- \sum_{l=1}^{l_0} \frac{2l+1}{l(l+1)} P_l^1(\cos\theta).$$

(The only term with $l = 0$ vanishes.)

The integral in equation (16) has the value $\cot \frac{1}{2}\theta$. Substituting this in (16) and the result in equation (14),

$$B(\theta) = \sum_{l=1}^{l_0} \left\{ (2l+1) \left[S_l(b) - \frac{a}{l(l+1)} \right] P_l^1(\cos\theta) \right\} + a \cot \tfrac{1}{2}\theta.$$

$|A(\theta)|^2$, $|B(\theta)|^2$, $\mathrm{Re}\, A(\theta)\, \mathrm{Re}\, B(\theta)$, and $\mathrm{Im}\, A(\theta)\, \mathrm{Im}\, B(\theta)$ are most easily calculated by applying equation 2.3 of the review article by Blatt and Biedenharn (1952).

REFERENCES

ADAIR, R. K., DARDEN, S. E., and FIELDS, R. E. 1954. Phys. Rev. **96**: 503.
BLATT, J. M. and BIEDENHARN, L. C. 1952. Revs. Mod. Phys. **24**: 258.
CONDON, E. U. and SHORTLEY, G. H. 1951. The theory of atomic spectra. Cambridge University Press, London.

HUBER, P. and BAUMGARTNER, E. 1953. Helv. Phys. Acta, **26**: 420.
JAHNKE, E. and EMDE, F. 1945. Tables of functions. 4th ed. Dover Publications, New York.
LONGLEY, H. J., LITTLE, R. N., and SLYE, J. M. 1952. Phys. Rev. **86**: 419.
RICAMO, R. 1953*a*. Helv. Phys. Acta, **26**: 423.
——— 1953*b*. Nuovo cimento, **10**: 1607.
SAMPLE, J. T., NEILSON, G. C., and WARREN, J. B. 1955. Can. J. Phys. **33**: 350.
SCHWINGER, J. 1948. Phys. Rev. **73**: 407.
WATSON, G. N. 1945. Theory of Bessel functions. 2nd ed. The MacMillan Co., New York.
WHITEHEAD, W. D. and SNOWDON, S. C. 1953. Phys. Rev. **92**: 114.

MAGNETIC SUSCEPTIBILITY OF LOW RESISTIVITY *n*-TYPE GERMANIUM[1]

By F. T. Hedgcock[2]

ABSTRACT

Some results on the magnetic susceptibility of *n*-type low resistivity polycrystalline germanium as observed between room and liquid nitrogen temperatures are presented. The contribution to the susceptibility from both the free and bound charge carriers has been derived from the experimental results and appears to vary inversely with temperature. An effective mass for the charge carriers in *n*-type germanium is found to be 0.16 of the free electron mass.

INTRODUCTION

The work up to the present time on the magnetic properties of germanium has been chiefly concerned with the determination of the susceptibility of pure germanium and only in the work of Stevens and Crawford (1953) and van Itterbeek *et al.* (1955) are any results given for impure germanium with known amounts of impurity. For this reason the following measurements were made on a more complete set of *n*-type polycrystalline specimens which include those having impurity concentrations that would class the semiconductor as essentially "metallic". The magnetic susceptibility of presumably impure germanium between 290°K. and 80°K. has also been measured by Owen (1912) and by Squire (1940). Stöhr and Klemm (1940) report measurements on germanium–antimony alloys but the concentrations of antimony are too great for the results to be interpreted in terms of semiconductor theory. Busch and Helfer (1954) have recently reported the magnetic susceptibility of pure germanium between 1200°K. and 40°K. while van Itterbeek *et al.* (1955) give measurements on some samples between room and liquid hydrogen temperatures.

To explain Owen's (1912) results on the temperature dependence of the susceptibility of germanium Aigrain, Dugas, and Etzel (1951) calculated the amount of impurity necessary, on the assumption that all of the charge carriers are bound at the temperature of liquid nitrogen and are free at room temperature. These calculations indicate impurity concentrations in solid solution of approximately 1%. This greatly exceeds the solid solubility limits commonly found for impurities in germanium: for instance Thurmond and Struthers (1953) have found the maximum solubility of antimony and copper in germanium to be 2×10^{-2} atomic % and 7×10^{-5} atomic % respectively. X-ray measurements, made by the author, on the lattice parameters of some germanium–antimony samples, are in agreement with Thurmond and Struthers' results and indicate that a solid solubility of antimony in germanium as

[1]Manuscript received October 4, 1955.
Contribution from the Physics Department, University of Western Ontario, London, Ontario.
Part of material contained in a thesis submitted to the faculty of the University of Western Ontario in partial fulfillment of the requirements for the degree of Doctor of Philosophy.
[2]At present National Research Laboratories Postdoctorate Fellow, Division of Pure Physics, National Research Council, Ottawa.

high as 1% is extremely unlikely. In fact only after prolonged annealing at 900°C. and subsequent quenching was there any lattice parameter change found in the alloys nominally containing 1% antimony. The results indicate a small increase in the lattice parameter of germanium which would be expected if antimony forms a substitutional solid solution in germanium of low solid solubility.

SPECIMEN PREPARATION AND METHOD OF MEASUREMENT

The specimen rods were prepared for us by Johnson Matthey and Mallory Ltd. by melting germanium together with various amounts of antimony up to 1% by weight. The alloys were melted by them in graphite in a reducing atmosphere, cast as an ingot, annealed and recast as rods $\frac{1}{4}$ in. in diameter and 5 to 6 in. in length. Microscopic examination made by us on sections of the rods as supplied showed the presence of excess antimony and other precipitated impurity, probably germanium oxide. In order to put the greatest possible amount of antimony into solid solution, the rods were subjected to long periods of annealing *in vacuo* (up to two weeks at 860°C.) and then quenched. Microscopic examination then showed that some second phase existed in the material but measurements of electrical resistivity indicated an increase in the amount of dissolved impurity. The amount of antimony actually in solid solution was deduced from the resistivity values using the results of Pearson, Struthers, and Theuerer (1950).

The susceptibility of the specimens was measured by the Gouy method, using a specially developed servo-balance apparatus.* Current for the magnet was supplied from a d-c. generator and stability of the magnetic field was ensured by automatic regulation of the current in the field coils of the generator.*

It is estimated that the measurements of the susceptibility have an absolute accuracy of 2% and a relative accuracy of 0.5%. Any specimens that showed ferrous impurity as indicated by the dependence of magnetic susceptibility on magnetic field strength were rejected.

DISCUSSION OF RESULTS

The susceptibility of various specimens as a function of temperature is shown in Fig. 1. The lowest curve refers to pure zone-refined germanium† and the upper curves to samples with successively greater amounts of impurity for which the material becomes increasingly diamagnetic. None of these specimens approaches Owen's value of 0.30×10^{-6} e.m.u./gm. at 100°K. so that his material must have been extremely impure. The curve for pure germanium agrees well with that found by previous workers (Stevens and Crawford 1953; van Itterbeek *et al.* 1955; Busch and Helfer 1954) and the most impure samples of Stevens and Crawford agree roughly with specimen F, though with a rather smaller negative slope.

The analysis of the susceptibility results will follow closely that originally

*To be described in separate publications.

†I am indebted to Dr. J. Rutter of the University of Toronto, Department of Metallurgy, for supplying this sample.

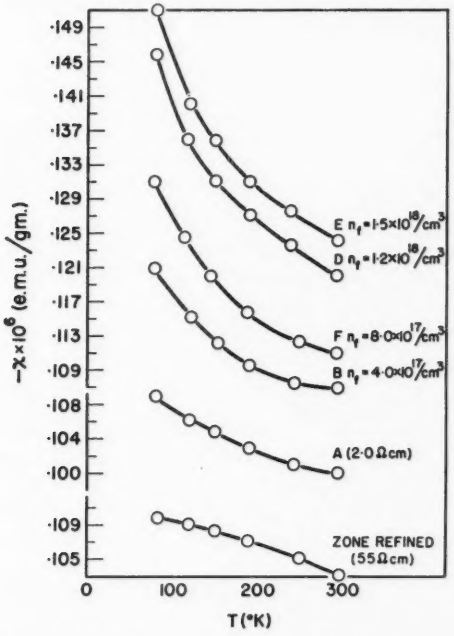

FIG. 1. The total susceptibility of a number of n-type Ge–Sb alloys as a function of temperature.

given by Busch and Mooser (1953) for their measurements on gray tin. χ_T, the total susceptibility of a semiconductor, may be regarded as made up of four parts:

χ_A — due to electrons in the valence band and inner shells.
χ_f — due to free electrons and mobile holes.*
χ_b — due to electrons and holes bound in impurity sites.
χ_p — due to precipitated impurity, lattice dislocations, vacancies, interstitial atoms, etc.

It may be remarked that this method of dividing the total susceptibility of a semiconductor into the above components is somewhat arbitrary and the division into χ_f and χ_b is based on the simple model of an electron (or hole) being bound in the coulomb field of an impurity site until sufficient thermal energy is acquired to ionize the trapped electron when it is then assumed free to move through the crystal lattice. The term χ_A is due to the (neutral) germanium atoms themselves and can be determined experimentally by measuring the susceptibility of high resistivity germanium below the temperature of the intrinsic region (i.e. approximately 650°K.). One might expect that χ_A would

*In the present n-type specimens the concentration of holes is negligible so that there will be no experimentally observable contribution to χ_T from χ_f or χ_b due to holes.

be temperature independent; however, previous measurements on high purity samples (Stevens and Crawford 1953; van Itterbeek *et al.* 1955; Busch and Helfer 1954) and the present results for the zone-refined specimen and specimen A indicate that χ_A varies significantly with temperature. At present no explanation for this anomalous behavior has been given.

Since the amount of precipitated impurity is small the temperature dependence of χ_T due to precipitated impurity should be negligible and in the temperature range under consideration it is unlikely that there will be any change in the number of lattice imperfections. We shall therefore assume that the contribution of χ_p to χ_T is temperature independent.

Now
$$\chi_T = \chi_f + \chi_b + \chi_p + \chi_A$$

and χ_A, as we have said, is determined by the data on pure germanium; so subtracting the curve for the pure substance we have:

$$\chi_{red} \equiv \chi_T - \chi_A = \chi_f + \chi_b + \chi_p$$

of which the first two terms are the susceptibility of the free and bound charge carriers and χ_p is temperature independent. Now if we assume a quasi free electron model for the electrons in the conduction band, the susceptibility of the charge carriers can be calculated theoretically by the analysis of Stoner (1935) extended by Wilson (1953) to take account of electron–lattice interaction by inclusion of the effective mass of the electron. In a non-degenerate electron gas the contribution to the mass susceptibility is given by

$$\chi_f = \frac{N_f \mu^2}{\rho k T}\left(1 - \frac{m^2}{3m^{*2}}\right) \tag{1}$$

where N_f is the number of free charge-carriers,

μ is the Bohr magneton,

m and m^* are the free and effective electron masses,

ρ is the density,

k is Boltzmann's constant,

T is the absolute temperature.

For a degenerate electron gas occurring in samples with high impurity concentrations at normal temperatures or in moderately impure samples at low temperatures, Fermi–Dirac statistics must be used and Eq. (1) is modified to

$$\chi_f = \frac{4m^*\mu^2}{\rho h^2}(3\pi^2 N_f)^{\frac{1}{3}}\left(1 - \frac{m^2}{3m^{*2}}\right) \tag{1a}$$

where h is Planck's constant and the other symbols have the same meaning as in Eq. (1).

The expression for the susceptibility contribution of the bound electrons, based on a hydrogen-like model, has the form (Busch and Mooser 1953)

$$\chi_b = \frac{N_b}{\rho}\left(\frac{\mu^2}{kT} - \frac{e^2 K^2 m^2 a_h^2}{6m^{*3}c^2}\right), \tag{2}$$

the first term being the paramagnetic spin contribution and the second the diamagnetic orbital component,

where N_b is the number of bound electrons,

e is the electron charge,

K is the dielectric constant of the material,

a_h is the first Bohr radius for the hydrogen atom,

c is the velocity of light,

and the other symbols have the same meaning as in Eq. (1).

The effective mass of electrons in the conduction band is unique only if the Fermi surface is a sphere. Cyclotron resonance experiments (Lax *et al.* 1954) have established the need for ellipsoidal energy surfaces to represent the conduction band in germanium. Enz (1955) has shown that by using the appropriate averaging process the value of $(m/m^*)^2$ to be used in Eq. (1) for ellipsoidal energy surfaces is given by

$$(2M_t+M_l)/3M_t^2\,M_l$$

where M_l and M_t are the longitudinal and transverse mass ratios. Using the values of 0.083 and 1.4 for M_t and M_l as determined by Lax *et al.* yields a value of 54 for $(m/m^*)^2$. It is obvious that a measurement of susceptibility on a cubic crystal such as germanium can give no information on the individual mass ratios, M_l and M_t.

The experimental results were originally interpreted on the assumption that N_f and N_b varied with temperature (cf. Putley 1949). With this approach it had to be assumed that m^* decreased with temperature. A similar assumption was found necessary by Debye and Conwell (1954) to fit theoretical curves to the data on the electrical properties of germanium. However the work of Hung and Gleissman (1950) on the Hall effect in n-type germanium suggests that at high impurity concentrations no bound charge carriers exist down to liquid nitrogen temperatures so that N_f and N_b are independent of temperature.

If then we assume that N_f and N_b are constant for the high impurity samples E, D, and F, and that the free charge carriers behave as a nondegenerate* electron gas, we see from equation (1) that χ_f should vary inversely with temperature. As can be seen in Fig. 2, χ_{red} does indeed vary linearly with $1/T$ as expected on the present interpretation of the results. Using the slopes of the lines in Fig. 2 for specimens E, D, and F an effective mass may then be calculated using equation (1). The value found is $0.16\pm.01\ m$ which agrees well with the value of $m/6$ deduced by Stevens and Crawford (1953) and also reasonably well with the value of $0.14\ m$ calculated from the previously mentioned data of Lax *et al.* (1954).

For sample B with an electron density of 4.0×10^{17} cm.$^{-3}$, as determined from a resistivity measurement, the assumption of a constant N_f leads to a value of $0.14\pm.01\ m$ for m^*. This apparent change in the effective mass can be interpreted in one of two ways; namely, that the effective mass is a function of

*A calculation of the degeneracy temperature for these impurity concentrations indicates a temperature between 60° and 100°K. depending on the effective mass chosen.

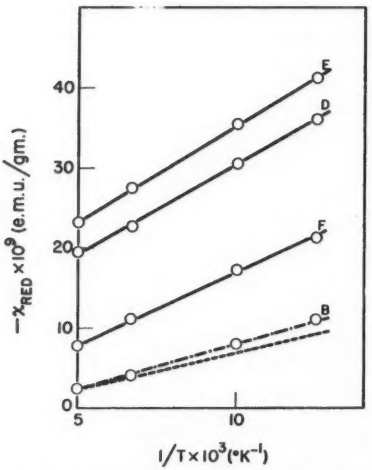

FIG. 2. The susceptibility of the free and bound charge carriers and the precipitated impurity in the Ge–Sb alloys as a function of $1/T$.

impurity concentration as indicated by the experimental evidence of Crawford *et al.* (1955) or that at lower temperatures some of the electrons are bound in impurity sites in *this* specimen. A determination of the Hall coefficient as a function of temperature for sample B indicates that the number of charge carriers is indeed not independent of temperature. It appears therefore that, at these moderately high impurity concentrations, some electrons are bound so that N_b now varies with temperature. For sample B, the Hall coefficient showed a change of approximately 20% between liquid nitrogen and room temperature. Assuming this change in the Hall coefficient is a measure of the change in N_f, which is probably true for a sample with the impurity concentration of B, a calculation of the temperature-dependent part of χ_{red} can be made from equations (1) and (2) using the m^* found for the less pure samples. The dashed line in Fig. 2 represents the calculated susceptibility of the free electron gas if N_f were constant, while the dotted line includes the calculated susceptibility of the bound electrons, the numbers N_f and N_b being based on the Hall coefficient measurements. As can be seen in Fig. 2 extremely good agreement with the experimental curve is found when χ_b is included in the expression for χ_{red}. It should perhaps be mentioned that the effective mass used in both expressions for the susceptibility of the free and bound charge carriers is the same, in conformity with the simple model on which equations (1) and (2) are based (cf. Debye and Conwell 1954).

It is intended to extend these measurements down to the temperatures of liquid helium and it should be possible, from the results, to obtain further useful information about the behavior of free and bound charge carriers in impure semiconductors.

ACKNOWLEDGMENTS

I wish to thank Dr. E. Mooser and Dr. W. Pearson for many helpful discussions and Dr. D. K. C. MacDonald and Dr. R. C. Dearle for their continued interest in the work. I would like to gratefully acknowledge the National Research Council Studentship and summer scholarship held in 1953–54. This research has been supported by the Defence Research Board.

REFERENCES

AIGRAIN, P. R., DUGAS, C. R., and ETZEL, H. W. 1951. Semiconducting materials. *Edited by* H. K. Henisch. Butterworth Scientific Publications, London.
BUSCH, G. and HELFER, N. 1954. Helv. Phys. Acta, **201**: 27.
BUSCH, G. and MOOSER, E. 1953. Helv. Phys. Acta, **26**: 611.
CRAWFORD, J. H., SCHWEINLER, H. C., and STEVENS, D. K. 1955. Phys. Rev. **99**: 1330.
DEBYE, P. and CONWELL, E. M. 1954. Phys. Rev. **93**: 693.
ENZ, C. 1955. Helv. Phys. Acta, **28**: 158.
HUNG, C. S. and GLEISSMAN, J. R. 1950. Phys. Rev. **79**: 726.
VAN ITTERBEEK, A., DE GREVE, L., and DUCHATEAU, W. 1955. Appl. Sci. Research, B, **4**: 300.
LAX, B., ZEIGER, H. J., and DEXTER, R. N. 1954. Physica, **20**: 818.
OWEN, M. 1912. Ann. Physik, **37**: 657.
PEARSON, G. L., STRUTHERS, J. D., and THEUERER, H. C. 1950. Phys. Rev. **77**: 809.
PUTLEY, E. H. 1949. Proc. Phys. Soc. **62**: 285.
SQUIRE, C. F. 1940. Phys. Rev. **58**: 202.
STEVENS, D. K. and CRAWFORD, J. H. 1953. Phys. Rev. **92**: 1065.
STÖHR, V. H. and KLEMM, W. 1940. Z. anorg. u. allgem. Chem. **244**: 205.
STONER, E. C. 1935. Proc. Roy. Soc. (London), A, **152**: 672.
THURMAND, C. D. and STRUTHERS, J. D. 1953. J. Phys. Chem. **57**: 831.
WILSON, A. H. 1953. Theory of metals. 2nd ed. Cambridge University Press, London.

METEOR ECHO DURATIONS AND VISUAL MAGNITUDES[1]

By Peter M. Millman and D. W. R. McKinley

ABSTRACT

The statistical relation between the radio echo duration and the visual magnitude has been investigated for approximately 3300 meteors observed on the combined Dominion Observatory–National Research Council program at Ottawa. Both echo durations and visual magnitudes were reduced to absolute values, defined as those for a meteor in the zenith at a height of 100 km. For meteors in the absolute magnitude range +5 to −5 a straight line relation exists between log absolute duration and absolute magnitude, longer durations corresponding to brighter meteors. Applying current meteor theory to these data indicates that a meteor of absolute magnitude +5 produces 2×10^{12} electrons per cm. of path length. For Perseid meteors the ratio between ionization produced and visual luminosity is almost constant in the range +5 to −5 absolute magnitude. For other meteors this ratio seems to decrease somewhat for the brighter objects. These results lead to higher electron densities for the bright meteors than had previously been estimated.

Since the summer of 1947 the Dominion Observatory and the National Research Council in Ottawa have cooperated in a combined program of meteor observation. In the course of this work a large number of meteor echoes has been recorded at the Ottawa station on a frequency of 32.7 Mc./sec. (McKinley and Millman 1949). Many of the more prominent echoes, corresponding to the overdense ionization trails with greater than 10^{12} electrons per cm. path length (Greenhow 1952; Kaiser and Closs 1952), were produced by meteors for which good visual observations were available.

It was early recognized that there was a general statistical relation between the observed durations of these echoes and the brightness of the meteors, the longer durations corresponding to the brighter meteors. Preliminary relations, based on 700 echoes, were published for the Perseid and Geminid meteors by Millman (1950). These values were found by sorting the meteors into classes of apparent visual magnitude and then averaging the logarithm of the duration in seconds for each class. These preliminary curves have been used by a number of investigators in discussing the theory of meteor echo formation (Greenhow and Hawkins 1952; Kaiser 1953; Lindblad 1952).

The 1950 curves were published to illustrate qualitatively a general relation and were not meant to be applied quantitatively to other problems. They are open to criticism on the following counts: (*a*) only apparent visual magnitudes of the meteors were used and these were not reduced to a standard absolute system; (*b*) the durations of the echoes were not reduced to a standard zenithal distance; (*c*) taking means of log durations artificially decreases the slope of the curve owing to the large statistical spread about the mean and the relatively small numbers of very long and very short duration echoes; (*d*) the number of echoes used was rather small considering the statistical spread of observed values.

[1]Manuscript received September 8, 1955.
Contribution from the Radio and Electrical Engineering Division, National Research Laboratories, and from the Dominion Observatory, Ottawa, Canada. Issued as N.R.C. No. 3826, and Contributions from the Dominion Observatory, Vol. 2, No. 20.

The present paper is an attempt to correct these faults. The observational material used consists of 3283 meteors observed in Ottawa during the years 1948, 1949, and 1950. For each meteor a recorded radio echo and a visual magnitude estimate were available. The echoes were recorded at Ottawa, lat. 45° 20′ 32″ N., long. 75° 38′ 05″ W., elevation 320 ft. above sea level, frequency 32.7 Mc./sec., transmitter peak power 400 kw., pulse width 20 μsec., receiver sensitivity 2×10^{-14} w., antennae—half-wave horizontal dipoles oriented N.–S. and mounted a quarter-wave above ground, display—range-time sweep. The visual magnitudes were recorded by a team of visual observers, six to eight in number, estimating to the nearest half magnitude by comparing the meteor with standard stars. Where two or more independent magnitude estimates were available these were averaged. The meteors were identified with the various better-known showers by a consideration of the date of observation, and the position, orientation, and general appearance of the visual trail. In many cases confirming evidence for the identification appeared in the radio echo. The distribution of numbers among the various showers was as follows, the generally accepted mean observed velocity in km./sec. being listed in brackets for each shower:

Shower	Number of meteors
Lyrids (49)	21
η Aquarids (64)	9
δ Aquarids (40)	158
Perseids (60)	1404
Orionids (66)	11
Leonids (72)	4
Geminids (35)	256
Non-shower	1420
Total	3283

It is evident from the above table that Perseids provide the best statistical material from the standpoint of numbers and homogeneity.

The absolute magnitude of a meteor is defined as the magnitude it would have if it were located in the observer's zenith at a height of 100 km. To convert to absolute magnitude the apparent visual magnitude must be corrected for the difference between the actual distance of the meteor and 100 km., and for the increased atmospheric absorption away from the zenith. A convenient table for the first correction can be computed by assuming that the brightness of a point source falls off inversely as the square of the distance. This is reproduced in Table I. In applying this table the mean ranges of the enduring parts of the echoes (*e* and *f* characteristics) were used.

The absorption correction was taken from the values given in the Handbuch der Astrophysik (Lundmark 1932), assuming the mean color index of meteors to be −1.8. This correction as used is listed in Table II. It may be noted here that, although Table II has been extended to an elevation of 5° for the sake of completeness, practically no meteors recorded by the radio equipment had elevations under 10° and very few were as low as 15° elevation since the maximum range recorded varied from 270 to 390 km. Mean elevation of the

TABLE I

DISTANCE CORRECTION FOR METEOR MAGNITUDE

Distance (km.)	Correction (mag.)	Distance (km.)	Correction (mag.)	Distance (km.)	Correction (mag.)
77		123		195	
	+0.5		−0.5		−1.5
81		128		204	
	+0.4		−0.6		−1.6
85		134		214	
	+0.3		−0.7		−1.7
89		141		224	
	+0.2		−0.8		−1.8
93		148		235	
	+0.1		−0.9		−1.9
97		155		245	
	0.0		−1.0		−2.0
102		162		256	
	−0.1		−1.1		−2.1
107		170		269	
	−0.2		−1.2		−2.2
112		177		282	
	−0.3		−1.3		−2.3
117		186		296	
	−0.4		−1.4		−2.4
123		195		310	

TABLE II

EXTINCTION CORRECTION FOR METEOR MAGNITUDES

Mean elevation (h)	Correction (mag.)	Mean elevation (h)	Correction (mag.)	Mean elevation (h)	Correction (mag.)
90°–74°	−0.0	14°–13½°	−1.2	7¾°	−2.4
73 –54	−0.1	13	−1.3	7½	−2.5
53 –40	−0.2	12 –12½	−1.4	7¼	−2.6
39 –33	−0.3	11½	−1.5	7	−2.7
32 –28	−0.4	11	−1.6	6¾	−2.8
27 –25	−0.5	10½	−1.7	6½	−2.9
24 –22	−0.6	10	−1.8	6¼	−3.0
21 –20	−0.7	9½	−1.9	6	−3.1
19 –18	−0.8	9	−2.0	5¾	−3.2
17½–17	−0.9	8¾	−2.1	5½	−3.3
16½–15½	−1.0	8½–8¼	−2.2	5¼	−3.4
15 –14½	−1.1	8	−2.3	5	−3.5

meteor trail was taken from the visual plot. All visual apparent magnitudes were reduced to visual absolute magnitudes through the use of Tables I and II.

The absolute duration of a meteor echo was defined as the duration that would be observed with the equipment employed if the meteor were in the zenith at a height of 100 km. To make the reduction from the observed duration to the absolute duration as defined above use was made of the curves published by McKinley (1953, Fig. 5). These curves were extended to cover ranges less than 100 km.

All meteors were now sorted into uniformly spaced classes for every 0.5 of

absolute magnitude and every 0.2 of log absolute duration. The resultant scatter diagram is reproduced in Fig. 1. It will be noted that in any one class of absolute magnitude or log absolute duration there is a wide scatter about

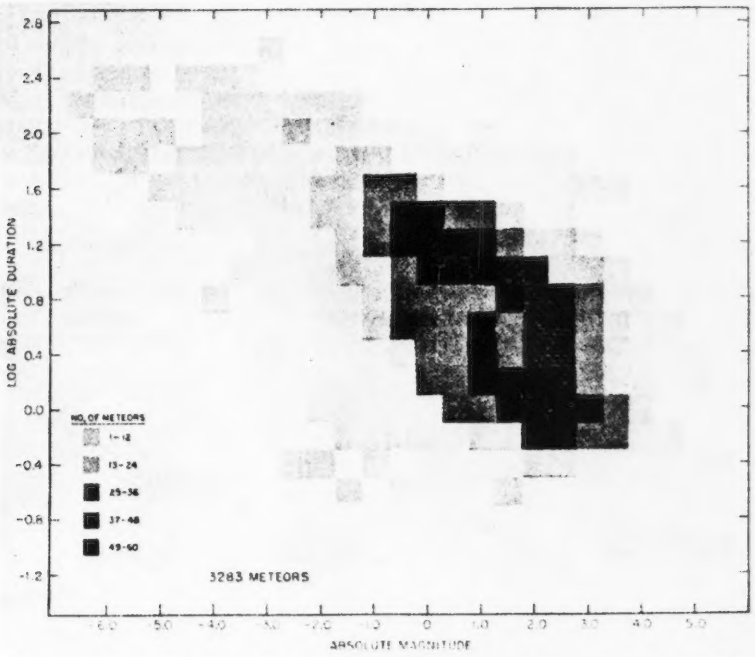

FIG. 1. Scatter diagram of the total observational material illustrating the statistical relation between the absolute visual magnitude of a meteor and the log absolute duration in seconds of its radio echo.

the mean. This results from a combination of real differences among the individual meteors with various forms of accidental and observational errors. It can best be handled as a single error function. For the absolute magnitude classes the scatter in log duration gives evidence of a double peak or maximum. The origin of this is due primarily to the non-homogeneity of the observational material, the bulk of which is made up of two categories, Perseid and Non-shower meteors. These have somewhat different duration characteristics and most of the tendency to a double maximum for log durations disappears when the material is separated into smaller, more homogeneous groups. In view of this, no attempt was made to reduce further the data as a whole. The four main groups, Perseids, Geminids, δ Aquarids, and Non-shower, were handled independently. Tables III to VI list the basic observational data for each of these groups, giving the numbers of meteors as sorted into the classes of absolute magnitude and log absolute duration.

TABLE III. PERSEIDS (1404 METEORS)

Log absolute duration	Absolute magnitude																							
	−6.5	−6.0	−5.5	−5.0	−4.5	−4.0	−3.5	−3.0	−2.5	−2.0	−1.5	−1.0	−0.5	0.0	0.5	1.0	1.5	2.0	2.5	3.0	3.5	4.0	4.5	5.0	5.5
2.6								1																	
2.4		1	1		1	1	1																		
2.2	1					1	2		3	1	1														
2.0		1	1	1		2	2	6	18	8	9	4	4	1		1									
1.8						1	4	1	5	8	13	11	9	2	2	1		1							
1.6						2	1	2	7	11	13	17	19	9	6	2	3	1	1						
1.4							1	3	3	10	15	21	23	21	9	6	2	1							
1.2								2	5	7	13	20	21	15	8	5	9	2	2						
1.0								1	1	4	14	17	18	20	11	16	10	6	4						
0.8						1			1	6	6	11	16	20	17	10	7	11	6	2	1				
0.6										1	2	10	20	13	18	12	7	14	5	3	1	1			
0.4										1	1	8	15	21	19	25	13	14	11	6	2	1	1		
0.2											1	2	7	14	24	22	24	24	19	6	5	1	1		
0.0										1		3	7	4	18	14	31	26	22	13	7	1	1		
−0.2												1	1	4	5	7	13	14	17	15	16	2	3		
−0.4												1		2	1	4	4	7	6	2	4	1			
−0.6													1		3	1	6	4	5	5	4	2	2		
−0.8																	1	2	1	1		1			
−1.0																	1	1	1		1	1		1	
−1.2																									

TABLE IV. GEMINIDS (256 METEORS)

Log absolute duration	Absolute magnitude																							
	−6.5	−6.0	−5.5	−5.0	−4.5	−4.0	−3.5	−3.0	−2.5	−2.0	−1.5	−1.0	−0.5	0.0	0.5	1.0	1.5	2.0	2.5	3.0	3.5	4.0	4.5	5.0	5.5
2.6																									
2.4																									
2.2																									
2.0		1		1		1			1																
1.8							2		2	1	5	1	1			1									
1.6								1	2	1	2	1	2	3	2					2					
1.4									1	2		2	3	7	3	6	1	1							
1.2									1	1		6	4	2	13	10	9	3							
1.0										1			1	3	5	7	7	8	6	2					
0.8										2			3	2	2	3	9	3	3	4	2				
0.6													2		3	1	1	3	4	2	1				
0.4								1							2	1	1	1		1	1				
0.2														3	3	3	3	3	1	2	1	1			
0.0													1	1	2	2		1	3	1	2				
−0.2														1		1	1	1	1	1	2	1			
−0.4															1	2	1				1				
−0.6																	1								
−0.8																1									
−1.0																				1					
−1.2																									

TABLE V. δ AQUARIDS (158 METEORS)

Log absolute duration	Absolute magnitude −6.5	−6.0	−5.5	−5.0	−4.5	−4.0	−3.5	−3.0	−2.5	−2.0	−1.5	−1.0	−0.5	0.0	0.5	1.0	1.5	2.0	2.5	3.0	3.5	4.0	4.5	5.0	5.5
2.6																									
2.4																									
2.2																									
2.0																									
1.8										1															
1.6										1	1		1	1		1	1								
1.4											1		3	3	2	3	3	1	2						
1.2											1	1	2		3	5	2		3						
1.0														1	3	2		6	4	3	1				
0.8															1	2	6	6	9	3		1			
0.6																2		3	3	3	3	2	1		
0.4																		1	2	2	3	2	1	1	
0.2															2			1	2	1	3	5		1	
0.0																			2	3	1	2	1		
−0.2																	2	2	3	1	1	1			
−0.4																									
−0.6																1	1			1				1	
−0.8																									
−1.0																		1							
−1.2																									

TABLE VI. NON-SHOWER (1420 METEORS)

Log absolute duration	Absolute magnitude −6.5	−6.0	−5.5	−5.0	−4.5	−4.0	−3.5	−3.0	−2.5	−2.0	−1.5	−1.0	−0.5	0.0	0.5	1.0	1.5	2.0	2.5	3.0	3.5	4.0	4.5	5.0	5.5
2.6																									
2.4																									
2.2							1	1	2																
2.0		1							4	2		2		2		2									
1.8		1	2		1	1	1	1	3	2	2	6	2	1		1	1		1						
1.6				1	1		1	1	1	3	3	12	3	10	2	2	2			1	1				
1.4					1	1	1			6	5	11	10	12	12	11	10	4							
1.2									2		9	7	13	23	25	22	12	8	9	7					
1.0									1	3	3	4	10	18	20	34	23	21	10	9	6				
0.8								1		1	1	6	10	12	14	20	27	27	23	18	4	4			
0.6											2	3	8	8	14	22	24	22	23	26	16	6	3		
0.4											2	2	4	6	11	13	14	31	31	19	13	12	4	1	
0.2										1	2	1	1	9	5	15	20	20	14	19	9	7	6	1	
0.0												1	1	4	4	10	18	15	25	22	17	6	4		
−0.2											1	1		3	2	7	6	21	15	12	5	2	1		
−0.4									1	1				3	3	2	2	8	8	10	2	1	1	1	1
−0.6											1		2	1	1	2	5	4	6	3	1	2	1	1	
−0.8															1	1	1	1	5	5	1	2	1		
−1.0															2			1	1	3	3	1	1		1
−1.2																	2		1					1	

It has been noted above that the relation previously published (Millman 1950) was found by averaging all log durations for each magnitude class. This method of averaging decreases the slope of the curve. The effect can best be seen by giving an illustration. In Fig. 2 the Perseid data have been plotted in two ways, (*A*) averages of log duration for each magnitude class—filled circles

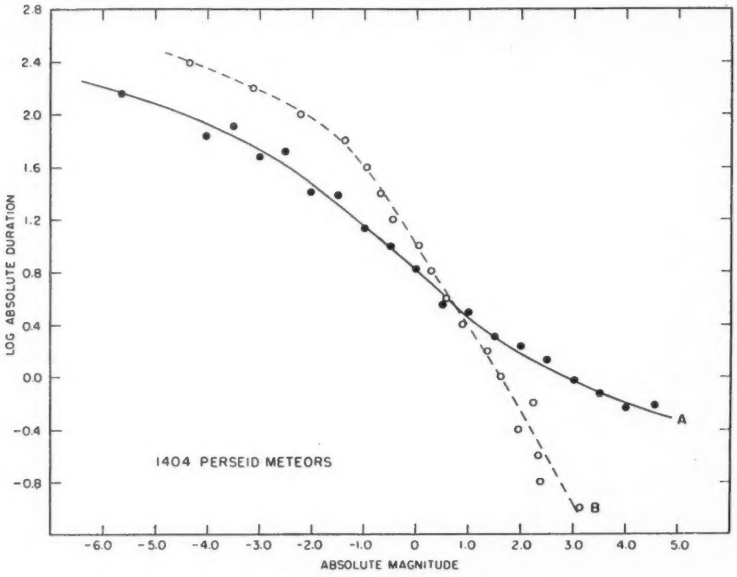

FIG. 2. Mean values for the Perseid meteors:
A—mean log absolute durations for absolute magnitude classes.
B—mean absolute magnitudes for log absolute duration classes.

and solid line, and (*B*) averages of magnitude for each log duration class—open circles and broken line. It will be seen that there is a marked difference between the two curves. Obviously the best statistical relation to use in any theoretical application to studies of the upper atmosphere is something between these two extremes.

As a preliminary to finding the best mean curve between absolute magnitude and log absolute duration, the error functions for scatter in the two coordinates were studied for the Perseids and for the Non-shower meteors. It was assumed that the form of the error function was constant over the entire range for each coordinate and that the observational material was essentially complete over approximately the central third of these ranges. On the basis of these assumptions mean error functions were determined and are listed in Table VII. These are given in terms of percentage of the observed material in each class listed in relation to the mean class. The figures are rounded off to the nearest half of one per cent. Owing to the greater homogeneity of the data the mean errors

TABLE VII

Error functions in absolute magnitude			Error functions in log absolute duration		
Δ mag.	Perseids	Non-shower	Δ log dur.	Perseids	Non-shower
−3.5		0.5%	1.4	0.5%	
−3.0		1.5	1.2	1.0	0.5%
−2.5	1.5%	2.5	1.0	1.5	1.5
−2.0	4.0	4.5	0.8	4.5	4.5
−1.5	8.5	7.0	0.6	8.5	9.0
−1.0	13.0	10.5	0.4	11.0	15.0
−0.5	16.0	14.0	0.2	13.5	17.0
0.0	17.5	17.0	0.0	16.5	14.5
+0.5	14.5	15.0	−0.2	15.5	11.5
+1.0	10.0	12.0	−0.4	13.0	9.0
+1.5	7.5	8.0	−0.6	7.5	6.5
+2.0	4.5	4.5	−0.8	4.0	4.5
+2.5	2.0	2.5	−1.0	2.0	3.0
+3.0	1.0	0.5	−1.2	1.0	2.0
			−1.4		1.0
			−1.6		0.5
	100.0%	100.0%		100.0%	100.0%
Mean error	0.91 mag.	0.98 mag.		0.38 log dur.	0.41 log dur.

for the Perseids are slightly smaller than for the Non-shower meteors but the difference is not as great as one would have expected from other considerations. The error functions determined from the 3283 meteors taken together give mean errors somewhat higher than those listed in Table VII.

	Mean errors	
Perseids	±0.91 mag.	±0.38 log dur.
Non-shower	±0.98	±0.41
All meteors	±1.06	±0.43

It is a little difficult to say how much of these mean errors is intrinsic in the meteors themselves and how much is observational error. The mean error of the original magnitude estimates may be taken as ±0.5 magnitude. If we consider the various reduction and reading errors we can place the observational mean error of a single absolute magnitude determination at between ±0.6 and ±0.7 magnitude and in log duration between ±0.2 and ±0.3. This leaves us ±0.7 magnitude and ±0.3 log duration as the scatter originally present in the meteors. These values should be regarded as only rough approximations.

Assuming the Perseid error functions of Table VII and using the methods of numerical integration, a correction was computed for each of the points in Fig. 2. The resulting corrected positions have been plotted in Fig. 3, significance of the data being indicated by three sizes of dots based on numbers of meteors contributing to each point. Although there is a very slight tendency for the points to be a little low for the very bright and very faint meteors it seems best to represent the relation by a straight line as was done previously. The points at the extremes of this line are represented by relatively few meteors and the magnitude estimates of these meteors are difficult to make and are more subject to systematic error.

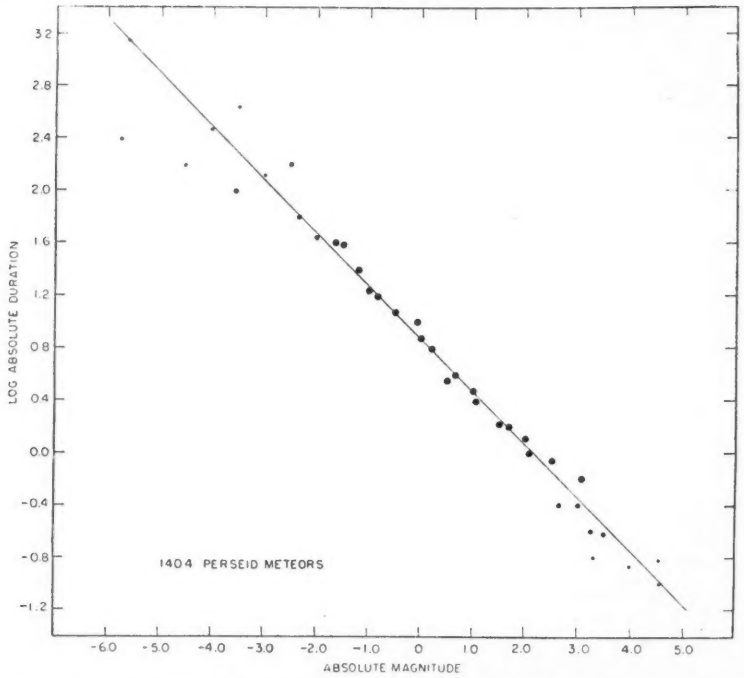

FIG. 3. Mean values for Perseid meteors after correction for the effect of the error function.

The observational material available for the Geminid and δ Aquarid meteors was not enough to make possible the determination of reliable error functions. Hence, the error functions for the Perseids were applied in the case of the other two showers and the mean points corrected in the same way as for the Perseids. The Non-shower meteors were reduced, using their error functions listed in Table VII. The best straight lines were now drawn through the corrected points for the Geminids, δ Aquarids, and Non-shower meteors. These, together with the Perseid line from Fig. 3, are plotted in Fig. 4. The equations for these lines are given below where T is the absolute duration in seconds and M is the absolute magnitude.

(1) $$\log T_P = 0.87 - 0.406\ M_P$$

(2) $$\log T_G = 1.15 - 0.349\ M_G$$

(3) $$\log T_D = 1.21 - 0.322\ M_D$$

(4) $$\log T_N = 1.10 - 0.378\ M_N$$

In the case of the Geminid and δ Aquarid curves there were not enough observational data to make a good determination of the relation and the results for these showers should be considered as tentative.

For comparison purposes the Perseid curve published by Millman (1950)

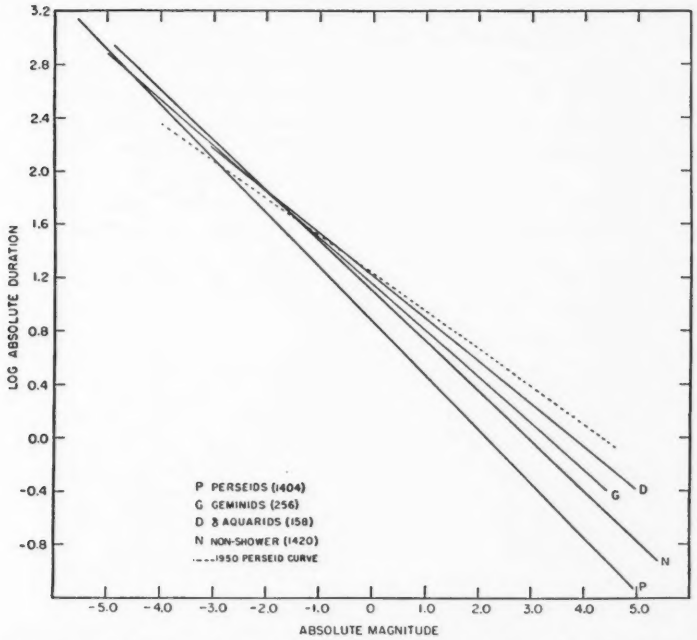

FIG. 4. Corrected mean relations between absolute magnitude and log absolute duration for various groups of meteors.

has been shown in Fig. 4 as a dotted line. The smaller slope of this earlier curve is due to the fact that only magnitude classes were averaged without any correction for the error function. Its position is above the final curve because it was drawn for apparent magnitude. Conversion to absolute magnitude would shift it approximately one magnitude interval to the left.

It will be noted that the curves in Fig. 4 are fairly close together for the bright meteors. At absolute magnitude -5 the over-all average duration for all types of meteors is 850 sec. As we move to the fainter meteors the echo duration for corresponding visual brightness is longer for the slower objects. In particular, the Geminid meteors have a smaller slope than the Perseid meteors, so that faint Geminids have echoes which last considerably longer than faint Perseids. This apparently anomalous effect is very likely due to the fact that on the average the enduring ionization occurs at a lower height for the slower meteors (Kaiser 1953; Millman 1950, 1954), and is hence subject to a smaller diffusion coefficient.

The material dealt with in this paper consists almost entirely of overdense ionization trails where the number of electrons per cm. path length, α, is greater than 10^{12} (Greenhow, 1952). In this case, according to Greenhow, the duration of an echo in seconds is

$$T = \alpha/4\pi DN_e, \tag{5}$$

where D is the diffusion coefficient in cm.^{2}/sec. and N_e is the critical electron density for the wavelength used. McKinley has shown (1953, Fig. 2) that there is a second order correction to the value for T given in equation (5) depending on the sensitivity of the transmitter–receiver system used in the observations. We will assume that equation (5), without correction, applies to observations made with the Ottawa equipment.

Greenhow and Neufeld (1955) have recently determined the variation of diffusion coefficient with height by a study of underdense meteor trails. The mean height of Perseid echoes measured at Ottawa by three-station triangulation is 99.3 km. and of Geminid echoes 91.6 km. (Millman 1954). The diffusion coefficients (Greenhow and Neufeld 1955) corresponding to these heights have a ratio whose log is 0.53. For observations made at a single wavelength, equation (5) may be written

$$\log T = \log \alpha - \log D + \text{const.} \tag{6}$$

To allow for the differences in the diffusion coefficients the Geminid curve in Fig. 4 should be lowered by 0.53 for comparison with the Perseid curve. This brings the Perseid and Geminid curves into coincidence near absolute magnitude +5 and we can conclude that the ratio between ionization and visual luminosity is roughly equal for the two showers at this magnitude. Making a reasonable assumption concerning the mean velocity of the Non-shower meteors, this curve also, when corrected for change in the diffusion coefficient with height, is in agreement with the other two at magnitude +5. The δ Aquarid curve does not agree as well but it is based on so few meteors that it is not very well determined, particularly at the lower end.

Assuming equation (6) to be correct, and taking an average D for any given shower, $\log T$ varies directly as $\log \alpha$. Since each drop in magnitude by one means an increase in visual luminosity by a factor of 2.512, it follows that a slope of -0.400 between $\log T$ and M indicates a constant ratio between ionization, or α, and visual luminosity for all magnitudes. As seen from equation (1) this is very nearly satisfied for the Perseid meteors. For our observations $N_e = 1.33\times10^7$; hence from equation (5)

$$\alpha = 1.67\times10^8\, DT. \tag{7}$$

If we take 100 km. as the best general average for the height of Perseid echoes, D is 1.35×10^5 cm.^{2}/sec. as determined by Greenhow and Neufeld, and for a zero magnitude Perseid meteor $\alpha = 1.7\times10^{14}$ from equation (7), or in round numbers 2×10^{14}.

Since the Perseid curve shows a nearly constant ratio between ionization and visual luminosity we can adopt $\alpha = 2\times10^{12}$ for Perseids of absolute magnitude +5. This value of α can also be adopted as a good average for the Geminid and Non-shower meteors. As we go to brighter meteors the corrected Geminid curve falls below the Perseid curve and at magnitude -5 the relative ionization for the Geminids has dropped by a factor of between 3 and 4 when compared with the Perseids. These results alter somewhat the conclusions of Greenhow and Hawkins (1952), which were based on our preliminary experi-

mental curve. The slopes of the final curves given here are in fair agreement with the theoretical curve plotted in Greenhow and Hawkin's paper (1952), and the indication is that there are more electrons present for the brighter meteors than was suggested in their paper. An upward revision of the number of electrons present in bright meteor trails will simplify the explanation of certain features of meteor spectra. Further consideration of this point will appear elsewhere.

Among those who assisted at various times in the reduction of basic data, the authors would like to express their thanks particularly to Miss Joan Stewart, who was chiefly responsible for compiling Tables III to VI.

REFERENCES

GREENHOW, J. S. 1952. Proc. Phys. Soc.(London), B, **65**: 169.
GREENHOW, J. S. and HAWKINS, G. S. 1952. Nature, **170**: 355.
GREENHOW, J. S. and NEUFELD, E. L. 1955. J. Atm. and Terrest. Phys. **6**: 133.
KAISER, T. R. 1953. Phil. Mag. Suppl. **2**: 495.
KAISER, T. R. and CLOSS, R. L. 1952. Phil. Mag. (Ser. 7), **43**: 1.
LINDBLAD, B.-A. 1952. Trans. Chalmers Univ. Technol. Gothenburg, No. 129.
LUNDMARK, K. 1932. Handbuch der Astrophysik, **V/1**: 566.
McKINLEY, D. W. R. 1953. Can. J. Phys. **31**: 758.
McKINLEY, D. W. R. and MILLMAN, P. M. 1949. Proc. I.R.E. **37**: 364.
MILLMAN, P. M. 1950. J. Roy. Astron. Soc. Can. **44**: 209.
——— 1954. Science, **120**: 325.

A MODIFICATION OF THE ONE-PARTICLE FORMULA FOR NUCLEAR GAMMA-RADIATION[1]

By P. R. Wallace

ABSTRACT

The one-particle theory of isomeric γ-transitions in nuclei consistently overestimates the probability per unit time of decay. It is shown that, by modifying the one-particle model to take account of the readjustment of the wave functions of all the nuclear particles during the predominantly one-particle transition, satisfactory agreement with experiment can be obtained. The fact that odd-proton transitions are depressed more than odd-neutron ones is attributed to the exchange character of the force giving rise to the readjustment.

INTRODUCTION

The nuclear shell (one-particle) model of nuclei has been used with considerable success as a basis for the analysis of isomeric γ-transitions in nuclei (Blatt and Weisskopf 1952, Chap. 12 and Appendix B; Moszkowski 1953; Stech 1952; Weisskopf 1951). It has however been noted, especially by Gottfried (1953), that the single-particle model tends to overestimate the transition probability by a sizable factor. In magnetic 2^4-pole ($M4$) transitions, for which on the whole both the data and their interpretation are most clear-cut, this factor is ≈ 50 to 100 in most cases. The discrepancy between theory and experiment is undoubtedly significant, and requires explanation.

It has also been noted by Graham and Bell (1953) that the transition probabilities for odd-proton $M1$ transitions fall further below the predictions of the single-particle model than do those for odd-neutron transitions. A study of Table 3-1 in Gottfried's thesis shows that this is also the case, on the average, for $M4$ transitions.

An explanation of these two discrepancies is offered, along the following lines: when one nuclear particle (P_1) makes a transition, the wave functions of all the other particles in the nucleus undergo a small change, due to the contribution of P_1 to the potential field in which they move. If ψ_f is the final-state wave function of the particle P_2, and ψ_i its initial-state wave function, and $\psi_f \neq \psi_i$, the transition probability is thereby decreased by a factor

$$1-f = \left| \int \psi_f^* \psi_i \, d\tau \right|^2, \tag{1}$$

where the integration is over the coordinates of the particle. Although individually the f's may be small, their large number in a heavy nucleus reduces the transition probability by just such a factor as that noted. The greater effect in odd-proton transitions may be attributed to the tendency, due to exchange force, for protons to interact most strongly on the average with neutrons, and vice versa. The greater numbers of neutrons will then accentuate the effect in the odd-proton case.*

[1]Manuscript received August 11, 1955.

Contribution of the Department of Mathematics, McGill University, Montreal, Quebec.

*It was once suggested by the author (Bull. Am. Phys. Soc. **30** (No. 1): 66. 1955) that the explanation lay in the effect of the Coulomb force. It now appears that this conclusion was based on an error of numerical calculation, and that the Coulomb force is somewhat too weak for the purpose.

It is true that the readjustment of the wave function of all the nuclear particles gives an additional contribution to the transition probability. This, however, may be seen to be small in the cases in which the transitions are "almost single-particle" ones. For suppose that the average factor by which the readjustment of a single particle cuts down the matrix element is $(1-f)$. Then the major contribution is decreased by a factor $(1-f)^{A-1}$, A being the number of nuclear particles. But in the case of the additional contributions the matrix element is in the first place smaller by a factor $\lesssim f$. It must then be multiplied by $(1-f)^{A-2}N$, where $N=\int \Psi_f^* \Psi_i \, d\tau$ for the particle P_1 and is very small. These additional contributions are then $\approx fN(A-1)$ times smaller than that from P_1. Since $f(A-1) \approx 1$, we see that they may be neglected.

These considerations apply to the case in which the transition is "almost" single-particle. They will not apply to the very strong even–even $E2$ transitions, nor to those cases in which the correct initial and final spin assignments require coupling the angular momenta of two or more particles (e.g. transitions of odd–odd nuclei).

MODIFICATION OF THE SINGLE-PARTICLE FORMULA

Let us designate the initial- and final-state wave functions of the particle P_1 which makes the transition by Ψ_i and Ψ_f respectively. Let us also designate the initial-state wave functions of the other nucleons by ψ_α.

Now the change in the potential due to the transition of P_1 may be written:

$$H' = \int (|\Psi_f(\mathbf{r}')|^2 - |\Psi_i(\mathbf{r}')|^2) \frac{V_0 \exp(-\mu|\mathbf{r}-\mathbf{r}'|)}{\mu|\mathbf{r}-\mathbf{r}'|} d^3\mathbf{r}' + H'', \tag{2}$$

where we have assumed a Yukawa interaction between particles. V_0 is the strength of the interaction and μ^{-1}, the π-meson Compton wavelength, is $\approx e^2/2mc^2$, i.e. half the classical electron radius. H'' is the Coulomb force contribution which we shall see is too small to be of much significance.

With regard to the exchange character of the force, it is of course not well enough known to be taken into account quantitatively. V_0 should presumably be taken to have somewhat different values depending on the relative symmetry of the wave functions of P_1 and the core particle.* It will be seen (equation (6) below) that the contributions from the various core particles appear additively in an exponent. We shall, for a first orientation, use a single (average) V_0, which will be carried through the calculations as a parameter. It will be found that best agreement with experiment will then be obtained with $V_0 \approx 40$ Mev. (compared with $V_0 \approx 53$ Mev. for the deuteron (Sachs 1953)). We shall then consider the effect of assuming the force to be a mixture of the ordinary and Majorana forms.

We may now apply simple perturbation theory to discuss the perturbation of the particle wave functions. We have for ψ_α', the final-state wave function corresponding to the initial state ψ_α:

$$\psi_\alpha' = N_\alpha \psi_\alpha + \sum_{\beta \neq \alpha} \frac{H'_{\alpha\beta}}{E_\alpha - E_\beta} \psi_\beta, \tag{3}$$

*Since the result will depend only on $|V_0|^2$ (equation (9)) the *sign* of V_0 is therefore of no concern for our purposes.

$H_{\alpha\beta}'$ being the matrix element of H' between the state ψ_α and any other state ψ_β in the nuclear potential. E_α and E_β are the energies of the states α and β respectively. The factor N_α must be chosen to normalize ψ_α', i.e.

$$N_\alpha = \left[1 - \sum_{\beta \neq \alpha} \frac{|H_{\alpha\beta}'|^2}{(E_\alpha - E_\beta)^2}\right]^{\frac{1}{2}}. \tag{4}$$

It follows that the readjustment factor $(1-f_\alpha)$ arising from the particle α is N_α^2. We may therefore put

$$f_\alpha = \sum_{\beta \neq \alpha} \frac{|H_{\alpha\beta}'|^2}{(E_\alpha - E_\beta)^2}. \tag{5}$$

But the product of all the factors $(1-f_\alpha)$ is

$$\Pi(1-f_\alpha) \approx \exp\left(-\sum_\alpha f_\alpha\right) = e^{-g} \tag{6}$$

where

$$g = \sum_{\beta \neq \alpha} \frac{|H_{\alpha\beta}'|^2}{(E_\alpha - E_\beta)^2}. \tag{7}$$

The α summation is over occupied states, the β one over all states in the nuclear potential.

METHOD OF CALCULATION

It would clearly be unduly tedious for our purposes to evaluate the summation in (7) for the aggregation of, say, spherical well or oscillator states. On the other hand, it is important to take account of the explicit form of the wave functions of the particle P_1. We shall use, for these, harmonic oscillator states. For all the other particles and states we shall simplify matters by using the Fermi gas approximation.

One must take care, however, in handling the denominators $(E_\alpha - E_\beta)^2$. There will, of course, be a finite spacing between E_α and the nearest available level E_β. The individual features of various nuclei will in fact be manifested at this point, through the details of level structure. In order, however, to get a reasonably accurate *statistical* result, we shall replace the summations by integrations, but omit from the β-summation a region of energy $1/2\rho(E_\alpha)$ on either side of E_α, $\rho(E_\alpha)$ being the density of energy levels of the Fermi gas at energy E_α.

We have, therefore, for g in equation (6)

$$\frac{1}{V^2}\int\int \frac{d^3\mathbf{k}_\alpha d^3\mathbf{k}_\beta}{(k_\alpha^2 - k_\beta^2)^2}\left(\frac{2M}{\hbar^2}\right)^2 \left|\int \exp[i(\mathbf{k}_\beta - \mathbf{k}_\alpha)\cdot\mathbf{r}]H'(\mathbf{r})\, d^3\mathbf{r}\right|^2 \frac{4V^2}{(8\pi^3)^2}, \tag{8}$$

where M is the nuclear mass, $\mathbf{k}_\alpha$ and $\mathbf{k}_\beta$ are the wave-numbers of the states α and β, and V is the nuclear volume. The $\mathbf{k}$-integrations are subject to the limitation mentioned in the previous paragraph, and the $\mathbf{r}$-integration runs only over the interior of the nucleus. However, this is also the range over which $H'(\mathbf{r})$ has an appreciable value, and consequently no serious error will be involved in extending the integration over all space. In any case, the "radius of the nucleus" is indefinite to within the distance $1/\mu$ in which $H'(\mathbf{r})$ falls off.

Making the approximation in question, then, we see that our result involves only the Fourier transform of $H'(\mathbf{r})$. Since $H'(\mathbf{r})$ is a convolution of $(|\Psi_f|^2-|\Psi_i|^2)$ and the interparticle potential, its Fourier transform is the product of the Fourier transforms of these quantities. Writing $\chi(\mathbf{k})$ for the transform of $(|\Psi_f|^2-|\Psi_i|^2)$, we have for g:

$$(9)\quad g=\left(\frac{2M}{\hbar^2}\right)^2\left(\frac{V_0}{\mu}\right)^2\frac{1}{16\pi^6}\int\int\frac{1}{(k_\alpha^2-k_\beta^2)^2}|\chi(\mathbf{k}_\alpha-\mathbf{k}_\beta)|^2\left[\frac{4\pi}{\mu^2+(\mathbf{k}_\alpha-\mathbf{k}_\beta)^2}\right]^2 \times d^3\mathbf{k}_\alpha d^3\mathbf{k}_\beta.$$

It must be borne in mind that the range of integration is such that

$$(10)\quad \left|\frac{\hbar^2}{2M}(k_\alpha^2-k_\beta^2)\right|\geqslant\frac{1}{2\rho(E_\alpha)}=\frac{2\pi^2}{V}\frac{\hbar^2}{2M}\frac{1}{k_\alpha}$$

or

$$(11)\quad |k_\alpha^2-k_\beta^2|\geqslant 2\pi^2/Vk_\alpha.$$

To evaluate the integral in (9), we introduce new variables $\mathbf{k}_\alpha$ (with range $|k_\alpha|<k_m$, corresponding to the highest filled state), and $\mathbf{K}=\mathbf{k}_\beta-\mathbf{k}_\alpha$, the range of which is limited by

$$(12)\quad |2\mathbf{k}_\alpha\cdot\mathbf{K}+\mathbf{K}^2|\geqslant 2\pi^2/Vk_\alpha.$$

It is now easy to do the integration over $\mathbf{k}_\alpha$ to get

$$(13)\quad g=\frac{32}{\pi^2}\frac{M^2}{\hbar^4}\frac{V_0^2}{\mu^2}\int\left[\frac{V}{6\pi^2}k_m^3-\frac{k_m}{2K}-\frac{1}{8}\ln\frac{|k_m-\tfrac{1}{2}K|}{k_m+\tfrac{1}{2}K}\right]|\chi(\mathbf{K})|^2\frac{1}{(\mu^2+K^2)^2} \times KdK\frac{d\Omega}{4\pi}.$$

The latter two terms in the square bracket of the integrand are negligible compared with the first; for

$$(14)\quad Vk_m^3/6\pi^2=\tfrac{1}{4}A$$

where A is the total number of particles in the nucleus. By comparison, the term $k_m/2K$ is unimportant owing to the fact that, for small K, $|\chi(K)|^2$ goes like K^4, so that this region contributes very little to the integral. The logarithmic term is also not important. Its singularity is integrable, and in any case occurs for $K=2k_m$, at which value the rest of the integrand is completely negligible. These terms have in fact been included in the numerical integration which follows, and are found not to influence the result significantly.

With respect to the leading term, it should be noted that we might have distinguished the contributions of neutrons and protons in the nucleus throughout. However, these contributions would be additive. Different k_m's would be appropriate for the two cases, but the sum of the terms $Vk_m^3/6\pi^2$ would still be $\frac{1}{4}A$.

To a good approximation we have, then,

$$(15)\quad g=\frac{8A}{\pi^2}\frac{M^2}{\hbar^4}\frac{V_0^2}{\mu^2}\int_0^\infty|\chi(\mathbf{K})|^2\frac{1}{(\mu^2+K^2)^2}KdK\frac{d\Omega}{4\pi}.$$

The angular integration may be performed explicitly, and the K-integration may be done numericaliy for each case of interest.

RESULTS

We shall confine our attention to $M4$ transitions. In fact, we should not expect any serious differences between the various $M4$ cases: $g_{9/2} \rightarrow p_{1/2}$, $h_{11/2} \rightarrow d_{3/2}$, $i_{13/2} \rightarrow f_{5/2}$. We shall therefore treat only the first of these.

In general, it would be necessary to distinguish the factors for transitions involving the various m_j states of the particle P_1. For $g_{9/2} \leftrightarrow p_{\frac{1}{2}}$, however, this is not necessary. For in fact the (magnitude)^2 of the $p_{\frac{1}{2}}$ functions is spherically symmetric, being given by

$$|\Psi(p_{\frac{1}{2}})|^2 = \frac{4}{15\pi^{3/2}} r^2\left(\frac{5}{2}-r^2\right)^2 e^{-r^2}. \tag{16}$$

Since only *relative* orientations of initial- and final-state wave functions are important, all m_j states of $g_{9/2}$ give the same result. We take, therefore, the case of $m_j = 9/2$, and we then find

$$|\Psi(g_{9/2})|^2 = \frac{1}{24\pi^{3/2}} r^8 \sin^8\theta\, e^{-r^2}, \tag{17}$$

where (r, θ) are polar coordinates.

We may now evaluate the Fourier transforms of these functions to get

$$|\phi(p_{\frac{1}{2}})|^2 = e^{-K^2/4}\left[1-\tfrac{1}{2}K^2+\frac{11}{120}K^4-\frac{1}{240}K^6\right] \tag{18}$$

and

$$|\phi(g_{9/2})|^2 = e^{-K^2/4}\left[1-K^2\sin^2\gamma+\frac{3}{16}K^4\sin^4\gamma-\frac{1}{96}K^6\sin^6\gamma+\frac{1}{6144}K^8\sin^8\gamma\right], \tag{19}$$

γ being the polar angle of the transform variable K.

The first of these wave functions corresponds to the oscillator level $n = 3$, the second $n = 4$; these are the levels appropriate to the known $M4$ transitions of this type. The units in the wave functions are so chosen as to make numerical coefficients as simple as possible. However, we must determine their relation to more natural units. If we choose the inflection point of the (wave function)^2 of the outer particle as the boundary of the nucleus, this yields a nuclear radius in our units of $\approx\sqrt{6} = 2.45$. Now the nuclear radius in conventional units is $1.4\times10^{-13}\,A^{1/3}$, whereas $\mu^{-1} = e^2/2mc^2 = 1.4\times10^{-13}$. Hence $\mu^{-1} = 2.45/A^{1/3}$ in our units. For the known $g_{9/2} \leftrightarrow p_{\frac{1}{2}}$ transitions A runs from 69 (Zn^{69}) to 115 (In^{115}). μ therefore ranges from 1.67 to 2. However, this variation does not affect the result very much, so we shall consider only an average value of 1.9 corresponding to $A \approx 100$.

We may now evaluate analytically the angular integrals in (15), after which the K-integration can be done numerically. We obtain the result:

$$g = 3.25\times10^{-5}\, V_0^2\, A \tag{20}$$

where V_0 is in Mev. It is interesting to note that the integrand in g begins to climb after $K = 0.8$, reaches a peak at about $K = 1.6$, and becomes negligible after $K \approx 3.2$. In our units $k_m \approx 4$, and hence, as remarked earlier, $k_m/2K$ is, in the whole significant range, $\ll A/4$, and $K = 2k_m$ is *outside* the significant range. Thus the neglect of the latter two terms in (13) was justified.

For $V_0 = 40$ Mev., and $A = 100$, we find that $g = 5.2$ and $e^{-g} = 0.0055$. For the 16 $M4$ isomers of this type listed by Gottfried, on the average $e^{-g} = 0.014$. This corresponds to $g = 4.25$ or $V_0 \approx 36$ Mev., which is a quite reasonable value.

CHARGE EFFECT

We have estimated the contribution from the Coulomb force, ignoring "interference" effects between Coulomb and nuclear force. This is probably justified because the Coulomb force has its greatest effect in the range in which the nuclear force contribution is insignificant, and also because the nuclear force must, for saturation, have one sign almost as often as the other. The Coulomb contribution then follows from (15) by putting $V_0/\mu \to e^2$, $\mu \to 0$, and $A \to Z$, i.e.

$$g_c = \frac{8Z}{\pi^2}\frac{M^2}{\hbar^4}e^2\int_0^K |\chi(K)|^2\frac{1}{K^3}\,dK\,\frac{d\Omega}{4\pi}. \tag{21}$$

For the $g_{9/2} \leftrightarrow p_{\frac{1}{2}}$ case, $Z \approx 50$, this gives only $g_c \approx 0.1$, which is too small to be a serious factor.

However, another factor giving rise to a difference between the odd-neutron and odd-proton cases is the effect of the exchange character of the forces. Let us assume that the nuclear force is a mixture of ordinary and Majorana force. The latter will be repulsive between antisymmetric pairs, attractive between symmetric pairs. Thus, V_0 may have two values, V_s and V_a, according as the core nucleons form symmetric or antisymmetric combinations with the outer particle P_1. Now if P_1 is a proton, the interaction will be V_s with one-quarter of the core protons, V_a with three-quarters of them. For core neutrons, the ratio will be $\frac{1}{2} : \frac{1}{2}$. If P_1 is a neutron, the situation is reversed. Designating by G the ratio $g/A\,V_0^2$ in (15), we now have for the odd-proton case

$$g_1 = GZ(\tfrac{1}{4}V_s^2+\tfrac{3}{4}V_a^2)+G(A-Z)(\tfrac{1}{2}V_s^2+\tfrac{1}{2}V_a^2) \tag{22}$$

while in the odd-neutron case

$$g_2 = G(A-Z)(\tfrac{1}{4}V_s^2+\tfrac{3}{4}V_a^2)+GZ(\tfrac{1}{2}V_s^2+\tfrac{1}{2}V_a^2). \tag{23}$$

The average of these is

$$\bar{g} = \tfrac{1}{2}(g_1+g_2) = GA(\tfrac{3}{8}V_s^2+\tfrac{5}{8}V_a^2); \tag{24}$$

this reflects the result, pointed out by Blatt and Weisskopf (1952, p. 147), that there are in the nucleus more antisymmetric than symmetric pairs in the ratio 5:3. The difference in the factors is

$$g_1-g_2 = G(A-2Z)\,\tfrac{1}{4}(V_s^2-V_a^2). \tag{25}$$

The ratio of this to $\bar{g}$ is

$$\frac{\Delta g}{\bar{g}} = \frac{A-2Z}{A}\,\frac{2(V_s^2-V_a^2)}{3V_s^2+5V_a^2}. \tag{26}$$

If V_s is considerably bigger than V_a,* this ratio becomes $\approx \frac{2}{3}(A-2Z)/A$.

*The "Serber force" (Hadley *et al.* 1949) has $V_a = 0$.

For the cases under consideration, this gives on the average odd-proton transitions about five-eighths as fast as comparable odd-neutron ones. On the average of cases considered by Gottfried, it is found that they are a little more than half as fast.

It may, of course, be argued that experimental errors make these small differences insignificant. We content ourselves with pointing out a difference of a factor of almost two in the data averaged over nearly 40 $M4$ transitions, and noting that some such effect might be expected theoretically.

COLLECTIVE MODEL

On the collective nuclear model of Bohr and Mottelson (1953), a reduction in the single-particle transition matrix element due to readjustment of the nuclear surface is to be expected, as they point out (p. 107). However, to obtain agreement with the observed results, it is necessary to postulate that the initial and final surface wave functions are almost orthogonal, which seems unlikely even in the case of strong coupling. The difficulty in getting large enough readjustment factors on this model arises from the suppression of a large number of degrees of freedom, no one of which would contribute seriously, but which, taken together, would have a considerable effect.

ACKNOWLEDGMENTS

The author wishes to acknowledge the support of the Summer Research Institute of the Canadian Mathematical Congress for the award of a Fellowship.

REFERENCES

BLATT, J. and WEISSKOPF, V. F. 1952. Theoretical nuclear physics. John Wiley & Sons, Inc., New York.

BOHR, A. and MOTTELSON, B. 1953. Kgl. Danske Videnskab. Selskab, Math.-fys. Medd. **27**.

GOTTFRIED, K. 1953. M.Sc. Thesis, McGill University, Montreal, Que.

GRAHAM, R. L. and BELL, R. E. 1953. Can. J. Phys. **31**: 377.

HADLEY, J., KELLY, E., LEITH, C., SEGRÉ, E., WIEGAND, C., and YORK, H. 1949. Phys. Rev. **75**: 351.

MOSZKOWSKI, S. A. 1953. Phys. Rev. **89**: 474.

SACHS, R. G. 1953. Nuclear theory. Addison-Wesley Press, Inc., Cambridge, Mass. p. 34.

STECH, B. 1952. Z. Naturforsch. **7a**: 401.

WEISSKOPF, V. F. 1951. Phys. Rev. **83**: 1073.

THE DECAY OF Re^{186} AND Re^{188} [1]

By M. W. Johns, C. C. McMullen, I. R. Williams, and S. V. Nablo

ABSTRACT

The energies and intensities of 13 gamma rays in Re^{188} have been measured by studying their external conversion spectra with a high resolution beta-ray spectrometer. An analysis of the beta-ray spectrum reveals groups with end points 2116 kev. (79%) and 1961 kev. (20%), and several low energy groups whose total intensity is of the order of 1%. The observed data can be consistently accounted for in terms of a decay scheme involving the following levels of Os^{188}: 0.0, 155.0, 633, 1086, 1306, 1461, 1765, 1941, and 1958 kev. This scheme is firmly supported by coincidence measurements. The spins of the first three levels listed are 0+, 2+, and 2+ and that of the 1461 kev. level is probably 0+.

The decay of Re^{186} is accompanied by gamma rays of the following energies and quantum intensities: 122.9 kev. (0.6%), 137.2 kev. (10%), 630.8 kev. (0.024%), and 768.2 kev. (0.024%). These values are in good agreement with those quoted in the literature, except for the intensities of the last two radiations.

INTRODUCTION

The n–γ reaction in rhenium leads to 91-hr. Re^{186} and 18-hr. Re^{188}. The 91-hr. activity has been extensively studied (Beach *et al.* 1949; Grant and Richmond 1949; Guss *et al.* 1954; Koerts 1954; Langer and Price 1949; Metzger and Hill 1951; Porter *et al.* 1955; Steffen 1951) and the measurements given here serve chiefly to confirm existing information. The 18-hr. activity is accompanied by a rich spectrum of beta- and gamma-radiations which were only partially resolved by workers using instruments of moderate resolution (Beach *et al.* 1949; Cork *et al.* 1948; Goodman and Pool 1947; Miller and Curtiss 1946; Richmond *et al.* 1952). This paper presents the results of a series of experiments carried out with a high resolution beta-ray spectrometer (Johns *et al.* 1953) and coincidence circuits and proposes a decay scheme well supported by coincidence measurements. Some of these results have already appeared in brief form (McMullen and Johns 1953 *a*, *b*).

APPARATUS AND METHODS

Nine sources of spec-pure rhenium powder, sealed in aluminum or quartz, were irradiated in the Chalk River or Brookhaven reactors for use as gamma sources. These were shipped by air express and had effective strengths of about 300 mc. upon arrival. The gamma radiations from these sealed sources were studied by examining the external conversion peaks which they produced in lead, uranium, or gold radiators of thicknesses from 0.4 to 20 mgm./cm.^{2} The annihilation radiation from the small amount of copper impurity in aluminum proved somewhat troublesome in early runs and made necessary a shift to quartz containers. All the radiations observed decayed with either the 18-hr. or the 91-hr. half-life expected, indicating that they are associated with either the Re^{188} or the Re^{186} nuclides.

Sources of less than 5 mc. of activity sealed in quartz vials were used for preparation of beta sources or for coincidence work. Such quartz vials were

[1]Manuscript received September 26, 1955.
Contribution from the Department of Physics, McMaster University, Hamilton, Ontario.

crushed under nitric acid and the resulting rhenium nitrate evaporated to dryness on the desired source backing. The beta sources used were sufficiently thin that the conversion peaks in the 50 kev. region possessed a full width at half maximum of less than 1% in momentum and showed no serious degradation on the low energy side.

The Geiger counter detector used in the earlier runs (Johns *et al.* 1953) was replaced by an anthracene crystal – 6291 photomultiplier combination for later measurements. This change made possible the 100% detection of electrons of energy down to 25 kev. without difficulty and removed the necessity for making counter-window absorption corrections for conversion lines in the 50 kev. region.

Details concerning the calibration of the spectrometer for energy and intensity measurements have already been described (Johns and Nablo 1954). External conversion peaks produced by the precisely known gamma rays of Co^{60}, Ir^{192}, and Cs^{137} and internal conversion lines from the thorium active-deposit were used as standards. The beta end points were obtained by extrapolation from the Fermi analyses. The errors quoted on all energy measurements are believed to include both statistical and systematic errors.

Two gamma-ray scintillation spectrometers using NaI(Tl) or anthracene crystals, 6292 photomultipliers, and single-channel pulse-height analyzers (Bell and Graham 1953) were used in a coincidence circuit of resolving time 1 μsec. β–γ, β–X, and γ–γ coincidences were studied in both Re^{186} and Re^{188} With one analyzer set to record the desired portion of the beta spectrum or the photopeak of one gamma ray, the gamma-ray spectrum was scanned with the other analyzer and both the single-channel and the coincidence spectra were recorded. From a comparison of the two, it was generally possible to draw significant conclusions concerning the decay scheme.

EXPERIMENTAL RESULTS—Re^{186}

The gamma rays observed in Re^{186} are described in Table I(*a*). The energies of the 123 and 137 kev. radiations were found both by external and internal conversion measurements. The intensities were all measured relative to the 137 kev. gamma ray whose absolute intensity was found in a manner to be explained later.

The intensities of the 631 and 768 kev. gamma rays relative to the 137 kev. radiation were measured by two independent methods. The first used the Siegbahn spectrometer to make a comparison of the L photopeak of the 137 kev. gamma ray in a 1.8 mgm./cm.^{2} uranium radiator with the K photopeaks of the high energy radiations in a 10 mgm./cm.^{2} uranium radiator. The calculation of intensity requires the use of a semiempirical formula relating peak height to radiator thickness and electron energy (Johns and Nablo 1954) and the assumption that the K-shell conversion efficiency is five times that of the L-shell. It was impossible to get a useful comparison through K peaks alone because of the serious energy degradation in the low energy peak. This method gave an intensity of 0.02% for the two high energy radiations. In the second method, the photopeaks of the three gamma rays under question

TABLE I

(*a*) GAMMA RAYS

Quantum intensity, %	Gamma-ray energy, kev.	Detection method and comment
0.6±0.2	122.9±0.4	1.8 mgm. U and internal conversion
10±2	137.2±0.2	1.8 mgm. U and internal conversion
0.024±0.010	630.8±0.8	10 mgm. U: coincidence with 137
0.024±0.010	768.2±1.0	10 mgm. U: no coincidence with 137

(*b*) BETA GROUPS

1064±2 kev.	76±4%	927±2 kev.	24±4%

(*c*) INTERNAL CONVERSION DATA

Transition	N_K	N_L	N_M+N_N	K/L	α_K
123 kev.	0.32%	0.74%	—	0.43±0.2	
137 kev.	4.65%	7.6%	1.4%	0.61±0.07	0.45±0.03

were compared in a NaI(Tl) scintillation spectrometer whose efficiency as a function of energy had previously been determined. This method gave 0.03%, in reasonable agreement with the 0.02% value.

A Fermi analysis of the Re^{186} beta spectrum, illustrated by curves A and B of Fig. 1, showed the clear-cut break 137 kev. from the end point obtained by

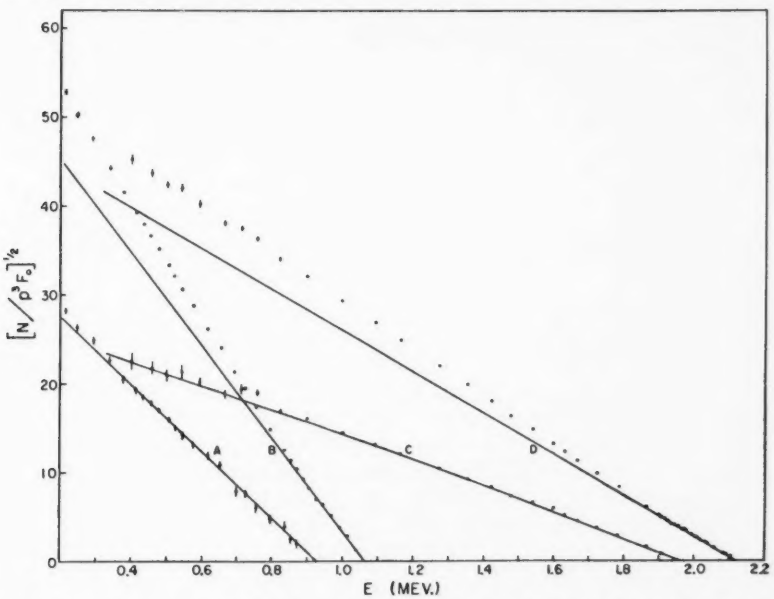

FIG. 1. Fermi analysis of the beta spectra of Re^{186} and Re^{188}. Curves A and B refer to Re^{186}, C and D to Re^{188}. The curvature of C probably represents a departure from allowed shape.

others (Guss *et al.* 1954; Langer and Price 1949) with the values for the energies and branching ratios given in Table I (*b*).

The conversion electron spectrum of Re^{186} is shown in Fig. 2 and the information obtained therefrom in Table I (*c*). It is quite clear from the values of α_K, the K/L, and the L_1: L_2: L_3 ratios that both the 123 and 137 kev. radiations

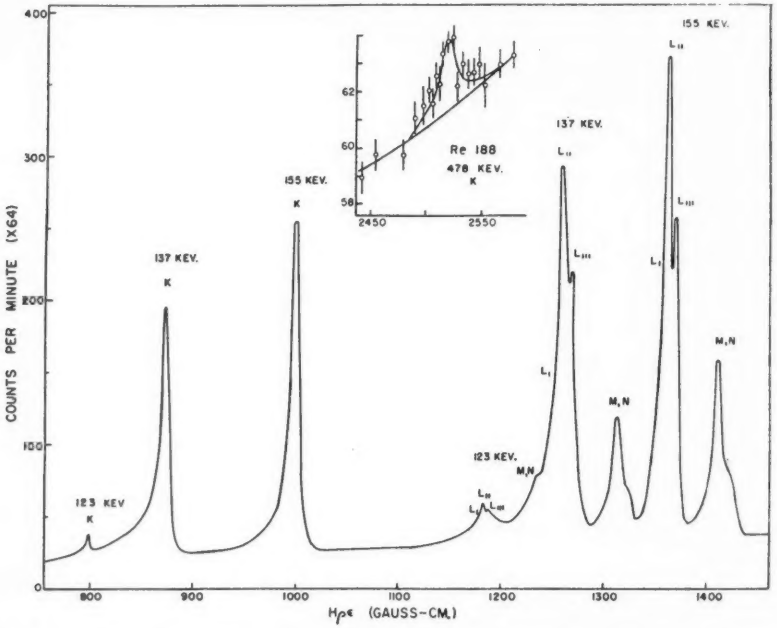

FIG. 2. Internal conversion peaks of Re^{186} and Re^{188}. The 123 and 137 kev. peaks are associated with Re^{186}, the 155 and 478 kev. peaks with Re^{188}. With an expanded momentum scale the *L* peaks can be resolved into components.

are *E*2 in character. Using the scintillation spectrometer, it was found that the number of *K*-shell X-rays from tungsten and osmium per 137 kev. quantum was 0.75 ± 0.02. Using the two scintillation spectrometers, the number of β–X coincidences per β–γ coincidence was found to be 0.43 ± 0.03. The latter ratio when corrected for the fluorescence yield of osmium gives a value of 0.45 ± 0.03 for the *K*-shell conversion coefficient of the 137 kev. transition. The difference between the measured ratios, 0.32 ± 0.05, similarly corrected, leads to a value of 0.34 ± 0.05 for the number of *K*-shell vacancies occurring in tungsten per 137 kev. quantum.

From the values of α_K and N_K given in Table I (*c*), it appears that the quantum intensity of the 137 kev. gamma ray is 10.3%. This value, combined with the 0.34 ratio above and corrected for the number of *K* X-rays following *K*-shell conversion of the 123 kev. gamma ray, leads to a *K*-capture branching

ratio of 3.2%, with roughly half of the transitions going to the 123 kev. level and the other half to the ground state. The 10.3% figure, when added to the number of K, L, M, and N electrons, gives an intensity of 24% for the 927 kev. beta group, in excellent agreement with the values found from the Fermi analysis. Gamma-gamma coincidence experiments showed clearly that the 631 kev. radiation is in coincidence with the 137 kev. gamma ray, while the 768 kev. radiation is not.

EXPERIMENTAL RESULTS—Re^{188}

(a) *Gamma Ray Energies and Intensities*

The external conversion spectrum of Re^{188} is presented in Fig. 3. All of the peaks were recorded at least five times. In addition, the reality of the weak

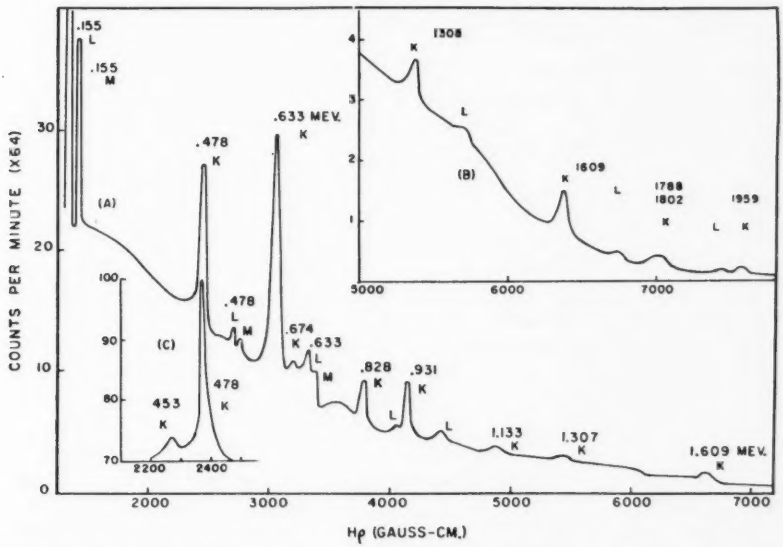

FIG. 3. Composite of the external conversion spectrum of Re^{188}. Curve A was obtained with a 19 mgm./cm.^{2} lead radiator, curve B with a 20 mgm./cm.^{2} uranium radiator, and curve C with a 1.8 mgm./cm.^{2} uranium radiator.

high-energy peaks was confirmed by removing the radiator and examining the underlying Compton distribution.

The energies and intensities of the gamma rays shown in Fig. 3 are tabulated in Table II. The errors quoted are twice the standard deviation of the mean, and include the effects of random errors in the determinations of the peak position and systematic errors due to calibration.

The relative intensities of the gamma rays were measured with respect to the 633 kev. radiation whose K-shell photoelectron peak stands out clearly in the spectrum.

TABLE II

GAMMA RAYS OF Re^{188}

Quantum intensity in per cent	Gamma-ray energy, kev.	Assignment	ΔE, kev.	Coincidences recorded with:
9.0	155.0±0.2	1 → 0	0.0	All but 633 and 1959 kev.
0.04	453.6±0.6	3 → 2	−0.5	633 kev. (uncertain)
0.63	478.2±0.2	2 → 1	−0.1	155 kev.
1.00	633.0±0.1	2 → 0	+0.1	828, 1133, and part of 1308 kev.
0.093	672.6±0.5	4 → 2	0.0	155 and 633 kev. (uncertain)
0.33	828.0±0.2	5 → 2	+0.1	633 and 155 kev.
0.41	931.0±0.1	3 → 1	+0.2	155 kev.
0.067	1132.8±0.8	6 → 2	−0.4	633 kev.
0.053	1307.9±0.7	4 → 0	−2.3	.....
		5 → 1	−1.9	155 kev.
		7 → 2	0.0	633 kev.
0.070	1609.8±0.8	6 → 1	+0.7	155 kev.
0.015	1783.0±0.7	7 → 1	3.0	155 kev.
0.027	1802.7±0.8	8 → 1	0.3	155 kev.
0.012	1959 ±2	8 → 0	−1.0	No γ-rays

Some difficulty was experienced in comparing the intensity of the 155 kev. radiation with that of the 633 kev. gamma ray because the K-photoelectron peak for the former falls in a region where energy degradation in the radiator is serious. This comparison was made using Au, Pb, and U radiators and also by comparing the L peak intensities, since these are not as subject to the effects of radiator degradation. In addition, the 155 kev. to 633 kev. intensity ratio was measured by means of the NaI(Tl) scintillation spectrometer and found to give a value of 8.9±0.5, in good agreement with the mean value 9.0 obtained from the beta-ray spectrometer determinations. Although the intensity estimates of Table II are believed to be self-consistent to within 20%, the absolute values may be in error by a somewhat larger amount since these depend on an absolute intensity determination of the 155 kev. radiation by a method to be described later.

An intensive search was made for possible cross-over transitions predicted from a decay scheme constructed on the basis of the stronger lines. This search resulted in the discovery of the 453.6 kev. radiation, and set upper limits on the intensities of three other possible transitions as follows: 375 kev. (<0.01%), 1086 kev. (<0.01%), and 1460 (<0.02%).

(b) γ–γ Coincidences

Typical coincidence spectra are shown in Figs. 4 and 5. With channel A set on the photopeak of the strong 155 kev. radiation, both the single-channel and the coincidence spectra were recorded. It is clear from Fig. 4 that the 478 kev. radiation is in coincidence with the 155 kev. gamma ray and that the 633 kev. line is not. This, together with the fact that 478.2+155.0 = 633.2, indicates that the first two excited states of Os^{188} lie at 155 and 633 kev. above the ground state. Since these two states are connected by means of the 478 kev. transition, it may be expected that all gamma rays in coincidence with the 633 kev. radiation will also appear to be in coincidence with the 155 kev. gamma ray with reduced intensity (0.32 according to Fig. 7).

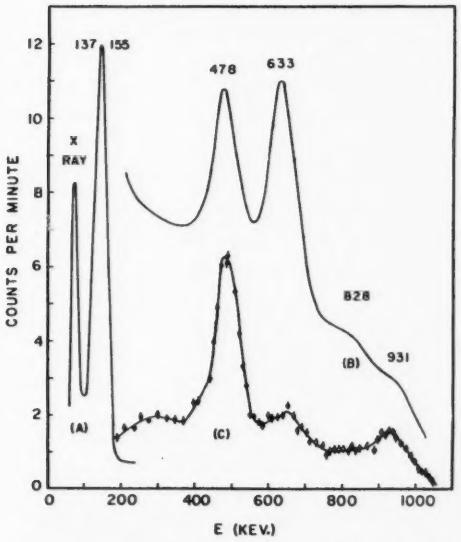

FIG. 4. NaI(Tl) scintillation spectrometer spectra of Re^{188} below 1 Mev. Curves A and B: single-channel spectra; curve C: coincidences with the 155 kev. gamma ray.

Although the 828 and 931 kev. photopeaks are poorly resolved in the single-channel spectrum, it is clear from the coincidence spectrum that the 931 kev. radiation is in full coincidence with the 155 kev. line. On the other hand, the 828 kev. radiation feeds the 155 kev. level indirectly, since its intensity in the coincidence spectrum has been reduced to roughly half that of the 931 kev. peak.

The weak 650 kev. peak which appears in the coincidence spectrum is partially due to coincidences with the Compton pulses from high energy gamma rays appearing in Channel A, but it also seems to include coincidences with the weak 673 kev. radiation, since in all cases the peak seems to be shifted to an energy higher than 633 kev.

Fig. 5 shows the high energy portion of the total spectrum as recorded in Counter B, together with the coincidence spectra associated with the 155 and 633 kev. gamma rays in Counter A. Counter B was covered with 3 mm. of lead to permit the use of stronger sources without pile-up. For coincidences with the 633 kev. radiation, Counter A was also covered with an equal amount of lead. With pile-up eliminated, the 828 and 931 kev. peaks are more clearly resolved than in Fig. 4. The 155 kev. radiation appears to be in coincidence with all the high energy radiations, except the 1959 kev. gamma ray. Fig. 5 shows clearly that the 828, 1133, and 1308 kev. radiations are in cascade with the 633 kev. gamma ray and that the 931 kev. radiation is not.

It was noticed that the photopeak observed for the 1308 kev. line in the high resolution beta-ray spectrometer was consistently too broad, indicating that

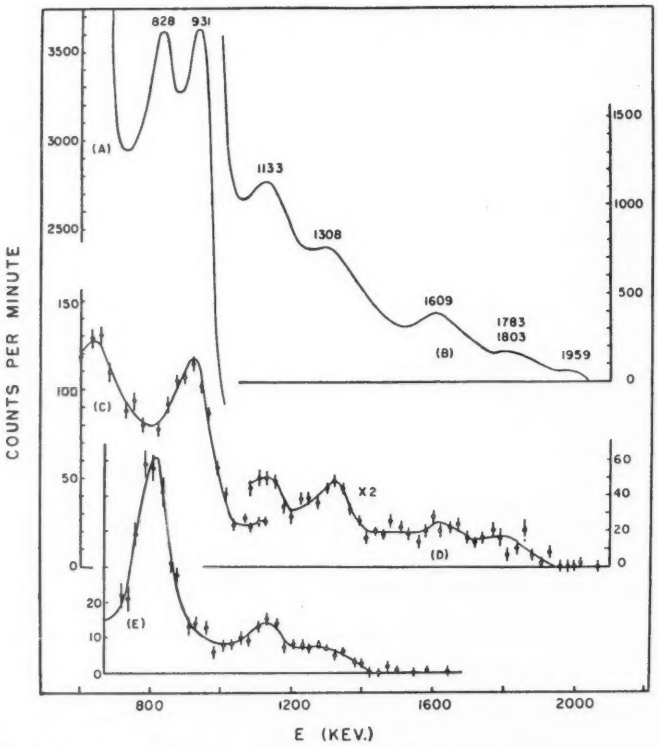

FIG. 5. NaI(Tl) scintillation spectrometer spectra of Re^{188} above 600 kev. Curves A and B: single-channel spectra; curves C and D: coincidences with the 155 kev. radiation; curve E: coincidences with 633 kev. radiation.

this line is really a close doublet. In the coincidence curves of Fig. 5 it is evident that the ratio of the 1133 to the 1308 kev. photopeak changes from 0.6 for the 155 kev. spectrum to 2.0 in the 633 kev. spectrum. This behavior is to be expected if the 1308 kev. radiation consists of a pair of gamma rays of roughly equal intensity and the same energy, one of which feeds the 155 kev. level directly, while the other member of the pair and the 1133 kev. radiation feed this level indirectly via the 633 kev. level.

The extension of curve E of Fig. 5 down to 300 kev. is not shown in the curve presented. This region was examined and found to show weak peaks at about 460 and 650 kev. These peaks are chiefly due to coincidences between the 478 or 633 kev. radiations in Channel A and pulses in the Compton distributions of high energy gamma rays appearing in channel B. From the apparent shifts of these peaks, we feel there is weak evidence for 453–633 kev. and 673–633 kev. coincidences.

The results of these experiments are summarized in the last column of Table II.

(*c*) *The Beta Spectrum*

Three separate beta sources were analyzed. This analysis was quite straightforward for energies above 1 Mev., but below this point it was complicated by the presence of conversion lines and by the necessity of subtracting a Re^{186} contribution which amounted to as much as half of the total counting rate at some points in the spectrum. Any systematic error, introduced by subtracting this contribution, would seriously affect the shape of the beta distribution below 1 Mev.

Curves C and D of Fig. 1 present the Fermi analysis of one of the sources studied. All showed the characteristic break at a point 155 kev. below the upper end point. Also, all showed a slight tendency to be concave to the energy axis. Since the amount of this curvature was not strictly reproducible in different runs, it is felt that it might have been partly due to errors in subtracting the Re^{186} component. However, a slight effect always appeared, above 1 Mev., suggesting that this spectrum exhibits the type of forbidden shape recently found in Re^{186} (Porter *et al.* 1955).

The end point of the high energy group is 2116 ± 2 kev., where the error quoted represents the maximum deviation from the mean obtained from the three independent determinations.

Instead of using the Fermi analysis to determine the end point of the lower energy beta group, it was assumed that this group fed the first excited state of Os^{188} at 155 kev. and therefore must have an end point of 1961 ± 2 kev. The analysis was then used to establish the intensities of the two groups, since it was clear from the gamma measurements that all the other beta groups combined would not give a contribution of more than 1.5% to the total beta spectrum. On the basis of these runs, the intensities of the 1961 and 2116 kev. groups are, respectively, $20\pm4\%$ and $79\pm4\%$, with roughly 1% allowed for the lower energy groups. These intensities were determined on the assumption that both spectra showed a forbidden shape but the departures from the allowed shapes are so small that the intensity values are not affected by this assumption.

Since both the beta groups represent first forbidden transitions ($\Delta I = 1$, yes) they may be expected to show small forbidden shape factors. The total beta spectrum may be described by the function

$$N/p = p^2F(Z, W)[C_1(W)(W_1-W)^2+fC_2(W)(W_2-W)^2] \tag{1}$$

where $C_1(W)$ and $C_2(W)$ are the energy-dependent shape factors for spectra with end points W_1 and W_2 and f is an intensity parameter for the second group. A calculation of these factors (Banerjee and Saha 1954) for a mixture of the scalar and pseudoscalar interactions with $\Delta I = 1$, yes, shows that C_1 and C_2 are of the form $C = C_0[1+aW-(b/W)+cW^2]$ where the parameters a, b, c are of the order 0.1 or less. For our purpose it was convenient to rearrange Equation (1) as

$$[N/p^3F(W_1-W)^2] = K[\{1-\alpha_1(W_1-W)+\beta_1(W_1-W)^2\} + f\{(W_2-W)/(W_1-W)\}^2\{1-\alpha_2(W_2-W_1)+\beta_2(W_2-W)^2\}]$$

where α_1, α_2, β_1, and β_2 are of the order of 0.1 or less.

In practice it was possible to obtain a fit to the data from each source by setting $\beta_1 = \beta_2 = 0$ and using values of α_1 and α_2 less than 0.1. Since the calculations involve a great many terms which are not simply related to the constants of beta decay, and since this method does not uniquely separate the two spectra, it seemed pointless to carry this analysis further.

TABLE III

INTERNAL CONVERSION DATA

Experimental values	Theoretical values	
155 kev. transition		
$N_K = 3.0 \pm 0.4\%$		
$N_L = 3.8 \pm 0.4\%$		
$N_M = 0.9 \pm 0.15\%$		
$N_N = 0.3 \pm 0.05\%$		
$K/L = 0.79 \pm 0.15$	$M1, 7.7; E1, 3.5; E2, 0.7$	*
$L_1 : L_2 : L_3$ $0.3 \pm 0.2 : 1.4 \pm 0.1 : 1.00$	$M1, 294 : 23 : 1.0; E1, 4.5 : 1.25 : 1.0;$ $E2, 0.41 : 1.30 : 1.00$	†
$\alpha_K = 0.40 \pm 0.05$	$M1, 1.73; E1, 0.11; E2, 0.33$	‡
478 kev. transition		
$N_K = 0.038 \pm 0.012\%$		
$\alpha_K = 0.06 \pm 0.02$	$M1, 0.08; E1, 0.007; E2, 0.02$	‡

*Goldhaber and Sunyar 1951.
†Gellman *et al.* 1952.
‡Rose *et al.* 1951.

(*d*) *Internal Conversion Coefficients*

The internal conversion spectrum shown in Fig. 2 is almost entirely associated with the 155 kev. transition. The electron conversion probability in each shell is expressed in Table III. The three components of the *L*-shell conversion electrons were sufficiently well resolved to allow a determination of the $L_1 : L_2 : L_3$ ratio.

The value of α_K might have been calculated from the data of Table II and the intensity of the 1961 kev. beta group as found from the Fermi analysis. Since this method is very sensitive to errors in the latter quantity, the value of α_K was measured directly by the technique used for the 137 kev. radiation in Re^{186}. With the beta counter set to detect only betas of energy greater than 1 Mev., all interference from Re^{186} was eliminated. It is clear from a comparison of the experimental and theoretical values in Table II that the 155 kev. transition is *E*2 in character. This assignment is in agreement with the conclusions of J. W. Mihelich (Scharff-Goldhaber 1953), who has also measured the $L_1 : L_2 : L_3$ ratio.

The data presented for the 478 kev. transition, though not as extensive, indicate that it must be predominantly *M*1 in character, though some mixture of *E*2 is not precluded.

(*e*) *Absolute Intensity of the 155 kev. Gamma Ray*

From the measured values of α_K and N_K, the absolute intensity of the 155 kev. gamma ray is $8 \pm 2\%$. Since the total number of conversion electrons

associated with this transition is $8\pm1\%$, the 1961 kev. beta group must represent $16\pm3\%$ of the disintegrations. This value is in reasonable agreement with the 20% figure found from the Fermi analyses, and leads to a mean value of $18\pm3\%$ for this intensity.

The best value for the absolute quantum intensity of the 155 kev. gamma ray from these data has been taken as half of the 18% figure or $9\pm2\%$. This value has been used to express all the gamma intensities of Table II on an absolute scale.

(f) Angular Correlation

Before the complexity of the gamma-ray spectrum was realized, angular correlation studies were made, using anthracene crystals covered with 3 mm. of lead and a fast coincidence circuit of resolving time 5×10^{-9} sec. Since there was no energy selection in this arrangement, except for the exclusion of the 155 kev. radiation, the apparatus was detecting the following γ–γ cascades: 828–633, 828–478, 1133–633, 1133–478, 1308–633, and 1308–478, of which the first two are much the strongest. The strongly anisotropic angular correlation pattern obtained was given by the equation $W(\theta)=1-0.229\cos^2\theta+0.537\cos^4\theta$. A unique interpretation of these data does not seem possible, but it is clear that some strongly anisotropic cascades such as 0–2–2, 0–2–0, or 0–1–0 must be involved.

DISCUSSION—Re^{186}

The experimental results reported for Re^{186} are summarized in the decay scheme of Fig. 6. This scheme is in close agreement with the results of Metzger and Hill (1951) and of Steffen (1951), except in a few minor points.

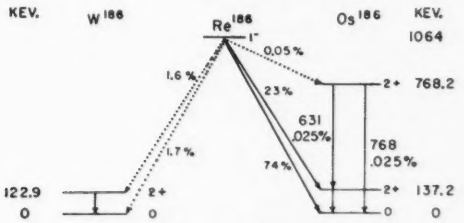

FIG. 6. Decay scheme of Re^{186}.

The most serious discrepancy lies in the intensity of the two high energy gamma rays, our value being only one eighth of the value, 0.2%, quoted by Metzger and Hill. Their intensity would have required that the K peaks of these radiations would be comparable in height to the 828 kev. K peaks in Re^{188} when our sources were first received. Actually, neither radiation was detectable until the Re^{188} activity had decayed away.

Our value of 3.2% for the number of disintegrations leading to K-capture is considerably smaller than the value obtained by Steffen but is in reasonable agreement with the value given by Metzger and Hill.

The end point of the beta spectrum agrees very well with values obtained by Langer and Price (1949) and by Guss, Killion, and Porter (1954), and the branching ratios agree well with those found by other workers (Metzger and Hill 1951; Porter *et al.* 1955; Steffen 1951). We found no evidence for the departures from the allowed shape found by Porter *et al.* (1955) but our method is not nearly as sensitive to such effects as the β–γ coincidence technique which they employed.

DISCUSSION—Re^{188}

The experimental results presented for Re^{188} can readily be accounted for in terms of the decay scheme of Fig. 7. All of the gamma rays assigned in Table II appear in this scheme. The agreement between the observed energies and those predicted from the decay scheme is excellent, the difference seldom being

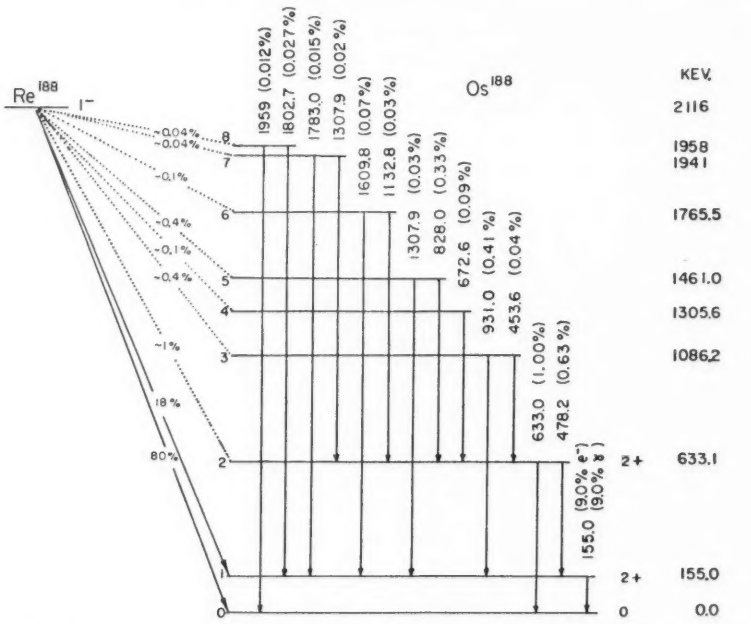

FIG. 7. Decay scheme of Re^{188}. Beta transitions shown as solid lines were obtained from the Fermi analysis; the others deduced from gamma-ray intensities.

greater than 0.5 kev. As has been pointed out, the 1307.9 kev. line is double, the unresolved lower energy component being the 1306 kev. radiation corresponding to the $5 \rightarrow 1$ transition. It is possible that this component also contains a contribution from the $4 \rightarrow 0$ transition, though no direct evidence for this exists.

The only level in the decay scheme which is unsupported by both energy and coincidence measurements is level 4 at 1305.6 kev. above the ground state.

Its assignment has been made purely on the basis of the weak 633–673 kev. coincidences observed.

From the internal conversion data presented, it is clear that the first two excited states of Os^{188} are both 2+ in character. The log f_0t values for the transitions to the 0, 155, and 633 kev. levels of Os^{188} are 8.1, 8.6, and 9.5, respectively, all characteristic of first-forbidden transitions with $\Delta I = 1$, yes. This strongly suggests that the ground state spin of Re^{188} is 1−. It is impossible from the data available to make unique spin assignments to the higher lying levels in Os^{188}. The absence of ground state transitions from the 1086, 1461, and 1765 kev. levels, and the log f_0t values, 9.2, 8.4, and 8.3, for the beta transitions to these levels, suggest that their spins may all be zero. The angular correlation data provide further support to this assignment in the case of the 1461 kev. level.

The decay scheme presented here differs from that of our preliminary report (McMullen and Johns 1953*a*) in the addition of a number of new levels and in the rejection of the 828 kev. level. Although the energy fit in the earlier scheme was excellent, it was not supported by coincidence experiments and it is impossible with the gamma energies present in this spectrum to design a unique scheme on an energy fit alone.

The lifetimes quoted in that report are too long by roughly a factor of 2 (McMullen and Johns 1953*b*). Our more recent measurements are consistent with the precise values given by Sunyar (1954) and are characteristic of *E*2 transitions.

The beta spectrum of Re^{188} seems to show a departure from the allowed shape, as was first suggested by Guss, Killion, and Porter (1954). An experiment such as that described by Porter *et al.* (1955) for Re^{186} is required to make a quantitative test of this behavior.

The log f_0t values for both Re^{186} and Re^{188} are very similar, with the low lying levels having a value around 8.0 and the higher levels ranging from 7.5 to 9.5. This suggests that the ground states of both Re^{186} and Re^{188} have the same spin and parity, almost certainly 1−.

ACKNOWLEDGMENTS

The sources for these experiments were obtained through the courtesy of Atomic Energy of Canada Limited, the United States Atomic Energy Commission, and the Brookhaven National Laboratory. We should like to express our appreciation to Mr. Paul Colsmann of the latter laboratory, who arranged irradiation and shipments with great despatch. We are grateful to Dr. R. L. Graham for supplying us with the circuit diagrams of the pulse height analyzers which were used and for helpful discussion (Bell and Graham 1953). We wish to thank Miss Agda Artna for assistance in the analysis of the data.

This work was supported by grants from the National Research Council of Canada and through scholarships awarded by that body and by the Research Council of Ontario to two of the authors.

REFERENCES

BANERJEE, M. K. and SAHA, A. K. 1954. Proc. Roy. Soc. (London), A, **224**: 472.
BEACH, L. A., PEACOCK, C. L., and WILKINSON, R. G. 1949. Phys. Rev. **76**: 1585.
BELL, R. E. and GRAHAM, R. L. 1953. A.E.C.L., Chalk River Laboratories. Private communication.
CORK, J. M., SHREFFLER, R. G., and FOWLER, C. M. 1948. Phys. Rev. **74**: 1657.
GELLMAN, H., GRIFFITH, B. A., and STANLEY, J. P. 1952. Phys. Rev. **85**: 944.
GOLDHABER, M. and SUNYAR, A. W. 1951. Phys. Rev. **83**: 906.
GOODMAN, L. J. and POOL, M. L. 1947. Phys. Rev. **71**: 288.
GRANT, P. J. and RICHMOND, R. 1949. Proc. Phys. Soc. A, **62**: 573.
GUSS, D., KILLION, L., and PORTER, F. T. 1954. Phys. Rev. **95**: 627A.
JOHNS, M. W. and NABLO, S. V. 1954. Phys. Rev. **96**: 1599.
JOHNS, M. W., WATERMAN, H., MACASKILL, D., and COX, C. D. 1953. Can. J. Phys. **31**: 225.
KOERTS, L. 1954. Phys. Rev. **95**: 1358L.
LANGER, L. M. and PRICE, H. C., JR. 1949. Phys. Rev. **76**: 641.
MCMULLEN, C. C. and JOHNS, M. W. 1953*a*. Phys. Rev. **91**: 418L.
——— 1953*b*. Phys. Rev. **91**: 1580E.
METZGER, F. R. and HILL, R. D. 1951. Phys. Rev. **81**: 300L; **82**: 646.
MILLER, L. C. and CURTISS, L. F. 1946. Phys. Rev. **70**: 983L.
PORTER, F. T., FREEDMAN, M. S., NOVEY, T. B., and WAGNER, F., JR. 1955. Phys. Rev. **98**: 214L.
RICHMOND, R., GRANT, P. J., and ROSE, H. 1952. Proc. Phys. Soc. A, **65**: 484.
ROSE, M. E., GOERTZEL, G., SPINRAD, B., HARR, J., and STRONG, P. 1951. Phys. Rev. **83**: 79.
SCHARFF-GOLDHABER, G. 1953. Phys. Rev. **90**: 587.
STEFFEN, R. M. 1951. Phys. Rev. **82**: 827.
SUNYAR, A. W. 1954. Phys. Rev. **95**: 626A.

THE SPECTRUM OF CN IN THE VACUUM ULTRAVIOLET[1]

By P. K. Carroll[2]

ABSTRACT

The spectrum of the CN radical has been investigated in the Schumann region using a three-meter vacuum spectrograph in the fourth order. A hollow cathode discharge through streaming helium, to which a trace of cyanogen was added, was used as source. Three new systems of bands were found in the region 1650–2100 Å. These involve two hitherto unknown states: a $^2\Sigma$ state designated by E, which gives rise to the transitions $E^2\Sigma \rightarrow X^2\Sigma$ and $E^2\Sigma \rightarrow A^2\Pi$, and an inverted $^2\Delta$ state designated by J, which gives rise to the transition $J^2\Delta \rightarrow A^2\Pi$. Rotational analyses of the bands have been made and the molecular constants evaluated. The new data, although not decisive, support the higher value (8.2 ev.) for the dissociation energy of CN.

I. INTRODUCTION

For many years only two band systems were known in the spectrum of CN: the "red system", $A^2\Pi \rightarrow X^2\Sigma$, which was investigated by Jenkins, Roots, and Mulliken (1932) and the violet system, $B^2\Sigma \rightarrow X^2\Sigma$, which was studied by Jevons (1926) and Jenkins (1928). Quite recently, however, Douglas and Routly (1955) have thoroughly investigated the spectrum in the region 2000–8500 Å and reported three new states: $D^2\Pi$, $F^2\Delta$, and $H^2\Pi$. These states give rise to four new band systems, $D^2\Pi \rightarrow X^2\Sigma$, $D^2\Pi \rightarrow A^2\Pi$, $F^2\Delta \rightarrow A^2\Pi$, and $H^2\Pi \rightarrow B^2\Sigma$, which lie in the near ultraviolet region. These authors also suggested that an investigation of the spectrum should be undertaken in the Schumann region with a view to extending our knowledge of the CN radical and in the hope of obtaining some information on its dissociation energy. The present work reports the extension of observations of the CN spectrum to 1600 Å and gives analyses of three new systems of bands in the region 1600–2100 Å.

II. EXPERIMENTAL

The source employed in the present experiments was essentially the same as that described by Douglas and Routly (1954, 1955). Helium was streamed rapidly through a hollow cathode discharge tube and a trace of C_2N_2 was added until the red system appeared strongly when the discharge was viewed through a pocket spectroscope. Under these conditions, it was found that the new ultraviolet bands were most readily observed. The spectrum was photographed on the three-meter normal incidence vacuum spectrograph which has been described by Bris and Herzberg (1954). Ilford Q II plates were used to record the spectra.

Sufficient resolution to study the fine structure of the new bands could be obtained only by photographing the spectrum in the higher orders. To prevent the strong emission at longer wavelengths from entering the slit of the spec-

[1]Manuscript received October 7, 1955.
Contribution from the Division of Pure Physics, National Research Council, Ottawa, Ontario. Issued as N.R.C. No. 3817.

[2]National Research Laboratories Postdoctorate Fellow 1953–55; at present with Physics Department, University College Dublin, Republic of Ireland.

trograph, a cylindrical lithium fluoride lens was employed in the manner described by Curry and Herzberg (1934). Although the emission is most intense in the slot of the cathode, there was sufficient light from the region of the electrodes to render it impossible to achieve adequate separation of wavelengths by the use of a foreprism alone. However, by using an auxiliary plano-convex lens to form a preliminary image of the source, satisfactory isolation of the orders could be achieved. This arrangement, devised by Dr. Herzberg, will be described in a forthcoming paper.

The analyses described in the following sections were made from plates taken in the fourth order and measured against second-order iron arc lines. The wavelengths of the Fe lines were taken from the M.I.T. tables (Harrison 1939) and converted to vacuum wavelengths using Edlèn's tables (1953). The relative wave numbers of unblended lines in a given set of measurements are believed to be correct to 0.06 cm^{-1}, although the absolute accuracy may be somewhat less than this. Lines separated by more than 0.45 cm^{-1} were distinctly resolved, corresponding to an experimental resolving power of about 120,000.

It was not possible to eliminate entirely some impurity spectra from the source. Thus the Lyman–Birge–Hopfield bands of nitrogen frequently appeared although they were always very weak. The $C^2\Sigma \rightarrow X^2\Sigma$ bands of N_2^+ were always present in considerable strength. These spectra undoubtedly arise from the decomposition of the C_2N_2 in the discharge and the subsequent formation of N_2 molecules. Fortunately the new bands lay almost entirely in regions free from nitrogen spectra.

III. THE $E^2\Sigma \rightarrow X^2\Sigma$ SYSTEM

In the region 1700–2050 Å, six simple bands strongly degraded to longer wavelengths were observed. These were readily identified as a transition from a $^2\Sigma$ state designated by E to the ground state $X^2\Sigma$. The wavelengths of the heads of the bands, their origins, and visual estimates of intensity are given in Table I. A reproduction of the (1–1) band is shown in Fig. 2. The 2040 Å

TABLE I

DATA FOR THE $E^2\Sigma \rightarrow X^2\Sigma$ SYSTEM

$(v'-v'')$	(1–1)	(0–1)	(0–2)	(0–3)	(0–4)	(0–5)
λ(vac.), Å	1706.613	1756.709	1821.198	1889.673	1962.476	2040.005*
ν_0	58588.41	56917.53	54901.56	52911.52	50948.16	49011.18*
I	5	1	3	5	4	2

*Quoted from Douglas and Routly (1954).

band had previously been observed by Douglas and Routly (1954) who considered it as being most probably due to an unknown singlet transition of CN^+.

The results of the present analyses are presented in Table II. The doublet fine structure is not resolved in any of the bands although its presence is detectable by a broadening of the lines for higher N values. The bands were

TABLE II

WAVE NUMBERS OF THE LINES OF THE $E^2\Sigma \rightarrow X^2\Sigma$ SYSTEM

N	(1–1) Band		(0–1) Band		(0–2) Band		(0–3) Band		(0–4) Band	
	$R(N)$	$P(N)$	$R(N)$	$P(N)$	$R(N)$	$P(N)$	$R(N)$	$P(N)$	$R(N)$	$P(N)$
1		58585.28					52916.71	52907.77		50944.52
2		80.65					18.38	03.51	50954.86	40.16
3	58595.58	75.20	56924.62	56904.28	54908.91	54888.02	19.21	898.42	56.05	35.24
4	95.28	69.02	24.62	897.84	08.91	82.05	19.21	92.62	56.05	29.53
5	94.26	61.95	23.60	90.97	08.13	75.32	18.67	86.01	55.81	23.22
6	92.41	54.15	21.93	83.29	06.68	67.95	17.40	78.85	54.88	16.22
7	89.77	45.58	19.45	74.89	04.37	59.74	15.34	70.93	52.99	08.51
8	86.32	36.21	16.09	65.71	01.32	50.83	12.66	62.24	50.51	00.12
9	82.09	26.14	12.02	55.70	897.64	41.19	09.20	52.88	47.43	891.07
10	77.07	15.22	07.18	44.92	93.15	30.76	05.05	42.83	43.57	81.35
11	71.22	03.52	01.53	33.32	87.87	19.63	00.27	32.05	39.14	71.00
12	64.62	490.98	895.14	21.00	81.86	07.82	894.61	20.56	34.00	59.90
13	57.24	77.72	87.95	07.93	75.12	795.10	88.37	08.37	28.17	48.16
14	49.03	63.61	79.95	794.06	67.59	81.70	81.39	795.44	21.67	35.74
15	40.07	48.79	71.21	79.46	59.47	67.63	73.70	81.88	14.44	22.68
16	30.26	33.14	61.73	64.06	50.48	52.77	65.27	67.58	06.67	08.95
17	19.70	16.68	51.35	47.81	40.72	37.14	56.11	52.58	898.16	794.53
18	08.32	399.44	40.31	30.89	30.25	20.77	46.36	36.87	89.03	79.45
19	496.22	81.40	28.48	13.12	19.09	03.66	35.85	20.45	79.11	63.68
20	83.20	62.55	15.79	694.58	07.19	685.84	24.60	03.32	68.63	47.31
21	69.50	43.00	02.34	75.31	794.44	67.30	12.66	685.59	57.45	30.28
22	54.98	22.64	788.26	55.29	80.94	47.96	00.01	67.08	45.58	12.44
23	39.61	01.43	73.34		66.91	28.08	786.66	47.81	33.00	694.09
24	23.49	279.50	57.55		52.05	07.18	72.64	27.90	19.79	75.01
25	06.53	56.81	41.01		36.53	585.76	57.91	07.23	05.96	55.21
26	388.89	33.28					42.46	585.86	791.44	34.84
27	70.52	08.90					26.20	63.88	76.21	14.15
28	51.15	183.99					09.48	41.35	60.35	592.08
29	31.05	58.15						17.91	43.84	69.74
30	10.27	31.41							26.67	46.89
31		04.14							08.84	23.79
32		075.81								

therefore treated as consisting of a single P and single R branch and the rotational constants were derived by the usual graphical method from the well-known relationship

$$\Delta_2 F(N) = 4B_v(N+\tfrac{1}{2}) - 8D_v(N+\tfrac{1}{2})^3.$$

Table III gives the constants for the bands. As the P and R lines in the (0–2) band are not fully resolved, the data for this band are not as accurate as for

TABLE III
CONSTANTS FOR THE $E^2\Sigma \rightarrow X^2\Sigma$ BANDS

	The $E^2\Sigma$ state		The $X^2\Sigma$ state				
	$v=0$	$v=1$	$v=1$	$v=2$	$v=3$	$v=4$	$v=5$
B	1.483_7	1.474_3	1.873_6	1.857_4	1.839_1	1.821_3	1.802*
D	4.3×10^{-6}	5.8×10^{-6}	7.3×10^{-6}	7.5×10^{-6}	7.4×10^{-6}	6.3×10^{-6}	

*Quoted from Douglas and Routly (1954).

the others. Comparison of the rotational constants and vibrational intervals for the ground state $X^2\Sigma$ as obtained in the present work with the results of previous workers (Jenkins, Roots, and Mulliken 1932 and Douglas and Routly 1955) shows excellent agreement. The constants for the upper state $E^2\Sigma$ are as follows:

$$T_0 = 58959.9 \text{ cm}^{-1},$$

$$B_e = 1.488_2, \quad \alpha_e = 0.009_3, \quad r_e = 1.324 \text{ Å}, \quad D = 5.1\times10^{-6},$$

$$\Delta G(\tfrac{1}{2}) = 1670.88 \text{ cm}^{-1}.$$

As only two vibrational levels are observed for state $E^2\Sigma$, it is not possible to derive a vibrational formula.

A perturbation is observed for low N values in the $v = 1$ level of the $E^2\Sigma$ state. Fig. 1 shows the difference between the rotational terms calculated from the rotational constants and the observed levels as determined from both the P and the R branches. The displacement of the lines is in accord with

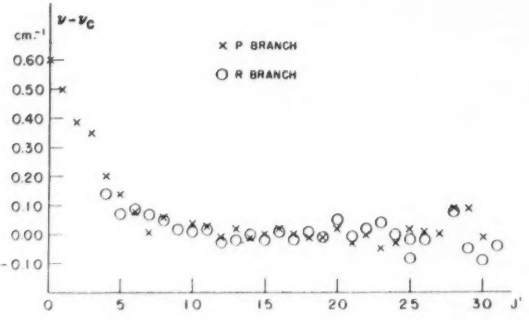

FIG. 1. The perturbation in the $v = 1$ level of the $E^2\Sigma$ state.

PLATE I

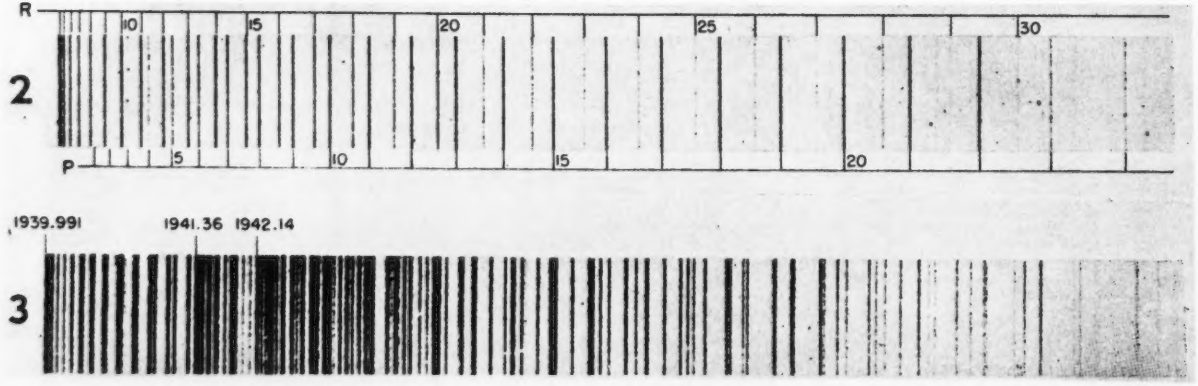

FIG. 2. The (1–1) band of the $E^2\Sigma \rightarrow X^2\Sigma$ system.
FIG. 3. The (1–0) band of the $E^2\Sigma \rightarrow A^2\Pi$ system.

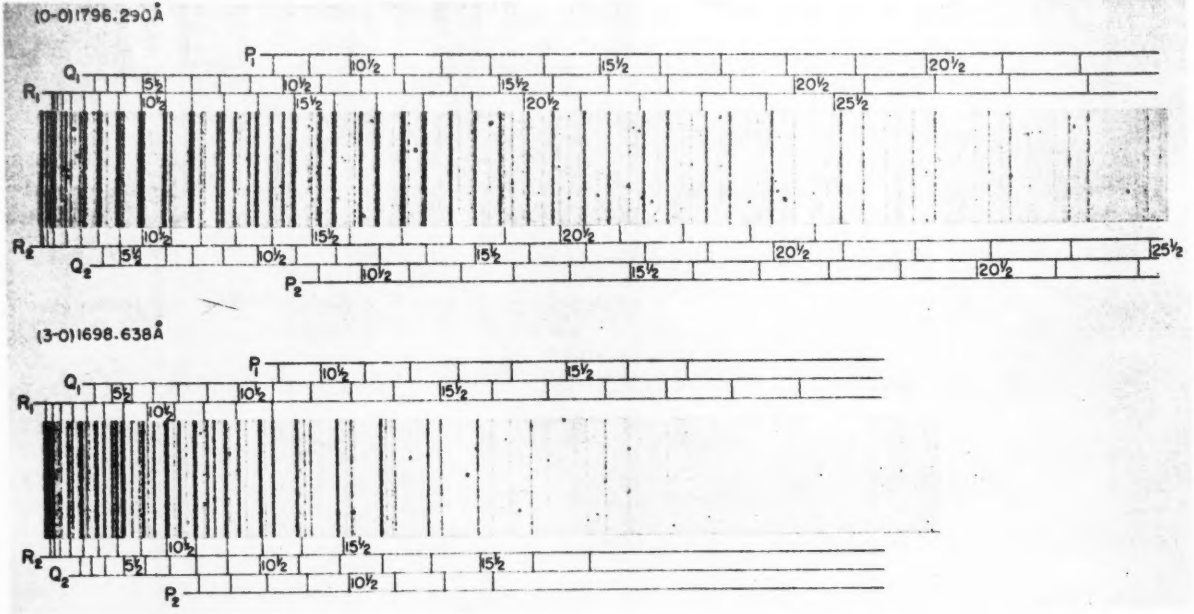

FIG. 4. The (0–0) and (3–0) bands of the $J^2\Delta \rightarrow A^2\Pi$ system.

what is expected for a rotational perturbation and both components of state $E^2\Sigma^+$ must be equally affected as no splitting of the lines is produced by the perturbation. It therefore seems that the perturbing state must be of species $^2\Sigma^+$. Clearly the origin of the perturbing vibrational level lies very close to that of the perturbed level, i.e., at 60631 cm^{-1}. It is interesting to note that Douglas and Routly (1955) reported a perturbation in the $H^2\Pi$ state which they also attributed to a $^2\Sigma^+$ state whose energy can be estimated as about 60910 cm^{-1}. Neither of the perturbations can be interpreted as being due to the higher levels of state $B^2\Sigma$, whose positions are known accurately up to $v = 19$ at 61377.7 cm^{-1}. If the high value of the dissociation energy (66000 cm^{-1}) is assumed, it is possible that one of the perturbations is due to a high vibrational level of the ground state ($v \sim 38$). Unfortunately an extrapolation of the available data on the ground state is too long to confirm or disprove this suggestion. In any event, it appears that there is at least one other $^2\Sigma^+$ state of CN which has so far escaped direct observation.

IV. THE $E^2\Sigma \rightarrow A^2\Pi$ SYSTEM

Amongst the strongest features in the spectrum were three bands in the region 1930–2100 Å. They were triple-headed, degraded to longer wavelengths, and appeared to be of fairly complex structure. The bands were of approximately equal intensity and from the vibrational intervals as calculated from corresponding heads they could readily be assigned to a transition from the new $E^2\Sigma$ state to the well-known $A^2\Pi$ state. This assignment was confirmed by the fact that the wave number interval between the first and third head in each band was close to the known doublet splitting for the $A^2\Pi$ state. Table IV gives the wavelengths of the heads of the bands together with the origins.

TABLE IV

DATA FOR THE $E^2\Sigma \rightarrow A^2\Pi$ SYSTEM

$(v'-v'')$	(1–0)	(0–0)	(0–1)
λ(vac.)	1939.991	2005.011	2079.527
	1941.36	2006.49	2081.13
	1942.14	2007.31	2082.01
ν_0(calc.)	51512.8	49841.9	48054.8

The latter were computed from the data for the $E^2\Sigma$ and $A^2\Pi$ states as obtained from other band systems of CN. Fig. 3 shows a reproduction of the (1–0) band and it can be seen that its general appearance is typical of that for a transition between a $^2\Sigma$ state and a $^2\Pi(a)$ state. The bands were not analyzed as they would yield little new information on the states involved.

V. THE $J^2\Delta \rightarrow A^2\Pi$ SYSTEM

Four bands degraded to longer wavelengths were observed in the region 1700–1800 Å and appeared to form a $v'' = 0$ progression. Although apparently single-headed, each band showed a fairly complex fine structure. If a further band at 1856 Å was assumed to be the (0–1) band, the lower state could be

identified as $A^2\Pi$. Another weak feature at 1670 Å was identified as the (4–0) band. Table V gives the head measurements of the bands together with visual estimates of intensity and the origins derived from the analyses (see below).

TABLE V

DATA FOR THE $J^2\Delta \rightarrow A^2\Pi$ SYSTEM

$(v'-v'')$	(0–1)	(0–0)	(1–0)	(2–0)	(3–0)	(4–0)
λ (Å)	1855.87	1796.290	1761.710	1729.216	1698.638	1669.806
ν_0	53880.04	55667.14	56761.08	57828.36	58869.68	59886.5
I	3	4	6	5	4	1

Analyses of the four strongest bands showed that the transition was from a new $^2\Delta$ state, designated by J, to the $A^2\Pi$ state. The single-headed appearance of the bands is due to the fact that the $^2\Delta$ state conforms to Hund's case a at low J values, is inverted, and has a spin splitting almost equal to that of the $A^2\Pi$ state which is also inverted. In a $^2\Delta \rightarrow {}^2\Pi$ transition where both states approximate to case a coupling, two subbands, $^2\Delta_{5/2} \rightarrow {}^2\Pi_{3/2}$ and $^2\Delta_{3/2} \rightarrow {}^2\Pi_{1/2}$, are expected. The former gives rise to three branches, P_1, Q_1, and R_1, while the latter similarly gives P_2, Q_2, and R_2 branches. Furthermore, the strongest branches should be the Q branches. These features are exhibited by the reproduction of the (0–0) band in Fig. 4. Strictly speaking, each line should be a doublet due to the Λ-type doubling in both the $^2\Delta$ and $^2\Pi$ states, but the resolution is not sufficient to show the doublet splitting which would very probably be less than 0.10 cm^{-1}.

The analyses of the (0–0), (1–0), (2–0), and (3–0) bands are presented in Table VI. To determine the band origins given in Table V, $Q_1(J)+Q_2(J)$ was plotted against $(J+\frac{1}{2})^2$ in which case the intercept on the axis at $(J+\frac{1}{2}) = 0$ gives $2\nu_0-8B'+2B''$ plus terms in D' and D'' which may be neglected. The origin of the (4–0) band was estimated from the head. To complete the data, the origin of the (0–1) band, which was not analyzed, was computed.

The molecular constants derived from the analyses are given in Table VII. Unfortunately it was not possible to determine the spin splitting constants A for both states from the analyses. However, it follows immediately from the Hill–Van Vleck formula, which gives the energy levels for doublet states with coupling intermediate between cases a and b, that

$$Q_1(J)-Q_2(J) = B''\sqrt{Y''(Y''-4)}\left[1+\frac{4(J+\frac{1}{2})^2}{Y''(Y''-4)}\right]^{\frac{1}{2}} - B'\sqrt{4Y'(Y'-4)}\left[1+\frac{4(J+\frac{1}{2})^2}{4Y'(Y'-4)}\right]^{\frac{1}{2}}$$

$$= B''\sqrt{Y''(Y''-4)}-B'\sqrt{4Y'(Y'-4)} + \left[\frac{B''}{2\sqrt{Y'(Y'-4)}}-\frac{B''}{2\sqrt{4Y''(Y''-4)}}\right]4(J+\tfrac{1}{2})^2+\ldots$$

TABLE VI

WAVE NUMBERS OF LINES IN THE $J^2\Delta \rightarrow A^2\Pi$ SYSTEM

J	P_1	Q_1	R_1	P_2	Q_2	R_2
			(0–0) Band			
1½					55663.60	
2½			55667.90		661.18	55670.27
3½		55656.02	667.56		658.12	669.96
4½		652.54	666.56		654.18	668.66
5½		648.28	664.75		649.44	666.56
6½		643.12	662.19		643.79	663.60
7½	55618.30	637.25	658.84	55617.36	637.25	659.71
8½	608.99	630.62	654.74	607.54	629.90	654.96
9½	599.04	623.20	649.67	596.69	621.77	649.44
10½	588.29	614.93	644.03	585.23	612.74	643.12
11½	576.64	605.87	637.44	572.55	602.90	635.77
12½	564.28	595.97	630.10	559.16	592.16	627.66
13½	551.08	585.23	621.95	544.99	580.55	618.67
14½	536.92	573.77	613.01	529.99	568.18	608.99
15½	522.02	561.41	603.31	514.11	554.91	598.33
16½	506.23	548.26	592.60	497.46	540.87	586.81
17½	489.89	534.26	581.19	480.00	525.93	574.49
18½	472.50	519.46	568.88	461.65	510.21	561.41
19½	454.31	503.81	555.75	442.53	493.64	547.34
20½	435.41	487.36	542.04	422.53	476.24	532.52
21½	415.50	470.23	527.21	401.66	457.94	516.83
22½	395.03	452.00	511.59	380.04	438.87	500.27
23½	—	433.19	495.18	357.48	418.96	482.35
24½	—	413.31	477.94	334.27	397.83	465.12
25½	—	392.57	459.89	—	—	—
26½	—	371.21	—	—	—	—
27½	—	348.98	—	—	—	—
28½	—	325.73	—	—	—	—
			(1–0) Band			
1½					56756.27	56762.60
2½		56754.00	56763.09		754.00	763.09
3½		751.15	762.50		750.86	762.60
4½		747.43	760.90	56734.97	746.75	760.90
5½		742.67	758.65	727.43	741.72	758.65
6½	56720.92	737.14	755.72	718.89	735.82	755.30
7½	712.11	730.89	751.99	709.53	729.12	751.15
8½	702.62	723.84	747.43	699.21	721.44	746.03
9½	692.35	715.92	742.04	688.04	712.77	740.04
10½	681.04	707.19	735.82	675.97	703.28	733.14
11½	668.97	697.61	728.96	663.07	692.87	725.39
12½	655.89	687.23	720.92	649.27	681.71	716.67
13½	642.30	675.97	712.11	634.47	669.54	707.19
14½	627.77	663.74	702.62	618.97	656.55	696.69
15½	612.11	650.89	692.05	602.52	642.63	685.39
16½	595.78	637.00	680.70	585.22	627.77	673.19
17½	578.50	622.32	668.51	567.05	612.11	660.07
18½	560.58	606.77	655.39	547.97	595.78	646.10
19½	541.69	590.42	641.48	528.12	578.50	631.24
20½	521.87	573.11	626.70	507.33	560.15	615.53
21½	501.25	554.93	611.13	485.81	541.05	598.99
22½	479.71	535.96	594.54	463.11	521.06	581.48
23½	457.31	516.10	577.06	439.73	500.13	563.08
24½	434.30	495.27	559.03	—	478.46	543.86
25½	—	473.66	539.74	—	455.83	523.71
26½	—	451.13	—	—	432.44	—
27½	—	427.58	—	—	—	—

TABLE VI (*Concluded*)

WAVE NUMBERS OF LINES IN THE $J^3\Delta \rightarrow A^3\Pi$ SYSTEM (*Concluded*)

J	P_1	Q_1	R_1	P_2	Q_2	R_2
			(2–0) Band			
$1\frac{1}{2}$					57823.04	57829.69
$2\frac{1}{2}$			57829.39		820.75	829.69
$3\frac{1}{2}$			829.12		817.36	828.81
$4\frac{1}{2}$		57814.36	827.79		813.00	827.15
$5\frac{1}{2}$		809.58	825.52	57793.74	807.75	824.50
$6\frac{1}{2}$		804.02	822.35	785.02	801.71	820.97
$7\frac{1}{2}$		797.48	818.30	775.40	794.58	816.41
$8\frac{1}{2}$		790.14	813.41	764.78	786.56	810.61
$9\frac{1}{2}$	57758.41	781.89	807.75	753.28	777.32	804.27
$10\frac{1}{2}$	747.01	772.87	801.05	—	767.56	796.93
$11\frac{1}{2}$	734.50	762.77	793.57	727.38	756.73	788.65
$12\frac{1}{2}$	721.11	751.87	785.02	713.11	744.98	779.40
$13\frac{1}{2}$	706.88	740.05	775.62	697.87	732.28	769.29
$14\frac{1}{2}$	691.78	727.38	765.43	681.79	718.69	758.15
$15\frac{1}{2}$	675.81	713.78	754.33	664.78	704.17	746.17
$16\frac{1}{2}$	658.89	699.32	742.25	646.79	688.85	733.24
$17\frac{1}{2}$	640.91	683.92	729.37	627.92	672.40	719.44
$18\frac{1}{2}$	622.18	667.61	715.50	608.12	655.14	704.55
$19\frac{1}{2}$	602.58	650.40	700.73	587.49	636.93	688.85
$20\frac{1}{2}$	581.93	632.30	685.06	565.89	617.83	672.40
$21\frac{1}{2}$	560.46	613.26	668.49	543.33	597.84	654.88
$22\frac{1}{2}$	538.15	593.29	650.99	519.96	576.91	636.34
$23\frac{1}{2}$	514.80	572.45	632.51	495.61	555.06	616.97
$24\frac{1}{2}$	490.60	550.70	613.26	470.38	532.32	596.63
$25\frac{1}{2}$	465.45	528.08	—	444.24	508.64	575.43
$26\frac{1}{2}$	439.45	504.47	—	417.12	484.02	553.30
$27\frac{1}{2}$	—	480.00	—	—	458.49	530.22
$28\frac{1}{2}$	—	454.53	—	—	432.08	506.19
$29\frac{1}{2}$	—	428.20	—	—	—	481.28
			(3–0) Band			
$1\frac{1}{2}$						
$2\frac{1}{2}$					58861.29	58870.13
$3\frac{1}{2}$			58870.68		857.89	869.17
$4\frac{1}{2}$		58855.60	869.17	58841.89	853.43	867.01
$5\frac{1}{2}$		850.93	866.55	—	847.98	864.20
$6\frac{1}{2}$		844.97	863.06	825.07	841.48	860.39
$7\frac{1}{2}$		838.22	858.73	815.22	834.06	855.45
$8\frac{1}{2}$		830.51	853.43	804.27	825.67	849.48
$9\frac{1}{2}$	58798.97	821.92	847.24	792.39	816.25	842.69
$10\frac{1}{2}$	787.01	812.33	840.09	779.59	805.94	834.76
$11\frac{1}{2}$	774.10	801.86	832.10	765.79	794.63	825.95
$12\frac{1}{2}$	760.14	790.47	823.04	750.83	782.36	816.25
$13\frac{1}{2}$	745.54	778.13	813.18	735.22	769.09	805.45
$14\frac{1}{2}$	729.87	764.86	802.41	—	754.91	793.77
$15\frac{1}{2}$	713.11	750.85	—	—	739.71	780.96
$16\frac{1}{2}$	694.03	735.22	—	—	725.59	—
$17\frac{1}{2}$	—	718.49	—	—	706.43	—
$18\frac{1}{2}$	—	700.95	—	—	—	—
$19\frac{1}{2}$	—	682.24	—	—	—	—
$20\frac{1}{2}$	—	662.64	—	—	—	—
$21\frac{1}{2}$	—	642.17	—	—	—	—

where $Y = A/B$ and terms involving D have been neglected. If, therefore, $Q_1(J)-Q_2(J)$ is plotted against $(J+\frac{1}{2})^2$, the intercept of the resulting curve on the ordinate gives $B''\sqrt{Y''(Y''-4)}-B'\sqrt{4Y'(Y'-4)}$. Using the data quoted by Herzberg (1950) for the $A^2\Pi$ state, the spin splitting constant A was

TABLE VII

CONSTANTS FOR THE $J^2\Delta \rightarrow A^2\Pi$ BANDS

	The $J^2\Delta$ state				The $A^2\Pi$ state
	$v = 0$	$v = 1$	$v = 2$	$v = 3$	$v = 0$
$B_{\frac{1}{2}}^*$	1.269_1	1.246_0	1.228_1	1.204_5	1.658_0
$B_{-\frac{1}{2}}^*$	1.320_6	1.302_7	1.279_2	1.258_2	1.753_8
B	1.294_8	1.274_0	1.253_2	1.232_3	1.706_6
D	6.7×10^{-6}	6.2×10^{-6}	6.8×10^{-6}	3.5×10^{-6}	5.7×10^{-6}
A	-26.68	-25.28	-25.22	-24.81	

calculated for the upper levels. The A value used for the $A^2\Pi$ state was obtained from the levels $v = 5$ and 6 so that the value for $v = 0$, which is required for the present work, may be somewhat different. It is possible, therefore, that a small, approximately constant, correction may be required for the A values of the $J^2\Delta$ state. However, the relative values of the A's given in Table VII are believed to be correct to 0.20 cm^{-1}. Thus, while A is probably constant for the levels $v = 1$, 2, and 3, it seems to be definitely different for $v = 0$. This is borne out by an examination of the plates which show that the relative positions of the R_1 and R_2 heads are different in the (0–1) and (0–0) bands from the relative positions of these heads in the other bands. Fig. 4 shows the effect at the heads of the (0–0) and (3–0) bands.

The constants for the $J^2\Delta$ upper state of the new system are

$T_0 = 64781.56\ cm^{-1}$,

$B_e = 1.305_6$, $\alpha_e = 0.020_7$, $r_e = 1.414$ Å, $D = 5.8\times10^{-6}$,

$T_e = 64223.97$, $\omega_e = 1121.76\ cm^{-1}$, $\omega_e x_e = 14.203\ cm^{-1}$,

$\omega_e y_e = 0.180\ cm^{-1}$.

The four bands which were analyzed have the $v = 0$ level of the $A^2\Pi$ state in common. Consequently, a fairly reliable value of B_0 was obtained. Combining this with the data of Jenkins, Roots, and Mulliken (1932) one derives values of B_e and r_e which are probably more accurate than those hitherto available. The values obtained are as follows:

$$B_e = 1.7151\ cm^{-1},$$

$$r_e = 1.233\ \text{Å}.$$

There are two features of interest in the new system. An examination of the plates shows that the over-all intensity of the (3–0) band is about the same as or slightly greater than that of the (0–0) band. But whereas the branches of the (0–0) band are well developed in a normal way out to fairly high J values, there is a rather marked fading out of the branches of the (3–0) band at intermediate J. The effect can be seen on Fig. 4 and is particularly obvious for the Q branches. In the (3–0) band, the intensity of the Q_2 branch drops rather suddenly from $Q_2(15\frac{1}{2})$ to $Q_2(17\frac{1}{2})$ after which no further lines are observed while the Q_1 branch fades out rather more gradually from $Q_1(16\frac{1}{2})$ to $Q_1(20\frac{1}{2})$.

The effect may be due to a predissociation although the presence of the (4–0) band presents a difficulty in this interpretation. However, it should be noted that the (4–0) band is very weak, and its presence would not be too surprising if the predissociation is assumed to be weak or forbidden.

The second point of interest is an anomaly in the fine structure of the (4–0) band. As mentioned in the previous paragraph, this band is weak and furthermore it is somewhat overlapped by nitrogen bands. Consequently there was little hope of making a full rotational analysis. However, it seemed that the two strong Q branches should be found. The Q_2 branch was, in fact, readily detected and traced for about 25 members. However, the Q_1 branch was not found even though the positions of the lines could be calculated quite accurately. It seems unlikely that it could have escaped observation despite the weakness and overlapping of the band and it must be concluded that the Q_1 branch has an anomalously low intensity. The reason for this is not clear.

VI. DISCUSSION

It was hoped that an investigation of the CN spectrum in the Schumann region might give some information on the dissociation energy of the molecule. Unfortunately no decisive result has been obtained. Nevertheless the results present some significant indications.

In the first place, it should be noted that the vibrational intervals for the $J^2\Delta$ state are quite small, and it therefore seemed worth while to carry out a Birge–Sponer extrapolation using the data for the origins. A linear extrapolation leads to a dissociation limit at 87500 cm^{-1} above the ground state. The $^2\Delta$ state can arise from the atomic combinations $C(^3P)+N(^2D)$, $C(^3P)+N(^2P)$, and $C(^1D)+N(^2D)$. The energies of the dissociation limits corresponding to these combinations are given in Table VIII, where each of the three suggested values for $D(CN)$, i.e., 50000 cm^{-1}, 56000 cm^{-1}, and 66000 cm^{-1} (see Douglas and Routly 1955 and Gaydon 1953), has been assumed in turn. It is seen that the result of the extrapolation is in closest agreement with the assumption that $D(CN)$ is 66000 cm^{-1} and that the $J^2\Delta$ state arises from the configuration $C(^3P)+N(^2D)$. This interpretation has a number of satisfactory features. It would mean that the two $^2\Delta$ states, F and J, observed for CN go to the lowest possible configuration which can give rise to $^2\Delta$ states, i.e. $C(^3P)+N(^2D)$, which does, in fact, produce two such states. An extrapolation for the $F^2\Delta$ state is not possible as only the $v = 0$ level is observed. However, the data available are at least consistent with the requirement that both states go to the same atomic products. Thus the $F^2\Delta$ state has a smaller internuclear distance than the $J^2\Delta$ state and we should therefore expect it to be more stable. In point of fact, $F^2\Delta$ lies 5098.8 cm^{-1} below the $J^2\Delta$ state.

It must be noted that the Birge–Sponer extrapolation is fairly long and consequently not of high accuracy. A slight modification of the $\Delta G-v$ curve would bring the result into agreement with the assumption that $D(CN)$ is 56000 cm^{-1} and that the $J^2\Delta$ state goes to the limit $C(^3P)+N(^2P)$ or $C(^1D)+N(^2D)$. But this would require that there is at least one $^2\Delta$ state other than F which lies below $J^2\Delta$ and which has escaped detection or that there is a

violation of the non-crossing rule. Quite a severe curvature of the $\Delta G - v$ curve is necessary to bring the results of the extrapolation into agreement with the other possibilities suggested in Table VIII. It therefore seems that if

TABLE VIII

POSSIBLE DISSOCIATION LIMITS FOR THE $J^2\Delta$ STATE

D(CN)	50000 cm^{-1}	56000 cm^{-1}	66000 cm^{-1}
C(^3P)+N(^2D)	69000 cm^{-1}	77000 cm^{-1}	87000 cm^{-1}
C(^3P)+N(^2P)	79000 cm^{-1}	85000 cm^{-1}	95000 cm^{-1}
C(^1D)+N(^2D)	79000 cm^{-1}	85000 cm^{-1}	95000 cm^{-1}

there are no abnormalities in the potential curve for the $J^2\Delta$ state, the simplest and most satisfactory interpretation of the present spectroscopic results is that D(CN) is 66000 cm^{-1} and that the states F and J go to the configuration C(^3P)+N(^2D).

It was suggested in Section V that the fading of the structure in the (3–0) band of the $J^2\Delta \rightarrow A^2\Pi$ system might be due to a predissociation. Unfortunately even if this is so it yields little information on D(CN). The energy at which the effect takes place (68420 cm^{-1}) is above the highest value suggested for the dissociation energy so that the predissociation does not set a useful upper limit to the value of D(CN). Furthermore, it is not possible to make an accurate estimate of the energy of the dissociation limit responsible for the predissociation. If D(CN) is 66000 cm^{-1} it would mean that the predissociation was due to the $^4\Pi$ state arising from the ground state products C(^3P)+N(^4S). Consequently the predissociation would be forbidden which is at least consistent with the observation that the (4–0) band of the $J^2\Delta \rightarrow A^2\Pi$ system is present though weak.

An energy level diagram for CN is shown in Fig. 5 in which all the known levels and transitions for the molecule are indicated. The dissociation energy was taken to be 66000 cm^{-1} and the dissociation limits arranged accordingly. The constants for the eight observed states of CN are collected in Table IX.

TABLE IX

CONSTANTS FOR THE KNOWN ELECTRONIC STATES OF CN

State	T_0 (cm^{-1})	ω_0 (cm^{-1})	$\omega_0 x_0$ (cm^{-1})	B_0 (cm^{-1})	r_0 (Å)	α (cm^{-1})	A (cm^{-1})
$J^2\Delta_i$	64781.56	1107.69	13.93	1.2948	1.419	0.0207	−25.1
$H^2\Pi_r$	60938.72	—	—	1.520	1.310	—	49.6
$F^2\Delta_r$	59682.80	—	—	1.374	1.378	—	28.8
$E^2\Sigma$	58959.9	—	—	1.4837	1.326	0.009_2	—
$D^2\Pi_i$	53954.99	995.93	8.78	1.155	1.503	0.013	−3.0
$B^2\Sigma$	25797.84	2143.7	20.2	1.962	1.153	0.023	—
$A^2\Pi_i$	9118.02	1799.72	12.61	1.7066	1.236	0.0174	−52.2
$X^2\Sigma$	0.00	2055.50	13.114	1.8903	1.175	0.01722	—

Douglas and Routly (1955) have listed the electron configurations and resulting doublet states that are expected for CN. The two new states, $E^2\Sigma$

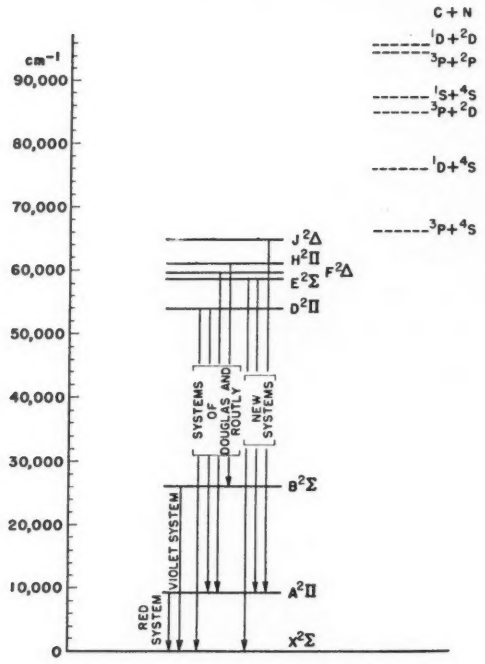

FIG. 5. Energy level diagram for CN.

and $J^2\Delta$, almost certainly arise from the configuration $KK(\sigma_g 2s)^2(\sigma_u 2s)^2(\pi_u 2p)^3(\sigma_g 2p)(\pi_g 2p)$ which produces two Σ_u^+, two Σ_u^-, and two Δ_u states. Thus, at present, only four of the states listed by Douglas and Routly have not been directly observed—two Σ_u^- states, a Π_u state, and a Σ_u^+ state. It is very likely that the latter is responsible for one of the perturbations mentioned in Section III.

The assignment of *g* and *u* symbols was suggested by Douglas and Routly because the absence of the $B-A$ transition seemed to indicate that there was sufficient symmetry in the molecule for $g-u$ properties to be important. The present work however would indicate that this is not the case. Thus the "forbidden" transition $J^2\Delta_u \rightarrow A^2\Pi_u$ appears quite strongly whereas the "allowed" $H^2\Pi_u \rightarrow X^2\Sigma_g$ system was not observed.

Further work remains to be done on the CN spectrum in the Schumann region. The spectrum should be investigated in the wavelength range below 1300 Å where Rydberg transitions might be observed which would give a value for the ionization potential of the molecule. An experiment of even more importance but of greater difficulty would be the observation of the absorption spectrum. In particular, absorption to states $D^2\Pi$, $E^2\Sigma$, $H^2\Pi$ should be observed and these transitions should give long upper-state progressions be-

cause of the considerable increase in internuclear distance in going from the ground state. There is some hope that in this way accurate extrapolations to dissociation limits might be made and D(CN) obtained.

ACKNOWLEDGMENT

In conclusion, the author would like to thank Dr. G. Herzberg and Dr. A. E. Douglas for many helpful discussions in the course of the work.

REFERENCES

BRIX, P. and HERZBERG, G. 1954. Can. J. Phys. **32**:110.
CURRY, J. and HERZBERG, G. 1934. Ann. Physik, **19**: 800.
DOUGLAS, A. E. and ROUTLY, P. M. 1954. Astrophys. J. **119**: 303.
——— 1955. Astrophys. J. Suppl. 9, Vol. **1**: 295.
EDLÈN, B. 1953. J. Opt. Soc. Amer. **43**: 339.
GAYDON, A. G. 1953. Dissociation energies. 2nd ed. Chapman & Hall, Ltd., London.
HARRISON, G. R. 1939. M.I.T. wavelength tables. John Wiley & Sons, Inc., New York.
HERZBERG, G. 1950. Spectra of diatomic molecules. 2nd ed. D. Van Nostrand Company, Inc., New York.
JENKINS, F. A. 1928. Phys. Rev. **31**: 539.
JENKINS, F. A., ROOTS, Y. K., and MULLIKEN, R. S. 1932. Phys. Rev. **39**: 16.
JEVONS, W. 1926. Proc. Roy. Soc. (London), A, **112**: 407.

THE EFFECT OF GROWTH CONDITIONS UPON THE SOLIDIFICATION OF A BINARY ALLOY[1]

By W. A. Tiller[2] and J. W. Rutter[3]

ABSTRACT

This investigation provides both a theoretical and an experimental analysis of the factors which affect the mode of solidification of a binary alloy. These factors are: (i) the concentration of solute in the melt (C_0); (ii) the rate of solidification (R); (iii) the temperature gradient in the melt at the solid–liquid interface (G). Extremely high purity lead was produced by zone refining and, from this material, crystals containing known concentrations of tin, silver, and gold were grown under a range of well-controlled growth conditions. The mode of solidification was investigated by a careful study of the change in appearance of the solid–liquid interface with a change in growth conditions. For a crystal containing a specific C_0 of solute it was observed that (*a*) the transition from a smooth interface to a cellular interface occurred at a critical ratio of G to R; (*b*) the width of the cells varied inversely as G and inversely as R; (*c*) the transition from a cellular interface to a dendritic interface exhibited a large orientation dependence, and for a constant orientation breakdown occurred at a critical ratio of G to $R^{\frac{1}{2}}$. The experimental observations confirm both the existence of a solute-rich layer of liquid adjacent to the solid–liquid interface and its quantitative features. From this agreement with theory the diffusion coefficients of tin, silver, and gold in liquid lead at 327°C. are determined. This work serves to illustrate the effect of extremely small amounts of particular solutes upon the development of substructures during solidification. A technique is proposed for obtaining a measure of the purity of low impurity content alloys.

INTRODUCTION

During the course of the past 10 years considerable effort has been spent in investigating the substructures that occur during the solidification of metals. Chalmers (1954) has recently given a very excellent account of these substructures that occur during the solidification of metals from the melt. In particular, he considers dendritic growth in pure metals, the macromosaic structure called "striations", the prismatic substructure known as "corrugations", and the topography of the solid–liquid interface. From the knowledge gained in these investigations it is now possible to systematize the study of solidification from the melt so that insight can be gained into the eventual prediction of all the observed phenomena associated with the liquid–solid transformation.

All phenomena observed to occur as a result of solidification from the melt can be broadly classified as various interactions between the three important variables of growth:

(i) K—the crystallographic features of the growing crystal,

(ii) T—the temperature distribution in the metal,

(iii) S—the solute distribution in the metal,

so that solidification can be represented symbolically by a growth function G, where

[1]Manuscript received September 6, 1955.
Contribution from the Department of Metallurgical Engineering, University of Toronto, Toronto, Ontario.

[2]Present address: Westinghouse Research Laboratories, East Pittsburgh, Pennsylvania, U.S.A.
[3]Department of Metallurgical Engineering, University of Toronto, Toronto, Ontario.

$$G = G(K, T, S). \tag{1}$$

The prominent features of crystal growth cannot be studied independently but only as the interaction between two of the above variables. If one considers the solidification of a pure metal, only the interaction between (i) and (ii) need be considered.

Consider, for example, the problem of dendritic growth in pure metals from the viewpoint expressed by Eq. 1. As shown by Weinberg and Chalmers (1951), a necessary condition for dendritic growth in pure metals is that the temperature must fall from the solid into the liquid, and that the direction of dendritic growth is, of course, determined by the crystallography of the growing crystal. In addition, Rosenberg and Winegard (1954) have shown that the rate of growth of dendrites is determined by the diffusion of heat ahead of the dendrite tip. Therefore, the dendritic structure which will be obtained in any given sample is the result of the interplay of crystallography K, and temperature distribution T, during freezing.

The terraced or stepped solid–liquid interface structures observed by Elbaum and Chalmers (1955) may also be considered in a similar way. These structures occur when solidification proceeds under conditions such that the temperature rises from the interface into the liquid. The detailed appearance of the interface structure depends very markedly upon the crystallographic orientation of the interface. Again it can be seen that the structure depends upon the factors K and T.

The problem of growth is further complicated by the existence of solute in the melt of metal to be solidified. The degree of complication will depend on the particular kinds of solute in the melt. Generally, the more dissimilar is the solute from the solvent, the greater is its effect upon the solidification process. A measure of its effectiveness is the "distribution coefficient" of the solute. This term is given the symbol "k", and is defined as the ratio of the concentration of solute in the solid at the solid–liquid interface to the concentration of the solute in the liquid adjacent to it. For $k = 1$ the solute creates no more distortion in the solid lattice than it does in the liquid, and so it may be very difficult to distinguish, for soldification purposes, the solute atom from the solvent atom in the lattice. If $k > 1$ then the solute raises the melting temperature of the solvent and thus increases the binding between the atoms of the solid. The atoms are therefore packed closer together. If $k < 1$, which is generally the case, the solute weakens the binding between the atoms and their interatomic distance is increased. The solute atom distorts the lattice locally to a degree depending on the departure from $k = 1$; i.e., if $k = 0.001$, then an atom of this type in the lattice causes a great deal of distortion and will have a great effect upon the solidification process.

Solutes having small distribution coefficients will create large distortions when they become attached to the solid–liquid interface and so will make it difficult for solvent atoms to sit on their regular adjacent lattice sites. It is likely then that the degree of solute-produced imperfection introduced into the solid by the solidification process will increase as k decreases. In this way

it can intuitively be seen that the presence of solute will have a large microscopic effect on the process of solidification.

The presence of solute will also have several large macroscopic effects on the properties of a metal crystal solidified from the melt; these can now be considered.

If one considers the solidification of a melt of a single-phase binary alloy then the most consistent feature that appears as a result of the freezing process is an end-to-end segregation of solute in the resulting ingot or casting. This is normal segregation in one dimension and results from the different solubilities of solute in the solid and the liquid. The problem of the resulting solute distribution in the solid has been treated by Pfann (1952), under the assumption of complete mixing in the melt. Tiller *et al.* (1953) have treated the same problem under the assumption of no convective mixing in the melt, taking into account the slow diffusion rate of solute in the liquid, and arrive at a different resulting distribution. The assumption of no convective mixing introduced many new features into the solidification process, one of which was the existence of a layer of solute-rich liquid at the solid–liquid interface. Wagner (1954) calculated the effect of natural convection due to this solute-rich layer and he showed that in general the effect of natural convection was negligible except for very slow rates of growth. He arrived at essentially the same conclusions as Tiller *et al.* (1953), that a layer of solute existed in the liquid adjacent to the interface which moved with the interface and that the distribution in this layer was governed by the rate of growth of the crystal and the rate of diffusion in the liquid.

In general, the normal segregation obtained in any particular specimen depends upon the solute distribution which occurs or is allowed to occur in the melt during freezing and upon the speed of freezing. Therefore, from the viewpoint of Eq. 1, this phenomenon may be considered as resulting from interaction of the factors S and T.

The existence of this solute distribution and its dependence on the rate of growth is sufficient to explain the phenomenon of "banding", observed by Stewart *et al.* (1951). They grew single crystals of lead containing polonium as a radioactive tracer and found by taking an autoradiograph of the crystal that the polonium was segregated into bands across the width of the crystal. These alternate dark and light bands on the autoradiograph showed the length of the crystal to be composed of bands of alternately high and low polonium content. Tiller (1953) showed that if a crystal is solidified at intermittent or fluctuating rates from a liquid alloy, bands of solute appear in the solid as a result of the change in growth rate, and furthermore that the growth technique of Stewart *et al.* was such that the growth was intermittent. The detailed mathematical analysis of this effect has been treated by Smith, Tiller, and Rutter (1955) who showed how it may be used in the production of semiconducting devices.

The effect of "banding" results from the influence of a change in speed of solidification on the solute distribution adjacent to the advancing interface and can, therefore, be classified as a T–S interaction phenomenon.

The existence of this solute distribution and its interaction with the temperature distribution in the liquid at the interface led Rutter and Chalmers (1953) to an explanation of the "corrugation" substructure which was observed to occur in impure metal crystals grown from the melt under a low temperature gradient in the liquid and rapid growth rates. They showed that the boundaries are regions rich in solute compared to the center of the cell, and that the cell size varied with the growth conditions. Thus, it can be seen that for a certain set of growth conditions the solute segregation is no longer one-dimensional, but occupies a three-dimensional cellular network in the metal.

Tiller *et al.* (1953) have predicted theoretically that the breakdown of a macroscopically smooth interface (which gives one-dimensional segregation) to an interface consisting of cellular projections (three-dimensional segregation) occurs at a certain critical ratio of temperature gradient, G, in the liquid at the interface to the rate of growth, R, as follows

$$G/R = -mC_0(1-k)/Dk \tag{2}$$

where m is the slope of the liquidus line, C_0 is the initial concentration of solute in the melt, D is the diffusion coefficient of the solute, and k is the distribution coefficient.

Walton *et al.* (1955) have investigated the onset of cellular growth for lead as solute in zone-refined tin, and found it to conform very accurately to the predicted results of Eq. 2. Morris *et al.* (1955) extended this study to show that for another critical ratio of these two parameters of growth, an interface of the cellular type breaks down into an interface which exhibits a dendritic pattern; i.e., the projections develop side branches.

Considering the foregoing investigations (Morris *et al.* 1955; Rutter and Chalmers 1953; Walton *et al.* 1955), it was felt that a systematic and carefully conducted study should be made to provide extensive quantitative information concerning the stability and the significant features of cellular and dendritic growth from the viewpoint expressed by Eq. 1. This work was primarily designed to definitely establish the existence of a solute-rich layer of liquid at the interface and the quantitative features of this solute distribution. It provides a theoretical and experimental analysis of the three-variable problem as exemplified by the solidification of a binary alloy.

The present work is also an attempt to awaken a full appreciation of the magnitude of the effect which very small amounts of particular solutes have upon the development of substructures that result from solidification from the melt.

EXPERIMENTAL TECHNIQUES

This experimental work was designed to study quantitatively the effect of varying amounts of a particular solute on the mode of solidification of a metal crystal. In order to carry out such experiments the following requirements must be met:

(1) Production of extremely pure metal and subsequent alloying with a particular solute.

(2) Solidification of these alloys under carefully controlled conditions.

(3) Measurement of the growth conditions.

(4) Observation of the effect of solidification.

Purification and Alloying

The solvent metal used in this research was 99.965% pure Fisher reagent lead which was zone-refined (Pfann 1952) to a very high order of purity. The zone refining was carried out in a 1 in. diameter vycor tube which had been coated with a carbon film to prevent the lead from sticking to it. This carbon film was produced by burning acetylene in the tube. The tube containing the bar was then placed in a movable chassis as shown in Fig. 1. This allowed

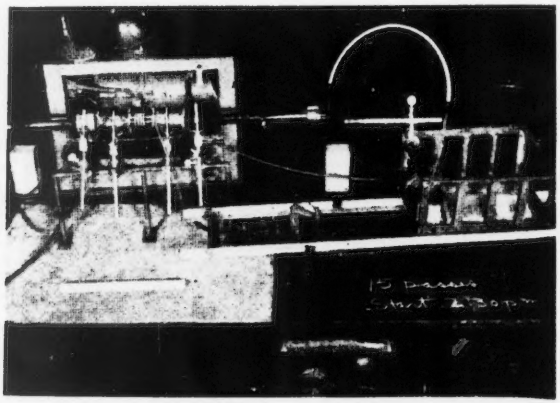

FIG. 1. Zone refining apparatus.

the tube to pass through an induction heating coil at a constant rate in order to produce and move a molten zone. A small flow of argon gas was passed through the tube in order to prevent oxidation of the sample. The argon used was first purified by passing it over titanium sponge at 850°C.

Since lead melts at 327°C., the natural cooling is not sufficient to maintain a short molten zone; therefore, cooling coils were placed on either side of the induction coil to extract enough heat to produce a molten zone of reasonable length. In order to insure that there was time for complete mixing in the liquid zone, the vycor tube was passed slowly through the induction coil. A rate of 0.3 cm./min. was found to be satisfactory. Each sample was given 20 passes to insure that enough purification had occurred. With respect to solutes having $k = 0.5, 0.01, 0.001$ it had an estimated impurity content of less than 10^{-3}, 10^{-5}, 10^{-6} atomic % respectively.

The zone-refined lead was tested for impurity content by anticipating the validity of Eq. 2. A crystal of the purified lead was grown under the most rapid growth rate ($R = 1.5$ cm./min.) and the lowest temperature gradient ($G = 2$°C./cm.) that were attainable with the apparatus used in these experiments. The decanted interface of the crystal showed no evidence of cellular

structure even under these severe conditions. This indicates that the purity was better than that specified above.

To this starting material various amounts of spectrographic tin were added to produce a range of alloys from $10^{-2}\%$ to 2% by weight. Alloys of electrolytically refined silver were also produced from $10^{-4}\%$ to $10^{-3}\%$ by weight. A single alloy of $5\times10^{-6}\%$ gold by weight was also produced.

Control of Conditions of Solidification

A large number of crystals of various solute contents were grown with a range of growth rates and under a range of temperature gradients in the liquid. The crystals were not grown using the Chalmers' technique (Chalmers 1953) of a horizontally travelling furnace because this method has inherent disadvantages when one wishes to vary independently both the rate of growth and the temperature gradient in the liquid. A new technique was therefore developed which will be referred to as the "thermal valve" technique. This will be discussed in detail below. These crystals were grown under a neutral atmosphere to eliminate oxidation of the metal so that a clean outer surface would be obtained for examination. At a critical stage during the growth of the crystal the liquid was rapidly separated from the solid by the decanting technique described by Elbaum and Chalmers (1955). This provided a means of investigating the appearance of the solid–liquid interface. The interface was studied for evidence of cellular or dendritic structure to provide information concerning the stability of different types of interfaces under a range of growth conditions.

Principles of Thermal Valve Technique

Consider a cylinder of metal, with an efficient cooling coil soldered to one end, positioned between two independently powered heating coils as shown in Fig. 2(*a*). These coils may be raised to a sufficiently high temperature to melt some of the metal and to produce a temperature distribution similar to that shown in Fig. 2(*b*) in the solid and the liquid. It can readily be seen that if coil 2, the "thermal valve", was made to decrease in temperature, then the temperature gradient in the solid behind the interface would be increased. This increased rate of heat extraction through the solid would produce the freezing of some of the liquid in order to satisfy the equation of continuity of heat flow given by

$$K_S\left(\frac{dT_S}{dx}\right)_{x=0} = L\rho R + K_L\left(\frac{dT_L}{dx}\right)_{x=0} \tag{3}$$

where K_S = thermal conductivity of the solid,
K_L = thermal conductivity of the liquid,
T_S = temperature distribution in the solid,
T_L = temperature distribution in the liquid,
L = latent heat of fusion,
ρ = density of solid,
R = rate of growth,
x = distance measured from the interface as origin.

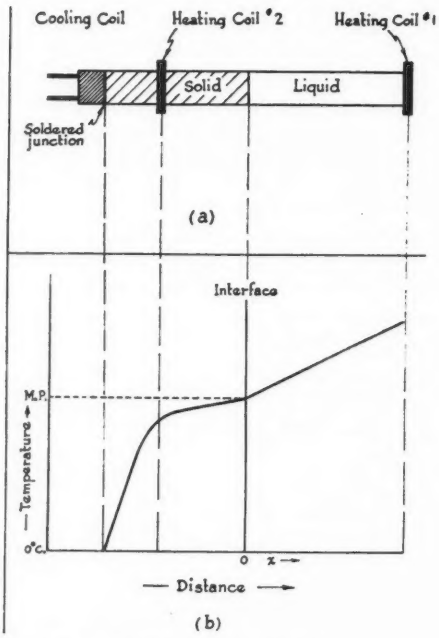

FIG. 2. (*a*) Schematic illustration of thermal valve technique.
(*b*) Representative temperature distribution produced by thermal valve.

However, if the interface is moved forward and the temperature of coil 1 remains unchanged, then the temperature gradient in the liquid will increase and growth will stop. It is therefore necessary to lower the temperature of the two coils at appropriate rates so that the crystal will solidify at a constant rate R and a constant temperature gradient G will be maintained in the liquid at all stages of growth. This condition has been treated theoretically in Appendix I and can be realized if the temperatures of the two coils (1 and 2 in Fig. 2(*a*)) follow the cooling rates

$$dT_1/dt = -GR$$

and

$$dT_2/dt = -[L\rho R^2/K_S + (K_L/K_S)GR]. \tag{4}$$

The furnace shown in Fig. 3 was built containing three heating coils wound on ceramic tubes which form a cage about the heating zone. These coils were powered by three variacs capable of delivering 1½ kva. each. Coils 2 and 3 were controlled at one temperature, while Coil 1 was controlled at another temperature.

To grow a crystal, the power distribution supplied to the coils was first adjusted to melt a portion of the sample and establish the desired temperature gradient in the liquid. To grow a crystal at any rate R, the temperatures

of the coils were then lowered at the rates predicted by Eq. 4. This was accomplished by feeding an e.m.f. in series with each of the control thermocouples at a rate that, when translated into the temperature scale of the thermocouples, was the same as that given by Eq. 4. This tended to cause the temperature indicators on the controllers to move up scale at this rate; however, the controllers decreased the power to the coils in order to keep the temperature indicating pointer on the control point. Since the added e.m.f. plus the e.m.f. from the thermocouple keeps the controllers on the control points, then the temperature of the coils must fall at a rate to compensate for that at which e.m.f. is added; i.e., the rate predicted by Eq. 4.

The e.m.f. was supplied by two gear-driven potentiometers which were connected to a shaft rotating at a constant speed. The rate of delivery of e.m.f. to the respective thermocouple circuit was controlled by setting the current in the potentiometer windings to a suitable value. A circuit diagram for the apparatus is shown in Fig. 4.

Single-crystal seeds were not used in these experiments since they were found to be very difficult to produce of the proper orientation and the proper solute concentration by the standard techniques. In zone-refined lead, grain boundaries have extremely high mobilities, so that if a stray is nucleated it may move rapidly into the rest of the crystal. Seed crystals containing five to ten crystallites were used in this investigation and were found to be adequate.

Measurement of Growth Conditions

The temperature gradient was measured with the aid of six iron–constantan thermocouples placed at 2 cm. intervals in the upper level of the graphite boat shown in Fig. 3. The thermocouple leads were passed out of the gas-tight system through a fusite terminal to a cold junction in a Dewar flask filled with ice and water, and connected through a rotating switch to a "Speedomax" recorder. The rotating switch served to connect each thermocouple in turn

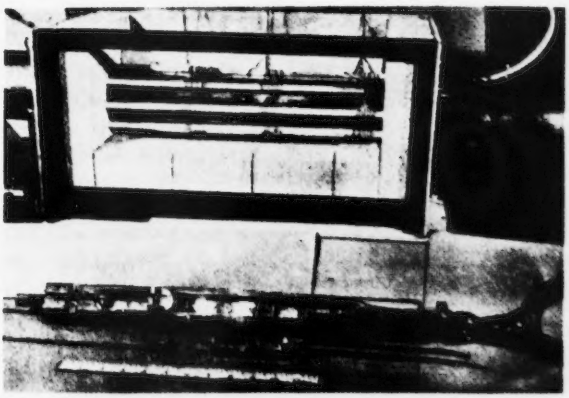

FIG. 3. View of thermal valve furnace with side bricks removed to show windings. Graphite boat assembly used for growing specimens is shown in foreground.

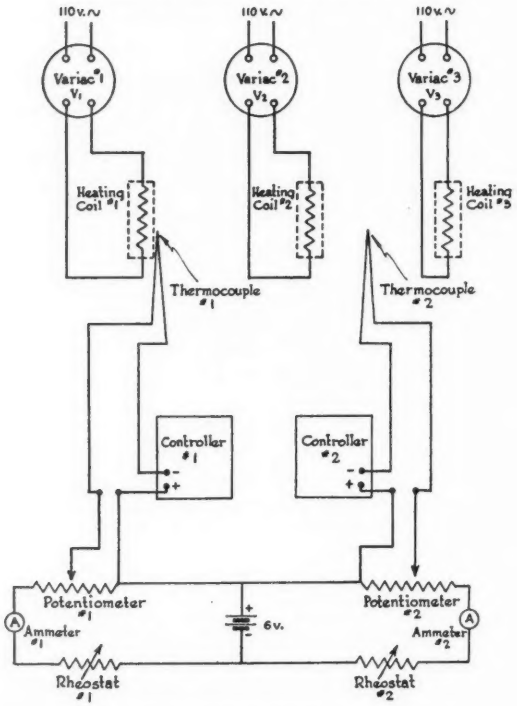

FIG. 4. Electrical circuit of crystal growing apparatus.

to the recorder for a period of five seconds once every 30 sec. The temperature gradient could be calculated by analyzing the time–temperature plot of the thermocouple readings (Morris *et al.* 1955). The crystal was grown until the interface reached one of the thermocouple positions and then the liquid was decanted. This allowed the temperature gradient at that position of the interface to be accurately measured from the slope of this thermocouple plot.

The rate of growth of the crystals was measured by putting ripple marks on the upper surface of the crystal every minute or half minute by periodic vibration of the liquid. The distance between these time markers could be measured accurately and, therefore, the rate of growth accurately determined.

The experimental features of this work have been described in more detail by Tiller (1955).

EXPERIMENTAL OBSERVATIONS

A large number of samples were solidified under a wide range of growth conditions. It was found that the manner in which the solidification takes place is characterized by the appearance of the solid–liquid interface during solidification; the interface may be smooth (Fig. 9), it may exhibit a cellular structure (Fig. 17), or it may exhibit a dendritic structure (Fig. 21). Therefore,

the experimental observations to be discussed refer largely to the features of the solid–liquid interface preserved for observation by the decanting technique previously mentioned. All of the photomicrographs appearing in this section were taken under bright field illumination.

Critical Growth Conditions Governing the Transition from a Smooth to a Cellular Interface

A series of lead crystals containing tin concentrations ranging from 10^{-2} to 1.5×10^{-1} weight % were grown under conditions in the neighborhood of the critical values predicted by Eq. 2. Crystals were produced over a small range of conditions for each concentration in order to determine, as precisely as possible, the conditions for which a smooth interface first became unstable. A series of lead crystals containing silver concentrations ranging from 10^{-4} to 10^{-3} weight % and a single alloy of 5×10^{-6}% gold in lead were similarly investigated.

The results of this series of experiments have been tabulated in Table I for lead–tin alloys, and Table II for lead–silver alloys and the lead–gold alloy.

TABLE I

C_0, wt. % Sn	R, cm./sec.	G, °C./cm.	G/R, °C./cm.²/sec.	Appearance of interface
0.01	0.0167	5.4	3.2×10^2	Irregular cells
0.01	0.0106	9.0	8.5×10^2	No cells
0.01	0.0167	6	3.6×10^2	Irregular cells
0.01	0.0092	5.7	5.7×10^2	No cells
0.01	0.0106	4.35	4.1×10^2	Pox
0.03	0.00735	8.2	11.2×10^2	Irregular cells and pox
0.03	0.0110	8.7	7.9×10^2	Cells
0.03	0.011	8.4	7.6×10^2	Cells
0.03	0.00767	8.8	11.5×10^2	No cells
0.03	0.00750	9.0	12.0×10^2	No cells
0.05	0.00416	4.0	9.6×10^2	Cells
0.05	0.00334	5.4	16.2×10^2	Pox
0.05	0.00867	13.8	15.9×10^2	Pox and irregular cells
0.05	0.00918	15.0	16.3×10^2	Pox
0.06	0.0100	7.5	7.5×10^2	Cells
0.06	0.00750	12.2	16.3×10^2	Pox and irregular cells
0.06	0.00717	12.0	16.7×10^2	No cells and irregular cells
0.06	0.0102	8.2	8.05×10^2	Cells
0.10	0.00700	13.5	19.3×10^2	Irregular cells
0.10	0.00466	15.0	32.2×10^2	No cells and pox
0.10	0.00567	12.0	21.2×10^2	Irregular cells and pox
0.10	0.00835	7.5	9.0×10^2	Regular cells
0.15	0.00567	13.0	23.0×10^2	Cells
0.15	0.00284	13.0	45.7×10^2	Pox
0.15	0.00333	13.0	39.1×10^2	Irregular cells
0.15	0.00333	16.2	48.5×10^2	Pox and no cells

TABLE II

C_0, wt. % Ag	R, cm./sec.	G, °C./cm.	G/R, °C./cm.²/sec.	Appearance of interface
1.0×10^{-4}	0.0183	4	2.2×10^{2}	Elongated cells
1.0×10^{-4}	0.0167	4.7	2.8×10^{2}	Elongated cells
1.0×10^{-4}	0.0167	7.0	4.2×10^{2}	Pox
1.0×10^{-4}	0.020	4.2	2.1×10^{2}	Elongated and regular cells
2.5×10^{-4}	0.020	6.3	3.1×10^{2}	Regular cells
2.5×10^{-4}	0.015	6.8	4.5×10^{2}	Elongated cells
2.5×10^{-4}	0.007	8.5	12×10^{2}	Beginnings of pox
2.5×10^{-4}	0.0083	8.6	10×10^{2}	Pox
2.5×10^{-4}	0.0125	7.7	6.2×10^{2}	Irregular cells
5.0×10^{-4}	0.0067	10.8	16.2×10^{2}	Irregular cells
5.0×10^{-4}	0.008	9.0	11.2×10^{2}	Elongated cells
5.0×10^{-4}	0.0057	12.7	22.3×10^{2}	Smooth interface
5.0×10^{-4}	0.0055	10.8	19.6×10^{2}	Dense pox
5.0×10^{-4}	0.0050	10.5	21×10^{2}	Pox
7.5×10^{-4}	0.0037	10.7	29×10^{2}	Dense pox
7.5×10^{-4}	0.0046	12.5	27×10^{2}	Pox, elongated cells, irregular cells
7.5×10^{-4}	0.0040	15	37×10^{2}	No cells

C_0, wt. % Au	R, cm./sec.	G, °C./cm.	G/R, °C./cm.²/sec.	Appearance of interface
5×10^{-6}	0.0173	5.2	3.0×10^{2}	Pox
5×10^{-6}	0.020	5.3	2.65×10^{2}	Elongated cells

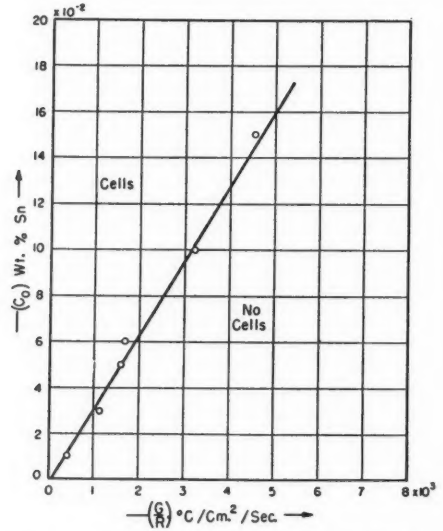

FIG. 5. Critical growth conditions governing the transition from a smooth to a cellular interface for lead–tin alloys.

The breakdown conditions for each concentration have been plotted in Fig. 5 for the lead–tin alloys, and Fig. 6 for the lead–silver alloys. The criterion used to establish the breakdown conditions for a smooth interface was the general occurrence of the pox-like structure shown in Fig. 11. These points lie on a straight line as predicted by Eq. 2. Eq. 2 states that breakdown

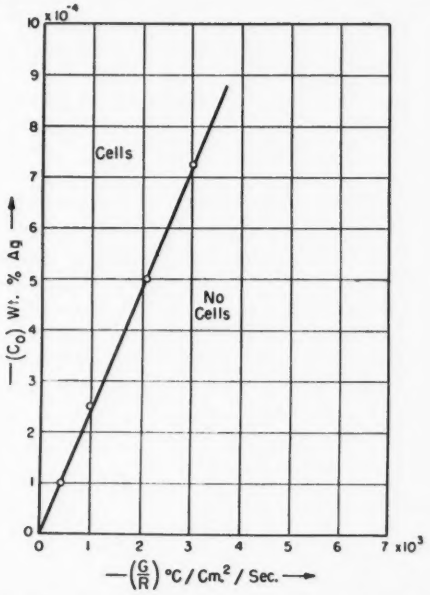

FIG. 6. Critical growth conditions governing the transition from a smooth to a cellular interface for lead–silver alloys.

depends on the ratio G/R and not on these parameters independently. To verify this, crystals were grown with a tin solute content of $C_0 = 5\times10^{-2}\%$, and breakdown was observed to occur for the following conditions: $R = 0.2$ cm./min., $G = 5.4$°C./cm.; $R = 0.5$ cm./min., $G = 13.8$°C./cm.; $R = 0.55$ cm./min., $G = 15.0$°C./cm. The rate of growth and the temperature gradient have been changed by a factor of three and yet the breakdown still occurs at a constant ratio of G to R. These conditions cover approximately the total range of gradients and speeds used in these experiments, thus verifying that the important factor is the ratio and not these parameters independently.

Topography of Cellular Interfaces

It was found possible to follow the change from a smooth interface to a cellular interface, and subsequently to study the variation in the appearance of the cells with changes in growth conditions. For convenience, conditions of solidification will be specified with reference to Fig. 5 by stating the portion of the diagram which represents them.

Crystals grown under conditions to the right of the transition boundary have a smooth interface which exhibits the general microstructure investigated by Elbaum and Chalmers (1955). There is no evidence of instability with this type of interface as shown in Fig. 9 (there is no constitutional supercooling). As the boundary is approached, the interface develops the pox-like structure shown in Fig. 10. With the aid of dark field illumination it was possible to determine that the pox are projections on the interface, and that they vary in size from 10^{-4} to 10^{-3} cm. in width. They first appear widely scattered but as the boundary is approached their density and size increases as shown in Fig. 11.

Just beyond the boundary the interface was observed to develop a mixture of irregular cells and pox. As conditions change away from the boundary into the cell region the pox tend to disappear while the irregular cells increase in both number and regularity. In this region it was observed that the irregular cells subdivide into elongated cells. Fig. 12 illustrates an interface exhibiting irregular cells and elongated cells. Note the density of the pox on the irregular cells as compared to their density on the elongated cells. The elongated cells appear to form by an abrupt faulting of the interface to produce a boundary depression with its long axis in a certain crystallographic direction in each crystal as shown by Fig. 13. Deforming the crystal to produce multiple slip gave all the possible (111) traces on the interface. Fig. 14 is a typical example showing that the long axis of the cell is approximately parallel to a (111) trace. In general, the long axis is within $\pm 5°$ of a (111) trace on the interface. However when the interface was a (111) plane the long axis would slowly curve to take up a range of directions which were not necessarily (111) traces. Fig. 15 shows an interface of elongated cells which are about 0.5 cm. long and 0.0075 cm. wide.

As conditions change so as to move further to the left of the transition boundary, the elongated cells subdivide into an array of nearly regular cells. This is illustrated in Fig. 16. Those crystals having their ⟨100⟩ axis perpendicular to the interface are the first to develop an array of close-packed cells. The crystallographic variation of this subdivision is fairly small.

Variation of Cell Size and Shape with Conditions of Solidification

A number of specimens having a concentration of $C_0 = 0.15\%$ tin in lead were grown with various R and G in order to investigate the change in cell size with these variables. It was desired to study the variation in cell size for an interface of constant crystallographic orientation. It was observed during preliminary experiments that only crystals with their axis in the ⟨100⟩ direction exhibited perfectly regular cells. Therefore, in this experiment, only interfaces were considered which exhibited the regular hexagonal structure. In this way it was possible to be certain that all cell size measurements were made on interfaces of the same orientation.

A decanted interface was obtained of each sample and the average cell size of about 1000 cells was measured from a photomicrograph such as that represented by Fig. 17. The results of these experiments have been tabulated in Table III and plotted in Fig. 7 as cell size vs. $1/RG$.

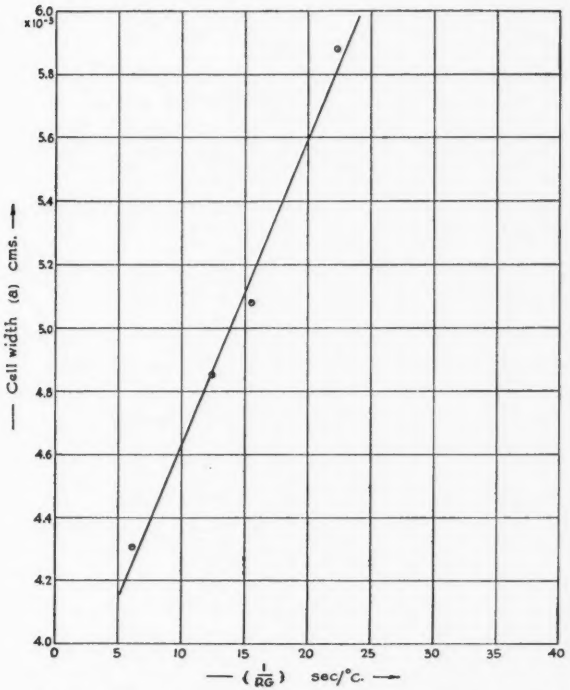

FIG. 7. Effect of growth conditions upon the cell width (a).

TABLE III

C_0, wt. % Sn	R, cm./sec.	G, °C./cm.	$1/RG$, sec./°C.	Cell size "a", cm.
0.15	10.8×10^{-3}	4.15	22.3	5.88×10^{-3}
0.15	14.2×10^{-3}	4.65	15.1	5.08×10^{-3}
0.15	16.7×10^{-3}	4.85	12.4	4.85×10^{-3}
0.15	23.0×10^{-3}	7.0	6.2	4.31×10^{-3}

It was found to be extremely difficult to determine a quantitative dependence of cell size on C_0 because of crystallographic effects that arose during the investigation. It was observed, however, that the cell size tended to increase as the concentration increased.

A very pronounced feature that was observed when crystals were grown under conditions lying in the range which produced cellular interfaces was the effect of the orientation of the interface on the shape of the cell. As mentioned previously, the regular cells shown in Fig. 17 occur only when the crystal axis is close to the dendrite axis. As the orientation of the crystal is changed the appearance of the cells is also changed. Some crystals exhibit four- and five-sided cells and the cell size may differ by a factor of three or four owing

to the difference in orientation of the interface presented to the liquid. This is shown in Fig. 18.

When the growth conditions are made more severe, i.e., R increased, C_0 increased, and G decreased, the cells become less regular and they project further into the liquid developing a definite cap-like appearance as shown in Fig. 19. These cells appear in some cases to project from the interface at an angle. It is likely that the axis of the cell tends to point in the dendrite direction and if this direction makes an angle with the interface normal, then the cells would not appear symmetrical.

Critical Growth Conditions Governing the Transition from a Cellular to a Dendritic Interface

A series of lead crystals containing tin concentrations ranging from 0.25% to 2.0% by weight were grown under conditions in the region of instability of a cellular interface. The appearance of the interface was studied for evidence of cellular or dendritic growth. During growth the top surface of the liquid was scraped clean, and after decanting the top surface was also studied for evidence which implied a cellular or dendritic type of growth.

Crystals were produced over a small range of conditions for each concentration in order to determine, as precisely as possible, the conditions for which a cellular interface first becomes unstable. These conditions will be termed the "breakdown conditions" for the particular concentration in question. The criterion used to establish the onset of dendritic growth was the general beginning of side-branching of the cells as shown in Fig. 20. It should be noted that this type of dendritic growth is somewhat different from the classical dendritic growth where the dendrites grow well out into a supercooled liquid and develop pronounced side branches. The type of dendritic growth discussed here is found to be a limited dendritic growth where the dendrite heads project about 10^{-2} cm. from the interface.

An experimenter would be faced with an almost insurmountable task to determine the breakdown conditions for every crystallographic orientation. However, it was observed that the first crystal to become unstable exhibited a high index interface, i.e., its orientation falls in the center of the stereographic triangle of a standard (100) projection, and the last crystal to break down exhibited the dendrite orientation. It was therefore possible to find the breakdown conditions for these two limiting cases. This could be done by observing the conditions for which the cells of any crystallite first became unstable, and the conditions for which the last cellular crystallite became unstable. It was assumed that one of the crystallites would have an orientation which falls near the center of the stereographic triangle, and another would have an orientation near the dendrite orientation. In general, by the shape of the cells, the orientation of the interface relative to the dendrite orientation could be closely determined.

The results of this series of experiments have been tabulated in Table IV; the lower and upper breakdown limits have been plotted in Fig. 8. A straight line can be drawn through the points which represent the instability of a high index interface and a second line through the points which represent the

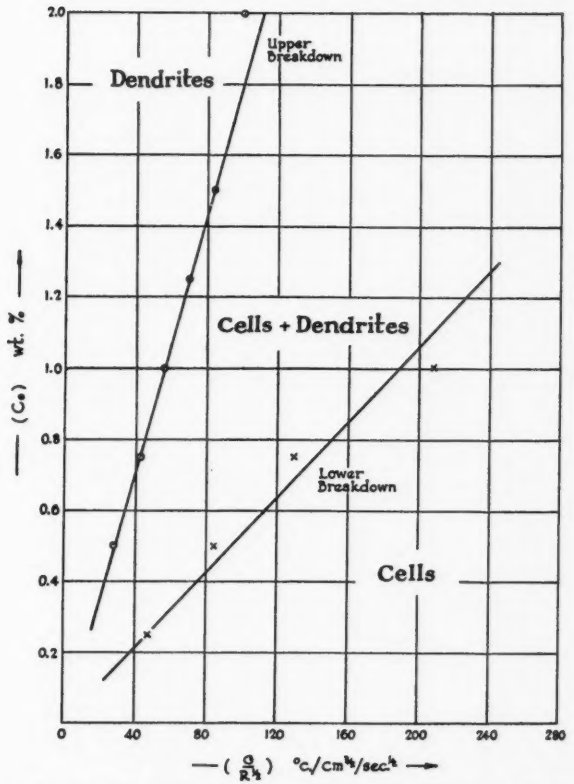

FIG. 8. Effect of growth conditions upon the transition from a cellular to a dendritic interface. The upper and lower curves show the limits of the orientation dependence.

TABLE IV

C_0, wt. % Sn	R, cm./sec.	G, °C./cm.	$G/R^{1/2}$	Interface appearance
0.25	12.5×10^{-3}	5.6	50.3	All cells
0.25	16.7×10^{-3}	9.0	68.0	All cells
0.25	20×10^{-3}	6.7	47.4	*Beginnings of side branching on one crystal, cells on others
0.50	18.4×10^{-3}	11.4	84	*Cells and beginnings of branched cells
0.50	8.34×10^{-3}	10.4	114	A few cells broken down, cells
0.50	21.3×10^{-3}	7.0	48	Dendrites, one region of cells
0.50	20×10^{-3}	3.9	27.6	**Dendrites, one region of unstable cells

TABLE IV (*Concluded*)

C_0, wt. % Sn	R, cm./sec.	G, °C./cm.	$G/R^{1/2}$	Interface appearance
0.75	10×10^{-3}	6	60	Cells and dendrites
0.75	10×10^{-3}	7.5	75	Cells and dendrites
0.75	7.5×10^{-3}	9.6	111	Cells and dendrites
0.75	7.5×10^{-3}	12.0	139	*All cells (very close to breakdown)
0.75	17×10^{-3}	5.6	43.1	**Dendrites, last region just breaking down
1.0	3.33×10^{-3}	12.0	208	*Cells, one region just breaking down
1.0	4.67×10^{-3}	12.0	176	Cells, few dendrites
1.0	6.66×10^{-3}	10.8	127	Cells, dendrites
1.0	11.3×10^{-3}	8.5	83.5	Dendrites, one region of cells
1.0	18.3×10^{-3}	9.1	67.5	**Dendrites, one region of unstable cells
1.0	22.5×10^{-3}	7.5	49.8	All dendrites
1.25	11.65×10^{-3}	13	103	Cells, unstable cells, dendrites
1.25	14.7×10^{-3}	11.5	95	Dendrites, one region of cells
1.25	16.7×10^{-3}	9.4	72.6	**Dendrites, one region of unstable cells
1.25	12.2×10^{-3}	7.4	67	Dendrites, one region of unstable cells
1.50	15.0×10^{-3}	10.4	84.4	Dendrites
1.50	13.3×10^{-3}	11.3	97.2	Dendrites, one region of unstable cells
1.50	14.3×10^{-3}	10.9	91.0	Dendrites, one region of unstable cells
1.50	14.3×10^{-3}	10.0	83.8	**Breakdown
2.0	12.3×10^{-3}	11.0	99.1	**Dendrites, last region of cells breaking down
2.0	15×10^{-3}	10.2	83.4	All dendrites
2.0	11.6×10^{-3}	11.0	102	Dendrites and cells
2.0				

*High index breakdown limit.
**Low index breakdown limit.

instability of an interface of the dendrite orientation. Between these two boundary lines the conditions are such that interfaces with orientations between these two extremes become unstable. The parameter $G/R^{\frac{1}{2}}$ was used for plotting purposes since it was determined that the breakdown conditions for a certain C_0 depend on the ratio $G/R^{\frac{1}{2}}$ and not on G or R independently. Using $C_0 = 1.25\%$, the upper breakdown was observed for the following

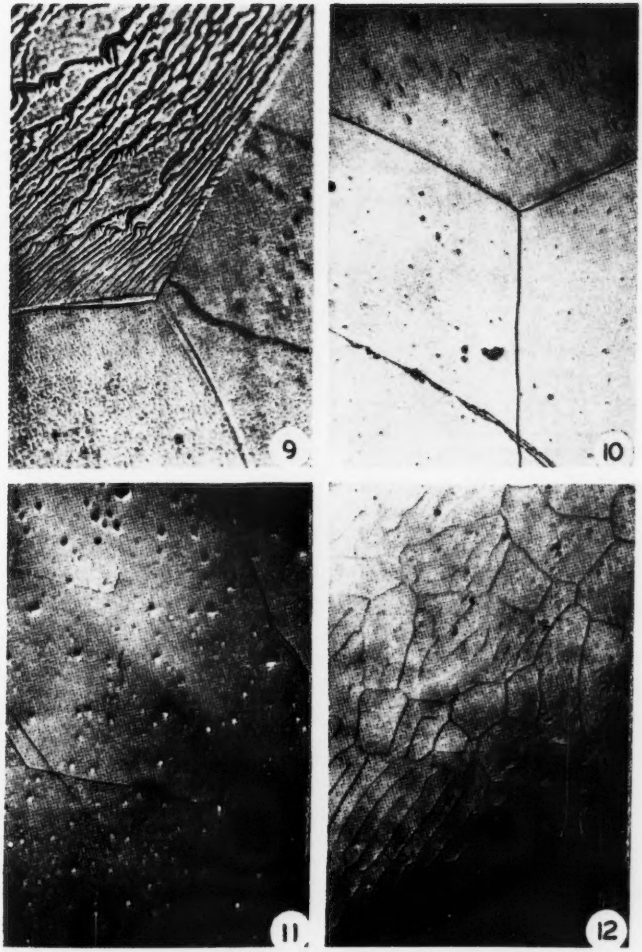

FIG. 9. Representative smooth interface. (100×)
FIG. 10. Initial formation of pox-like structure. (100×)
FIG. 11. Interface exhibiting well-developed pox and beginnings of irregular cells. (100×)
FIG. 12. Interface exhibiting irregular cells subdividing into elongated cells. (40×)

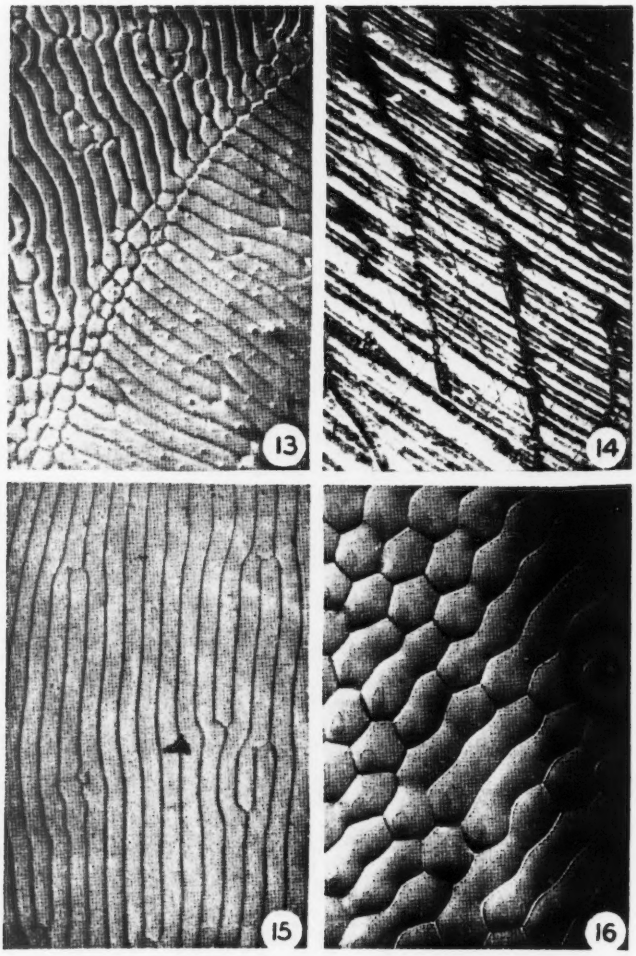

FIG. 13. Interface exhibiting elongated cells in two adjacent grains. (40×)
FIG. 14. Interface exhibiting elongated cells with traces of duplex slip. The vertical slip traces are approximately parallel to the direction of the elongated cell boundary. (150×)
FIG. 15. Interface exhibiting extremely long cells, 0.5 cm.×0.0075 cm. (40×)
FIG. 16. Interface exhibiting subdivision of elongated cells to nearly regular hexagonal cells. (100×)

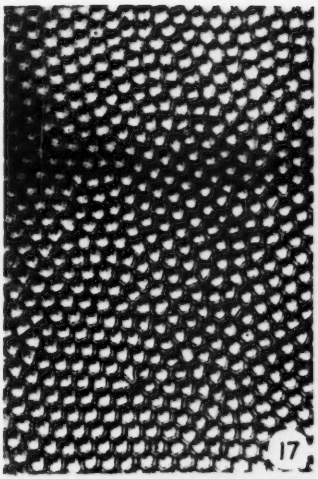

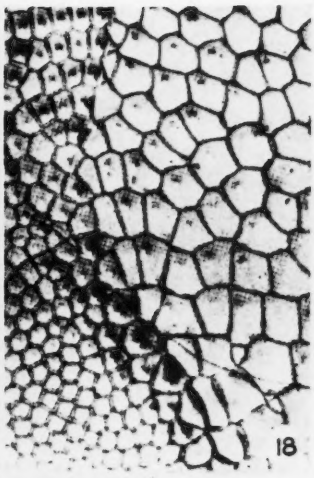

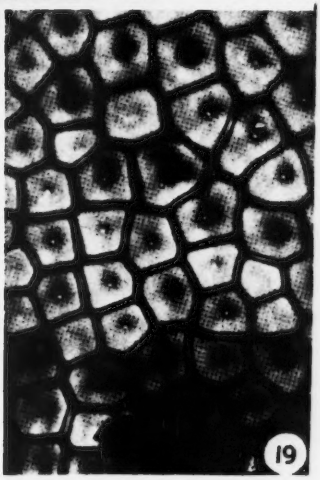

FIG. 17. Interface exhibiting regular cells. Representative photomicrograph used for measurement of cell size. (50×)

FIG. 18. Interface exhibiting effect of crystallographic orientation upon the cell size and cell shape. (50×)

FIG. 19. Interface exhibiting well-developed cellular projections.

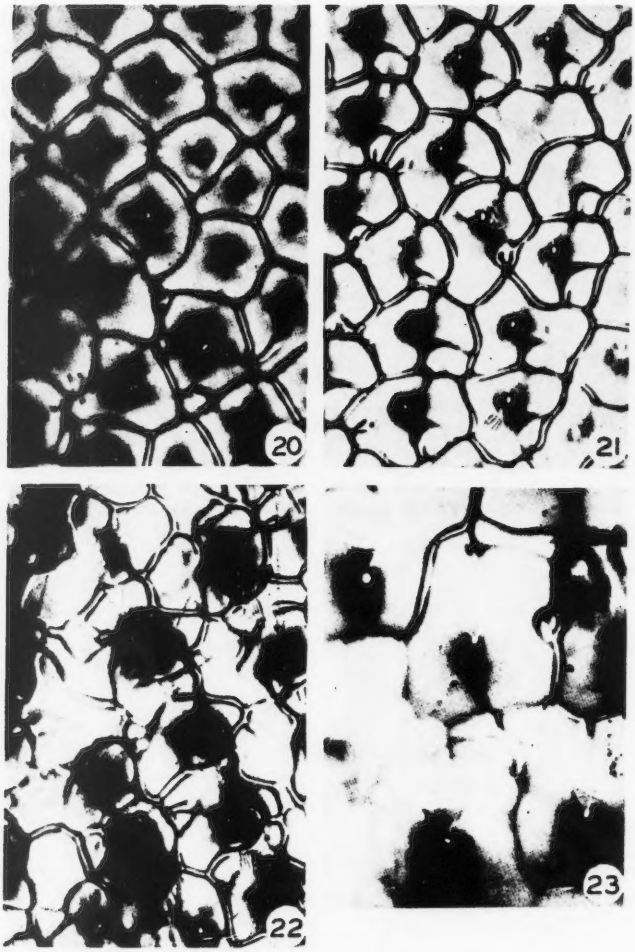

FIG. 20. Interface exhibiting initial instability of a cellular interface resulting in side-branching. (100×)
FIG. 21. Interface exhibiting further development of side-branching. (100×)
FIG. 22. Interface exhibiting well-developed dendritic features. (100×)
FIG. 23. Dendritic interface exhibiting pyramidal projections inclined to the specimen axis. (100×)

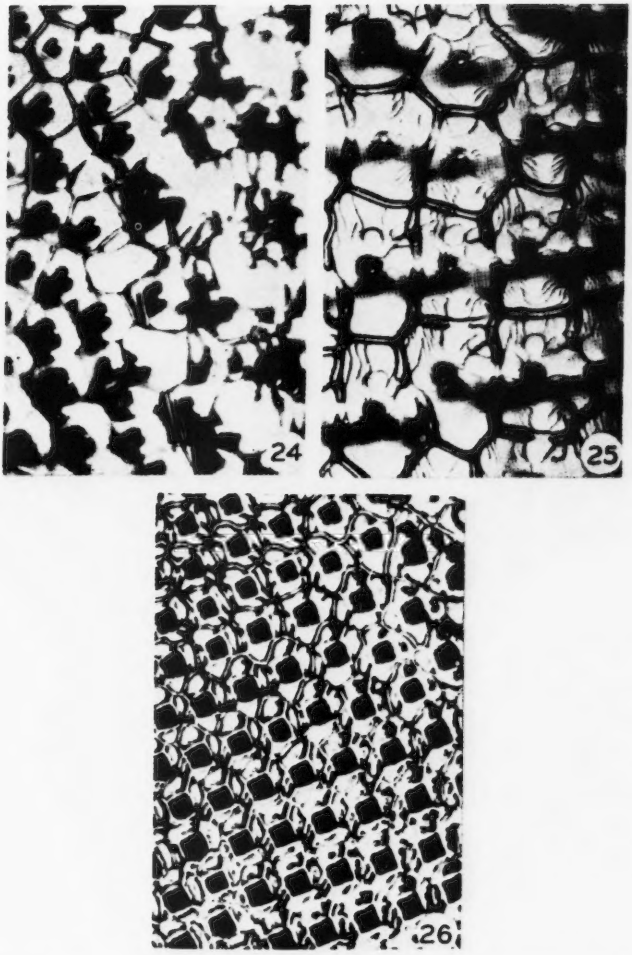

FIG. 24. Interface exhibiting the effect of orientation upon the formation of dendrites. (100×)
FIG. 25. Approximately (100) type interface exhibiting dendritic breakdown. (250×)
FIG. 26. Approximately (100) type interface exhibiting truncated pyramidal projections. (100×)

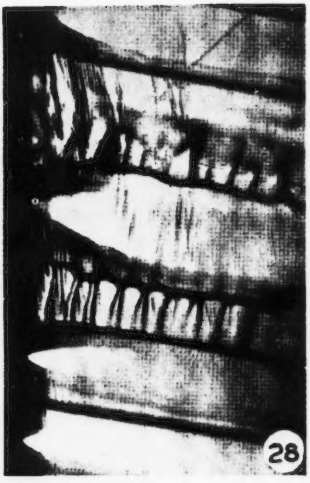

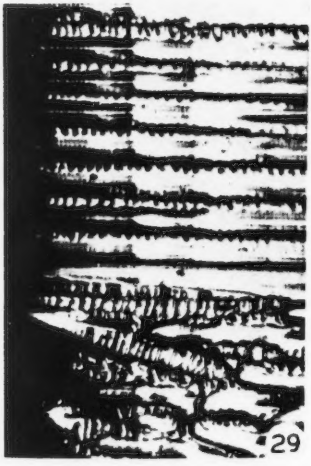

FIG. 27. Upper surface exhibiting typical corrugation structure. (100×)
FIG. 28. Upper surface exhibiting initial formation of dendrites as evidenced by the oscillation of the corrugation boundary. (250×)
FIG. 29. Upper surface exhibiting different stages of dendrite formation in adjacent grains. (100×)

conditions: $R = 1.0$ cm./min., $G = 9.4$°C./cm.; $R = 0.75$ cm./min., $G = 7.6$°C./cm.; $R = 0.4$ cm./min., $G = 5.8$°C./cm. These conditions cover approximately the total range of gradients and speeds used in the experiments dealing with the transition from a cellular to a dendritic interface, thus serving to indicate that the important factor is the ratio $G/R^{\frac{1}{2}}$ and not these parameters independently. It was also found that plotting C_0 versus $G/R^{\frac{1}{2}}$ gave a linear plot.

The Topography of Dendritic Interfaces

It was found possible to follow the changes from a cellular interface to a dendritic interface, and subsequently to study the variation in appearance of dendritic interfaces with changes in the growth conditions. As mentioned previously, crystals grown under conditions to the right of the lower breakdown curve exhibit an interface of a cellular nature as shown in Fig. 19. As the boundary is approached the square type of cells, characteristic of the orientation in the center of the stereographic triangle, become unstable and develop curved boundaries. The next stage in the development is that small regions of boundary form on the sides of the cells as shown in Fig. 20. This is the first evidence of side branching of the cells. As the lower transition boundary is crossed, the cell boundaries become greatly curved and develop further side branching (Fig. 21). As conditions move into the region between the two curves, the dendrites, as they should now be called, develop a very characteristic appearance (Fig. 22), with curved boundaries, side branches, and a central projection extending a considerable distance into the liquid. This is illustrated best by Fig. 23, which shows the projection extending into the liquid at an angle to the specimen axis.

As shown by Fig. 24, the breakdown has a large orientation dependence. It can be seen that a crystal on one side of the grain boundary exhibits well-developed dendrites, whereas the crystal on the other side exhibits stable cells.

As the upper breakdown curve is approached it is observed that only those crystallites having the dendrite orientation exhibit stable cells. Interfaces of this type have been observed to exhibit a definitely characteristic microstructure such as that studied by Elbaum and Chalmers (1955). As the growth conditions approach the upper boundary the cell walls begin to curve and breakdown occurs by what appears to be the overlapping of one of the cells into another. This is illustrated in Fig. 25. As the upper transition boundary is reached, the cells develop a truncated pyramid in the center of the cell which extends into the liquid. This is illustrated by Fig. 26.

Topography of the Free Surface in the Transition Zone

The upper surface of the crystal was investigated as a function of the growth conditions in the transition region to supplement the interface study. It was found that the upper surface of the crystal supplied additional information which could be incorporated to present a three-dimensional picture of the transition from a cellular substructure to a dendritic or branched substructure.

Figure 27 illustrates the appearance of the corrugations on the upper sur-

face. It can be seen that in one crystal the corrugations intersect the upper surface at an angle, so that the interface would present the unsymmetrical, large cells to the liquid. In another crystal the corrugations are running parallel to the upper surface of the crystal and, therefore, present the symmetrical cells to the liquid. The corrugations in these crystals appear to be perfectly constant in size and shape, so that the interfaces of the crystals represented by these corrugations would be of a stable cellular form.

However, when the interface tends to become unstable, this is observed on the top surface as an oscillation of the corrugation boundaries as shown in Fig. 28. Fig. 29 illustrates the crystallographic effects of dendritic breakdown on the upper surface. It can be seen that the crystal with corrugations intersecting the upper surface at a large angle exhibits well-developed dendrites, whereas the crystal with the corrugations running parallel to the upper surface has only just broken down.

SUMMARY OF OBSERVATIONS

(1) The breakdown of a macroscopically smooth interface to a cellular interface exhibits the linear variation $C_0 = A(G/R)$ as predicted by Eq. 2, where A is the constant of proportionality. It was determined that the ratio G/R was the important parameter in this relationship, and not R or G independently.

(2) The above relationship exhibits a small crystallographic dependence. The breakdown conditions are slightly different for interfaces of different orientation, both crystals containing the same C_0.

(3) In the transition region, the interface develops a pox-like structure as a stage of development prior to cell formation.

(4) The cells first appear to be irregular and elongated just inside the transition zone. As the cellular region is approached, the elongated cells subdivide to form smaller, almost regular, cells.

(5) The direction of the elongated cell boundaries provides information concerning the crystallographic orientation of the crystal. The direction of the elongated cell boundary coincides with a (111) trace on the interface.

(6) The variation in cell size for the dendrite orientation, as a function of R and G, is shown to have the form $a = B(1/RG)$, where a is the cell size and B is the constant of proportionality. The cell size is observed to increase with an increase in C_0.

(7) The magnitude of the crystallographic effect increases in the cellular region. Interfaces exhibit four-sided and five-sided cells as well as hexagonal cells. The cells for one orientation may be three or four times larger than the cells for another orientation. The high index interface exhibits the enlarged cells.

(8) The breakdown from cells to dendrites depends upon the crystallographic orientation of the interface. Crystals having orientations which fall in the center of the stereographic triangle of a standard (100) projection break down first. Breakdown for these high index interfaces can be described

by the linear relationship $C_0 = C'(G/R^{\frac{1}{2}})$, where C' is the constant of proportionality. Crystals having the dendrite orientation break down last. Breakdown for this low index interface was found to exhibit the linear variation $C_0 = C''(G/R^{\frac{1}{2}})$, where C'' is the constant of proportionality. It was found that $G/R^{\frac{1}{2}}$ was the important parameter in these relationships, and not G or R independently.

(9) In this transition region the cells project further into the liquid than previously. The cell boundaries curve and develop side-branches as they break down into dendrites. As the cells break down into dendrites they develop pyramidal projections extending into the liquid.

(10) Observations were made on the top surface of the crystal which supplemented and corroborated the interface observations.

DISCUSSION

The experiments carried out on the smooth interface – cellular interface transition serve to endorse the validity of the theoretical considerations concerning the stability of a smooth interface. Thus, the authors have definitely established that a solute-rich layer of liquid adjacent to the interface exists, and that the distribution of solute in this layer exhibits the quantitative features predicted by Tiller *et al.* (1953), i.e.,

$$C_L = C_0\left(1+\frac{1-k}{k}\,e^{-(R/D)x}\right) \tag{5}$$

where C_L represents the solute distribution in the liquid, and x refers to distance measured from the interface into the liquid.

This work has also served to verify that there is a possibility of producing a constitutionally supercooled zone of liquid adjacent to the interface, and that if this unstable zone exists the interface will alter shape in an attempt to eliminate the instability. From the viewpoint expressed by Eq. 1, it can be seen that the development of a cellular interface with its subsequent three-dimensional segregation is mainly due to the interaction of two of the important variables of growth T and S. The effect of K is very slight for the breakdown of a smooth interface to a cellular interface. This small dependence is probably due to the slightly different surface area presented to the liquid by crystals of different orientation (different surface topography), as shown in Fig. 9.

The experiments show that although the rate of solidification R changes by an order of magnitude the breakdown of a smooth to a cellular interface can be described by a constant distribution coefficient k. Therefore, the rate of deposition of atoms from the liquid onto the solid for the rates considered does not appear to affect the fundamental processes involved in equilibrium freezing as exemplified by the equilibrium diagram. This is a reasonable conclusion since even for the slow rates of growth used in this investigation the net rate of deposition of atoms in a line perpendicular to the interface is of the order of 10^5/sec.

Figures 5 and 6 show that the breakdown of a smooth interface to a cellular

interface is described by a linear relationship between C_0 and the ratio G/R as predicted by Eq. 2. From the slope of the transition boundary the diffusion coefficient for the solute in liquid lead at the melting temperature of lead can be calculated. The results of this calculation have been tabulated in Table V.

TABLE V

Solute	m, °C./wt.%	k	C_0, wt.%	G/R, °C./cm.²/sec.	D, cm.²/sec.
Sn	−3	0.56	3×10^{-2}	1.0×10^{3}	7.0×10^{-5}
Ag	−9.2	0.04	5×10^{-4}	2.1×10^{3}	5.3×10^{-5}
Au	−7.5	0.006	5×10^{-6}	0.3×10^{3}	2.1×10^{-5}

The accuracy of these calculations depends very largely upon the accuracy of the parameters m and k. The experimental determination of the breakdown conditions can be made accurate to within 5%, whereas m and k must be taken from equilibrium diagram data for low concentrations and assumed to be unchanged for dilute solutions.

No measurement of the diffusion coefficients of tin or silver in lead are available for comparison; however, they fall in the expected range. Jost (1952) gives a value for gold in lead to be $D = 3.7\times10^{-5}$ cm.²/sec. at 500°C. This value can be extrapolated to the melting temperature of lead by using the activation energy for viscous flow as the activation energy for diffusion. Using 2.5 kcal./mole as the activation energy, the value of a diffusion coefficient becomes $D = 2.3\times10^{-5}$ cm.²/sec., which is quite good agreement with this measured value.

It is often found to be very difficult to estimate accurately the slope of the liquidus line for dilute solutions; however m can be eliminated from Eq. 2 by utilizing the Vant'Hoff relation which relates the differences of the slopes of the liquidus and solidus lines on the equilibrium diagram to the latent heat of fusion L and the absolute melting temperature of the solvent T_0, so that

$$m = -\frac{R^{+}T_0^{2}}{L}(1-k). \tag{6}$$

Eq. 2 then becomes transformed to

$$G/R = \frac{R^{+}T_0^{2}}{L}\,\frac{C_0}{D}\,\frac{(1-k)^{2}}{k}, \tag{7}$$

where R^{+} is the universal gas constant, and C_0 is measured in mole fractions.

Equation 7 may be tested by using the values of m and k tabulated in Table V with m corrected to be in the right units. It is found to be in error by as much as 50% for these values of m and k. However, Eq. 7, though not as accurate as Eq. 2, is very useful for some purposes.

As has been shown by Walton *et al.* (1955), this technique may be used to give a measure of the purity of any metal. Consider the following example. Assume that for a lead crystal the growth conditions were $R = 1$ cm./min., $G = 1$°C./cm., and that the decanted interface had a smooth appearance.

Let D be approximately 5×10^{-5} cm.^{2}/sec. for all possible solutes. Then by inserting these values in Eq. 7 it can be stated that the lead is purer than

$$\begin{aligned} C_0 &= 10^{-3} \text{ atomic \% for } k = 0.5, \\ &= 10^{-4} \text{ atomic \% for } k = 0.1, \\ &= 10^{-5} \text{ atomic \% for } k = 0.01, \\ &= 10^{-6} \text{ atomic \% for } k = 0.001. \end{aligned}$$

The lead will be purer than indicated above since breakdown had not occurred under these conditions. This provides an analysis of the impurity content in terms of the distribution coefficient; a chemical analysis can be arrived at by grouping the elements into their respective ranges of k. Since the ratio L/T_0 is a constant for any crystallographic system (entropy of fusion), it can be seen that the higher the melting point of the solvent the greater is the order of the purity that can be analyzed for.

It is hoped that these results have served to illustrate the importance of very minute quantities of particular solutes (5×10^{-6}% of gold in lead) in producing substructures as a result of the solidification process.

Interface Topography

The presence of the pox-like structure in the region of the transition zone between smooth and cellular interfaces appears to be the first manifestation of the attempt, by the interface, to redistribute solute in order to eliminate a small amount of constitutional supercooling. The first pox to appear on the interface are probably chance fluctuations in conditions which are able to produce local regions of constitutional supercooling. As the general conditions approach the instability, the density of the pox increases. It is likely that when the amount of solute to be redistributed becomes too great the pox are replaced by the cellular structure. The density of the pox on the irregular cells is observed to be much greater than on the elongated cells. When the amount of cell boundary is increased there is no need for the pox and they disappear.

In all considerations dealing with the size and the shape of the cells it is necessary to make two assumptions: (i) The cell will try to eliminate the constitutional supercooling by providing a solute sink into which the excess solute can diffuse. (ii) The crystal at all times will try to minimize its free energy; to this end it will try to minimize its interfacial energy by minimizing its solid–liquid surface area. The cell width will therefore try to be as large as the growth conditions will permit; this is reasonable since the smaller the cell width for a constant cell depth the greater is the interfacial energy of the system.

When the elongated cells form they appear to do so by a faulting of the interface. They do not appear to be a development from the pox but seem to be a quite separate attempt to relieve the constitutional supercooling by forming a solute sink. Contrary to the information of Blaha (1955) these boundaries do have orientation characteristics. The formation of these elongated cells increases the interfacial area; however, the increase in interfacial energy is minimized since the cell boundaries are traces of (111) planes and the cell walls are thus low energy (111) surfaces.

When the amount of constitutional supercooling to be eliminated is increased, the elongated cells subdivide to provide more cell boundary into which solute can diffuse. Fig. 16 shows the gradual distortion of the elongated cell to produce more regular cells, and then the abrupt faulting to produce a sharp boundary at these points.

Figure 7 represents the experimental results which illustrate the variation in cell size, as a function of the growth parameters R and G. These results show that the cell width varies inversely as the temperature gradient and inversely as the rate of growth in agreement with the work of Rutter and Chalmers (1953). The cell width is inversely proportional to R since the rate of movement of the interface governs the time allowed for the diffusion of solute which must be redistributed to produce a stable cellular interface. The cell width is inversely proportional to G since the temperature gradient governs the extent to which the cell projects into the liquid. The further does the cell project into the liquid the greater is the lateral diffusion gradient of solute, so that the solute can diffuse further in the time allowed for redistribution. The longer is the projection, the wider can it be and still redistribute the solute. Therefore, since the length of the projection is inversely proportional to G, then so also is the width.

It was observed that the size and shape of the cells bear a marked dependence upon the orientation of the interface. This anomalous effect is probably dependent upon the interfacial energy of the particular orientation considered.

Rutter and Chalmers (1953) have shown that if crystals having their dendrite axis at an angle to the growth direction are grown under conditions which fall in the middle of the cellular range, then the corrugations align themselves in the growth direction. However, if the growth conditions are made more severe, the corrugations try to align themselves along their dendrite direction. This same observation was made in the present investigation. As the conditions approach the upper limit of the cellular range, the cells become asymmetrical on the interface and the projections exhibit an axis which appears to be the dendrite axis of the crystal making an angle to the interface normal. The traces of these inclined projections on the upper surface of the crystal (Fig. 27) further substantiate the observation that the cellular shape for crystals having nondendritic orientations is asymmetrical with respect to the interface normal. It is probably this asymmetrical shape of the cell that makes it unstable and break down to dendrites before the symmetrical cell. It is very likely that the intercell region, because of its asymmetry, becomes unstable for the same reasons but under less severe conditions than for the symmetrical intercell region.

Breakdown of a Cellular Interface to a Dendritic Interface

Figure 8 shows that the lower and upper breakdown curves are linear when plotted in the form

$$C_0 = B'(G/R^{\frac{1}{2}}), \qquad C_0 = B''(G/R^{\frac{1}{2}})$$

where B' and B'' are the proportionality constants. Therefore,

(i) if $G/R^{\frac{1}{2}} > C_0/B'$, the interface is completely cellular;

(ii) if $C_0/B' > G/R^{\frac{1}{2}} > C_0/B''$, the interface of a polycrystalline sample will exhibit cells and dendrites;

(iii) if $G/R^{\frac{1}{2}} < C_0/B''$, the interface is completely dendritic.

It has been shown that both increasing the solute concentration in the melt and decreasing the temperature gradient tend to lengthen the projections on the cellular interface. It has also been shown that increasing the rate of growth tends to decrease the cell width. Therefore, by decreasing the gradient and increasing both the rate of growth and the solute concentration the depth to width ratio of the cells can be increased. It is immediately apparent that the further the projections extend ahead of the rest of the interface, the more solute will there be at the base, and therefore the greater will be the chance that it will become constitutionally supercooled. This effect is enhanced by the fact that the longer the cells become with respect to the width the more will the isotherms become distorted in this intercell region. It must be remembered that latent heat is being evolved at the surface of the cell as solidification proceeds. Some of this heat will diffuse to the intercell region and tend to flatten the temperature gradient. Both of these effects will tend to produce constitutional supercooling in this intercell region. The cells cannot decrease in width to lower the concentration at the base of the cells, and thus eliminate the instability, because this would only produce a greater instability. When constitutional supercooling is produced in this region the cellular interface will be unstable. This instability will reach a critical value for a certain ratio of depth to width of the cell, thus causing the onset of dendritic growth as was observed. If C_0 is increased the projection will become longer as well as wider. It was observed that the increase in projection length is much greater than the increase in cell width; therefore, for the same G and R the ratio depth/width of the cell increases with C_0. This indicates that as C_0 is increased the ratio $G/R^{\frac{1}{2}}$ does not need to be as great to produce breakdown as was observed experimentally.

These results can be compared with the work of Morris *et al.* (1955) on the same system. They studied the breakdown from cells to dendrites by observing the conditions under which the corrugations in the upper surface began to develop noticeable side-branches. They observed only the upper surface, and considered only corrugations which ran parallel to the axis of the crystal, so that they were effectively observing the upper breakdown limit. Their results were plotted as the ratio G/R with the emphasis being placed on this ratio rather than the parameter $G/R^{\frac{1}{2}}$ as was observed in this investigation. However, as was observed during the course of this investigation, the observations of the upper surface provide a much coarser criterion for interface instability than observations of the interface itself. For this reason the half power dependence of the rate of growth could not probably have been deduced. If the results of Morris *et al.* are plotted as C_0 versus $G/R^{\frac{1}{2}}$ they produce a wide scatter about the upper breakdown limit. It can be said, therefore, that there is no real disagreement between the results of these workers and of the present investigation. The present investigation provides a much more

complete, and therefore more accurate, study of the instability of a cellular interface.

It can be concluded from this work that the phenomena associated with the solidification of a binary alloy are essentially caused by interactions between the three important variables of growth. The crystallographic variable is seen to increase in importance from an insignificant effect for a macroscopically smooth interface to a very pronounced effect for the onset of dendritic growth, whereas the temperature distribution and the solute distribution have a pronounced effect throughout.

ACKNOWLEDGMENTS

The authors gratefully acknowledge the financial assistance of Canadian Patents and Development Ltd., and the National Research Council of Canada, throughout the course of this work.

APPENDIX I

It is of interest to be able to grow crystals at a constant rate R under a constant temperature gradient G_L in the liquid by lowering the temperatures of the coils 1 and 2 shown in Fig. 2(*a*) at specified rates. The gradients in the solid and the liquid at the interface must be maintained constant during growth for this to occur. Consider the following schematic diagram:

$$\begin{array}{ccccc} I & \overset{x}{} & I & \overset{y-x}{} & I \\ \hline T_2 & & T_M & & T_1 \end{array}$$

where T_1 is the temperature of coil 1,
T_2 is the temperature of coil 2,
T_M is the temperature of the interface,
x is the distance of the interface from the beginning of the specimen,
y is the total length of the charge, solid and liquid.

From the diagram it can be seen that

$$G_L = (T_1 - T_M)/(y-x) \text{ and } G_S = (T_M - T_2)/x.$$

It can be seen that for a constant rate of growth, $x = Rt$. Therefore,

$$T_1 = T_M + G_L(y - Rt),$$

$$T_2 = T_M - G_S Rt.$$

The continuity of heat flow must satisfy Eq. 3 at the interface; i.e.,

$$K_S G_S - K_L G_L = L\rho R \qquad \text{at the interface.}$$

Therefore $$G_S = (L\rho R + K_L G_L)/K_S$$

and $$T_2 = T_M - L\rho R^2 t/K_S - K_L G_L Rt/K_S.$$

To find the rate at which T_1 and T_2 must decrease in order to have a constant G_L and a constant R it is only necessary to differentiate T_1 and T_2 with respect to time. Therefore, in order to solidify a crystal at a constant

rate R, under a constant temperature gradient G_L, the temperature of coils 1 and 2, respectively, must decrease at the following rates:

$$dT_1/dt = -G_L R,$$

$$dT_2/dt = -G_S R = -(L\rho R^2/K_S + K_L G_L R/K_S).$$

REFERENCES

BLAHA, F. 1955. Metall, **9**: 390.

CHALMERS, B. 1953. Can. J. Phys. **31**: 132.

——— 1954. Trans. Am. Inst. Mining Met. Engrs. **200**: 519.

ELBAUM, C. and CHALMERS, B. 1955. Can. J. Phys. **33**: 196.

JOST, J. 1952. Diffusion. Academic Press, Inc., New York. p. 479.

MORRIS, W., TILLER, W. A., RUTTER, J. W., and WINEGARD, W. C. 1955. Trans. Am. Soc. Metals, **47**: 463.

PFANN, W. 1952. Trans. Am. Inst. Mining Met. Engrs. **194**: 747.

ROSENBERG, A. and WINEGARD, W. C. 1954. Acta Metallurgica, **2**: 342.

RUTTER, J. W. and CHALMERS, B. 1953. Can. J. Phys. **31**: 15.

SMITH, V. G., TILLER, W. A., and RUTTER, J. W. 1955. Can. J. Phys. **33**: 723.

STEWART, M. T., THOMAS, R., WAUCHOPE, K., WINEGARD, W. C., and CHALMERS, B. 1951. Phys. Rev. **83**: 657.

TILLER, W. A. 1953. M.A.Sc. Thesis, University of Toronto, Toronto, Ont.

——— 1955. Ph.D. Thesis, University of Toronto, Toronto, Ont.

TILLER, W. A., JACKSON, K. A., RUTTER, J. W., and CHALMERS, B. 1953. Acta Metallurgica, **1**: 428.

WAGNER, C. 1954. Trans. Am. Inst. Mining Met. Engrs. **200**: 154.

WALTON, D., TILLER, W. A., RUTTER, J. W., and WINEGARD, W. C. 1955. Trans. Am. Inst. Mining Met. Engrs. **203**: 1023.

WEINBERG, F. and CHALMERS, B. 1951. Can. J. Phys. **29**: 382.

OBSERVATIONS ON STARS AND HEAVY PRIMARIES RECORDED IN EMULSIONS FLOWN IN VIKING ROCKET NO. 9 [1]

By Herman Yagoda

ABSTRACT

Methods for the preparation of fresh nuclear emulsions for use in the study of cosmic radiation by rocket exposures are described. Shattering and mechanical damage is minimized by substituting transparent plastics for the glass support. By casting the emulsion on a temporary microporous medium such as plaster of Paris, emulsions 2 mm. thick can be dried in about six days without appreciable loss of sensitivity. Strong, thin-walled housings for the emulsions are described. The star production rate in emulsions flown in the mesosphere to a peak altitude of 217 km. is 1180 ± 280 cc.$^{-1}$ d.$^{-1}$ and is 1.45 ± 0.17 times greater than similar measurements in the stratosphere (30 km.). The augmentation of nuclear disintegrations can be accounted for by the opening up of the effective solid angle for star-producing radiation during the rocket flight. Energetic stars with three or more shower particles record with a frequency of 278 ± 30 cc.$^{-1}$ d.$^{-1}$, about three times greater than in a balloon flight at the same geomagnetic latitude. For large showers $N_s = 6$, the N/P ratio is about 0.17. The observational ratio of M to H nuclei based on a spectrum of 238 heavy primary tracks is 2.6$_4$. When corrected for fragmentation in surrounding matter this ratio is reduced to 2.5 ± 0.5. The omnidirectional flux of heavy primaries $Z \geqslant 6$ at the top of the atmosphere is 7.62 meter^{-2} sec.$^{-1}$ sterad.$^{-1}$. An analysis of the zenith angle distribution of the heavy primaries shows that the unidirectional flux is in fair agreement with geomagnetic theory for zenith angles $< 60°$. The directional flux for $\theta > 60°$ is about two times greater than predicted by theory.

I. INTRODUCTION

High altitude rockets have been employed extensively in the study of cosmic radiation above the sensible atmosphere, employing telemetering systems for transmitting the data during flight to ground level receiving stations (Newell 1953). The counter telescopes, usually sensitive over a small solid angle, provide poor statistics during the brief period of high altitude flight, and the complex apparatus must be considered of an expendable nature. While nuclear emulsions would appear ideal for these studies because of their small weight, large sensitive volume, and their ability to record tracks incident from all directions, comparatively little work has been done with them, largely because of the necessity of physical recovery of the emulsions after flight termination.

Following the first recovery of plates from a V-2 rocket (Yagoda *et al.* 1950) a series of successive failures were encountered which terminated with the firing of Aerobee NRL-10 on May 5, 1952. Study of the emulsion recovered from this flight (a 2050 μ thick, 7 cm. disk made from Ilford G5 gel) showed a star intensity of 4800 ± 100 cc.$^{-1}$ d.$^{-1}$ ($\geqslant 3$ prongs) and the passage of nine heavy primary nuclei.

This experiment suggested that by the recovery of larger areas of emulsion important information could be secured on the charge spectrum of the heavy primaries reaching the top of the atmosphere, and that possibly definitive evidence could be secured for the abundance of lithium, beryllium, and boron

[1]Manuscript received August 9, 1955.
Contribution from the National Institutes of Health, Bethesda, Maryland, U.S.A.

nuclei in the primary beam. It was also difficult to reconcile the high intensity of stars recorded in the mesosphere, about six times greater than that observed in stratosphere balloon flights conducted at the same geomagnetic latitude, with theoretical expectations.

A shortcoming of the nuclear emulsion in brief rocket exposures is its continuous sensitivity between manufacture and development. The rocket flight time of about seven minutes' duration is an insignificant fraction of the total sensitive age which usually exceeds three weeks if the plates are manufactured abroad. For certain phenomena, such as heavy primary tracks and large shower stars, the accumulated low altitude background does not interfere with the measurements. The low energy star background is greatly reduced by preparing the emulsions at the launching grounds shortly before flight. This could be done in conjunction with the launching of Viking rocket No. 9 from White Sands, New Mexico, on December 15, 1952.

II. EXPERIMENTAL

The emulsions were prepared from Ilford G5 gel flown to the launching area in paper-insulated containers which kept the temperature below 20°C. At the elevation of White Sands (1230 meters, $\lambda = 41°$ N.) the star-producing radiation is about three to four times greater than at sea level. In order to reduce the background during the drying of the plates, the darkroom was located in the basement of a massive concrete building. While awaiting flight, measurements were made of star production in the darkroom and in free air outdoors. The respective rates were 1.05 ± 0.33 and 2.64 ± 0.34 stars cc.$^{-1}$ d.$^{-1}$ at the two localities[2] showing that the heavy building served to attenuate the star-producing radiation by a factor of about 2.5.

When the plates were dry—two to six days, depending on thickness—the loaded cameras were stored in the control room adjoining the launching platform. This is a very massive structure of concrete and steel for which the average absorption length is estimated at 1800 gm. cm.$^{-2}$. Under 2000 gm. cm.$^{-2}$ of clay George and Evans (1951) observed the formation of 0.0066 stars cc.$^{-1}$ d.$^{-1}$ at $\lambda = 55°$ N. This figure, normalized to the ratio of star rates above the absorber, suggests that the star production rate in the control room was of the order of 0.015 cc.$^{-1}$ d.$^{-1}$.

Preparations intended for use at ground level were coated on subbed-glass secured from Ilford Ltd. The preweighed glass was mounted to a circular plastic frame lubricated with a thin film of Dow-Corning Silicone stopcock grease. The molds were leveled and filled with molten gel at 50 ± 3°C. taking care to remove air bubbles by pouring through several folds of moist cheesecloth. When set the molds were covered with a 1.5 mm. thick rigid sheet of plaster of Paris and dried by circulating air at 50% R.H. When nearly dry the molds were taken apart and the plates stored above potassium carbonate

[2]This free air exposure can be compared with an independent measurement (Pomeroy 1951) made at Albuquerque, New Mexico, at an elevation of 1580 meters. Pomeroy found the intensity of stars ($\geq$ 5 prongs) to be between 1.31 and 1.21 cc.$^{-1}$ d.$^{-1}$ after correction for accumulated background. On the same basis our White Sands measurements correspond to 1.25 ± 0.23 cc.$^{-1}$ d.$^{-1}$.

in equilibrium with its saturated solution until they reached constant weight, ±0.1 gm. This procedure not only reduces background by eliminating the high-altitude airplane flight from England, but also provides a precise measure of the quantity of emulsion deposited. For computing the volume and thickness of the coatings a density of 3.80 gm. cm.$^{-3}$ was employed, based on experimental measurements on emulsion dried under the above conditions.

Several of the glass-coated preparations were flown as glass-to-glass sandwiches together with a thick film of Duco cement. This procedure increases the rigidity of the unit and the flexible bonding possibly reduced shattering. One of these "safety-glass" emulsions was recovered in perfect condition, and in a second, while the glass shattered, the emulsion coatings were intact. In general, it is best to avoid the use of glass backings and to coat the emulsion on transparent plastics. Disks of Lucite or Plexiglass are cut to fit the camera (Fig. 1), are degreased with carbon tetrachloride and washed in a warm

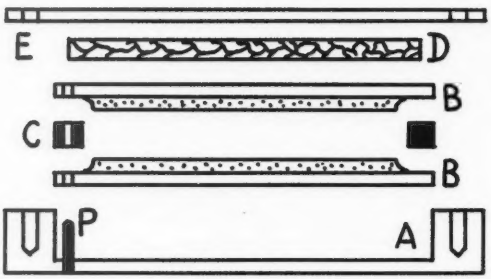

FIG. 1. Cross-sectional view of two-plate rocket camera.

A. Bottom cup machined from a solid disk of Dural alloy 0.5 in. thick, provided with a steel centering pin P. B. Subbed lucite carrying emulsion layers. C. Bakelite spacer ring. D. Layer of sponge rubber. E. Aluminum cover secured to cup A by means of machine screws.

detergent until the surface loses its water repellency. The disks are rinsed in distilled water and dipped in a freshly prepared 2% solution of gelatin in water at 40°C. When dry the "subbed-plastic" is attached to the mold with the aid of Dow-Corning Silicone stopcock grease and filled with molten gel. This subbing procedure permits the emulsion to dry uniformly without appreciable lateral creep for preparations whose final thickness is less than 600 μ. The adherence of the coating is nonpermanent. The emulsion coating usually separates as a result of impact of the instrument section. If still found adhering, the emulsion disk is readily separated by flexing the lucite, or by drying the emulsion above a desiccant.

For the preparation of emulsion disks whose thickness is $\geqslant 1000\ \mu$ we employ microporous sheets of plaster of Paris as the supporting base. This novel medium has the advantage that the gel can dry rapidly through both the upper and lower interface, thereby preserving the sensitivity of the gel which ordinarily tends to deteriorate during long drying periods at 25° to 28°C. Also.

after high speed impact of the instrument section, the plaster appears to take the shock of landing, and the pulverized base, unlike shattered glass, does not cut into or damage the emulsion. Residual adhering plaster, being slowly water soluble, is readily removed during the early stages of photographic processing.

The plaster supports are prepared in a mold composed of two sheets of plate glass separated by an aluminum frame 3 mm. thick in which a hole 102 mm. in diameter is machined with slightly tapering walls. Forty grams of plaster of Paris is added to 32 cc. of 25% ethyl alcohol contained in a 100-cc. beaker to which a drop of aerosol wetting agent has been added. This is mixed thoroughly and air bubbles which reach the surface are destroyed by directing a stream of ether vapor from an inverted wash bottle. The alcohol increases the setting time, permitting opportunity for the ascension and destruction of occluded air. When the mix reaches the consistency of sour cream it is transferred to the mold aiming for a cone-like deposition. The second plate glass is placed on the apex of the cone and is gently depressed until it reaches the aluminum frame. The plaster is allowed to set (two to three hours) with the upper glass weighted down with a 1 kgm. mass. When completely dry the plaster disk is subbed by immersion in a solution containing 2% gelatin and 0.1% glycerin by weight at 40°C. It is dried to constant weight at a relative humidity of about 50%. The plaster disk is attached to the lucite-ring mold by means of molten paraffin wax.

For purposes of high altitude exposure the emulsions must be placed in a light-tight housing sufficiently strong to withstand stresses accompanying the impact of the instrument section.[3] Part of the damage is secondary in character and is caused by direct hits of instruments torn loose from their mountings. The shock of landing per se does not appear to augment fog or weaken the latent image. If recovery of the instrument section is delayed, a fading of the latent image occurs, accelerated by the high temperature prevailing in the desert. In order to minimize fading by hydrogen peroxide vapors the aluminum alloy cameras are coated with a film of paraffin wax, and all direct metal-to-emulsion contacts are avoided.

Cameras with the greatest life-expectancy must have one member designed to withstand large stresses, such as by the incorporation of a thick I-beam or ring-structure. The main features of the latter are shown in Fig. 1. The basic design can also be modified to house rectangular emulsion sheets by suitable machining of a thick slab of aluminum alloy (Dural 24 ST). These housings introduce about 1 gm. cm.$^{-2}$ absorber. The absorber can be reduced to 0.2 gm. cm.$^{-2}$, with an increased risk of mechanical damage, by taping the emulsion to the rocket skin as described in Fig. 2. The isothermal processing procedure for the development of 1.5–2 mm. thick emulsions (Yagoda 1955) was employed on all the emulsions recovered.

[3]The impact velocity is reduced to about 300 mi. per hr. by severing the instrument section from the main body by means of a timed explosive charge when the descending vehicle is at about 40 miles altitude (Rosen *et al.* 1954).

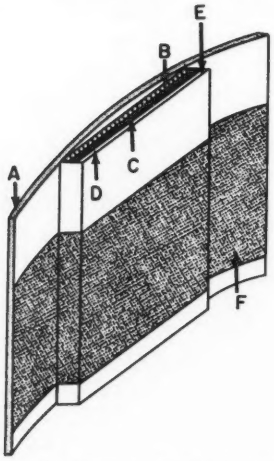

FIG. 2. Method for mounting emulsions on Rocket skin for cosmic-ray exposures with a minimum of absorber.

A. Rocket skin. B. Corrugated paper cardboard. C. Emulsion wrapped in black paper and water-impervious "Parafilm". D. Plastic backing plate, 1.5 mm. thick lucite. E. Layer of white rubberized adhesive tape surrounding B–C–D. F. Layer of rubberized "Mystic-Tape" for securing unit to inside rocket skin.

III. FLIGHT CHARACTERISTICS

While the flight of a high altitude rocket is brief as compared with a stratosphere balloon exposure, the characteristics of the essentially parabolic trajectory can be established with a high degree of precision. For purposes of comparing intensities of cosmic radiation in the mesosphere with those available from measurements in the stratosphere, it is convenient to consider the portion of the rocket trajectory AKB of Fig. 3 when the vehicle is above 30 km. The time interval AB then constitutes the duration of the mesosphere cosmic-ray exposure, which for this flight is 407.5 ± 1 sec.

The intensity of events, such as cosmic-ray stars, produced during the mesosphere exposure is secured by the difference in population of equal volumes of flown and control emulsions of identical age and history. This differential has to be corrected for stars accumulated by the flown material while it is ascending to and falling from the 30 km. level. These corrections are computed by a graphical integration of OA and BP with the aid of a function of star production at a given elevation, I, with atmospheric depth, x. For the White Sands region, $\lambda = 41°$ N., our measurements indicate that in G5 emulsions star production is adequately expressed, for correction purposes, by the equation

$$I = 890\, e^{-x/150}. \tag{1}$$

The correction for the ascending limb OA is straightforward as path OA is usually known precisely from telescopic and radar measurements. For Viking 9 this correction is 0.15 stars (>3 prongs) cc.$^{-1}$. With the aid of a drag curve secured on the fall of V-2 No. 49 it is estimated that 0.29 stars cc.$^{-1}$ accumu-

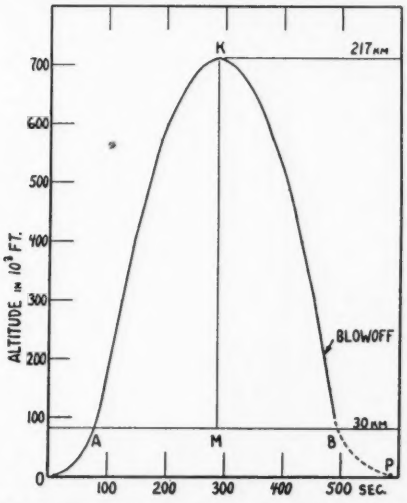

FIG. 3. Time–altitude trajectory of Viking No. 9.

lated during the descent of the instrument section over path BP. The total ascent and descent correction employed is 0.45 ± 0.1 stars cc.$^{-1}$.

The control plates remain at the launching site and the flown material resides at the impact point until recovery is effected. If the two points differ in elevation a third correction is necessary. This can be computed from the difference in atmospheric depth between the impact and launching points and the elapsed time. If O and P differ by ± 300 meters, then the corrections as evaluated from Eq. (1) are -0.56 and $+0.24$ cc.$^{-1}$ d.$^{-1}$, respectively. In the present exposure the impact point was only 33 meters below the elevation of the launching area and since recovery was effected in less than 10 hr., this correction was found to be too small to warrant application.

IV. STAR PRODUCTION IN THE MESOSPHERE

The emulsions were scanned with a $22\times$ Leitz oil immersion objective and $10\times$ wide field oculars allowing a 25% field overlap between successive traversals. Since the population of stars and tracks was small, it is believed that a detection efficiency close to 100% was achieved. The flown and the control emulsions were scanned by the same observer, using the identical criteria for small star acceptance.

A comparative histogram of the star-size distribution in the flown and control group of five-day-old emulsions is shown in Fig. 4. Stars of a given number of black and gray tracks N_h are further differentiated into:

(a) shower tracks ($\leqslant 1.5$ minimum) absent,

(b) stars having at least one minimum ionization track,

(c) stars initiated by a charged primary and exhibiting a shower of $\geqslant 3$ minimum ionization tracks.

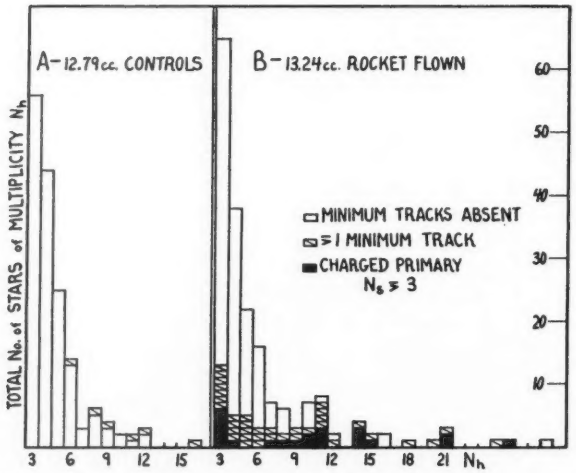

FIG. 4. Comparative histograms of star size distribution on flown and control emulsions. The control histogram A is composed of background stars recorded in 3.88 cc. of the α-group of emulsions, 7.65 cc. of the β-group, and 1.26 cc. of emulsion exposed in the darkroom at White Sands. The rocket-exposed histogram B is based on observations in 13.24 cc. of freshly made emulsion (α-group).

The rocket-flown emulsions are characterized by a large fraction of (*b*) and (*c*) stars, and a pronounced tail of high energy stars of $N_h > 15$.

The relative position of the emulsions is shown in Fig. 5, and Table I summarizes the star populations observed in the several preparations of similar age and position. This study shows an essentially uniform star produc-

TABLE I

VARIATION OF STAR DIFFERENTIAL WITH POSITION IN ROCKET

Position	Star count	Emulsion vol., cc.	Stars, $cc.^{-1}$	Differential between flown and controls	
				ΔP observed	ΔP corrected
α-Controls	34	3.88	8.75±1.5*	—	—
No. 69 at 97 in.	48	3.44	13.95±2.0	5.20±1.7†	4.75±1.5
Nos. 57, 70, 71, and 72 at 64 in.	95	6.43	14.78±1.5	6.03±1.4	5.58±1.3
Nos. 63, 64, 65, 66 at 97 in.	47	3.37	13.92±2.0	5.17±1.7	4.72±1.5
No. 61 at 450 in.	92	5.85	15.72±1.6	6.97±1.5	6.52±1.4
Average all α-emulsions	282	19.09	14.76±0.9	6.01±1.6	5.56±1.4

*The errors are statistical based on the square root of the star counts.

†The probable error in the estimation of the differential star population ΔP was estimated as

$$\pm 0.67(\Delta P)[(S_r+S_c)\bar{v}]^{\frac{1}{2}}/(S_r-S_c)\bar{v}$$

where $\bar{v}$ is the average of the volumes of rocket and control emulsions scanned and S_r and S_c represent the star populations per unit volume in the exposed and control preparations, respectively.

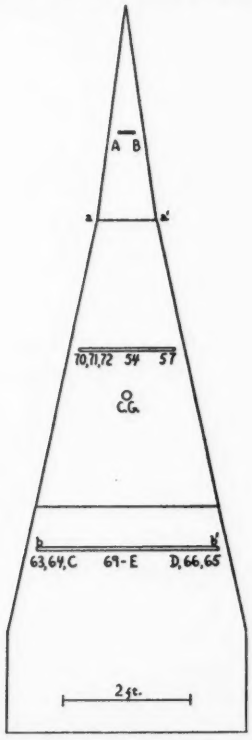

FIG. 5. Relative disposition of emulsions in upper instrument section of Viking No. 9. All cameras were mounted vertically in close proximity to the rocket skin, which measured 0.040 in. of Al above line *aa'*, and 0.050 in. in the section below it. The total mass above line *bb'* is estimated to be 304 lb. with its center of mass located 29.3 in. above *bb'*. These emulsions can be considered to be embedded in a spherical space equivalent to the volume of the cone containing an average density of 0.21 gm. cm.$^{-3}$ of absorber and an average absorption path of 11.5 gm. cm.$^{-2}$. Emulsions No. 61 and F were mounted near the motor section about 450 in. below the rocket tip in the vicinity of about 1500 lb. of metal.

tion rate at all levels of the instrument section. Preparation No. 61 located near the motor section in close proximity to large masses of metal shows a somewhat higher star intensity. Within the limits of the statistical uncertainty all four estimates in Table I are consistent with an average value of ΔP, corrected for rise and fall to the 30 km. level, of 5.56 ± 1.30 cc.$^{-1}$. On the basis of a flight time of 407 sec. above 30 km., this differential corresponds to an average star production rate in the mesosphere of 1180 ± 280 cc.$^{-1}$ d.$^{-1}$. Two independent measurements secured from preparations which had aged while awaiting flight of the vehicle (exposures β and γ of Table II) are in fair agreement with this estimate.

The several rocket and balloon flights made at geomagnetic latitude 41° N. are compared in Table II. While the rocket exposures yield a consistently

TABLE II

COMPARISON OF ROCKET AND BALLOON FLIGHT STAR INTENSITIES AT $\lambda = 41°$N.

Vehicle	Date	Altitude in km.		Exposure, sec.	Star intensity, cc.$^{-1}$ d.$^{-1}$
		Max.	Av.		
Rocket exposures at White Sands, New Mexico					
V-2 No. 49	9-29-49	150.7	80.4	324	5420±1300*
Aerobee 10	5-5-52	128.3	65.4	287	4800±1000
Aerobee 13	2-12-53	137.0	71.3	300	4460±1200
Viking 9 α	12-15-52	217	124	407	1180±280
β					1070±300
γ					1240±450
Balloon exposures at Pyote, Texas					
732	3-27-52	33.1	32	22,800	950±90
738	5-8-52	30.2	29	26,600	610±42
740	5-22-52	31.0	30	19,800	930±73
879	8-29-52	30.6	30	31,800	760±60
337 W†	1-31-54	~32	31	~21,600	824±50
Average balloon flight					815±104

*The original value of 5000±800 stars cc.$^{-1}$ d.$^{-1}$ cited by Yagoda *et al.* (1950) has been revised to conform to a more accurate time–altitude trajectory for the flight.

†Launched from Goodfellow Air Force Base, San Angelo, Texas. The geomagnetic latitude of this locality is estimated at $\lambda = 40° 37'$ N.

higher star intensity than the balloon observations, the three rocket flights are not in good agreement with each other. The deviations among the rocket estimates may originate from the following factors:

(1) Errors inherent in securing the differential ΔP when the absolute star population in the control plate is high and the volume scanned is relatively small. A two-fold deviation in the magnitude of ΔP appears frequently in individual plates of small volume. This sampling uncertainty may be responsible for the high values indicated by the V-2 No. 49 and Aerobee No. 10 flights. The emulsions exposed on Aerobee No. 13 were manufactured in England and accumulated a large background of 74.7±4.1 stars cc.$^{-1}$ at the time of development which made the determination of ΔP especially difficult.

(2) The instrument section of the Aerobee rocket is small and heavily loaded with equipment. Hence emulsions exposed in close proximity to the high density of matter in the Aerobees are more apt to receive secondary star-producing radiation than those exposed in the spacious Viking.

(3) The sampling time of rocket flights is brief and individual readings may possibly reflect fluctuations in the flux of star-producing radiation reaching the top of the atmosphere.

Comparing the Viking star intensities with balloon observations at about 30 km. indicates that a ratio of 1.45±0.24 between the mesosphere and the stratosphere exposures is observed. This increment largely originates from the following factors:

(1) from the opening of the solid angle within which star-producing radiation can reach the emulsion,

(2) from secondary radiation impinging on the detector from matter within the instrument section,

(3) from albedo particles originating in the heavy motor section and reflected upwards into the emulsions some 40 ft. above.

The star increment ΔP secured from the Viking No. 9 observations can be employed to estimate the flux of the star-producing radiation I_s^0 if we assume that the range of the star-producing radiation in emulsion λ is of the same magnitude as observed in condensed matter such as ice (Harding *et al.* 1949) or aluminum (Bernardini *et al.* 1949) $\lambda \simeq 200$ gm. cm.$^{-2}$, and ignore transition effects:

$$\Delta P = \rho\Omega I_s^0/\lambda. \tag{2}$$

I_s^0 is estimated to be 0.12 ± 0.03 cm.$^{-2}$ sec.$^{-1}$ sterad.$^{-1}$ using $\rho = 3.8$ gm. cm.$^{-3}$ and $\Omega = 6.2$ steradians. This flux can be interpreted as an average unidirectional flux, and as such can be compared with the average unidirectional flux of 0.131 ± 0.005 cm.$^{-2}$ sec.$^{-1}$ sterad.$^{-1}$ measured in counters flown above the atmosphere in rockets by Van Allen (1953) and Gangnes *et al.* (1949). For zenith angles $\leqslant 63°$ Perlow *et al.* (1952) reports a lower value for the average flux of $0.079\pm.005$ cm.$^{-2}$ sec.$^{-1}$ sterad.$^{-1}$. The close agreement of the flux magnitude, as evaluated from the present emulsion study, with the rocket counter measurements is a further confirmation that $\Delta P = 5.56\pm1.30$ cc.$^{-1}$ represents the correct or normal value and that the higher estimates secured on the early V-2 and Aerobee rocket exposures may be erroneous or represent abnormal fluctuations.

V. STAR AUGMENTATION MECHANISM

The effective solid angle $\bar{\omega}$ of incident radiation of mean free path λ reaching the detector located at an atmospheric depth x can be computed from the Gross transformation:

$$\bar{\omega}(x) = \frac{\int J(x,\theta)\, d\omega}{J_v(x)} = \frac{2\pi\epsilon_1(x/\lambda)}{e^{-x/\lambda}} \tag{3}$$

where the exponential integral $\epsilon_1(x) = x\int_x (e^{-s}/s^2)\, ds$ is evaluated by Rossi (1952). Since the vehicle is constantly altering the altitude of the detector an average solid angle for the entire flight $\Omega_{(\lambda)}$ above 30 km. is computed by a numerical integration of the time–altitude trajectory in terms of $\bar{\omega}$.

The variation of $\bar{\omega}$ with atmospheric depth (in units of x/λ) is shown in Fig. 6. The circles indicate independent estimates of $\bar{\omega}$ made from the experimental rocket measurements of air masses m as a function of zenith angle θ reported by Pressly (1953). These were computed by a numerical integration of

$$\bar{\omega} = \int_0^{\pi/2} \sin\theta\, e^{-m(\theta)/\lambda} d\theta \Big/ e^{-m_0/\lambda} \tag{4}$$

where m_0 is the air mass from the vertical at a fixed altitude. The two methods are in good agreement, but the direct air mass measurements yield a solid angle about three per cent greater than estimated by the Gross transformation. The difference originates because in $x = x_0/\cos\theta$, $x \to \infty$ as $\theta \to \pi/2$, whereas observationally $m \doteq x$ assumes a large but finite value.

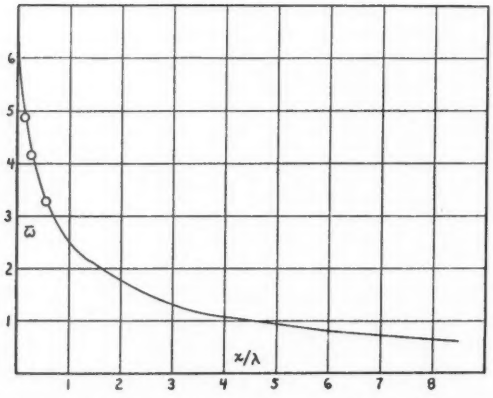

FIG. 6. Variation of effective solid angle $\bar{\omega}$ in steradians as a function of x/λ.

The variation of $\bar{\omega}$ during the flight of Viking 9 is shown in Fig. 7 as computed for a collision mean free path of high-energy nucleons in air of 110 gm. cm.$^{-2}$. The value of Ω_{110} for the rocket flight above the 30 km. level is 6.22 steradians, whereas the effective solid angle subtended by emulsions in a balloon flight at about 30 km. is 4.83 steradians. We can therefore anticipate a star augmentation of $6.22/4.83 = 1.29$ as a result of the greater number of cosmic-ray primaries reaching the rocket plates. The measured ratio of star intensities for the two exposures is $1180\pm280/815\pm104 = 1.45\pm0.17$. The close agreement between these ratios, on the basis of the above simple model, indicates that the greater part of the measured ΔP value originates from primary radiation and that only about 10 per cent of ΔP is attributable to secondary star-producing radiation created in the rocket body and to albedo effects. Measure-

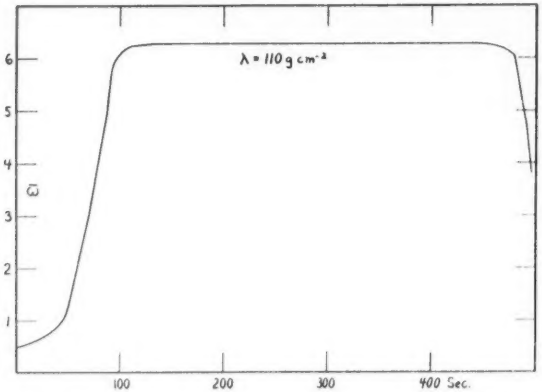

FIG. 7. Variation of effective solid angle for the star-producing radiation with time after launching of Viking rocket No. 9.

ments of the albedo (Winckler and Anderson 1954) at $\lambda = 40°$ N. indicate that it is not more than five per cent of the incident flux for particles of $\beta > 0.7$ in any upward direction.

VI. SHOWER STARS

As shown in Fig. 4 large shower stars $N_s \geqslant 3$ are virtually absent in the control plates and constitute 1.31 cc.$^{-1}$ of the fresh rocket exposed emulsions. It is therefore reasonable to assume that this category of stars recorded during the high altitude flight of the vehicle, and that their frequency, will be largely independent of the age and low-altitude history of the plates. A total of 87 shower stars were observed in the scanning of 66.3 cc. of flown emulsion. Their distribution according to shower size and the charge of incident particle is shown in Fig. 8. Collectively, these energetic stars are produced in the

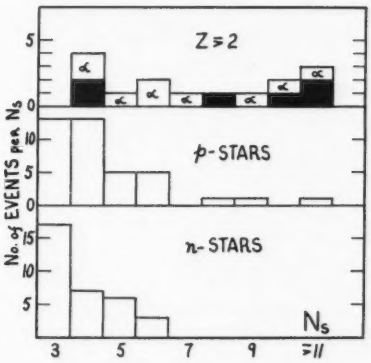

FIG. 8. Histogram of shower stars as a function of number of shower particles, N_s. The stars are classified in accordance with the nature of the particle initiating the disintegration. The black blocks represent events initiated by heavy primary nuclei $Z \geqslant 6$ from which three or more singly charged minimum ionization particles emerge.

mesosphere with a frequency of 278 ± 30 cc.$^{-1}$ d.$^{-1}$. About 25 per cent of these stars are jets associated with four or less gray and black tracks ($N_h \leqslant 4$), a typical example of which is illustrated in Fig. 13.

For comparative purposes, a 2.90 cc. volume of emulsion flown in the stratosphere (Flight 337 W, Table II) was carefully examined for shower stars using the same acceptance criteria as in the examination of the rocket plates. These occurred with a frequency of 91 ± 11 cc.$^{-1}$ d.$^{-1}$, indicating that stars with $N_s \geqslant 3$ record about three times more frequently in the rocket than in the balloon exposure. It is noteworthy that this increment cannot be explained in its entirety by the increase in the effective solid angle at rocket elevations. The large effect may originate from the small sample of comparative shower stars available from the Texas balloon flight. The discrepancy is diminished by comparing with the Bristol data (Fig. 9) which are of greater statistical significance (Camerini *et al.* 1951).

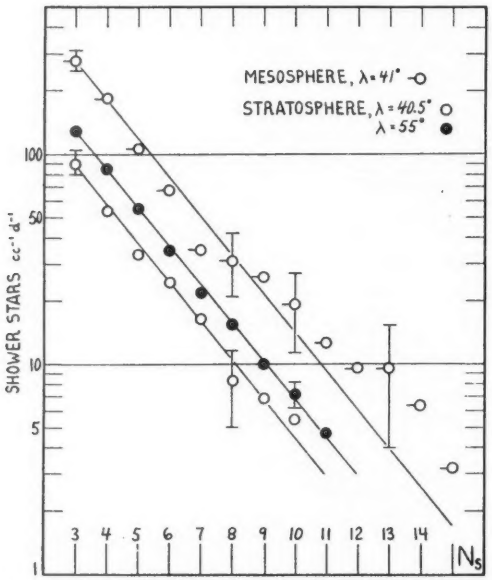

FIG. 9. Integral shower size distribution for shower stars with $N_s \geqslant 3$ as a function of the number of shower particles, N_s.

VII. THE NEUTRON–PROTON RATIO

Owing to their instability, it is not likely that an appreciable flux of neutrons enters the top of the atmosphere. However, a high ratio of neutron to proton induced stars has been observed even at the highest altitudes reached by balloons. Since it is known that the incident primary radiation is composed predominantly of charged particles, this implies that the observed neutron component must be created locally at an exceedingly rapid rate. It is therefore of interest to compare the N/P ratio (we define P as a star initiated by a charged primary of $Z \geqslant 1$ associated with three or more shower particles) observed in Viking 9 exposure with available data at balloon elevations.

The data summarized in Table III indicate that the N/P ratios for the rocket and balloon exposures at $\lambda = 41°$ N. are indistinguishable within the

TABLE III

VARIATION OF THE N/P STAR RATIO WITH ELEVATION

Exposure	Maximum altitude, km.	λ	Integral value of N/P ratio	
			$N_s \geqslant 3$	$N_s \geqslant 5$
Viking 9	217	41° N.	0.61±0.14	0.38±0.15
337 W	~31	40.5° N.	0.50±0.09	0.32±0.15
Camerini *et al.* (1951)	~21	~55° N.	0.35	0.30
Engler and Haber-Schain (1954)	~30	~55° N.	—	0.14

limits of statistical error. The lowest N/P ratio reported is that of Engler and Haber-Schain (1954) who limited the observations to primaries of high energy (65 Mc^2) with $N_s \geqslant 5$. The large number of neutron induced shower stars observed in the rocket flight can be attributed to the large mass of associated instrumentation (~300 lb.) in proximity to the emulsions. The present data (Fig. 8) indicate that the N/P ratio diminishes with increasing N_s, and that when $N_s \geqslant 6$, the ratio is 0.17 for the rocket exposure. A further discussion of this ratio is best postponed until the data on Viking 10 become available. In this flight the emulsions were exposed in the very tip of the rocket with only the rocket skin and the camera mass directly above them, and the probability for charge exchange is thus greatly reduced.

VIII. OBSERVATIONS ON SLOW MESONS

In examining the emulsions for nuclear evaporations a tally was also made of π–μ events and σ-stars that came to rest in the sensitive layers. By correcting for starless negative mesons (1.35 $\sigma = \pi^-$) and for pions that recorded at low altitude, rough estimates of the frequency of pion termination and of the π^- to π^+ ratio have been made, and compared with similar measurements at balloon elevations. Table IV shows that the ratio of π^- to π^+ mesons terminating is

TABLE IV

COMPARISON OF SLOW MESON INTENSITIES AND PION CHARGE RATIOS ON ROCKET AND BALLOON FLIGHTS

Exposure	Pions terminating cc.$^{-1}$ d.$^{-1}$	π^-/π^+
Viking 9	405±240	2.34±0.9
Balloons	55±8	2.02±0.6

essentially the same in the rocket and balloon emulsions and that negative π-mesons predominate. The data suggest that the charged pion production rate is ~7 times greater in the rocket than in the balloon exposures. This is not unreasonable in view of the large mass of the rocket and the known copious production of mesons in the interaction of cosmic-ray primaries with heavy target nuclei.

In order to reach the emulsions, the mesons observed to terminate traversed on the average ~12 gm. cm.$^{-2}$ of matter (see Fig. 5) enclosed in the instrument section. This suggests that the pions tallied were ejected from nuclear interactions with a kinetic energy of ~46 Mev. The local production of the mesons is further indicated by the observation of eight σ-mesons and two π–μ events which originated from stars within the emulsion. Collectively this corresponds to the production of 21±7 pion ejects cc.$^{-1}$ d.$^{-1}$ during the rocket flight. In a set of emulsions of comparable thickness (Table II, flight 732) exposed at ~30 km. the internal slow meson production rate was 10.7±1.1 cc.$^{-1}$ d.$^{-1}$

The ratio of slow pions ($E \leqslant 46$ Mev.) to stars in the rocket flight is 0.35, which is to be compared with 0.068 in balloon flights at the same geomagnetic latitude. Comparing these ratios with similar data evaluated by Camerini

et al. (1949) shows that the rocket while in flight serves as an efficient π-meson generator:

Flight	Slow meson-star ratio
Viking 9 at λ 41° N.	0.35
30 km. at λ 41° N.	0.068
~24 km. at λ 55° N.	0.062 with lead
	0.040 without lead
~3.4 km., Jungfraujoch	0.11

The scanning of the emulsions did not reveal any tracks attributable to τ^+-mesons or K^+-particles. A small number of the latter category may have been incorporated in the π^--meson tally, since no mass measurements were made on meson tracks terminating with the production of a single gray or near minimum prong.

IX. HEAVY PRIMARY SPECTRUM

Measurements on heavy primary tracks were confined chiefly to thick emulsions (Table V) in order to provide a statistically significant number of

TABLE V

HEAVY PRIMARIES RECORDED DURING FLIGHT OF VIKING NO. 9

Emulsion	Station	Emulsion thickness, μ	No. of tracks of $Z \geqslant 6$	Tracks cm.$^{-2}$ per flight
A*	23	1850	41	0.76
B*	23	1860	47	0.87
C	69	1840	30	0.57
D	69	1920	20	0.57
E	69	1910	27	0.69
54	64	1140	33	0.67
69	97	732	40	0.85
61	450	2300	8	0.32

*Emulsions A and B were mounted on the sun follower and had a fixed azimuthal orientation for the first 200 sec. of flight. Beyond this point the spin of the rocket proved too large for the operation of the sun follower.

δ-rays along all measurable tracks. The linear density of δ-rays was established for δ-ray ranges $\geqslant 1.8$ μ using 55× Koristka long working distance objective and 25× eyepieces. As a primary charge calibration the δ-ray density along 4× minimum relativistic alpha particle tracks was measured using narrow angle beams of such particles which originated from the collision of heavy primaries. Since the rocket exposure was conducted at $\lambda = 41°$ N. the earth's magnetic field deflects nonrelativistic heavy primaries with minimum energies of arrival of less than 3.2 Bev. per nucleon. Hence, it was assumed that all heavy primary tracks recorded were moving at relativistic velocity and that their charge Z was given by

$$Z = 2(\delta_z/\delta_\alpha)^{\frac{1}{2}}$$

where δ_z and δ_α represent delta rays per 100 μ of track (corrected for dip) along the heavy primary tracks and the alpha particle calibration tracks.

Owing to the brevity of the exposure and the freshness of the emulsions a correction for track-coincident background electron tracks was found to be too small to warrant application.

Because of the small number of heavy primary tracks recorded it was not practical to base the spectrum exclusively on tracks which recorded at small angles with the emulsion plane. Comparison of histograms A and B of Fig. 10

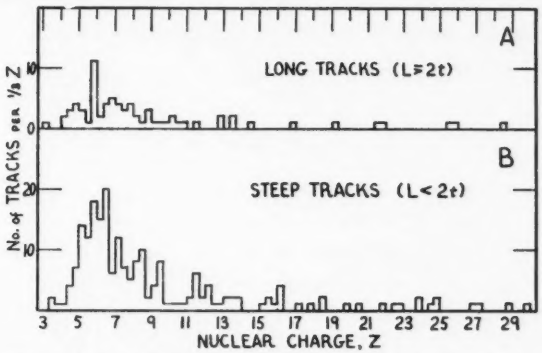

FIG. 10. Histographs showing distribution of measured heavy primary charges.

shows that essentially the same charge distribution is secured using only the long or the steep tracks in emulsions of thickness t. A quantitative comparison for the ratio of M ($6 \leqslant Z \leqslant 10$) to H ($Z > 10$) nuclei is tabulated below:

Ratio	M/H
Long tracks, $L \geqslant 2t$	3.10
Steep tracks, $L < 2t$	2.45
All tracks, $L \geqslant t$	2.66 ± 0.39

The principal advantage of the long flat tracks resides in the fact that the peaks of adjacent light elements, such as the C, N, and O nuclei, appear to be resolved. In all subsequent discussion of the flux the data on all tracks have been combined.

In the scanning of the emulsions for tracks of $Z \geqslant 6$, a number of tracks were observed which on the basis of their delta-ray densities might be Li, Be, or B nuclei. No effort was made to include all the L-nuclei ($3 \leqslant Z \leqslant 5$) quantitatively, and the members of this group shown in Fig. 10 probably constitute a small fraction of the total primary and secondary flux. That some were picked up under low power survey suggests that very few tracks of $Z \geqslant 6$ escaped detection. Originally a more careful independent survey for the L-nuclei was planned, but in the course of this work a large block of emulsion was recovered from Viking No. 10 which was flown in the very tip of the nose cone, virtually free from surrounding matter. In the present experiment the emulsions were surrounded by about 300 lb. of irregularly distributed instrumentation, and since this circumstance would make it very

difficult to recognize a primary flux among the secondary fragmentation products, it was decided to expend the effort on the more favorable exposure. Further discussion on the relative abundance of L-nuclei in the primary cosmic-ray beam will be postponed until the results from the new flight become available.

As is well known, in a certain velocity range the tracks of slow He, Li, Be, and B nuclei ejected as fragments from nuclear disruptions may be confused with the tracks of relativistic particles of charge $3 \leqslant Z \leqslant 7$. Owing to the large thickness of the emulsions very few spurious tracks are believed to be included in the primary charge spectrum shown in Fig. 11. In most

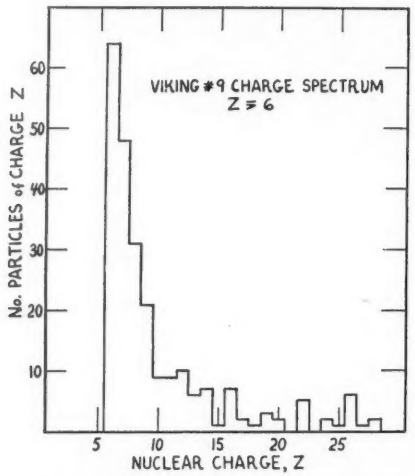

FIG. 11. Charge spectrum of heavy primary nuclei of $Z \geqslant 6$.

instances locally produced heavy fragments could be observed to either terminate within the emulsion layer, or be traced back to a star, and if they crossed both emulsion surfaces, the range was usually adequate to note the absence of high energy delta rays. When a relativistic heavy primary made a collision in the emulsion, any resulting heavy fast fragments were excluded from the spectrum. Likewise, the eight tracks recorded in emulsion 61 were omitted because the exposure favored the recording of secondary particles. The following conclusions can be drawn from the analysis of the residual 238 heavy primary tracks:

1. The ratio of medium to heavy nuclei as directly recorded during the flight of Viking No. 9 is 2.66 ± 0.39. The M/H ratio corrected for collisions in residual air and surrounding instrumentation is estimated at 2.5 ± 0.5 at the top of the atmosphere. This value may be compared with a ratio of ~ 2 deduced by Noon and Kaplon (1955) from heavy primary collisions observed in emulsions flown in the stratosphere above White Sands.

2. The medium group of nuclei are composed chiefly of carbon, nitrogen, and oxygen which appear to diminish in that order. This is also in agreement with the Rochester balloon observations (Kaplon *et al.* 1954).

3. Fluorine and neon constitute 12.6% of all nuclei of $Z \geqslant 6$. It is doubtful whether the delta-ray count is sufficiently reliable to distinguish between the two elements, and it is possible that some of the tracks listed as fluorine may represent the tail ends of the oxygen and neon peaks. If the fluorine peak is given full significance its cosmic-ray abundance is particularly striking in view of the very small astrophysical abundance of this element. The rocket observations suggest that the ratio of fluorine to silicon tracks is about three, whereas from Brown's data (1949) on astrophysical abundances the ratio of F to Si is 0.009. A small fraction of the tracks identified as fluorine may have originated locally in the instrument section as a result of the fragmentation of heavier nuclei, but this would not account for the 300-fold discrepancy between the cosmic and astrophysical abundances.

4. Among the heavy elements the ratio (Z = 12 to 17)/(Z = 18 to 28) = 33/23 = 1.43. Eisenberg (1954) has computed a value of 2.1 for this ratio. In general, the rocket exposure indicates a larger abundance of the very heaviest nuclei than is usually observed in balloon observations. This is to be expected in view of the small collision mean free path in air for heavy nuclei. Particles with a charge $Z > 20$ constitute about seven per cent of the $Z \geqslant 6$ flux. Proper identification in this region is very difficult owing to the exceedingly high density of delta rays, and the charge assigned to individual tracks may be in error by ± 3 charge units.

X. HEAVY PRIMARY FLUX AT THE TOP OF THE ATMOSPHERE

Table V shows that the number of heavy primary tracks recorded per unit area of emulsion varies with respect to the position of the detector in the rocket. In particular, casting No. 61 located near the massive (1500 lb.) motor section exhibits a flux about 50 per cent smaller than the plates in the instrument section. Plates A and B mounted in the very tip of the nose cone probably represent the closest approximation to the true incident flux, as the local absorber is there a minimum estimated at 5 ± 3 gm. cm.$^{-2}$ (chiefly aluminum). The average uncorrected omnidirectional flux indicated by these plates is 6.39 ± 0.68 m.$^{-2}$ sec.$^{-1}$ sterad.$^{-1}$. On the assumption that the M/H ratio is 2.66, the corresponding observational fluxes for the medium and heavy nuclei are, in the same units, $I_M = 4.64$ and $I_H = 1.75$.

Correcting for collision loss in the aluminum instrumentation ($\lambda_M = 37$, $\lambda_H = 27$ gm. cm.$^{-2}$) and in the residual integrated air mass ($\Omega_M = 6.12$, $\Omega_H = 6.11$ steradians) yields as the primary flux at the top of the atmosphere:

$$I_M{}^0 = 5.46 \pm 1.0 \text{ (m.}^2 \text{ sec. sterad.)}^{-1},$$

$$I_H{}^0 = 2.16 \pm 0.5,$$

$$I_{Z>6}^0 = 7.62 \pm 1.0.$$

This value is compared in Table VI with other estimates of the heavy primary flux secured at the same geomagnetic latitude in an ionization chamber

TABLE VI

HEAVY PRIMARY FLUX AT TOP OF ATMOSPHERE AT $\lambda = 41°$ N.

Exposure	Maximum altitude, km.	Particles m.$^{-2}$ sec.$^{-1}$ sterad.$^{-1}$		
		M-nuclei	*H*-nuclei	$Z > 6$
Viking 9	217	5.46±1.0	2.16±0.5	7.62±1.4
Van Allan (1951) V-2 No. 48	101	~10	~3	
Kaplon, Peters, Reynolds, and Ritson (1952)	28	5.9±0.7*	2.4±0.3†	8.3±1.0
Kaplon, Noon, and Racette (1954)	27	7.1±1.3	2.6±0.9	9.7±1.8

*Flux refers to C, N, O nuclei.
†Flux refers to $Z > 10$ nuclei.

flown in the nose cone of V-2 rocket No. 48 by Van Allen (1951) and with two stratosphere balloon flights at White Sands carrying emulsions. The highest values of the flux are reported by Van Allen, but these are stated to be upper limits, and the pulse data may not have been corrected adequately for bursts induced by nuclear disintegrations. The flux estimated from the Viking No. 9 observations is in general somewhat lower than indicated by the two balloon estimates. The largest uncertainty originates in the correction for collision loss in surrounding matter. If the omnidirectional flux is based on all 238 tracks and the average absorption path is taken as 11.5 gm. cm.$^{-2}$ (see Fig. 5 for basis of this estimate), then the flux of heavy primaries of $Z > 6$ is increased to 8.1 m.$^{-2}$ sec.$^{-1}$ sterad.$^{-1}$, which agrees more closely with the balloon observations.

XI. ZENITH ANGLE DISTRIBUTION OF HEAVY PRIMARIES

Zenith angles of the 238 heavy primary tracks with respect to the vertical rocket axis have been made by measuring the angle α between the track and the apparent vertical, and the dip angle β. In plates exposed with the emulsion plane perpendicular to the horizon, the zenith angle θ is given by

$$\cos\theta = \cos\alpha \cos\beta. \tag{5}$$

With this geometric arrangement it can be shown that the directional flux $J_{\Delta\theta}$ is related to the number of tracks N in the angular interval $\Delta\theta$ passing through the vertical plate area S by:

$$N = J_{\Delta\theta} S K_\theta \tag{6}$$

where

$$K_\theta = 2(\theta_2 - \theta_1) - (\sin 2\theta_2 - \sin 2\theta_1). \tag{7}$$

The results of this analysis (Table VII) show that the unidirectional flux is fairly uniform over the entire upper hemisphere. Only in the 0° to 15° angular interval is there a large deviation from the mean, and this is attributable to statistical fluctuations as only four tracks were observed within the interval.

It is of interest to compare the unidirectional flux of the heavy primary nuclei with predictions of geomagnetic theory, particularly because, in the

TABLE VII

UNIDIRECTIONAL FLUX OF HEAVY PRIMARIES

$\Delta\theta$	K_v	N	Flux at top of atmosphere (m.$^{-2}$ sec.$^{-1}$ sterad.$^{-1}$)
0–15°	0.0236	4	16.9 ±8.5
15–30	0.1576	13	8.3 ±2.4
30–45	0.3896	32	8.2 ±1.5
45–60	0.6576	42	6.4 ±1.0
60–75	0.8896	76	8.5 ±1.0
75–90	1.0236	71	6.9 ±0.8
0–30°	0.181	17	9.4 ±2.3
30–60	1.047	74	7.1 ±0.8
60–90	1.913	147	7.7 ±0.6
0–45°	0.5708	49	8.57±1.2
45–90	2.5708	189	7.36±0.5

rocket exposure, experiment and theory are not complicated by the presence of an appreciable atmosphere. The large spin of the vehicle precluded the study of East–West azimuthal asymmetry. However, by integration over 360° of azimuth, it was possible to compare the zenith angle distribution of the 238 heavy primary tracks with deductions from the Lemaitre–Vallarta theory.[4]

At a point of observation with the geomagnetic latitude λ the minimum energy of arrival of charged particles in Störmer units r entering at zenith angles θ and azimuth ϕ is given by

$$r = (\cos^2\lambda)[1+(1-\sin\theta\cos\phi\cos^3\lambda)^{\frac{1}{2}}]^{-1}. \tag{8}$$

This Störmer cone is valid only for $\theta \leqslant 40°$ at $\lambda = 41°$ N.; at larger zenith angles a correction has to be introduced for the earth's shadow. For $\theta > 40°$ values of r combining the Störmer cone and the earth's shadow were available from computations of Alpher (1950) at $\lambda = 40°$, and these were corrected to $\lambda = 41°$ of the launching locality by interpolation. The Störmer values were converted into cutoff energies for protons E_p by the relationship:

$$E_p = \frac{300\, m_0c^2}{e}\left[\left(1+\frac{r^4Z^2e^2M^2}{m_0^2c^4R^4}\right)^{\frac{1}{2}}-1\right]\ldots \text{ev.}, \tag{9}$$

which evaluates to

$$E_p = 0.939[(1+6.633\times10^{38}\, r^4\, R^{-4})^{\frac{1}{2}}-1]\ldots \text{Bev.} \tag{10}$$

using 8.06×10^{25} gauss cm.^{3} for the earth's dipole moment M and the DuMond and Cohen (1953) values for the atomic constants. As pointed out by Vallarta (1948), the cutoff energy is subject to two small corrections, (*a*) one taking account of the distance between the earth's magnetic center and the point of observation; and (*b*) an angular correction for the angle between the magnetic vertical and the gravitational vertical. For the White Sands locality (*a*)

[4]The available aspect data on the rocket flight indicate that the longitudinal axis of the rocket was oriented within ±5° with respect to the vertical. A maximum deviation of 23° occurred at 150 sec. after launching as a result of fuel burnout. This lasted for about 10 sec. and the zenith angles of a small number of tracks recorded during this period are erroneous.

amounts to a diminution in E_p of $0.73\pm0.5\%$. Its application to equation (10) would tend to increase the unidirectional flux by about 0.2 per cent, and in view of its large uncertainty it has not been applied. Likewise, the angular correction (b) is $<3°$, a quantity well within the error of our zenith angle determinations.

In equation (10) R represents the distance from the dipole to the point of observation. At White Sands the distance between the dipole and sea level[5] is 6.371×10^8 cm. which has to be increased by the relatively small, but significant, distance reached by the rocket. If H is the peak elevation, the average elevation of the rocket above the earth's surface, assuming a perfect parabolic trajectory, is $\bar{h} = \frac{2}{3}H$. For the Viking No. 9 exposure the final value of R used in equation (10) is estimated at 6.516×10^8 cm. For heavy primaries of charge $2Z \simeq A$ the energy per nucleon $\epsilon = E_{A,Z}/A$ is thus

$$\epsilon = 0.939[(1+919.7\,r^4)^{\frac{1}{2}}-1] \ldots \text{Bev.} \tag{11}$$

The unidirectional flux j_θ was evaluated by combining equation (11) with the integral energy spectrum for heavy primary nuclei deduced by Kaplon, Peters, Reynolds, and Ritson (1952):

$$j_\theta(\epsilon) = 28/(\epsilon+1)^{1.38\pm0.15}\ \text{m.}^{-2}\,\text{sec.}^{-1}\,\text{sterad.}^{-1}. \tag{12}$$

In computing $j_\theta(\epsilon)$, readings of $r(\theta, \Delta\phi)$ were taken at 10° intervals of ϕ

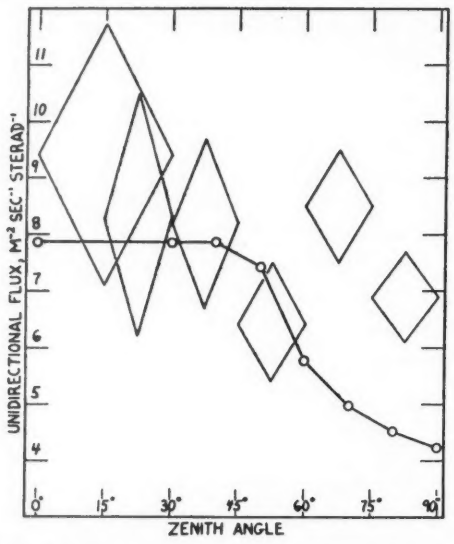

FIG. 12. Comparison of observational zenith angle distribution (diamonds) of unidirectional flux with predictions from geomagnetic theory (line).

[5]This value was computed by J. A. O'Keefe, U.S. Army Map Service, from measurements of the distance between the earth's center and White Sands, New Mexico, viz. 6,372,238 meters.

at a fixed zenith angle, each converted into a corresponding flux value, and these averaged over 360° of azimuth, $\bar{j}_\theta$.

This function, based on the Störmer and shadow cones, is plotted in Fig. 12 and compared with the experimental estimates of the unidirectional flux. For zenith angles $\leqslant 40°$ the magnitude of the computed and observed flux is in surprisingly good agreement. The largest deviation from geomagnetic theory occurs at zenith angles $>60°$, a region in which our measurements have the smallest statistical uncertainty.

If we combine our data into two large angular groups of $\theta_1 \leqslant 45°$ and $\theta_2 > 45°$, then it would appear that the corresponding fluxes $\bar{j}_1$ and $\bar{j}_2$ are in very rough agreement with the main features of the computed geomagnetic function, since $\bar{j}_2$ is about 15 per cent less than $\bar{j}_1$. In general, Fig. 12 suggests an appreciably larger flux at $\theta \geqslant 60°$ than can be anticipated from geomagnetic theory. The correlation between theory and experiment would be improved by the following factors:

1. If the exponent in the power law equation (12) was in error by $\sim$10 per cent and a lower limit of $(\epsilon+1)^{1.2}$ was employed in the computation.

2. The application of a precise longitudinal correction factor for the White Sands region would reduce the magnitude of the energy cutoff, and hence increase the unidirectional flux.

3. It has been suggested by Simpson (1954) that the pertinent geomagnetic latitude is that at the point of observation and not the one usually taken at the earth's surface. This shift in the magnetic latitude coordinate might be of the order of 3° or 4° at the very high elevations reached by the rocket. If we assume that $\lambda = 44°$ at points high above the atmosphere then the plateau flux is increased to 9.8, and at large zenith angles the flux is raised to 5.0 particles m.$^{-2}$ sec.$^{-1}$ sterad.$^{-1}$.

Directional studies of the total charged cosmic-ray intensity above White Sands have been made by other investigators employing rocket telemetering techniques. Experiments of this nature have the advantage that the direction of the counter telescope can be correlated during flight with the aspect of the vehicle by means of photographs of the earth taken at known time intervals. Measurements made by Singer (1950), Gangnes *et al.* (1949), and Perlow *et al.* (1952) are consistent in exhibiting high values of the unidirectional intensity at large zenith angles $\gtrsim 60°$. Singer attributes this to an albedo component of about 35 per cent of the total charged particle intensity. Perlow and co-workers ascribe the increased intensity at large zenith angles to decreased shadowing of the bottom of their telescope by the earth, permitting radiation to enter the counter from the lower hemisphere.

This effect is not noticeable from our measurements on the heavy primary component. In interacting with air nuclei the relativistic secondaries from the fragmentation proceed downward and hence do not contribute to the splash albedo. Likewise, owing to the large collision cross-section of the heavy primaries with air nuclei, particles approaching from the lower hemisphere are destroyed by collision in traversing the large air mass ($\sim 8 \times 10^4$ gm. cm.$^{-2}$) before reaching the emulsions even at the peak of the rocket trajectory.

XII. HEAVY PRIMARY COLLISIONS

In the examination of the group of thick γ-emulsions flown on Viking No. 9, 10 interactions of heavy primary nuclei have been observed in which the particle is destroyed catastrophically, or emerges from the collision with a reduction in charge $\geqslant 1$. These events are described in Table VIII, and while

TABLE VIII

CHARACTERISTICS OF HEAVY PRIMARY COLLISIONS

Event	Emulsion	Charge of incident particle	No. of fragmentation products				
			Z^1	α	p	$\pi^{\pm}$	N_h
1	B	6	0	1	4	0	4
2	B	6	5	0	1	0	3
3	D	6	0	1	4	0	0
4	E	6	0	2	2	0	16
5	A	8	7	0	1	0	14
6	A	11	0	2	7	25	12
7	D	11	9	0	2	0	4
8	E	13	0	3	7	0	2
9	C	14	0	2	10	4	15
10	B	16	0	3	10	0	2

their number is statistically small, they provide interesting information on the fragmentation tendency of the first generation of heavy nuclei entering the atmosphere.

(1) In three of the events the primary gave rise to a heavy relativistic secondary proceeding in the same direction, but of reduced charge. Of particular interest are events No. 2 and 7 in which a boron and a fluorine nucleus are produced locally. This indicates that the charge spectrum compiled in Fig. 11 may be adulterated with secondary particles originating from collision processes in the rocket skin and from massive matter within the instrument section. In the examination of one track an associated closely parallel beam of relativistic alpha particles was observed (Fig. 14) clearly indicating that this carbon nucleus had originated in a distant collision process, and was excluded from the data. This secondary phenomenon, however, can only be recognized when the singly and doubly charged satellite particles are fairly close to the $Z \geqslant 6$ member and limits the elimination process to fairly close-by collisions.

(2) In eight of the events there is no evidence for fast meson production as the number of singly charged minimum particles observed must be assigned to fast protons in order to conserve the estimated charge of the primary.

(3) The ratio of relativistic protons to alpha tracks (excluding fast mesons) produced in these collisions is about the same for incident M and H nuclei and averages $48/13 = 3.7$.

(4) On the basis of the length of heavy primary track surveyed a rough estimate can be made of the collision mean free paths. The results are compared in Table IX with the more statistically significant results reported by Noon and Kaplon (1955) from balloon observations at White Sands. The

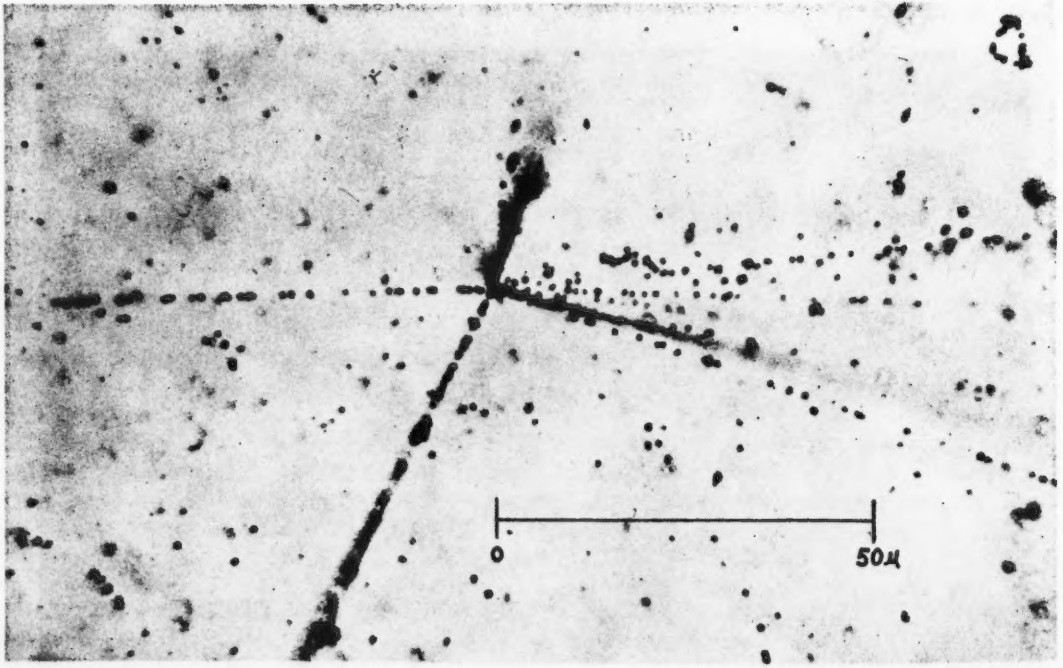

FIG. 13. Shower of 10 relativistic singly charged particles initiated by a primary proton. The shower has an angular width of 0.35 radians and is associated with four other black and gray tracks; only about six of the shower particles are visible in the particular focal setting. Basis $E = 2/\phi_1^2$, the energy of the particle initiating the shower is estimated at ~90 proton mass units.

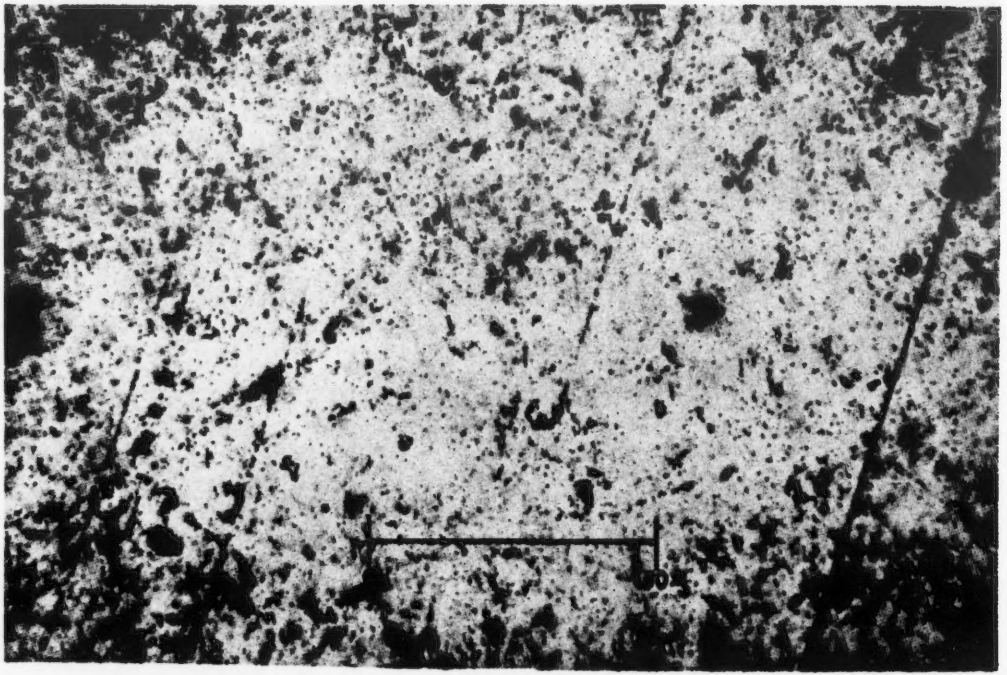

FIG. 14. Photomicrograph of the track of a carbon nucleus accompanied by three relativistic alpha particle tracks recorded in emulsion No. 54. From the angle between the carbon track and its accompanying satellites it is estimated that the particles originated in a fragmentation process located 3.14 cm. from the point of observation. Based on a root mean square angle of 0.0053 radians between the α-tracks and the carbon track, the energy is estimated at 11 Bev. per nucleon, basis $\epsilon = 0.057/\sqrt{\theta^2}$.

TABLE IX

COLLISION CROSS SECTIONS OF HEAVY NUCLEI IN EMULSION

Exposure	Mean charge of incident flux	No. collisions	λ in gm. cm.$^{-2}$
Viking 9	7.2±0.6	5	42 ±19
Stratosphere*	7.3±0.3	60	59.4±7.8
Viking 9	16.4±2	5	17 ±8
Stratosphere	15.4±0.4	37	34.7±5.6

*Based on observations of Noon and Kaplon (1955) in a balloon flight at White Sands.

available rocket data suggest a somewhat larger collision cross section than that observed in the balloon exposures, particularly in the case of the *H* nuclei.

ACKNOWLEDGMENTS

It is a pleasure to acknowledge the aid received from the Naval Research Laboratory in securing high altitude flights in NRL–Aerobee and Viking rockets, and for hospitality and special laboratory facilities extended to the writer in the B.O.Q. at White Sands in conjunction with the Viking No. 9 exposures. M. W. Rosen was particularly gracious in allowing the exposure of the older emulsions as well as those prepared shortly before firing. Appreciation is expressed to Edmund J. Habib for the speedy recovery of the emulsions. The writer is indebted to Homer E. Newell, Jr. for discussions on problems of geometry and for the suggestion of the use of the rocket air-mass determinations in conjunction with the Gross transformation. Opportunity is taken to thank the members of the U.S. Office of Naval Research Skyhook Project for the high altitude balloon exposures.

REFERENCES

ALPHER, R. A. 1950. Theory of geomagnetic effects on cosmic radiation. Applied Physics Lab., Silver Spring, Md. JHU–CF–1308 Unpublished. Summary available in J. Geophys. Research, **55**: 437.
BERNARDINI, G., CORTINI, G., and MANFREDINI, A. 1949. Phys. Rev. **76**: 1792.
BROWN, H. 1949. Revs. Mod. Phys. **21**: 625.
CAMERINI, U., COOR, T., DAVIES, J. H., FOWLER, P. H., LOCK, W. O., MUIRHEAD, H., and TOBIN, N. 1949. Phil. Mag. **40**: 1084.
CAMERINI, U., DAVIES, J. H., FOWLER, P. H., FRANZINETTI, C., MUIRHEAD, H., LOCK, W. O., PERKINS, D. H., and YEKUTIELI, G. 1951. Phil. Mag. **42**: 1241.
DUMOND, J. W. M. and COHEN, E. R. 1953. Revs. Mod. Phys. **25**: 691.
EISENBERG, Y. 1954. Phys. Rev. **96**: 1382.
ENGLER, A. and HABER-SCHAIN, U. 1954. Phys. Rev. **95**: 1700.
GANGNES, A. V., JENKINS, J. F., and VAN ALLEN, J. A. 1949. Phys. Rev. **75**: 57.
GEORGE, E. P. and EVANS, J. 1951. Proc. Phys. Soc. A, **64**: 193.
HARDING, J. B., LATTIMORE, S., LI, T. T., and PERKINS, D. H. 1949. Nature, **163**: 319.
KAPLON, M. F., PETERS, B., REYNOLDS, H. L., and RITSON, D. M. 1952. Phys. Rev. **85**: 295.
KAPLON, M. F., NOON, J. H., and RACETTE, G. W. 1954. Phys. Rev. **96**: 1408.
NEWELL, H. E., JR. 1953. High altitude rocket research. Academic Press, Inc., New York.
NOON, J. H. and KAPLON, M. F. 1955. Phys. Rev. **97**: 769.
PERLOW, G. J., DAVIS, L. R., KISSINGER, C. W., and SHIPMAN, J. D., JR. 1952. Phys. Rev. **88**: 321.
POMEROY, D. 1951. Phys. Rev. **84**: 77.
PRESSLY, E. C. 1953. Phys. Rev. **89**: 654.
ROSEN, M. W., BRIDGER, J. M., and SNODGRASS, R. B. 1954. Naval Research Lab. Rept. 4407.

ROSSI, B. 1952. High energy particles. Prentice-Hall, Inc., New York. p. 542.
SIMPSON, J. A. 1954. National Science Foundation Cosmic Ray Conference, Duke University, Durham, N.C. III–34. Unpublished.
SINGER, S. F. 1950. Phys. Rev. **77**: 729.
VALLARTA, M. S. 1948. Phys. Rev. **74**: 1837.
VAN ALLEN, J. A. 1951. Phys. Rev. **84**: 791.
——— 1953. Nuovo cimento, **10**: 630.
WINCKLER, J. R. and ANDERSON, K. 1954. Phys. Rev. **93**: 596.
YAGODA, H. 1955. Rev. Sci. Instr. **26**: 263.
YAGODA, H., DE CARVALHO, H. G., and KAPLAN, N. 1950. Phys. Rev. **78**: 765.

LETTERS TO THE EDITOR

Under this heading brief reports of important discoveries in physics may be published. These reports should not exceed 600 words and, for any issue, should be submitted not later than six weeks previous to the first day of the month of issue. No proof will be sent to the authors.

Note on the $T = 3/2$ State in N^{15} *

Recent work (Douglas *et al.* 1955) on the $C^{14}(d, p)C^{15}$ reaction indicates a Q-value for this reaction of -0.96 Mev. rather than $+0.12$ Mev. as previously reported (Ajzenberg and Lauritsen 1955). This value may be combined with the Q-value for $C^{14}(p, \gamma)N^{15}$ of 10.215 ± 0.007 Mev. to give the mass difference C^{15}–N^{15} of 9.732 Mev. The position of the $T = 3/2$ state in N^{15} corresponding to the ground state of C^{15} is then calculated to be 11.79 ± 0.10 Mev. when corrected for coulomb energy in the manner suggested by Peaslee (1954). In the authors' paper (Bartholomew *et al.* 1955) on the reaction $C^{14}(p, \gamma)N^{15}$, a broad state of spin $1/2+$ at excitation 11.61 Mev. was reported which had the characteristics of a $T = 3/2$ state. The newly reported Q-value for the $C^{14}(d, p)$ reaction now makes it seem probable that this $T = 3/2$ state in N^{15} corresponds to the ground state of C^{15} rather than an excited state as was suggested in the above paper (Bartholomew *et al.* 1955). If this interpretation is correct, it implies that C^{15}, with one $d_{5/2}$ neutron and two holes in the proton p-shell, has a ground state spin of $1/2+$ similar to F^{19}, which has three $d_{5/2}$ particles.

AJZENBERG, F. and LAURITSEN, T. 1955. Revs. Mod. Phys. **27**: 77.

BARTHOLOMEW, G. A., BROWN, F., GOVE, H. E., LITHERLAND, A. E., and PAUL, E. B. 1955. Can. J. Phys. **33**: 441.

DOUGLAS, R. A., BROER, J. W., and CHIBA, R. 1955. Bull. Am. Phys. Soc. **30** (No. 7): 26.

PEASLEE, D. C. 1954. Phys. Rev. **95**: 717.

RECEIVED NOVEMBER 9, 1955.

PHYSICS DIVISION,
ATOMIC ENERGY OF CANADA LIMITED,
CHALK RIVER, ONTARIO.

G. A. BARTHOLOMEW
A. E. LITHERLAND
E. B. PAUL
H. E. GOVE

*Issued as A.E.C.L. No. 262.

The Role of the 1.30 Mev. Gamma-ray in the Decay of In^{114}

Since 1949, a large number of papers have been published dealing with the K-capture component in the decay of 50-day In^{114}. In particular, workers in this laboratory (Johns, McMullen, Donnelly, and Nablo 1954; Johns, Waterman, MacAskill, and Cox 1953) reported gamma-rays of the following energies and quantum intensities: 556 ± 1 kev. (3.6×10^{-2}), 576 ± 3 kev. (1×10^{-3}), 722 ± 1 kev. (3.5×10^{-2}), 1271 ± 6 kev. (3×10^{-4}), and 1300 ± 3 kev. (1.5×10^{-3}). A coincidence lead absorption experiment indicated that the 556 kev. radiation was in cascade with both the 722 and 1300 kev. gamma-rays and the authors postulated a level at 1856 kev. in Cd^{114} to account for these results. In view of the work of Lu, Kelly, and Wiedenbeck (1954), who failed to find any evidence for 556–1300 kev. coincidences, and the disturbing fact that our decay scheme could not be reconciled with the results obtained in studies of capture gamma-rays in Cd^{114} (Kinsey and Bartholomew 1953; Motz 1953), it was decided to repeat both the energy and coincidence measurements with the more refined techniques developed during the last two years.

The gamma-rays were studied by external conversion in a large magnetic spectrometer (Johns and Nablo 1954; Johns, Waterman, MacAskill, and Cox 1953), using a 10 mgm./cm.^{2} uranium radiator in place of the 20 mgm./cm.^{2} lead radiator employed in the earlier work and with much improved counting statistics. These experiments give a value of 1299 ± 2 kev. $(2.0 \pm 0.4 \times 10^{-3})$ for the highest energy radiation, in excellent agreement with the earlier determination. However, the two weak gamma-rays of energy 576 and 1271 kev. did not appear, upper limits for their intensities being set, respectively, at 3×10^{-4} and 1×10^{-4} quanta per disintegration.

The results of the coincidence measurements are shown in Fig. 1. Two NaI(Tl) scintillation gamma-ray spectrometers with single channel pulse-height analyzers were used in a coincidence circuit of 1 μsec. resolving time. Each counter was covered with 7.5 gm./cm.^{2} of lead to eliminate pile-up created by the strong 192 kev. radiation. Curve A shows the In^{114} pulse-height

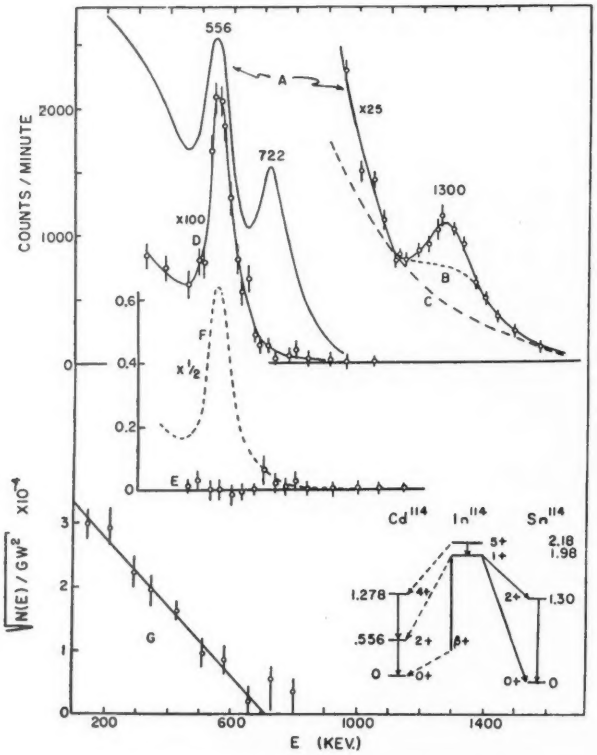

FIG. 1. Gamma–gamma and beta–gamma coincidence spectra of In^{114}.

distribution in each of the single spectrometers. The 1300 kev. peak is much augmented in this spectrum by solid-angle pile-up. Curve B shows the true height of this peak obtained by reducing the solid angle to 1% of the value used for Curve A. An estimate of the intensity of the 1300 kev. radiation based on Curve B is in good agreement with the value obtained by external conversion. Curve C represents the bremsstrahlung spectrum produced by a source of Y^{90}, a pure beta-ray emitter with approximately the same end-point as In^{114}. It is clear that the sharply-falling background of Curve A above 1.1 Mev. is due to bremsstrahlung caused by stoppage of 2 Mev. beta-rays in the lead absorber.

The gamma–gamma coincidence spectrum obtained when the fixed channel was set on the 722 kev. photopeak and the window of the other spectrometer was moved across the spectrum is shown in Curve D. The results obtained in the same way with the fixed channel set on the 1300 kev. photopeak are presented in Curve E. The data for the latter case have been corrected for a small chance contribution which was at no point in the spectrum greater than 0.02 counts/min. These curves show clearly that the 556 kev. gamma-ray is in coincidence with the 722 kev. radiation and not in coincidence with the 1300 kev. radiation. Curve F represents the spectrum of 1300–556 kev. coincidences expected on the basis of the measured intensity of the 1300 kev. radiation and the decay scheme reported in our previous work. It is clear that less than 1.5% of the 1300 kev. gamma-rays can be in cascade with the 556 kev. radiation.

The spectrum of beta-rays in coincidence with the 1300 kev. radiation was studied in the same way as the gamma–gamma coincidence spectrum described above. For this purpose, one of the NaI(Tl) crystals was replaced by an anthracene crystal covered with 25 mgm./cm.^{2} of aluminum to prevent detection of the abundant conversion electrons from the 192 kev. transition. The beta spectrum was scanned with a 30 kev. window while the fixed channel

remained focused on the photopeak of the 1300 kev. gamma-ray. The coincidence rates obtained were very low ($\sim$0.1 per minute at 500 kev.) but were from 2 to 10 times the chance rate and 50 times the cosmic coincidence rate. To eliminate any possibility that the observed coincidences were due to scattering associated with the bremsstrahlung spectrum, a comparison experiment was carried out with a Y^{90} source of about the same strength. The chance coincidence rate was nearly the same as for In^{114} but there were no true coincidences in the region above 150 kev. It seems clear that the β–γ coincidences observed in indium are due to beta-rays feeding a level at 1300 kev. in In^{114}. A calculation of the number to be expected on the assumption that this group had the same intensity as the 1300 kev. gamma-ray gave a value within 30% of the number actually recorded, which represents good agreement in view of uncertainties in the solid angles and efficiencies of detection of the counters.

A Fermi plot of the β–γ coincidence spectrum, corrected for chance, is presented in Curve G. The spectrum appears to be well-behaved and has an end-point of 710 ± 50 kev. Both the beta and gamma spectrometers were calibrated frequently during the month required to build up reasonable statistics, using Cs^{137} sources in the indium source position. Drifts in the electronics over this period did not change the calibration by more than 50 kev.

A decay scheme proposed on the basis of the above experiments is presented in Fig. 1. The spins of the three levels in Cd^{114} have recently been uniquely determined as 0–2–4 through the polarization – angular correlation experiments of Brazos and Steffen (1955). Consequently the 1.278 Mev. level must be fed from the 5+ state of In^{114}. With the rejection of the 1.856 Mev. level originally proposed (Johns, McMullen, Donnelly, and Nablo 1954), this decay scheme is now concordant with the results of capture gamma-ray studies. *K*-capture transitions to the 556 kev. level of Cd^{114} are to be expected but seem to be weak.

It was originally pointed out by Nussbaum and Van Lieshout (1953) that there should be a beta-transition to an excited state of Sn^{114} of energy $\sim$1.2 Mev. and they set an upper limit on its intensity of 3×10^{-3} particles per disintegration. From our experiments, it is clear that this group has an intensity of 2×10^{-3} and an end-point of 700 kev. Such a transition has a log *ft* value of 5.5, characteristic of an allowed spectrum. Consequently, the 1.30 Mev. level in Sn^{114} represents the first excited state in that nuclide and almost certainly has spin 2 and even parity.

A recent communication from Dr. Motz of the Brookhaven National Laboratory indicates that he has arrived at essentially the same conclusions through an independent and somewhat different group of experiments.

The financial assistance of the National Research Council of Canada and the Research Council of Ontario is gratefully acknowledged.

BRAZOS, J. N. and STEFFEN, R. M. 1955. Phys. Rev. **99**: 1645A.
JOHNS, M. W., MCMULLEN, C. C., DONNELLY, R. J., and NABLO, S. V. 1954. Can. J. Phys. **32**: 35.
JOHNS, M. W. and NABLO, S. V. 1954. Phys. Rev. **96**: 1599.
JOHNS, M. W., WATERMAN, H., MACASKILL, D., and COX, C. D. 1953. Can. J. Phys. **31**: 225.
KINSEY, B. B. and BARTHOLOMEW, G. A. 1953. Can. J. Phys. **31**: 1051.
LU, D. C., KELLY, W. H., and WIEDENBECK, M. L. 1954. Phys. Rev. **95**: 121.
MOTZ, H. T. 1953. Phys. Rev. **90**: 355A.
NUSSBAUM, R. H. and VAN LIESHOUT, R. 1953. Physica, **19**: 451L.

RECEIVED OCTOBER 31, 1955.
DEPARTMENT OF PHYSICS,
MCMASTER UNIVERSITY,
HAMILTON, ONTARIO.

M. W. JOHNS
I. R. WILLIAMS
D. E. BRODIE

Line Source with Progressive Phase Shift

In evaluating the energy radiation from an acoustic line source with progressive phase shift, Thiessen (1955) obtained an integral representation (his equation [2]). Instead of the somewhat awkward development of equation [4] the integral can be readily expressed in a simple closed form containing tabulated functions, and furthermore asymptotic approximations are readily made for the cases where $R = l/\lambda$ is large.

We have quite generally

$$\int_a^b \frac{\sin^2 x\, dx}{x^2} = \frac{\sin^2 a}{a} - \frac{\sin^2 b}{b} + \mathrm{Si}(2b) - \mathrm{Si}(2a)$$

which may be evaluated for all values of the limits $b = \pi R(1-\alpha)$ and $a = -\pi R(1+\alpha)$.

When R and $R\alpha$ are both integers the first two sine terms vanish and the simple expression $\mathrm{Si}\ 2\pi R(1-\alpha) + \mathrm{Si}\ 2\pi R(1+\alpha)$ results. Thus for the values of $R = 5$, 10, and 20 chosen by Thiessen this latter expression may be used for α equal to zero or to any multiple of 0.2, 0.1,

and 0.05 respectively, and this provides sufficiently closely-spaced values to derive the curves of the type given in Fig. 3.

If the ordinate of Fig. 3 is denoted by y, we then have

$$y = \frac{\mathrm{Si}\, 2\pi R(1-\alpha) + \mathrm{Si}\, 2\pi R(1+\alpha)}{2\ \mathrm{Si}\, 2\pi R}.$$

Now for $x > 2$, $\mathrm{Si}\, x \sim \frac{\pi}{2} - \frac{\cos x}{x}$ to better than 0.4%.

For $\alpha = 1$,

$$y = \tfrac{1}{2}$$

corresponding to a common intersection point at $-3db$ in Fig. 3.

For $\alpha \gg 1$,

$$y = 1/\pi^2 R(\alpha^2 - 1).$$

Some discrepancies in Thiessen's curves near $\alpha = 2$ may be noted by comparison with this formula. These forms show the transition from the almost constant value of radiated energy up to $\alpha = 1$ to the rapidly decreasing region when α exceeds unity.

THIESSEN, G. J. 1955. Can. J. Phys. **33**: 618.

RECEIVED DECEMBER 5, 1955.
R. E. BURGESS
DEPARTMENT OF PHYSICS,
UNIVERSITY OF BRITISH COLUMBIA,
VANCOUVER, BRITISH COLUMBIA.

$\Delta M = \pm 2$ Transitions in Dilute Gadolinium Ethyl Sulphate

The seven $\Delta M = \pm 1$ transitions in dilute gadolinium ethyl sulphate [$4f^7$, $^8S_0$] have been extensively studied by Bleaney, Scovil, and Trenam (1954) using a single field modulation or video paramagnetic resonance spectrometer. However, they did not report the detection of any higher order transitions. The new double field modulation spectrometer developed by Buckmaster and Scovil (unpublished) possesses sufficient sensitivity in wide band operation (8 kc.) to permit the six $\Delta M = \pm 2$ transitions to be observed at liquid oxygen temperature (90°K.) with signal-to-noise ratios of about 1000:1. The values of the spectroscopic splitting factor (g) and splitting parameters for the spin-Hamiltonian developed by Elliott and Stevens (1953) are given in this letter for the transitions in both the parallel and perpendicular directions to the crystal symmetry axis.

The transitions corresponding to $\Delta M = \pm 2$ arise from the admixing of the wave functions describing the energy levels due to the largest off-diagonal term $P_3^3(S_+)$ in the spin-Hamiltonian (Elliott and Stevens 1953). Theoretically, this term is not present when the direction of the magnetic field is parallel to the hexagonal symmetry axis of the crystal. This has been experimentally verified. The intensity of these transitions in this direction is less than that detectable with the maximum sensitivity of our spectrometer (10^{-1} gm. 290°K.).

In Table I, the values of $g_\parallel$ and $g_\perp$ as calculated from measurements of the $\Delta M = \pm 1$ and ± 2 transitions are given. These measurements were performed on the same crystal of gadolinium ethyl sulphate magnetically diluted with the isomorphous, diamagnetic lanthanum salt in the ratio of about one part in two hundred. The magnetic field values used for the calculations for the parallel direction from $\Delta M = \pm 2$ transitions were obtained by extrapolation from measurements at small angles on each side of this direction.

TABLE I

"g" VALUES FOR DILUTE GADOLINIUM ETHYL SULPHATE

Temperature (°K.)	$g_\parallel$		$g_\perp$	
	$\Delta M = \pm 1$	$\Delta M = \pm 2$	$\Delta M = \pm 1$	$\Delta M = \pm 2$
290	1.9908±0.001		1.9905±0.001	
90	1.9880±0.001	1.9902±0.002	1.9901±0.001	1.9901±0.001

The splitting parameters, which are defined in the same manner as in Bleaney, Scovil, and Trenam (1954) and calculated from the same data as used for Table I, are given in Table II. The values of these parameters for the perpendicular direction have been corrected for the effect of the largest off-diagonal term $P_3^3(S_+)$.

TABLE II

SPLITTING PARAMETERS FOR DILUTE GADOLINIUM ETHYL SULPHATE
$T = 90°K.$

Transition direction		b^0_2	b^0_4	b^0_6	b^0_8
$M = \pm 1$	∥	$+205.4 \pm 2$	-3.61 ± 0.6	$+0.98 \pm 0.5$	
	⊥	$+202.2 \pm 2$	-4.79 ± 0.3		$+0.2 \pm 1.0$
$M = \pm 2$	∥	$+206.2 \pm 2$	-3.98 ± 0.3	$+0.41 \pm 0.3$	
	⊥	$+204.7 \pm 2$	-4.50 ± 0.3		$+4.2 \pm 0.5$

Fig. 1 shows an oscillogram of the six $\Delta M = \pm 2$ transitions when the magnetic field is oriented with respect to the crystal symmetry axis so that the total separation of these transitions is about five hundred gauss. The low field transition appears at the right in Fig. 1.

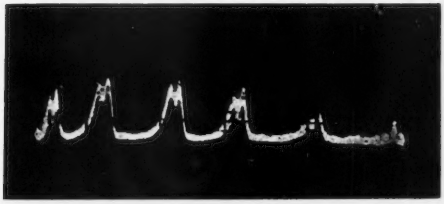

FIG. 1

A more complete study of these transitions is presently being undertaken. Measurements, at 5° intervals, of the behavior of these transitions as a function of the angle between the direction of the magnetic field and the symmetry axis of the crystal are being made.

BLEANEY, B., SCOVIL, H. E. D., and TRENAM, R. S. 1954. Proc. Roy. Soc. A, **23**: 15.
BUCKMASTER, H. A. and SCOVIL, H. E. D. Unpublished.
ELLIOTT, R. J. and STEVENS, K. W. H. 1953. Proc. Roy. Soc. A, **219**: 387.

RECEIVED DECEMBER 5, 1955.
H. A. BUCKMASTER
PHYSICS DEPARTMENT,
UNIVERSITY OF BRITISH COLUMBIA,
VANCOUVER, CANADA.

THE PHYSICAL SOCIETY

MEMBERSHIP of the Society is open to all who are interested in Physics.

FELLOWS pay an Entrance fee of £1 1*s*. ($3.00) and an Annual Subscription of £2 2*s*. ($6.00).

STUDENTS: A candidate for Studentship must be between the ages of 18 and 26, and pays an Annual Subscription of 7*s*. 6*d*. ($1.10).

MEETINGS: Fellows and Students may attend all Meetings of the Society including the annual Exhibition of Scientific Instruments and Apparatus.

PUBLICATIONS include the *Proceedings of the Physical Society*, published monthly in two sections, and *Reports on Progress in Physics*, published annually. Volume XVII, 1954, is now available (price 50*s*. ($7.15)). Members are entitled to receive many of the Publications at a reduced rate.

Further information can be obtained from:

THE PHYSICAL SOCIETY

1, LOWTHER GARDENS, PRINCE CONSORT ROAD

LONDON, S.W.7, ENGLAND

CANADIAN JOURNAL OF CHEMISTRY

Notes to Contributors

Manuscripts

(i) ***General.*** Manuscripts, in English or French, should be typewritten, double spaced, on paper 8½ × 11 in. **The original and one copy are to be submitted.** Tables and captions for the figures should be placed at the end of the manuscript. Every sheet of the manuscript should be numbered.

Style, arrangement, spelling, and abbreviations should conform to the usage of this journal. Names of all simple compounds, rather than their formulas, should be used in the text. Greek letters or unusual signs should be written plainly or explained by marginal notes. Superscripts and subscripts must be legible and carefully placed.

Manuscripts and illustrations should be carefully checked before they are submitted. Authors will be charged for unnecessary deviations from the usual format and for changes made in the proof that are considered excessive or unnecessary.

(ii) ***Abstract.*** An abstract of not more than about 200 words, indicating the scope of the work and the principal findings, is required, except in Notes.

(iii) ***References.*** References should be listed **alphabetically by authors' names,** numbered, and typed after the text. The form of the citations should be that used in this journal; in references to papers in periodicals, titles should not be given and only initial page numbers are required. All citations should be checked with the original articles and each one referred to in the text by the key number.

(iv) ***Tables.*** Tables should be numbered in roman numerals and each table referred to in the text. Titles should always be given but should be brief; column headings should be brief and descriptive matter in the tables confined to a minimum. Vertical rules should be used only when they are essential. Numerous small tables should be avoided.

Illustrations

(i) ***General.*** All figures (including each figure of the plates) should be numbered consecutively from 1 up, in arabic numerals, and each figure referred to in the text. The author's name, title of the paper, and figure number should be written in the lower left corner of the sheets on which the illustrations appear. Captions should not be written on the illustrations (see Manuscripts (i)).

(ii) ***Line Drawings.*** Drawings should be carefully made with India ink on white drawing paper, blue tracing linen, or co-ordinate paper ruled in blue only; any co-ordinate lines that are to appear in the reproduction should be ruled in black ink. Paper ruled in green, yellow, or red should not be used unless it is desired to have all the co-ordinate lines show. All lines should be of sufficient thickness to reproduce well. Decimal points, periods, and stippled dots should be solid black circles large enough to be reduced if necessary. Letters and numerals should be neatly made, preferably with a stencil (**do NOT use typewriting**) and be of such size that the smallest lettering will be not less than 1 mm. high when reproduced in a cut 3 in. wide.

Many drawings are made too large; originals should not be more than 2 or 3 times the size of the desired reproduction. In large drawings or groups of drawings the ratio of height to width should conform to that of a journal page but the height should be adjusted to make allowance for the caption.

The original drawings and one set of clear copies (e.g. small photographs) are to be submitted.

(iii) ***Photographs.*** Prints should be made on glossy paper, with strong contrasts. They should be trimmed so that essential features only are shown and mounted carefully, with rubber cement, on white cardboard with no space or only a very small space (less than 1 mm.) between them. In mounting, full use of the space available should be made (to reduce the number of cuts required) and the ratio of height to width should correspond to that of a journal page (4¾ × 7¼ in.); however, allowance must be made for the captions. Photographs or groups of photographs should not be more than 2 or 3 times the size of the desired reproduction.

Photographs are to be submitted in duplicate; if they are to be reproduced in groups one set should be mounted, the duplicate set unmounted.

Reprints

A total of 50 reprints of each paper, without covers, are supplied free. Additional reprints, with or without covers, may be purchased.

Charges for reprints are based on the number of printed pages, which may be calculated approximately by multiplying by 0.6 the number of manuscript pages (double-spaced typewritten sheets, 8½ × 11 in.) and including the space occupied by illustrations. An additional charge is made for illustrations that appear as coated inserts. The cost per page is given on the reprint requisition which accompanies the galley.

Any reprints required in addition to those requested on the author's reprint requisition form must be ordered officially as soon as the paper has been accepted for publication.

Contents

Page

The Geomagnetic Latitude Effect on the Nucleon and Meson Component of Cosmic Rays at Sea Level—*D. C. Rose and J. Katzman* - 1

Some Notes on the Theory of Thermal-neutron Reactors—*J. D. Stewart* - 20

Radiation Resistance of Dipoles in an Interface Between Two Dielectrics—*James R. Wait* - - - - - - - - - - - - - - - 24

Transient Fields of a Vertical Dipole over a Homogeneous Curved Ground—*James R. Wait* - - - - - - - - - - - - - - - 27

Small-angle Scattering of Fast Polarized Neutrons by Heavy Nuclei —*J. T. Sample* - - - - - - - - - - - - - - - - - - - 36

Magnetic Susceptibility of Low Resistivity *n*-Type Germanium—*F. T. Hedgcock* - - - - - - - - - - - - - - - - - - - 43

Meteor Echo Durations and Visual Magnitudes—*Peter M. Millman and D. W. R. McKinley* - - - - - - - - - - - - - - - - 50

A Modification of the One-particle Formula for Nuclear Gamma-radiation—*P. R. Wallace* - - - - - - - - - - - - - - - 62

The Decay of Re^{186} and Re^{188}—*M. W. Johns, C. C. McMullen, I. R. Williams, and S. V. Nablo* - - - - - - - - - - - - - - - 69

The Spectrum of CN in the Vacuum Ultraviolet—*P. K. Carroll* 83

The Effect of Growth Conditions upon the Solidification of a Binary Alloy—*W. A. Tiller and J. W. Rutter* - - - - - - - 96

Observations on Stars and Heavy Primaries Recorded in Emulsions Flown in Viking Rocket No. 9—*Herman Yagoda* - - - - - - 122

Letters to the Editor:

Note on the $T = 3/2$ State in N^{16}—*G. A. Bartholomew, A. E. Litherland, E. B. Paul, and H. E. Gove* - - - - - - - - - 147

The Role of the 1.30 Mev. Gamma-ray in the Decay of In^{111}—*M. W. Johns, I. R. Williams, and D. E. Brodie* - - - - - - - 147

Line Source with Progressive Phase Shift—*R. E. Burgess* - - 149

$\Delta M = \pm 2$ Transitions in Dilute Gadolinium Ethyl Sulphate—*H. A. Buckmaster* - - - - - - - - - - - - - - - - - - 150

Printed in Canada *by* University of Toronto Press